APPLIED COMPUTATIONAL ELECTROMAGNETICS SOCIETY JOURNAL

September 2016
Vol. 31 No. 9
ISSN 1054-4887

The ACES Journal is abstracted in INSPEC, in Engineering Index, DTIC, Science Citation Index Expanded, the Research Alert, and to Current Contents/Engineering, Computing & Technology.

The illustrations on the front cover have been obtained from the research groups at the Department of Electrical Engineering, The University of Mississippi.

THE APPLIED COMPUTATIONAL ELECTROMAGNETICS SOCIETY
http://aces-society.org

EDITOR-IN-CHIEF

Atef Elsherbeni
Colorado School of Mines, EECS Dept.
Golden, CO 80401, USA

ASSOCIATE EDITORS-IN-CHIEF

Sami Barmada
University of Pisa. ESE Dept.
Pisa, Italy, 56122

Mohammed Hadi
Kuwait University, EE Dept.
Safat, Kuwait

Alistair Duffy
De Montfort University
Leicester, UK

Mohamed Bakr
McMaster University, ECE Dept.
Hamilton, ON, L8S 4K1, Canada

Abdul Arkadan
Marquette University, ECE Dept.
Milwaukee, WI 53201, USA

Paolo Mezzanotte
University of Perugia
I-06125 Perugia, Italy

Antonio Musolino
University of Pisa
56126 Pisa, Italy

Marco Arjona López
La Laguna Institute of Technology
Torreon, Coahuila 27266, Mexico

EDITORIAL ASSISTANTS

Matthew J. Inman
University of Mississippi, EE Dept.
University, MS 38677, USA

Shanell Lopez
Colorado School of Mines, EECS Dept.
Golden, CO 80401, USA

EMERITUS EDITORS-IN-CHIEF

Duncan C. Baker
EE Dept. U. of Pretoria
0002 Pretoria, South Africa

Robert M. Bevensee
Box 812
Alamo, CA 94507-0516, USA

Allen Glisson
University of Mississippi, EE Dept.
University, MS 38677, USA

Ahmed Kishk
Concordia University, ECS Dept.
Montreal, QC H3G 1M8, Canada

David E. Stein
USAF Scientific Advisory Board
Washington, DC 20330, USA

EMERITUS ASSOCIATE EDITORS-IN-CHIEF

Yasushi Kanai
Niigata Inst. of Technology
Kashiwazaki, Japan

Levent Gurel
Bilkent University
Ankara, Turkey

Erdem Topsakal
Mississippi State University, EE Dept.
Mississippi State, MS 39762, USA

Alexander Yakovlev
University of Mississippi, EE Dept.
University, MS 38677, USA

Ozlem Kilic
Catholic University of America
Washington, DC 20064, USA

Fan Yang
Tsinghua University, EE Dept.
Beijing 100084, China

EMERITUS EDITORIAL ASSISTANTS

SEPTEMBER 2016 REVIEWERS

THE APPLIED COMPUTATIONAL ELECTROMAGNETICS SOCIETY

JOURNAL

Vol. 31 No. 9 September 2016

TABLE OF CONTENTS

A New Power Series Solution Approach to Solving Electrically Large Complex Electromagnetic Scattering Problems

Sadasiva M. Rao and Michael S. Kluskens

Naval Research Laboratory
Washington DC 20375, USA.

Abstract – In this work, we present a new power series solution procedure to obtain induced currents and scattered fields on a large conducting body due to a plane wave incidence. The procedure follows standard method of moments approach yet is applicable to electrically large problems. The first step involves approximating the given structure via standard geometrical discretization and defining the conventional basis functions to approximate the induced current. The next step involves gathering the total number of basis functions into a small number of groups thereby casting the moment matrix into a collection of submatrices representing self and mutual interaction between the groups. Next, the procedure involves eliminating the interaction of two immediate neighbors on any selected group. This process results in a diagonally-dominant moment matrix assuming the group size is sufficiently large. Also the procedure sets the matrix blocks residing on either side of the diagonal block to zero. The new matrix equation can be solved in many ways efficiently. However, this work proposes using power series approach to obtain accurate solution results. The present approach is simple, efficient, highly amenable for parallel processing, and retains all the advantages of conventional method of moments scheme. Several numerical examples are presented to validate the numerical method.

Index Terms – Electromagnetic fields, Integral equations, Method of moments, Numerical methods.

I. INTRODUCTION

The method of moments (MOM) solution technique [1] - [5], one of the most popular methods for solving electromagnetic scattering and radiation problems, is limited by excessive computational and memory requirements if applied in a conventional way to electrically large scattering problems. The objective of the present work is to overcome this MOM limitation and apply the procedure to truly complex and practical problems.

There exist several new algorithms which seem to overcome the limitation of MOM. Notable among them are: a) recently developed fast multipole method (FMM) using matrix approximations to reduce the memory and computational time requirements [6], and adaptive cross approximation (ACA) method [7]. However, both are approximate methods and the accuracy of the overall solution depends on the level approximation and may become expensive when high accuracy solutions are desired. Further, FMM also sacrifices one of the most important advantages of MOM, i.e., the ability to handle multiple right hand sides in a simple manner.

In a recent work, Killian et al. [8] have proposed a method to solve the electromagnetic scattering by electrically large conducting bodies via MOM. The procedure involves dividing the body into relatively large subsections and, using some simple numerical steps, the mutual-coupling between a given subsection and related nearby subsections is transformed into self-coupling. The resulting current distribution, sufficiently accurate on major part of the body, is later improved to the desired degree of accuracy on the whole body by using an iterative scheme. Although the central idea of this procedure is quite novel, the numerical procedure presented is cumbersome, inefficient, and not easily applicable to complex practical problems.

The present work adopts the central idea of [8]. However, the new procedure presented here completely modifies the numerical scheme using several important steps. The present procedure is more efficient by several orders, very stable, accurate and easily and efficiently applicable to complex practical problems. The modifications and resulting novelty of the new procedure are enumerated in the following:

- For the new procedure to work well, a diagonally-strong, preferably diagonally-

Submitted On: February 5, 2016
Accepted On: March 14, 2016

dominant, moment matrix is required to begin with. A simple scheme is devised in this work to obtain such a moment matrix for complex two and three-dimensional objects. The scheme involves renumbering the basis functions using a distance criterion and adopting Galerkin scheme wherein the basis functions are also used as testing functions. We note that this step is the most important modification as discussed further.

- The cumbersome search process for the near-field basis functions, necessary for the algorithm presented in [8] but made the procedure inefficient, is totally eliminated. This step makes the algorithm not only fast but also highly suitable for parallel processing, and much more user-friendly.
- The new method involves dividing the total number of basis functions into groups of equal size. The equal size criterion makes the algorithm much more simple and efficient than [8].
- The mathematical steps in the new algorithm are simple and represent mere algebraic manipulations. Hence, any standard MOM algorithm can be easily converted into adopting the procedure presented in this work.

In the following section, we present the detailed mathematical steps describing the algorithm. In Section III, we present several important empirical guidelines to apply the procedure successfully. In Section IV, we present several numerical results to test the validity of the technique. Finally, Section V discusses important conclusions along with possible improvements and future work to be undertaken in this area.

II. NUMERICAL SOLUTION PROCEDURE

Consider an electrically large perfectly electric conductor (PEC) problem given by,

$$\boldsymbol{L}\boldsymbol{I} = \boldsymbol{V}, \tag{1}$$

where $\boldsymbol{L}$, $\boldsymbol{I}$, and $\boldsymbol{V}$, are the integral equation operator, unknown vector describing the induced currents, and known excitation vector representing the incident field, respectively. The integral equation operator adopted in this work is the combined field operator given by,

$$\begin{aligned} \boldsymbol{Z}_{CFIE} &= \gamma \boldsymbol{Z}_{EFIE} + \eta(1-\gamma)\boldsymbol{Z}_{MFIE}, & (2)\\ \boldsymbol{Y}_{CFIE} &= \gamma \boldsymbol{Y}_{EFIE} + \eta(1-\gamma)\boldsymbol{Y}_{MFIE}, & (3) \end{aligned}$$

where $0 \leq \gamma \leq 1$ is a constant depending on the problem and η is the impedance of the medium. For open body problems, we let $\gamma = 1$ and for closed bodies γ is typically 0.5. In Eq. (3), the quantities $\boldsymbol{Z}_{EFIE}$, $\boldsymbol{Z}_{MFIE}$ represent $N \times N$ matrices and $\boldsymbol{Y}_{EFIE}$ and $\boldsymbol{Y}_{MFIE}$ represent $N \times 1$ column actors, respectively, where N represents the number of the unknowns in the MOM scheme. Further, these quantities are obtained by applying the MOM procedure to the integral equations given by,

$$\boldsymbol{E}^{i}_{tan}(\boldsymbol{r}) + \boldsymbol{E}^{s}_{tan}(\boldsymbol{r}) = 0,\ \boldsymbol{r} \in S_c \tag{4}$$

and

$$\boldsymbol{J}(\boldsymbol{r}) = \hat{n} \times (\boldsymbol{H}^{i}(\boldsymbol{r}) + \boldsymbol{H}^{s}(\boldsymbol{r})),\ \boldsymbol{r} \in S_c \tag{5}$$

where $(\boldsymbol{E}^i, \boldsymbol{H}^i)$ and $(\boldsymbol{E}^s, \boldsymbol{H}^s)$ are the incident and scattered fields, respectively, $\boldsymbol{J}$ is the induced current, S_c is the conductor surface, $\hat{n}$ represents the unique outward normal to S_c, and the subscript "*tan*" represents the tangential component.

To begin the numerical procedure we follow the conventional MOM and approximate the current distribution on the given electrically large perfectly conducting (PEC) structure using standard subdomain functions. Thus, for two dimensional problems we use linear segments and define pulse basis functions [3]; whereas, for three dimensional problems, we use planar triangular subsections and define Rao-Wilton-Glisson (RWG) basis functions [9] for the solution of electromagnetic scattering problem.

Next, we order the basis functions using a distance criterion measured from a reference point, either from one end of the scatterer or from a convenient point on the scatterer. This arrangement makes the first basis function closest to the reference point and the last one the farthest. This is a very important step in the new algorithm which eventually eliminates the cumbersome search procedure for nearest neighbors adopted in [8]. We also note that the actual location of the reference point is of no importance and does not affect the final results in any way.

Using the basis functions also as testing functions and following the standard method of moments procedure, the operator equation can be transformed into a matrix equation given by,

$$\boldsymbol{Z}\boldsymbol{X} = \boldsymbol{Y}. \tag{6}$$

where $\boldsymbol{Z} = \boldsymbol{Z}_{CFIE}$ is a $N \times N$ matrix and $\boldsymbol{X}$ and $\boldsymbol{Y} = \boldsymbol{Y}_{CFIE}$ are the unknown and known column vectors of dimension N, respectively. Note that, because of the re-ordering of the basis functions as mentioned before, in each row of the $\boldsymbol{Z}$-matrix, the diagonal element is the largest element magnitude-wise and off-diagonal elements progressively decrease away from the diagonal element.

Next, we assemble the total number of basis functions into groups with each group containing a fixed number of micro-basis functions. Here, we note that each group corresponds to a block of elements in the global MOM matrix. Again, this step is in contrast to the procedure adopted in [8] where each group may have different size making the bookkeeping cumbersome.

Let us divide the N basis functions into P groups, with $M = N/P$ elements in each group. The $\boldsymbol{Z}$-matrix may be written as:

$$\boldsymbol{Z} = \begin{bmatrix} \boldsymbol{Z}_{11} & \boldsymbol{Z}_{12} & \boldsymbol{Z}_{13} & \cdots & \boldsymbol{Z}_{1P} \\ \boldsymbol{Z}_{21} & \boldsymbol{Z}_{22} & \boldsymbol{Z}_{23} & \cdots & \boldsymbol{Z}_{2P} \\ \boldsymbol{Z}_{31} & \boldsymbol{Z}_{32} & \boldsymbol{Z}_{33} & \cdots & \boldsymbol{Z}_{3P} \\ \vdots & \vdots & \vdots & \vdots & \vdots \\ \boldsymbol{Z}_{P1} & \boldsymbol{Z}_{P2} & \boldsymbol{Z}_{P3} & \cdots & \boldsymbol{Z}_{PP} \end{bmatrix}, \tag{7}$$

where each $\boldsymbol{Z}_{ij}, i = 1, 2, \cdots, P, j = 1, 2, \cdots, P$ represents a submatrix of $M \times M$. In a similar manner, we can express the column vector $\boldsymbol{Y}$ as:

$$\boldsymbol{Y} \;=\; [\boldsymbol{Y}_1, \boldsymbol{Y}_2, \boldsymbol{Y}_3, \cdots, \boldsymbol{Y}_P]^T, \tag{8}$$

where the superscript "T" represents the transpose.

Next, we transform the Eq. (6) to,

$$\tilde{\boldsymbol{Z}}\boldsymbol{X} = \tilde{\boldsymbol{Y}}, \tag{9}$$

where $\tilde{\boldsymbol{Z}} = \boldsymbol{R}_1\boldsymbol{Z}$, $\tilde{\boldsymbol{Y}} = \boldsymbol{R}_1\boldsymbol{Y}$, and

$$\boldsymbol{R}_1 \;=\; \begin{bmatrix} \boldsymbol{I} & \boldsymbol{R}_{12} & \boldsymbol{R}_{13} & \boldsymbol{O} & \boldsymbol{O} & \boldsymbol{O} \\ \boldsymbol{O} & \boldsymbol{I} & \boldsymbol{O} & \boldsymbol{O} & \boldsymbol{O} & \boldsymbol{O} \\ \boldsymbol{O} & \boldsymbol{O} & \boldsymbol{I} & \boldsymbol{O} & \boldsymbol{O} & \boldsymbol{O} \\ \vdots & \vdots & \vdots & \vdots & \vdots & \vdots \\ \boldsymbol{O} & \boldsymbol{O} & \boldsymbol{O} & \boldsymbol{O} & \cdots & \boldsymbol{I} \end{bmatrix}. \tag{10}$$

$\boldsymbol{R}_{12}$ and $\boldsymbol{R}_{13}$ are $M \times M$ matrices with unknown coefficients, and $\boldsymbol{I}$ and $\boldsymbol{O}$ are $M \times M$ identity and null matrices, respectively.

Considering the first row of the $\tilde{\boldsymbol{Z}}$-matrix, we have:

$$\begin{aligned} \tilde{\boldsymbol{Z}}_{11} &= \boldsymbol{Z}_{11} + \boldsymbol{R}_{12}\boldsymbol{Z}_{21} + \boldsymbol{R}_{13}\boldsymbol{Z}_{31} \\ \tilde{\boldsymbol{Z}}_{12} &= \boldsymbol{Z}_{12} + \boldsymbol{R}_{12}\boldsymbol{Z}_{22} + \boldsymbol{R}_{13}\boldsymbol{Z}_{32} \\ \tilde{\boldsymbol{Z}}_{13} &= \boldsymbol{Z}_{13} + \boldsymbol{R}_{12}\boldsymbol{Z}_{23} + \boldsymbol{R}_{13}\boldsymbol{Z}_{33} \\ \vdots\;\; & \vdots \;\; \vdots \\ \tilde{\boldsymbol{Z}}_{1P} &= \boldsymbol{Z}_{1P} + \boldsymbol{R}_{12}\boldsymbol{Z}_{2P} + \boldsymbol{R}_{13}\boldsymbol{Z}_{3P}. \end{aligned}$$

Next, we solve for $\boldsymbol{R}_{12}$ and $\boldsymbol{R}_{13}$ by forcing the elements of $\tilde{\boldsymbol{Z}}_{12}$ and $\tilde{\boldsymbol{Z}}_{13}$ to zero. Thus, we solve

$$\boldsymbol{Z}_{12} + \boldsymbol{R}_{12}\boldsymbol{Z}_{22} + \boldsymbol{R}_{13}\boldsymbol{Z}_{32} \;=\; 0, \tag{11}$$

$$\boldsymbol{Z}_{13} + \boldsymbol{R}_{12}\boldsymbol{Z}_{23} + \boldsymbol{R}_{13}\boldsymbol{Z}_{33} \;=\; 0, \tag{12}$$

simultaneously, which results in a solution of $2M \times 2M$ matrix with M right hand sides. Once, $\boldsymbol{R}_{12}$ and $\boldsymbol{R}_{13}$ are known, it is trivial to obtain $\tilde{\boldsymbol{Y}}$. Note that the procedure described so far sets the interaction between groups 1 and 2 ($\tilde{\boldsymbol{Z}}_{12}$) and between groups 1 and 3 ($\tilde{\boldsymbol{Z}}_{13}$) to zero and makes $\tilde{\boldsymbol{Z}}_{11}$ dominant block in the row.

By applying a similar procedure to rows $2, 3, \cdots, P$ and each time solving a $2M \times 2M$ matrix, we can generate a new matrix equation, given by,

$$\overline{\boldsymbol{Z}}\boldsymbol{X} = \overline{\boldsymbol{Y}}, \tag{13}$$

where the new $\overline{\boldsymbol{Z}}$-matrix is given by

$$\begin{bmatrix} \tilde{\boldsymbol{Z}}_{11} & \boldsymbol{O} & \boldsymbol{O} & \cdots & \tilde{\boldsymbol{Z}}_{1,P-2} & \tilde{\boldsymbol{Z}}_{1,P-1} & \tilde{\boldsymbol{Z}}_{1P} \\ \boldsymbol{O} & \tilde{\boldsymbol{Z}}_{22} & \boldsymbol{O} & \cdots & \tilde{\boldsymbol{Z}}_{2,P-2} & \tilde{\boldsymbol{Z}}_{2,P-1} & \tilde{\boldsymbol{Z}}_{2P} \\ \tilde{\boldsymbol{Z}}_{31} & \boldsymbol{O} & \tilde{\boldsymbol{Z}}_{33} & \cdots & \tilde{\boldsymbol{Z}}_{3,P-2} & \tilde{\boldsymbol{Z}}_{3,P-1} & \tilde{\boldsymbol{Z}}_{3P} \\ \vdots & \vdots & \vdots & \vdots & \vdots & \vdots & \vdots \\ \tilde{\boldsymbol{Z}}_{P1} & \tilde{\boldsymbol{Z}}_{P2} & \tilde{\boldsymbol{Z}}_{P3} & \cdots & \boldsymbol{O} & \boldsymbol{O} & \tilde{\boldsymbol{Z}}_{PP} \end{bmatrix}$$

and

$$\overline{\boldsymbol{Y}} \;=\; \left[\tilde{\boldsymbol{Y}}_1, \tilde{\boldsymbol{Y}}_2, \tilde{\boldsymbol{Y}}_3, \tilde{\boldsymbol{Y}}_4, \cdots, \tilde{\boldsymbol{Y}}_P\right]^T.$$

We note that the $\overline{\boldsymbol{Z}}$-matrix in Eq. (13) represents a diagonally-dominant matrix assuming sufficient number of basis functions are collected in a group.

Next, let $\overline{\boldsymbol{Z}} = \overline{\boldsymbol{Z}}_d + \overline{\boldsymbol{Z}}_{off}$ where $\overline{\boldsymbol{Z}}_d$ includes only diagonal blocks of the $\overline{\boldsymbol{Z}}$-matrix and $\overline{\boldsymbol{Z}}_{off}$-matrix includes the remaining blocks. We now have,

$$\begin{aligned} \left[\overline{\boldsymbol{Z}}_d + \overline{\boldsymbol{Z}}_{off}\right]\boldsymbol{X} &= \overline{\boldsymbol{Y}} \\ \Rightarrow \overline{\boldsymbol{Z}}_d\left[\boldsymbol{I} + \overline{\boldsymbol{Z}}_d^{-1}\overline{\boldsymbol{Z}}_{off}\right]\boldsymbol{X} &= \overline{\boldsymbol{Y}} \\ \Rightarrow \left[\boldsymbol{I} + \overline{\boldsymbol{Z}}_d^{-1}\overline{\boldsymbol{Z}}_{off}\right]\boldsymbol{X} &= \overline{\boldsymbol{Z}}_d^{-1}\overline{\boldsymbol{Y}} \\ \Rightarrow [\boldsymbol{I} + \boldsymbol{U}]\boldsymbol{X} &= \boldsymbol{X}_0. \end{aligned} \tag{14}$$

In Eq. (14), $\boldsymbol{X}_0 = \overline{\boldsymbol{Z}}_d^{-1}\overline{\boldsymbol{Y}}$ and $\boldsymbol{U} = \overline{\boldsymbol{Z}}_d^{-1}\overline{\boldsymbol{Z}}_{off}$.

Finally, the solution $\boldsymbol{X}$ may be obtained by expanding Eq. (14) in power series as,

$$\begin{aligned} \boldsymbol{X} &= [\boldsymbol{I} + \boldsymbol{U}]^{-1}\boldsymbol{X}_0 \\ &= \left[\boldsymbol{I} - \boldsymbol{U} + \boldsymbol{U}^2 - \boldsymbol{U}^3 + \cdots\right]\boldsymbol{X}_0 \\ &= \boldsymbol{X}_0 - \boldsymbol{U}\boldsymbol{X}_0 + \boldsymbol{U}[\boldsymbol{U}\boldsymbol{X}_0] \\ &\quad -\boldsymbol{U}(\boldsymbol{U}[\boldsymbol{U}\boldsymbol{X}_0]) + \cdots. \end{aligned} \tag{15}$$

The necessary and sufficient condition for the power series in Eq. (15) to converge is the Frobenius norm [10] $||\boldsymbol{U}|| \leq 1$. To achieve this condition, it may be easier to enforce $||\overline{\boldsymbol{Z}}_d^{-1}|| \cdot ||\overline{\boldsymbol{Z}}_{off}|| \leq 1$. The norms of $\overline{\boldsymbol{Z}}_d^{-1}$ and $\overline{\boldsymbol{Z}}_{off}$ can be easily computed while generating these terms and ensure that the necessary condition is satisfied. Alternatively, one may adopt the following procedure.

We note that,

$$\begin{aligned} ||\overline{\boldsymbol{Z}}_d^{-1}|| &= \frac{||\overline{\boldsymbol{Z}}_d^{-1}|| \cdot ||\overline{\boldsymbol{Z}}_d\boldsymbol{X}_0||}{||\overline{\boldsymbol{Z}}_d\boldsymbol{X}_0||} \\ &\leq \frac{||\overline{\boldsymbol{Z}}_d^{-1}|| \cdot ||\overline{\boldsymbol{Z}}_d|| \cdot ||\boldsymbol{X}_0||}{||\overline{\boldsymbol{Y}}||} \\ &= \kappa_d\frac{||\boldsymbol{X}_0||}{||\overline{\boldsymbol{Y}}||}, \end{aligned} \tag{16}$$

where $\kappa_d = ||\overline{\boldsymbol{Z}}_d^{-1}|| \cdot ||\overline{\boldsymbol{Z}}_d||$ represents the condition number of $\overline{\boldsymbol{Z}}_d$.

Next, we define $\overline{\boldsymbol{Y}}_e = \overline{\boldsymbol{Z}}\boldsymbol{X}_0 - \overline{\boldsymbol{Z}}_d\boldsymbol{X}_0 = \overline{\boldsymbol{Z}}_{off}\boldsymbol{X}_0$ and we have,

$$\begin{aligned} ||\overline{\boldsymbol{Z}}_{off}|| &= \frac{||\overline{\boldsymbol{Z}}_{off}|| \cdot ||\overline{\boldsymbol{Z}}_{off}^{-1}\overline{\boldsymbol{Y}}_e||}{||\overline{\boldsymbol{Z}}_{off}^{-1}\overline{\boldsymbol{Y}}_e||} \\ &\le \frac{||\overline{\boldsymbol{Z}}_{off}|| \cdot ||\overline{\boldsymbol{Z}}_{off}^{-1}|| \cdot ||\overline{\boldsymbol{Y}}_e||}{||\boldsymbol{X}_0||} \\ &= \kappa_{off}\frac{||\overline{\boldsymbol{Y}}_e||}{||\boldsymbol{X}_0||}, \end{aligned} \tag{17}$$

where $\kappa_{off} = ||\overline{\boldsymbol{Z}}_{off}^{-1}|| \cdot ||\overline{\boldsymbol{Z}}_{off}||$ represents the condition number of $\overline{\boldsymbol{Z}}_{off}$.

Combining Eqs. (16) and (17), we have,

$$||\overline{\boldsymbol{Z}}_d^{-1}|| \cdot ||\overline{\boldsymbol{Z}}_{off}|| \le \kappa_d\kappa_{off}\frac{||\overline{\boldsymbol{Y}}_e||}{||\overline{\boldsymbol{Y}}||} \tag{18}$$

and, to satisfy the condition $||\boldsymbol{U}|| \le 1$, we must ensure that

$$\frac{||\overline{\boldsymbol{Y}}_e||}{||\overline{\boldsymbol{Y}}||} \le \frac{1}{\kappa_d\kappa_{off}}. \tag{19}$$

We note that, it is not really necessary to compute the condition numbers κ_d and κ_{off} but ensure that the fraction $\frac{||\overline{\boldsymbol{Y}}_e||}{||\overline{\boldsymbol{Y}}||}$ is a small number. Our various numerical experiments suggested that this number must be less than 0.4. It is because the described numerical implementation ensures that matrices $\overline{\boldsymbol{Z}}_d$ and $\overline{\boldsymbol{Z}}_{off}$ are well-conditioned matrices. Obviously, if the $\frac{||\overline{\boldsymbol{Y}}_e||}{||\overline{\boldsymbol{Y}}||}$ is not less than the empirical value then the solution may diverge and the procedure needs to be reimplemented by increasing the group size.

Alternatively, it is also possible to solve Eq. (13) by carrying out the following mathematical and numerical operations:

1. Obtain $\boldsymbol{X}_0$ as before by solving the equation $\overline{\boldsymbol{Z}}_d\boldsymbol{X}_0 = \overline{\boldsymbol{Y}}$.
2. Obtain $\overline{\boldsymbol{Y}}_0$ by performing $\overline{\boldsymbol{Y}}_0 = \overline{\boldsymbol{Z}}\boldsymbol{X}_0$. Then, we have $\overline{\boldsymbol{Z}}\boldsymbol{X} = \overline{\boldsymbol{Y}}$ and $\overline{\boldsymbol{Z}}\boldsymbol{X}_0 = \overline{\boldsymbol{Y}}_0$.
3. Thus, we have $\overline{\boldsymbol{Z}}(\boldsymbol{X} - \boldsymbol{X}_0) = (\overline{\boldsymbol{Y}} - \overline{\boldsymbol{Y}}_0)$, which is in the same form as Eq. (13). Hence, the process can be repeated till we have convergence. Note that, for the iterative process to converge, we must satisfy Eq. (19).

III. IMPLEMENTATION, GUIDELINES, AND OBSERVATIONS

The procedure developed so far can be applied to any MOM problem involving PEC bodies. Assuming that we have an electrically large problem to solve, we present a few important pointers to develop the solution in an efficient manner:

- **Implementation**
    - **Symmetric matrix** - We note that the procedure described so far uses same functions for expansion and testing resulting in Galerkin procedure and symmetric $\boldsymbol{Z}$-matrix. However, it is common to use approximations in the testing procedure thus destroying the symmetry property [9]. This problem can be easily remedied by taking the average of Z_{ij} and Z_{ji} for $j = 1, 2, \cdots, N$ and $i = 1, 2, \cdots, j$. This procedure is fairly common and, given reasonable number of unknowns for the problem, does not result in loss of accuracy [9]. In fact, many commercial algorithms prefer this approach to take advantage of the symmetric matrix and thereby reducing the storage requirements.
    - **Sorting the basis functions** - The algorithm requires that the basis functions be ordered according to distance measured from a reference point. The placement of the reference point is not critical. It may be placed at one end or just outside the structure. It is quite easy to measure the distance to the center of each basis function i.e., to the center of the linear segment (edge) for two (three) dimensional problems. Then, one may use any efficient sorting algorithm to order the basis functions.
    - **Generating groups** - The geometry of the problem is divided up into disjoint groups. One way of obtaining the number of groups is to select a reasonable group size, i.e., number of basis functions in the group, and divide the total number of basis functions by the group size. It is important to note that a relatively few number of basis functions in a group would cause the solution to diverge. Hence, it is recommended to make the group division using distance criterion such as 0-10λ in the first group, 10-20λ in the second group, and so on for two dimensional problems, assuming the reference point is the center of the first basis function. For three dimensional problems, the guide lines are 0-3λ in the first group, 3-6λ in the second group, and so on. Further, it is also recommended that one would be better off by choosing as many number of basis functions in a group as possible since it would make the power series solution to converge faster.

  - **Storage requirements** - Note that it is efficient to store only the diagonal blocks of the $\overline{\boldsymbol{Z}}$-matrix and the coefficient matrices. Thus, the storage required is $P*M^2 = N*M$ for diagonal blocks and $2P*M^2 = 2N*M$ for coefficient matrices. The $\boldsymbol{U}$-matrix is not stored and computed as needed since only a couple terms in the power series are needed for accurate solution. Thus, the total required storage is $3N*M$.
- **Guidelines**
  - It is necessary, convenient, and hence, recommended to perform sorting and grouping before beginning the electromagnetic solution. However, this only needs to be done once.
  - One may develop a simple algorithm to develop the diagonal blocks of $\overline{\boldsymbol{Z}}$-matrix and may be performed either serially or in parallel. Obviously, parallel solution reduces the computation time drastically and one can achieve almost linear efficiency with the number of processors since computation of each block is independent from another block.
  - If a sufficient number of basis functions are assembled into a group, only a few terms are required in the power series solution. Generally, one or two terms are sufficient for accurate solution. For very large problems involving several hundred thousand unknowns, it is recommended to use as much a large group matrix as possible. For such cases, even one term in the power series may be sufficient. It is cautioned that an insufficiently smaller group size may require large number of terms in the power series to converge and may even diverge.
- **Observations**
  - We observe that, although the numerical procedure presented in this work is a substantial improvement to [8], the remarks concerning the usage of CPU time, parallel processing, and efficiency are also applicable for the present work. Further, this procedure eliminates several time consuming steps and hence results in higher efficiency. In Table 1, we present the actual elapsed CPU time, in seconds, for conventional MOM procedure and power series procedure. The computer used for this purpose is Intel Core2 computer at 2.66 GHz clock speed running a single thread. We note that the computational times in this work follow $\bigcirc(N^2)$ trend.

Table 1: The elapsed tine in seconds as a function of unknowns

No. of Unknowns	MOM	Power Series
792	3.04	4.72
2,997	45	34
6,270	410	294
8,355	916.18	441
13,500	3,662	1,645
25,080	22, 353	5,204
53,856	147,600	27,720

  - Since this procedure is designed to handle electrically large problems, one may be able to judiciously vary the order of integration depending upon the location of source and field points.
  - We observe that the procedure presented in this work is more amenable for parallel processing as compared to the conventional MOM. To illustrate this point, we present an almost linear scaling of the CPU time with number of processors as shown in Fig. 1. Note that a ship like object modeled with 216,000 basis functions and a group size of 1400 is used for generating this data.

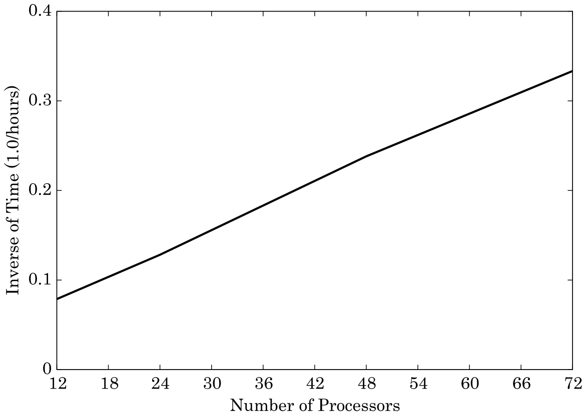

Fig. 1. Inverse of elapsed time as a function of number of processors.

IV. NUMERICAL RESULTS

In this section, we present a few representative numerical results involving both two- and three-dimensional bodies for validation purposes. We present the bistatic/monostatic radar cross section (RCS) calculations of several objects and compare either with the standard method of moments solution or exact solution where available. We note that the current distribution is also checked and found to be of the same level of accuracy as the RCS for all the

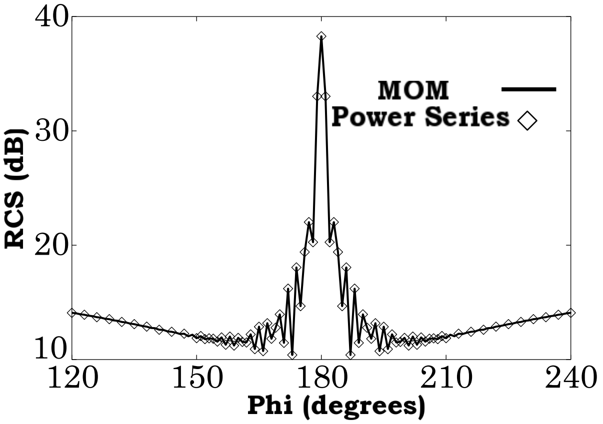

Fig. 2. RCS of a two-dimensional conducting cir-cular cylinder of 100λ circumference illuminated by a TM wave.

representative examples even though we present current distribution on a three-dimensional finite cylinder case only for the sake of completeness. Further, for all the results presented in this section, only two terms are used in the power series solution.

The first example is a two-dimensional circular cylinder with a perimeter=100λ illuminated by a transverse magnetic (TM) plane wave. The circumference of the cylinder is divided into 1000 linear segments. Figure 2 shows the bistatic RCS as a function of the azimuthal angle ϕ. We compare the results of the present method with the standard MOM solution. For the present solution, the total number of basis functions has been grouped into 5 groups. The comparison is excellent between these two procedures.

The next example is a two-dimensional square cylinder, side length=50λ, illuminated by TM plane wave as shown in the inset of Fig. 3. The square cross section is approximated by 2,000 unknowns for MOM solution. For the present method, the group size is 200 with 10 groups in total. We present the bistatic RCS as a function of the azimuthal angle ϕ and compare with MOM solution as shown in Fig. 3. The comparison is excellent for this example also.

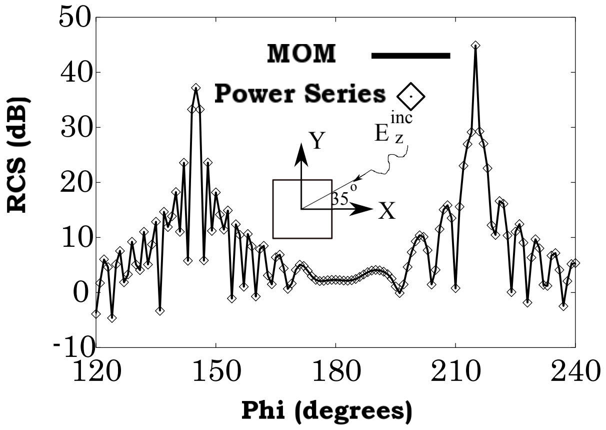

Fig. 3. RCS of a two-dimensional square cylinder of 200λ circumference illuminated by a TM wave.

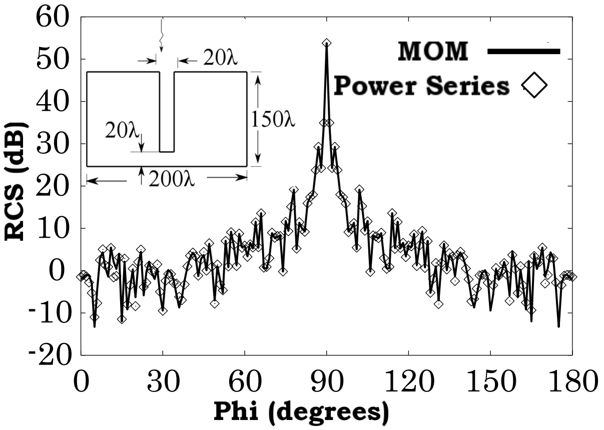

Fig. 4. RCS of a two-dimensional complex cross-section cylinder of 960λ circumference illuminated by a TM wave.

As a third example, we consider a two dimensional cylinder with complex cross section illuminated by TM plane wave as shown in the inset Fig. 4. The total circumference of the cylinder is 960λ, approximated by 9,600 unknowns, and divided into 5 groups for the present solution. Figure 4 shows the bistatic RCS compared as a function of the azimuthal angle ϕ to the MOM solution.

Next, we present the case of a large circular cylinder with a circumference of 100,000λ. The circumference is approximated by one million unknowns and divided into 1000 groups. Once again, only two terms in the power series solution is used. The RCS for this case is shown in Fig. 5. Although no comparison is shown here, this case is presented to highlight the capability of the present method to easily handle very large problems.

Next, we consider three-dimensional problems.

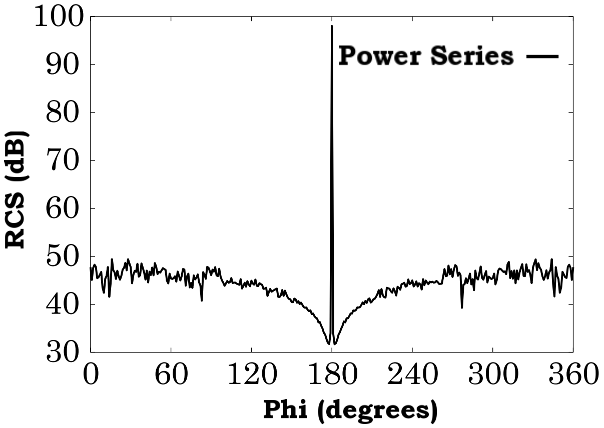

Fig. 5. RCS of a two-dimensional conducting cir-cular cylinder of 100, 000λ circumference illuminated by a TM wave.

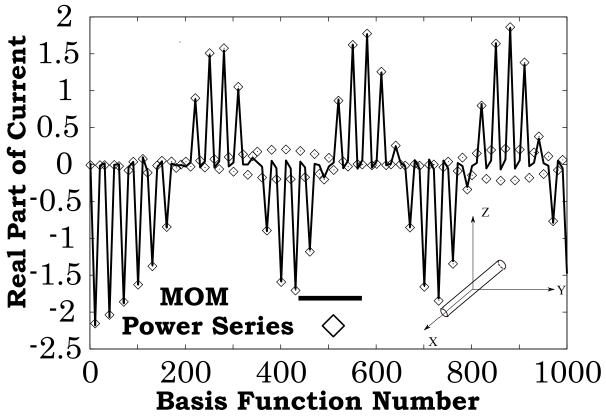

Fig. 6. Real part of the current distribution on a three-dimensional conducting cylinder, $L = 20\lambda$ and radius $a = 0.318\lambda$, placed along the x-axis illuminated by a x-polarized, z-traveling plane wave.

Consider a long conducting cylinder, $L = 20\lambda$ and radius $a = 0.318\lambda$, closed at both ends.The cylinder is placed along the x-axis and illuminated by a x-polarized plane wave traveling along the z-axis. The cylinder is approximated by 6270 RWG basis functions. For the present solution method, the total number of basis functions are divided into 10 groups with each group consisting 627 basis functions. In Fig. 6, we present the real part of the induced current as a function of basis function numbers. Note that only a part of the figure, i.e., basis functions from 1 to 1000, is presented for the sake of clarity. The bistatic RCS for this case is shown in the Fig. 7 and compared with the MOM solution. We note a good comparison of the present method with MOM solution for both current distribution and RCS. Although not presented here, the imaginary part of the current shows similar level of comparison.

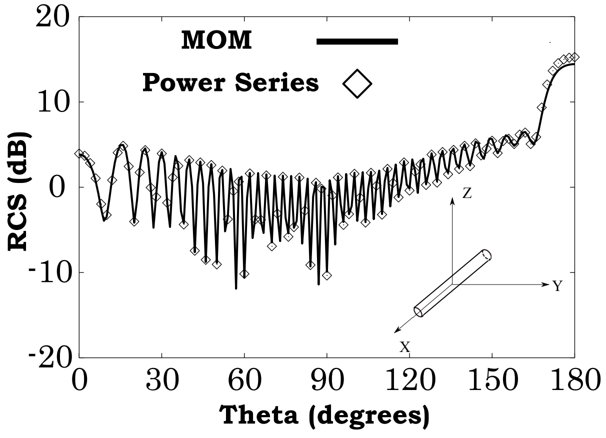

Fig. 7. RCS of a three-dimensional conducting cylinder, $L = 20\lambda$ and radius $a = 0.318\lambda$, placed along the x-axis illuminated by a x-polarized, z-traveling plane wave.

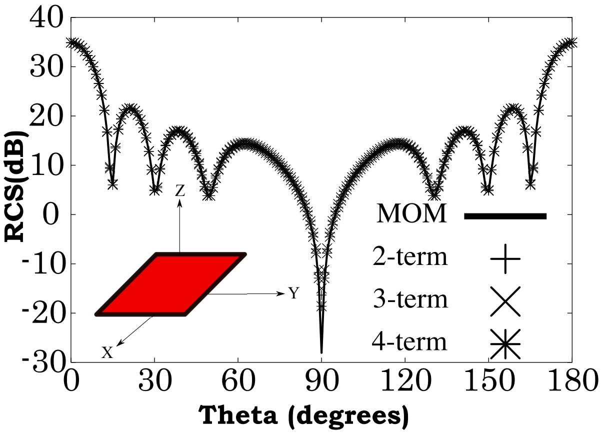

Fig. 8. RCS of a three-dimensional conducting square plate, $L = 4\lambda$, placed along the xy-plane il-luminated by a x-polarized, z-traveling plane wave.

Next, consider a 4λ square plate placed in the xy-plane and illuminated by a x-polarized plane wave traveling along the z-axis. The plate is approximated by 5,000 triangles resulting in 7,400 basis functions. For the present solution method, the total number of basis functions are divided into 10 groups with each group consisting of 740 basis functions. The bistatic RCS for this case is shown in the Fig. 8 and compared with the MOM solution. The comparison of the present method with MOM solution is again very good except at $\theta = 90^0$ where the MOM procedure presents a deeper null. For this example, we added more terms in the power series to show the convergence of the procedure. It is noted that after two terms, the results did not change appreciably except at the null region.

Next, we consider two conducting spheres, with radii of 3.0λ and and 5.0λ illuminated by a x-polarized plane wave traveling along the z-axis. The

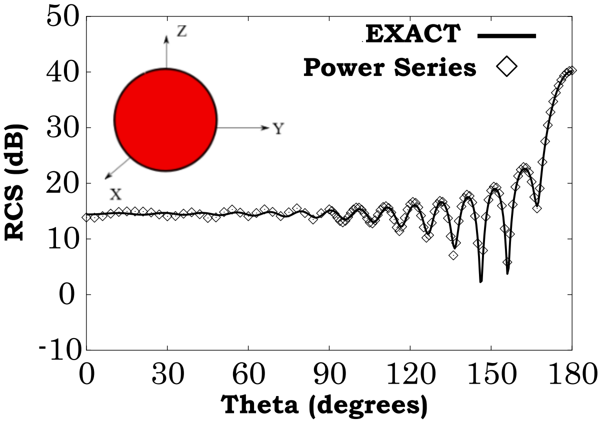

Fig. 9. RCS of a three-dimensional conducting sphere, radius $a = 3\lambda$, placed with center coinciding with the origin and illuminated by a x-polarized, z-traveling plane wave. Number of unknowns=29,400. Number of groups=50.

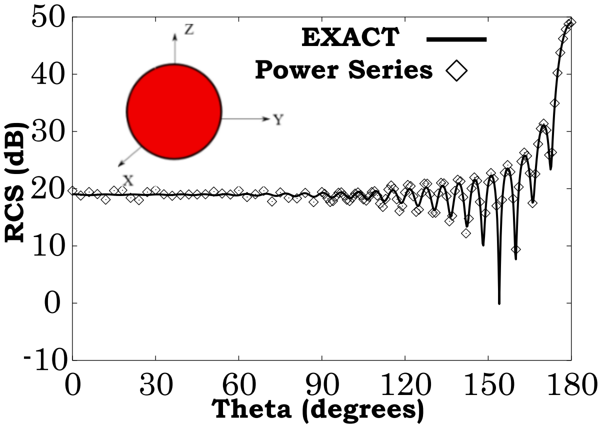

Fig. 10. RCS of a three-dimensional conducting sphere, radius $a = 5\lambda$, placed with center coinciding with the origin and illuminated by a x-polarized, z-traveling plane wave. Number of unknowns=93,750. Number of groups=125.

spheres are approximated by 29,400 and 93,750 basis functions, respectively. The group size for the 3.0λ case is 588 implying 50 groups in total. Similarly, the group size for the 5.0λ case is 750 and a total of 125 groups. The bistatic RCS for these two cases is shown in the Figs. 9 and 10, respectively and compared with exact Mie series [11] solution. We note a reasonably good comparison for each example with only two terms in the power series.

Now, we consider more complex, non-canonical objects to illustrate the usefulness of the proposed method. Consider an aircraft-type model illuminated by a x-polarized plane wave traveling along the z-axis. The object is located in the XY-plane with nose along the x-axis. The largest dimensions of the aircraft along x, y and z directions are 11.6λ, 9.2λ, and 1.6λ, respectively. The aircraft is approximated by 25,080 basis functions as shown in Fig. 11. For the power series solution, the total number of basis functions is divided into 12 groups with 2090 basis functions in each group. The bistatic RCS along XZ-plane is shown in Fig. 12. The power series solution is compared with MOM solution and we note a reasonably good comparison for this complex structure.

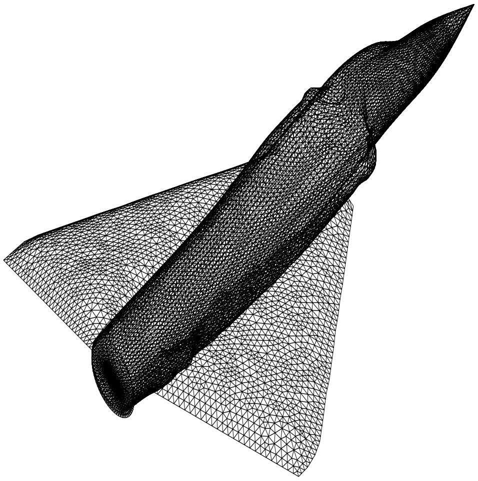

Fig. 11. Triangulated model of an aircraft.

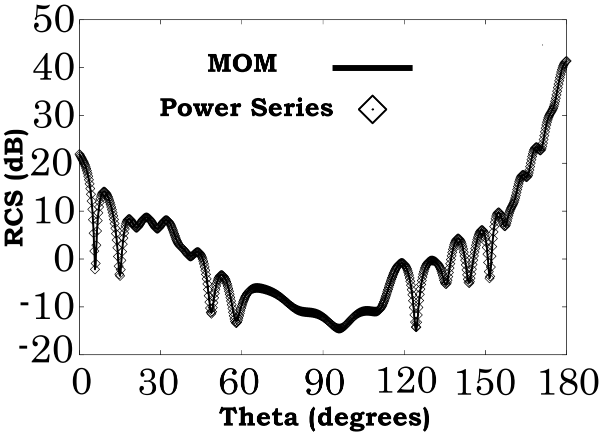

Fig. 12. RCS of an aircraft-type object. Number of unknowns=25,080. Number of groups=12.

Next, we consider a 91 meter ship-like object illuminated by a 100 MHz, x-polarized plane wave traveling along the z-axis. The width and length of the object is along the x and y-axis, respectively. The largest dimensions of the ship-like object along x, y and z directions are 7.5m, 91.5m and 12.4m, respectively. The ship-like object is approximated by 53,832 basis functions as shown in the inset of Fig. 13. For the power series solution, the total number of basis functions is divided into 20 groups with

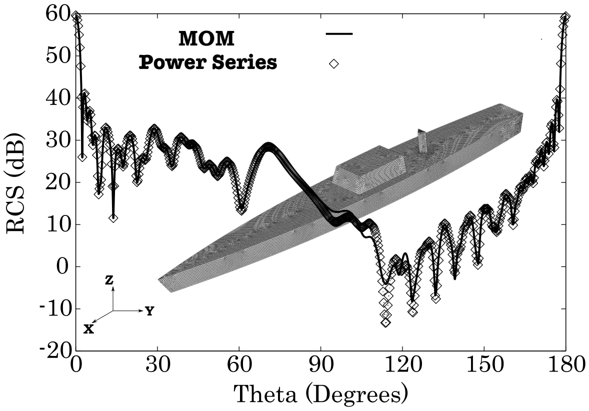

Fig. 13. Bistatic RCS of a 91 m ship-type object at 100 MHz. Number of unknowns=53,856. Number of groups=20.

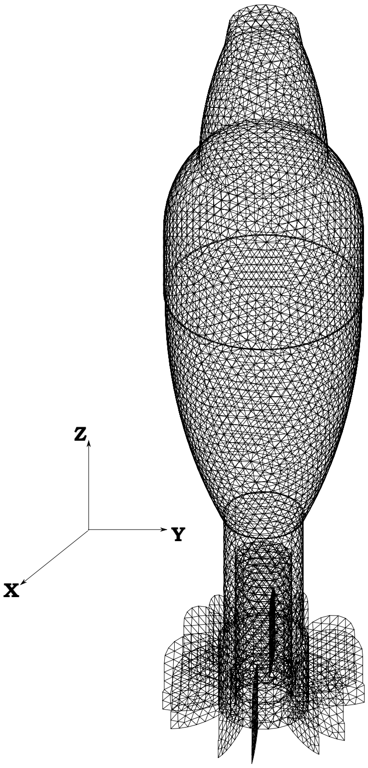

Fig. 14. Triangulated model of a cylindrical-shaped object.

2693 basis functions in each group. The bistatic RCS along YZ-plane is shown in Fig. 13. The power series solution is compared with MOM solution and we note an excellent comparison for this complex structure.

Next, we present a few examples to illustrate the ability of the present work to accurately predict the monostatic radar cross-section. Consider a complex cylindrical-shaped object as shown in the Fig. 14. The height of the object is 105 mm and is cylindrically symmetric along the z-axis. The object is illuminated by 10 GHz plane wave and approximated with 13010 basis functions. For the power-series method, the total number of basis functions are divided into 10 groups with 1301 functions in each group. We present the mono-static elevation RCS of this object using both the conventional MOM and the power series solution method in Fig. 15 and the comparison is excellent between the two methods.

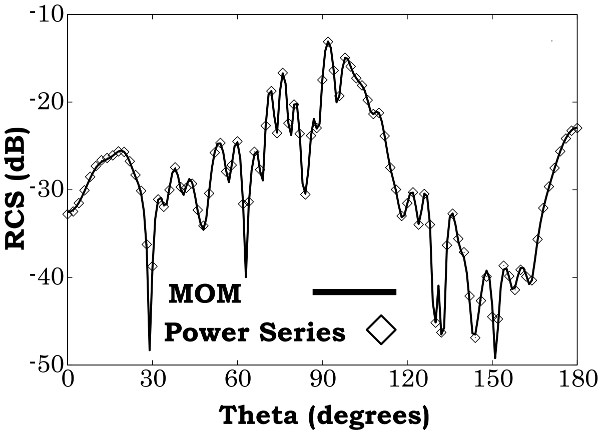

Fig. 15. Monostatic RCS of a cylindrical-shaped object shown in Fig. 14. Number of unknowns=13,010. Number of groups=10.

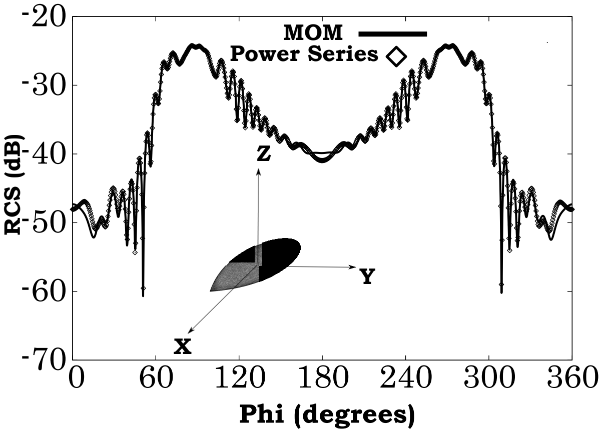

Fig. 16. Monostatic RCS of NASA Almond at 10 GHz. Number of unknowns=46,680. Number of groups=20.

Next, we consider the azimuthal monostatic RCS of NASA Almond ($252mm \times 98mm \times 32mm$), shown in the inset of Fig. 16, at 10 GHz. The electric field is polarized along the z-axis. The object is approximated with 46,680 basis functions. For the power-series method, the total number of basis functions are divided into 20 groups with 2334 functions in each group. For comparison, we also present the conventional MOM. We note excellent comparison between the two methods.

Next, we calculate the elevation ($\phi = 90^0$-cut) monostatic RCS of ship-type object as shown in the inset of Fig. 17. The dimensions and the place of the object is same as in the bistatic ship-type object case. The ship is illuminated by 100 MHz plane wave and polarized along z-direction (height). The object is approximated by 53,856 basis functions and divided into 20 groups for power series solution. It can be seen that there is good comparison between the MOM solution and the present method.

As a final example, again consider the 91 meter ship-like object as shown in the inset of Fig. 18. The purpose of this example is to demonstrate the capability of the present method to handle electrically large, complex shaped objects using MOM involving around million unknowns. The object is illuminated

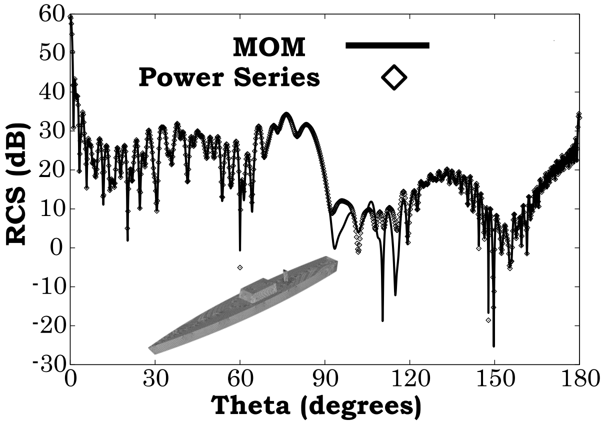

Fig. 17. Monoistatic RCS of a 91m ship-type object at 100 MHz. Number of unknowns=53,856. Number of groups=20.

by a 500 MHz, y-polarized plane wave traveling along the z-axis. To obtain scattering from a higher frequency, the ship is approximated by 864,800 basis functions. For the power series solution, the total number of basis functions is divided into 400 groups with 2162 basis functions in each group. The bistatic RCS along YZ-plane is shown in Fig. 18.

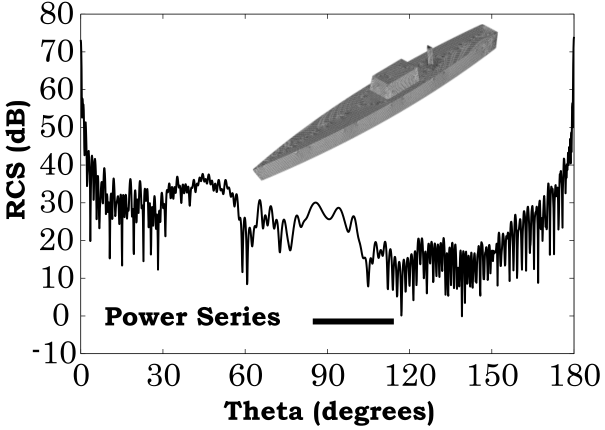

Fig. 18. Bistatic RCS of a 91 m ship-type object a 500 MHz. Number of unknowns=864,800. Number of groups=400.

V. CONCLUSIONS

In this work, we present a new and efficient algorithm to solve the electrically large electromagnetic scattering problems utilizing the MOM formulation. The present method, while handling electrically large PEC bodies, retains all the conventional advantages of MOM, *viz.* accuracy of solution, ability to handle multiple excitation vectors, applicable to scattering and radiation problems, and ability to calculate both near and far-field patterns.The algorithm can be made more efficient using GPU's, more efficient parallel processing, and implementing the adaptive cross approximation (ACA) procedure to reduce the computation of distantly located blocks from the source block [7]. However, some of the aforementioned improvements are not made yet and may be reported in the near future. Lastly, since the method can be viewed as a purely algebraic method, it is envisaged that the method may be applied to any MOM problem with minor modifications.

ACKNOWLEDGEMENTS

This research was conducted under the Naval Research Laboratory Base Program sponsored by the Office of Naval Research. Also, the authors would like to express their appreciation to Dr. Daniel Faircloth, IERUS Technologies, Inc, for providing the input data for Fig. 14.

REFERENCES

[1] R. Harrington, *Field Computation by Moment Methods*, New York, Macmillan, 1968.

[2] E. K. Miller, L. Medgyesi-Mitschang, and E. H. Newman, *Computational Electromagnetics - Frequency-Domain Method of Moments*, IEEE Press, New York, 1992.

[3] W. C. Gibson, *The Method of Moments in Electromagnetics*, Chapman & Hall, Boca Raton, FL, 2008.

[4] T. K. Sarkar, "A note on the choice of weighting functions in the method of moments," *IEEE Transactions on Antennas and Propagation*, vol. 33, pp. 436-441, 1985.

[5] T. K. Sarkar, A. R. Djordjevic, and E. Arvas, "On the choice of expansion and weighting functions in the method of moments," *IEEE Transactions on Antennas and Propagation*, vol. 33, pp. 988-996, 1985.

[6] J. Song, C. C. Lu, and W. C. Chew, "Multilevel fast multipole algorithm for electromagnetic scattering by large complex objects," *IEEE Transactions on Antennas and Propagation*, vol. 45, pp. 1488 - 1493, October 1997.

[7] J. Shaeffer, "Direct solve of electrically large integral equations for problem sizes to 1M unknowns," *IEEE Transactions on Antennas and Propagation*, vol. 56, pp. 2306-2313, 2008.

[8] T. N. Killian, S. M. Rao, and M. E. Baginski, "Electromagnetic scattering from electrically large arbitrarily-shaped conductors using the method of moments and a new null-field generation technique," *IEEE Transactions on Antennas and Propagation*, vol. 59, pp. 537-545, 2011.

[9] S. M. Rao, D. R. Wilton, and A. W. Glisson, "Electromagnetic scattering by surfaces of arbitrary shape," *IEEE Transactions on Antennas and Propagation*, vol. 30, pp. 409-418, 1982.

[10] G. H. Golub and C. F. Van Loan, *Matrix Computations*, 3rd ed. Baltimore, MD: Johns Hopkins, 1996.
[11] R. Harrington, *Time Harmonic Electromagnetic Fields*, New York, IEEE Press, 2001.

Formulations for Modeling Voltage Sources with RLC Impedances in the FDTD Method

Veysel Demir

Department of Electrical Engineering
Northern Illinois University, DeKalb, IL 60115, USA
vdemir@niu.edu

Abstract **─** Voltage sources are modeled with constant resistive internal impedances when simulated in the finite-difference time-domain (FDTD) method in most of the applications. However, some applications, such as an RFID tag antenna in radiation mode, require modeling of voltage sources with frequency dependent complex impedances. If the frequency dependent behavior of the complex impedance of a voltage source follows that of an RLC circuit, the voltage source can be modeled with an RLC internal impedance in the FDTD method for wide-band simulations. This paper presents FDTD formulations to model a voltage source with an RLC impedance for the cases where the RLC circuit is a series or a parallel connected RL, RC, or an RLC configuration.

Index Terms **─** Finite-difference time-domain method, impedance modeling, source modeling.

I. INTRODUCTION

Integration of complex behavior of lumped components and sources into the finite-difference time-domain (FDTD) [1, 2] simulations has been an active research area during the past decades. Though there are various types of local sources that can be used as the excitation of an FDTD simulation, voltage source is the most common one and several formulations are available in the literature to integrate a resistive voltage source into the FDTD method [3-8]. However, in some applications the input impedance of a voltage source needs to be modeled as a reactive impedance. For instance, a radio-frequency identification (RFID) chip can be modeled as an equivalent of a voltage source together with an RLC circuit in the radiation mode [9]. For such applications where reactive impedances need to be considered, the reactive nature of the voltage source impedance needs to be modeled by appropriate formulations in the FDTD method to achieve wide-band time domain analyses. This paper presents formulations for the cases where the impedance of a voltage source is an equivalent of an RLC circuit; updating equations for series or parallel connected RL, RC, and RLC configurations are presented here.

When a lumped component is modeled in the FDTD method, the updating equation is developed assuming that the lumped component lies along an edge of a Yee cell. A voltage source with a complex impedance can be simulated by placing the source component of the voltage source along an edge of a Yee cell while placing the impedance component along the edge of the neighboring Yee cell to form a series connection, thus occupying two cells length of space in the FDTD grid. The goal here is to formulate the updating equation such that both the source and the impedance components are placed along a single edge of a Yee cell.

Various methods have been presented in the literature to incorporate arbitrary lumped devices and networks into the FDTD method [10-16]. It should be mentioned that modeling a voltage source can be considered as an extension to modeling a load, as will be discussed in the following section, therefore, some of these general load modeling methods can be extended to model voltage sources as well where the load is considered as the impedance of the voltage source.

Here, we present development of FDTD updating equations for each of the RLC configurations based on the auxiliary differential equation (ADE) method [17-21], one of the well-established methods to model dispersive materials in the FDTD method. Next section presents development of updating equations for configurations in consideration. The following section discusses the validity and accuracy of the presented formulations.

II. UPDATING EQUATIONS FOR VOLTAGE SOURCE MODELING

Following the procedure in [3], we utilize the impressed current density $\bar{J}$ in Maxwell's magnetic field curl equation:

$$\nabla \times \bar{H} = j\omega\varepsilon\bar{E} + \bar{J} , \tag{1}$$

to model a voltage source in FDTD. Figure 1 illustrates model of a voltage source and its impedance Z_S along an edge of a Yee cell oriented in the z direction. For the voltage source, we can express the impressed current

Submitted On: September 15, 2015
Accepted On: March 17, 2016

density as:

$$J_z = \frac{I_S}{\Delta x \Delta y}, \tag{2}$$

where the current is,

$$I_S = \frac{\Delta V + V_S}{Z_S}. \tag{3}$$

Here, V_S is the source voltage and ΔV is the voltage induced along the cell edge, which can be expressed in terms of the electric field as:

$$\Delta V = E_z \Delta z. \tag{4}$$

We can therefore express the current density in terms of the source voltage and the electric field as:

$$J_z = \frac{\Delta z}{\Delta x \Delta y}\frac{1}{Z_S}E_z + \frac{1}{\Delta x \Delta y}\frac{1}{Z_S}V_S. \tag{5}$$

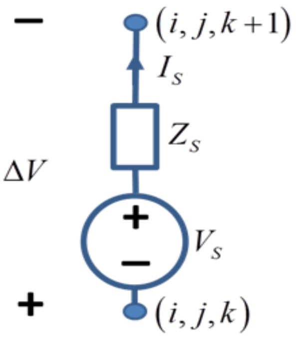

Fig. 1. A voltage source with an internal impedance of Z_S.

A. Modeling a voltage source with a series RLC impedance

For a series RLC circuit, the impedance is:

$$Z_S = R + j\omega L + \frac{1}{j\omega C} = \frac{j\omega CR - \omega^2 CL + 1}{j\omega C}, \tag{6}$$

which leads (5) to:

$$J_z = \frac{\Delta z}{\Delta x \Delta y}\frac{j\omega C}{j\omega CR - \omega^2 CL + 1}E_z + \frac{1}{\Delta x \Delta y}\frac{j\omega C}{j\omega CR - \omega^2 CL + 1}V_S. \tag{7}$$

We can write (7) briefly as:

$$J_z = j\omega Q + \frac{1}{\Delta x \Delta y}F. \tag{8}$$

The term Q is in the form of a single term Lorenzian as:

$$Q = \frac{\Delta z C}{\Delta x \Delta y}\frac{1}{j\omega CR - \omega^2 CL + 1}E_z = \frac{\psi}{\omega_0^2 + 2j\omega\delta - \omega^2}E_z, \tag{9}$$

where $\psi = \frac{\Delta z}{\Delta x \Delta y L}$, $\delta = \frac{R}{2L}$, and $\omega_0 = \frac{1}{\sqrt{LC}}$. Then construction of updating equation including the Q term is similar to the one for modeling Lorentzian dispersive medium as presented in [21]. Following the procedure in [21], we can construct an ADE from (9) as:

$$\left(\frac{\partial^2}{\partial t^2} + 2\delta\frac{\partial}{\partial t} + \omega_0^2\right)Q = \psi E_z, \tag{10}$$

which can be expressed in discrete time using central difference approximation at time step n as:

$$\frac{Q^{n+1} - 2Q^n + Q^{n-1}}{(\Delta t)^2} + \delta\frac{Q^{n+1} - Q^{n-1}}{(\Delta t)^2} + \omega_0^2 Q^n = \psi E_z^n. \tag{11}$$

Equation (11) can be arranged to calculate the future value of Q, such that,

$$Q^{n+1} = \frac{2 - (\Delta t)^2\omega_0^2}{\delta\Delta t + 1}Q^n + \frac{\delta\Delta t - 1}{\delta\Delta t + 1}Q^{n-1} + \frac{(\Delta t)^2\psi}{\delta\Delta t + 1}E_z^n. \tag{12}$$

The additional source term in (8) is denoted as F. From (7) and (8), we can write:

$$\left(j\omega CR - \omega^2 CL + 1\right)F = j\omega C V_S. \tag{13}$$

This equation can be expressed in time domain as:

$$CL\frac{\partial^2}{\partial t^2}F + CR\frac{\partial}{\partial t}F + F = C\frac{\partial}{\partial t}V_S. \tag{14}$$

The term F can be calculated analytically or numerically for a given time waveform V_S before the FDTD iterations start. For instance, if we use second order accurate central difference for (14) we obtain an iterative equation to calculate F for all time steps as:

$$F^{n+0.5} = \left(\frac{4L - 2(\Delta t)^2/C}{2L + R\Delta t}\right)F^{n-0.5} + \left(\frac{R\Delta t - 2L}{2L + R\Delta t}\right)F^{n-1.5} + \frac{\Delta t}{2L + R\Delta t}\left({V_S}^{n+0.5} - {V_S}^{n-1.5}\right). \tag{15}$$

Using (8) in (1) and transforming into time domain, we obtain:

$$\left(\nabla \times \bar{H}\right)_z = \varepsilon\frac{\partial}{\partial t}E_z + \frac{\partial}{\partial t}Q + \frac{1}{\Delta x \Delta y}F, \tag{16}$$

which leads to an FDTD updating equation for a voltage source with a series RLC impedance as:

$$E_z^{n+1} = E_z^n + \frac{\Delta t}{\varepsilon}\left(\nabla\times\bar{H}\right)_z^{n+0.5}$$
$$-\frac{1}{\varepsilon}\left(Q^{n+1}-Q^n\right)-\frac{1}{\varepsilon}\frac{\Delta t}{\Delta x\Delta y}F^{n+0.5}. \qquad (17)$$

The field update procedure can be summarized as follows: At every time step, magnetic field components are updated as usual. Next, the new value of Q is calculated using its past values and the past values of E_z using (12). Then, E_z is updated using the past value of E_z and magnetic field components, current value of F, as well as the current and past values of Q as in (17).

B. Modeling a voltage source with a series RL impedance

We can develop the equations for a series RL configuration starting from series RLC equations; we assume that capacitance is infinite. Then (9) becomes:

$$Q = \frac{\Delta z}{\Delta x\Delta yL}\frac{1}{j\omega R/L-\omega^2}E_z. \qquad (18)$$

Then we can use $\psi = \frac{\Delta z}{\Delta x\Delta yL}, \delta = R/2L, \omega_0 = 0$, which leads (12) to:

$$Q^{n+1} = \frac{2}{\left(\delta\Delta t+1\right)}Q^n + \frac{\left(\delta\Delta t-1\right)}{\left(\delta\Delta t+1\right)}Q^{n-1} + \frac{\left(\Delta t\right)^2\psi}{\left(\delta\Delta t+1\right)}E_z^n. \qquad (19)$$

Using infinite capacitance value, (15) becomes:

$$F^{n+0.5} = \left(\frac{4L}{2L+R\Delta t}\right)F^{n-0.5} + \left(\frac{R\Delta t-2L}{2L+R\Delta t}\right)F^{n-1.5}$$
$$+\frac{\Delta t}{2L+R\Delta t}\left({V_S}^{n+0.5}-{V_S}^{n-1.5}\right). \qquad (20)$$

FDTD updating equation for a voltage source with a series RL impedance is (17), where Q and F are calculated using (19) and (20), respectively.

C. Modeling a voltage source with a series RC impedance

If we use the equations for the series RLC case in Section A as is and just let $L=0$, we face a few problems to formulate the series RC case. First of all the terms ψ, δ, and ω_0 tend to infinity as L tends to zero. Thus, (12) cannot be used.

It is possible to go back to (9) and let $L=0$ there and derive an equation to calculate Q. However, notice that, the relationship between Q and E is a second order derivative when L is non-zero and it reduces to a first order derivative for $L=0$ when moving from (9) to (10). When the equation is a second order derivative, then it is more convenient and accurate to calculate Q at integer time steps (i.e., as Q^{n+1} or Q^n) using E^n and using the derivative of Q in (16) (or difference of Q in (17)) rather than Q itself in (16) (or $Q^{n+0.5}$ in (17)). When L is zero and (9) leads to a first order derivative, then it is more convenient and accurate to calculate Q at half integer time steps as $Q^{n+0.5}$ and reformulate (16) to use Q directly rather than its derivative. Hence, a new formulation that uses Q directly is needed instead of (16) and such a formulation can be derived by going back to (1). The details of this procedure are presented below.

The admittance of a series RC circuit is:

$$Y_S = \frac{j\omega C}{j\omega CR+1} = \frac{1}{R}\left(\frac{j\omega CR}{j\omega CR+1}\right)$$
$$=\left(\frac{1}{R}-\frac{1}{j\omega CR^2+R}\right). \qquad (21)$$

Using (21) in (5) yields:

$$J_z = \frac{\Delta z}{\Delta x\Delta y}\left(\frac{1}{R}-\frac{1}{j\omega CR^2+R}\right)E_z$$
$$+\frac{1}{\Delta x\Delta y}\left(\frac{1}{R}-\frac{1}{j\omega CR^2+R}\right)V_S. \qquad (22)$$

Using J_z in (1) leads to:

$$\left(\nabla\times\bar{H}\right)_z = j\omega\varepsilon E_z + \frac{\Delta z}{\Delta x\Delta yR}E_z + \frac{1}{\Delta x\Delta yR}V_S$$
$$-\frac{\Delta z}{\Delta x\Delta y}\frac{1}{j\omega CR^2+R}E_z - \frac{1}{\Delta x\Delta y}\frac{1}{j\omega CR^2+R}V_S. \qquad (23)$$

First three terms on the RHS are equivalent to the equation for a resistive voltage source. The fourth term can be expressed as:

$$Q = \frac{\Delta z}{\Delta x\Delta y}\frac{1}{j\omega CR^2+R}E_z, \qquad (24)$$

which leads in discrete time domain to:

$$Q^{n+0.5} = \frac{\left(2CR-\Delta t\right)}{\left(2CR+\Delta t\right)}Q^{n-0.5}$$
$$+\frac{2\Delta t\Delta z}{\left(2CR+\Delta t\right)R\Delta x\Delta y}E_z^n. \qquad (25)$$

We can use the source terms (the third and fifth terms) in (23) to write:

$$F = V_S - \frac{1}{j\omega CR+1}V_S = \frac{j\omega CR}{j\omega CR+1}V_S, \qquad (26)$$

which leads to:

$$\frac{\partial}{\partial t}F + \frac{1}{CR} = \frac{\partial}{\partial t}V_S. \qquad (27)$$

In discrete time, (27) yields:

$$F^{n+0.5} = \frac{2CR-\Delta t}{2CR+\Delta t} F^{n-0.5}$$

$$+\frac{2CR}{2CR+\Delta t}\left({V_S}^{n+0.5} - {V_S}^{n-0.5}\right). \qquad (28)$$

We can obtain an updating equation from (23) as:

$$E_z^{n+1} = K_1 K_2 E_z^n + K_2\left(\nabla\times\bar{H}\right)_z^{n+0.5}$$

$$+K_2 Q^{n+0.5} - K_2 \frac{1}{\Delta x \Delta y R} F^{n+0.5}, \qquad (29)$$

where

$$K_1 = \frac{\varepsilon}{\Delta t} - \frac{\Delta z}{2\Delta x \Delta y R}, \qquad (30)$$

and

$$K_2 = \left(\frac{\varepsilon}{\Delta t} + \frac{\Delta z}{2\Delta x \Delta y R}\right)^{-1}. \qquad (31)$$

FDTD updating equation for a voltage source with a series RC impedance is (29), where Q and F are calculated using (25) and (28), respectively.

D. Modeling a voltage source with a parallel RLC impedance

For a parallel RLC circuit, the source admittance becomes:

$$Y_S = \frac{1}{Z_S} = \frac{1}{R} + \frac{1}{j\omega L} + j\omega C, \qquad (32)$$

which leads (5) to:

$$J_z = \frac{\Delta z}{\Delta x \Delta y} Y_S E_z + \frac{1}{\Delta x \Delta y} Y_S V_S. \qquad (33)$$

Using (33), we can write (1) in open form as:

$$\left(\nabla\times\bar{H}\right)_z = j\omega\left(\varepsilon + \frac{\Delta z}{\Delta x \Delta y} C\right) E_z$$

$$+\left(\frac{\Delta z}{\Delta x \Delta y}\frac{1}{R}\right) E_z + \frac{\Delta z}{\Delta x \Delta y L} Q + \frac{1}{\Delta x \Delta y} F, \qquad (34)$$

where

$$Q = \frac{1}{j\omega} E_z, \qquad (35)$$

and

$$F = Y_S V_S = \left(\frac{1}{R} + \frac{1}{j\omega L} + j\omega C\right) V_S. \qquad (36)$$

We can derive an updating equation for Q using (35) as:

$$Q^{n+0.5} = Q^{n-0.5} + \Delta t E_z^n. \qquad (37)$$

This $Q^{n+0.5}$ term can be calculated at every time step using E_z^n and can be used to update E_z^{n+1}. Equation (36) leads to:

$$j\omega LRF = \left(-\omega^2 CLR + j\omega L + R\right) V_S, \qquad (38)$$

which can be transformed into discrete time domain using the central difference approximation to obtain an iterative equation to calculate F as:

$$F^{n+0.5} = F^{n-1.5} + \frac{\left(2CR+\Delta t\right)}{R\Delta t} V_S^{n+0.5}$$

$$+\frac{\left(2\Delta t^2 R/L - 4CR\right)}{R\Delta t} V_S^{n-0.5} + \frac{\left(2CR-\Delta t\right)}{R\Delta t} V_S^{n-1.5}. \qquad (39)$$

Finally, (34) can be transformed into discrete time domain using the central difference approximation to obtain:

$$E_z^{n+1} = K_1 K_2 E_z^n + 2R\Delta x \Delta y \Delta t K_2 \left(\nabla\times\bar{H}\right)_z^{n+0.5}$$

$$-2\left(R/L\right)\Delta z \Delta t K_2 Q^{n+0.5} - 2R\Delta t K_2 F^{n+0.5}, \qquad (40)$$

where

$$K_1 = \varepsilon \Delta x \Delta y 2R + \Delta z C 2R - \Delta z \Delta t, \qquad (41)$$

and

$$K_2 = \left(\varepsilon \Delta x \Delta y 2R + \Delta z C 2R + \Delta z \Delta t\right)^{-1}. \qquad (42)$$

FDTD updating equation for a voltage source with a parallel RLC impedance is (40), where Q and F are calculated using (37) and (39), respectively.

E. Modeling a voltage source with a parallel RL impedance

We can use the equations developed for the parallel RLC configuration to model the parallel RL case: we just set the capacitance as zero in all respective equations in Section II.D such that:

$$F^{n+0.5} = F^{n-1.5} + \frac{1}{R} V_S^{n+0.5}$$

$$+\frac{2\Delta t}{L} V_S^{n-0.5} - \frac{1}{R} V_S^{n-1.5}, \qquad (43)$$

$$K_1 = \varepsilon \Delta x \Delta y 2R - \Delta z \Delta t, \qquad (44)$$

and

$$K_2 = \left(\varepsilon \Delta x \Delta y 2R + \Delta z \Delta t\right)^{-1}. \qquad (45)$$

F. Modeling a voltage source with a parallel RC impedance

We can use the equations developed for the parallel RLC configuration to model the case of parallel RC circuit: we just set the inductance as infinite in all respective equations in Section II.D. Equation (39) becomes:

$$F^{n+0.5} = F^{n-0.5} + \frac{\left(2CR+\Delta t\right)}{R\Delta t} {V_S}^{n+0.5}$$

$$+\frac{\left(-4C\right)}{\Delta t} V_S^{n-0.5} + \frac{\left(2CR-\Delta t\right)}{R\Delta t} {V_S}^{n-1.5}. \qquad (46)$$

The updating equation for electric field can be obtained as:

$$E_z^{n+1} = K_1 K_2 E_z^n + 2R\Delta x \Delta y \Delta t K_2 \left(\nabla \times \bar{H}\right)_z^{n+0.5}$$
$$-2R\Delta t K_2 F^{n+0.5}, \tag{47}$$

where K_1 and K_2 are the same as (41) and (42), respectively.

G. Modeling a voltage source across multiple FDTD cells

The updating equations presented above are developed for a voltage source connected across an edge of a single cell. Another case that needs consideration is where the voltage source is defined across multiple three dimensional FDTD cells. Such a case is discussed in [22] as an extension to the source modeling formulation presented in [4].

Here, as a simple procedure, we can assign an equivalent voltage, resistance, inductance, and capacitance values to each cell edge contained in the volume of the voltage source region and still use the above equations to update the associated electric fields.

For instance, Fig. 2 illustrates a voltage source across multiple cells. Here each edge is assigned an equivalent voltage of $V_{S,eq}$ and impedance of $Z_{S,eq}$, where $Z_{S,eq}$ can be a parallel or series connection of R_{eq}, L_{eq}, and/or C_{eq}. The indices *is*, *js*, and *ks*, indicate the start node of the region where the voltage source is located, whereas the indices *ie*, *je*, and *ke*, indicate the end node. Number of cells in the voltage source region is $nx = ie - is$, $ny = je - js$, $nz = ke - ks$, in the x, y, and z directions, respectively. The equivalent voltage for an edge can be obtained by:

$$V_{S,eq} = \frac{1}{nz} V_S. \tag{48}$$

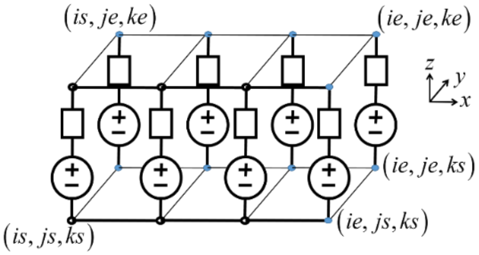

Fig. 2. A voltage source with an internal impedance across multiple cells.

The equivalent impedance is:

$$Z_{eq} = \frac{(nx+1)(ny+1)}{nz} Z_S, \tag{49}$$

which leads to:

$$R_{eq} = \frac{(nx+1)(ny+1)}{nz} R, \tag{50}$$

$$L_{eq} = \frac{(nx+1)(ny+1)}{nz} L, \tag{51}$$

and

$$C_{eq} = \frac{nz}{(nx+1)(ny+1)}. \tag{52}$$

III. VALIDATION OF FORMULATIONS

In this section we present results of some example cases to demonstrate the validity and accuracy of the presented formulations. Figure 3 shows two parallel PEC plates terminated by a voltage source and a load. Each plate is 1 mm by 2 mm in size. The separation between the plates is 1 mm. This geometry is simulated using $\Delta x = 1mm$, $\Delta y = 1mm$, and $\Delta z = 1mm$ cell size. In the simulations the voltage source V_S is excited by a derivative of Gaussian waveform. In the following tests each time a different source impedance configuration is modeled using the values of $R = 50\Omega$, $L = 5nH$, and $C = 10\,pF$. The load is modeled as a 50Ω resistor.

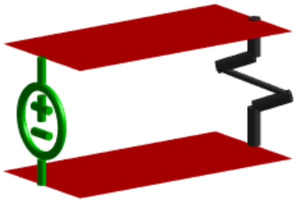

Fig. 3. Two parallel PEC plates terminated by a voltage source and a load.

During impedance calculations after the simulations were performed, it was observed that a capacitance in parallel with the load and source exists at the position of the load and the source. This numerical parasitic reactance in the FDTD grid has been discussed in the literature and correction procedures were suggested [6], [23-25].

The parasitic capacitance along the location of the voltage source in Fig. 3 is determined as $C_P = 0.0175\,pF$ by initial FDTD analyses for the cell size being used. To extract the simulated impedance of the voltage source, the effect of this capacitance is removed from the calculated impedances in the following example test cases.

It should be noted that a value for the numerical parasitic capacitance can be obtained by:

$$C_z = \varepsilon \frac{\Delta x \Delta y}{\Delta z}, \tag{53}$$

where C_z is the capacitance related to the edge of a cell in the z direction as proposed by [24]. In Fig. 3, two parasitic capacitors can be imagined along the two edges of the voltage source. These capacitors are connected in parallel and their equivalent capacitance can be calculated as $C_P = 0.0177\,pF$ using (53), which agrees well with the above determined value out of the simulations.

Figure 4 shows the model of the voltage source together with the parasitic capacitor C_P. In each test case the sampled voltage (V_1) and current (I_1) are captured on the voltage source in Fig. 4 and then the source impedance is calculated as:

$$Z_S = \frac{V_{S1}-V_1}{I_S} = \frac{V_{S1}-V_1}{I_1+I_C}, \qquad (54)$$

where $I_C = j\omega C_P V_1$.

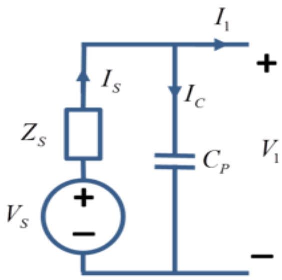

Fig. 4. Equivalent model of a voltage source including the parasitic capacitance.

Figures 5 to 10 show the results of different test cases, where the expected impedances of the voltage sources are compared with the ones obtained from FDTD simulations using (54). The results show very good agreement on a wide frequency range.

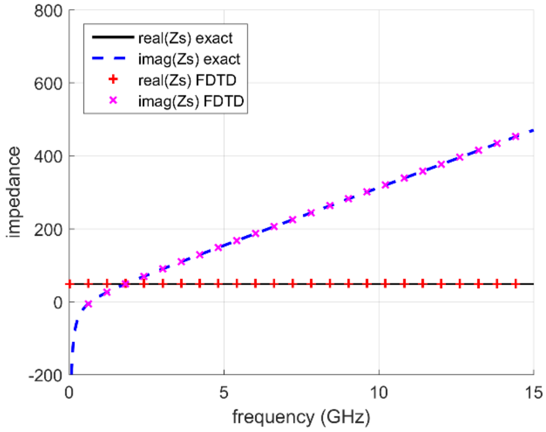

Fig. 5. Impedance of a voltage source as a series RLC.

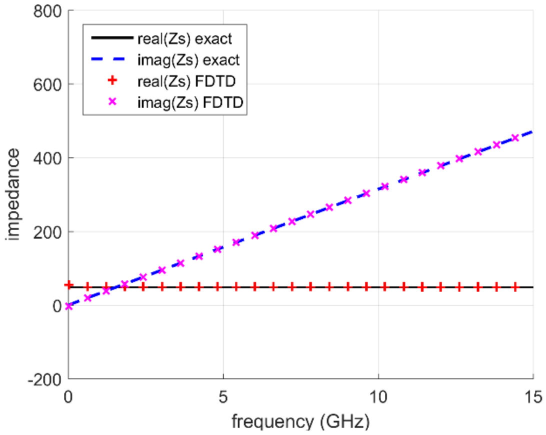

Fig. 6. Impedance of a voltage source as a series RL.

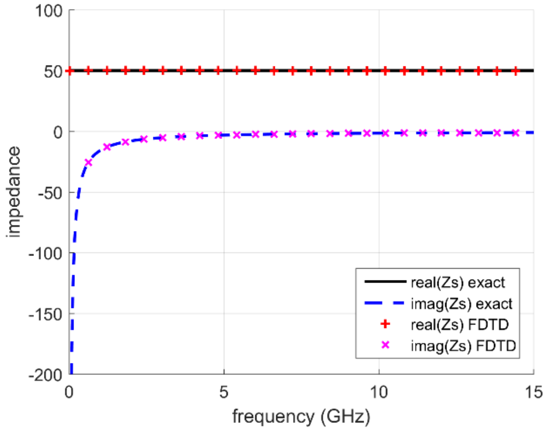

Fig. 7. Impedance of a voltage source as a series RC.

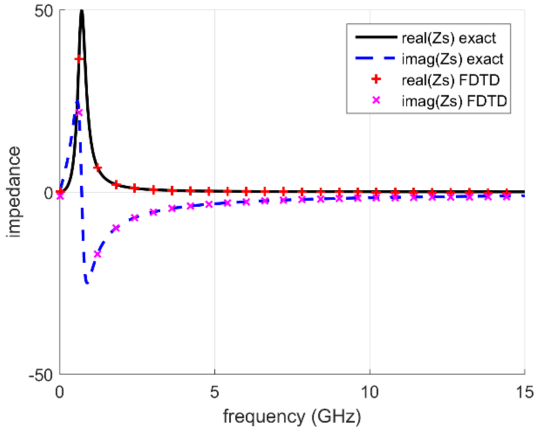

Fig. 8. Impedance of a voltage source as a parallel RLC.

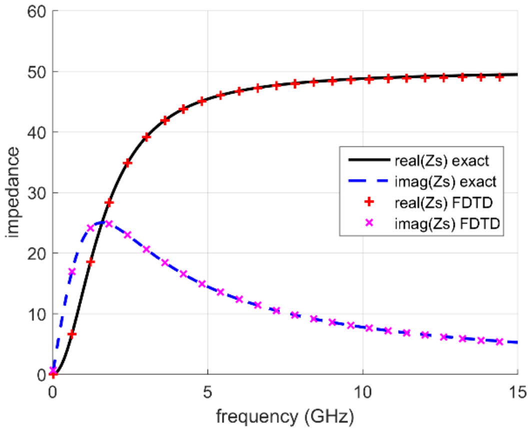

Fig. 9. Impedance of a voltage source as a parallel RL.

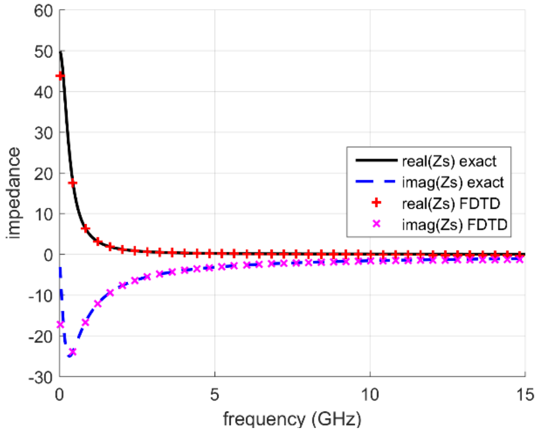

Fig. 10. Impedance of a voltage source as a parallel RC.

IV. CONCLUSION

Formulations are presented to model a voltage source with an RLC internal impedance in the FDTD method. It has been shown that these formulations can be used to model the RLC impedance of a voltage source on a wide frequency band. It should be noted that while these formulations are developed to model voltage sources with RLC impedances, they can be equivalently used to model passive RLC impedances as well by simply removing the source terms from the equations.

REFERENCES

[1] A. Taflove and S. C. Hagness, *Computational Electrodynamics*. Artech House, Boston, 2005.

[2] A. Z. Elsherbeni and V. Demir, *The Finite-difference Time-domain Method for Electromagnetics with MATLAB Simulations*. SciTech Pub., Raleigh, NC, 2009.

[3] M. Piket-May, A. Taflove, and J. Baron, “FD-TD modeling of digital signal propagation in 3-D circuits with passive and active loads,” *IEEE Transactions on Microwave Theory and Techniques*, vol. 42, no. 8, pp. 1514-1523, 1994.

[4] W. Sui, D. A. Christensen, and C. H. Durney, “Extending the two-dimensional FDTD method to hybrid electromagnetic systems with active and passive lumped elements,” *IEEE Transactions on Microwave Theory and Techniques*, vol. 40, no. 4, pp. 724-730, 1992.

[5] O. P. M Pekonen, J. Xu, and K. I. Nikoskinen, “Rigorous analysis of circuit parameter extraction from an FDTD simulation excited with a resistive voltage source,” *Microwave and Optical Technology Letters*, vol. 12, no. 4, pp. 205-210, 1996.

[6] R. Gillard, S. Dauguet, and J. Citerne, “Correction procedures for the numerical parasitic elements associated with lumped elements in global electromagnetic simulators,” *IEEE Transactions on Microwave Theory and Techniques*, vol. 46, no. 9, pp. 1298-1306, 1998.

[7] R. M. Mäkinen and M. Kivikoski, “A stabilized resistive voltage source for FDTD thin-wire models,” *IEEE Transactions on Antennas and Propagation*, vol. 51, no. 7, pp. 1615-1622, 2003.

[8] S. Watanabe and M. Taki, “An improved FDTD model for the feeding gap of a thin-wire antenna,” *IEEE Microwave and Guided Wave Letters*, vol. 8, no. 4, pp. 152-154, 1998.

[9] Higgs 4 IC Datasheet, Available at: http://www.alientechnology.com/wpcontent/uploads/Alien-Technology-Higgs-4-ICDatasheet.pdf.

[10] J. Pereda, F. Alimenti, P. Mezzanotte, L. Roselli, and R. Sorrentino, “A new algorithm for the incorporation of arbitrary linear lumped networks into FDTD simulators,” *IEEE Transactions on Microwave Theory and Techniques*, vol. 47, no. 6, pp. 943-949, 1999.

[11] J.-Y. Lee, J.-H. Lee, and H.-K. Jung, “Linear lumped loads in the FDTD method using piecewise linear recursive convolution method,” *IEEE Microwave and Wireless Components Letters*, vol. 16, no. 4, pp. 158-160, 2006.

[12] C.-C. Wang and C.-W. Kuo, “An efficient scheme for processing arbitrary lumped multiport devices in the finite-difference time-domain method,” *IEEE Transactions on Microwave Theory and Techniques*, vol. 55, no. 5, pp. 958-965, 2007.

[13] Z.-H. Chen and Q.-X. Chu, “FDTD modeling of arbitrary linear lumped networks using piecewise linear recursive convolution technique,” *Progress in Electromagnetics Research*, vol. 73, pp. 327-341, 2007.

[14] P. Ciampolini, P. Mezzanotte, L. Roselli, and R. Sorrentino, “Accurate and efficient circuit simulation with lumped-element FDTD technique,”

IEEE Transactions on Microwave Theory and Techniques, vol. 44, no. 12, pp. 2207-2215, 1996.

[15] V. S. Reddy and R. Garg, "An improved extended FDTD formulation for active microwave circuits," *IEEE Transactions on Microwave Theory and Techniques*, vol. 47, no. 9, 1603-1608, pp. 1999.

[16] T.-L. Wu, S.-T. Chen, and Y.-S. Huang, "A novel approach for the incorporation of arbitrary linear lumped network into FDTD method," *IEEE Microwave and Wireless Components Letters*, vol. 14, no. 2, pp. 74-76, 2004.

[17] R. M. Joseph, S. C. Hagness, and A. Taflove, "Direct time integration of Maxwell's equations in linear dispersive media with absorption for scattering and propagation of femto second electromagnetic pulses," *Optics Letters*, vol. 16, no. 18, pp. 1412-1414, 1991.

[18] O. P. Gandhi, B.-Q. Gao, and J.-Y. Chen, "A frequency-dependent finite-difference time-domain formulation for general dispersive media," *IEEE Transactions on Microwave Theory and Techniques*, vol. 41, no. 4, pp. 658-665, 1993.

[19] T. Kashiwa and I. Fukai, "A treatment by the FDTD method of the dispersive characteristics associated with electronic polarization," *Microwave and Optical Technology Letters*, vol. 3, no. 6, pp. 203-205, 1990.

[20] M. Okoniewski, M. Mrozowski, and M. A. Stuchly, "Simple treatment of multi-term dispersion in FDTD," *IEEE Microwave and Guided Wave Letters*, vol. 7, no. 5, pp. 121-123, 1997.

[21] Y. Takayama and W. Klaus, "Reinterpretation of the auxiliary differential equation method for FDTD," *IEEE Microwave and Wireless Components Letters*, vol. 12, no. 3, pp. 102-104, 2002.

[22] C. H. Durney, W. Sui, D. A. Christensen, and J. Zhu, "A general formulation for connecting sources and passive lumped-circuit elements across multiple 3D FDTD cells," *IEEE Microwave and Guided Wave Letters*, vol. 6, no. 2, pp. 85-87, 1996.

[23] W. Thiel and L. P. B. Katehi, "Some aspects of stability and numerical dissipation of the finite-difference time-domain (FDTD) technique including passive and active lumped elements," *IEEE Transactions on Microwave Theory and Techniques*, vol. 50, no. 9, pp. 2159-2165, 2002.

[24] L. Borzetta, F. Alimenti, P. Ciampolini, P. Mezzanotte, L. Roselli, and R. Sorrentino, "Numerical parasitic reactances at the interface between FDTD mesh and lumped elements," *1999 IEEE MTT-S International Microwave Symposium Digest*, vol. 4, pp. 1585-1588, 1999.

[25] W. Thiel and W. Menzel, "Full-wave design and optimization of mm-wave diode-based circuits in finline technique," *IEEE Transactions on Microwave Theory and Techniques*, vol. 47, no. 12, pp. 2460-2466, 1999.

Veysel Demir is an Associate Professor at the Department of Electrical Engineering at Northern Illinois University. He received his Bachelor of Science degree in Electrical Engineering from Middle East Technical University, Ankara, Turkey, in 1997. He studied at Syracuse University, New York, where he received both a Master of Science and Doctor of Philosophy degrees in Electrical Engineering in 2002 and 2004, respectively. During his graduate studies, he worked as a Research Assistant for Sonnet Software, Inc., Liverpool, New York. He worked as a visiting Research Scholar in the Department of Electrical Engineering at the University of Mississippi from 2004 to 2007. He joined Northern Illinois University in August 2007 and served as an Assistant Professor until August 2014. He has been serving as an Associate Professor since then.

Simulation Validation of Experimental Tests for Automotive System EMC Developmental Tests

Giacomo Braglia [1], Alistair Duffy [2], and Sami Barmada [1]

[1] Department of Energy, Systems, Territory and Construction Engineering
University of Pisa, 56122 Pisa, Italy
braglia.giacomo@gmail.com, sami.barmada@unipi.it

[2] School of Engineering and Sustainable Development
De Montfort University, Leicester, LE1 9BH, United Kingdom
apd@dmu.ac.uk

Abstract **─** The development and testing of automotive (sub)systems, particularly for Electromagnetic Compatibility (EMC), usually requires expensive test facilities. This paper describes the use of electromagnetic simulation to demonstrate the level of confidence that can be placed in measurements taken in more general laboratories, thus giving an estimate of the accuracy these facilities can provide. This is important in order to enable/allow more developments in automotive systems from research and development teams without standards compliant test facilities. This is, itself, important because of current developments in all-electric and autonomous vehicles. This paper demonstrates, through the use of full wave simulation representing a theoretically ideal environment compared with two different practical approaches, that EMC analysis can be undertaken with a reasonable estimation of accuracy and provides a framework for pre-compliance or developmental testing.

Index Terms **–** Automotive engineering, EMC, pre compliance tests, radiated emissions.

I. INTRODUCTION

The number and complexity of electric and electronic systems in modern automobiles has increased dramatically over recent years. The advent of the ‘driverless car’ is set to increase that further. As a consequence, electromagnetic compatibility (EMC) is of great concern from both an operational and safety viewpoint. In the automotive environment, the source of the radiated emissions are frequently the connecting cables rather than the devices that the cables connect. These cables may be electrically long and can radiate efficiently [1].

The International Standard dealing with automotive EMC is “CISPR 25” [2], which contains the limits and the procedures for the measurement of radio disturbances for automotive components and subsytems as well as a complete vehicle. It recommends the use of Absorber-Lined Shielded Enclosures (ALSE) in radiated emissions measurements tests, most commonly this is a semi anechoic chamber.

Given that rectifying EMC problems becomes costlier the later they are discovered, there is clear benefit in the use of pre-compliance and developmental tests in order to reduce the costs [3] as well as testing during development. This paper is concerned with comparing measurements and simulation results to provide that confidence measure. Moreover, two approaches to obtain measured results are discussed by way of “triangulating” the conclusions. These are measurement of a full system and prediction of the full system behaviour based on elemental measurements. This paper is only concerned with common mode currents as these represent the most significant source of radiation.

Recently, reference [4] proposed a method, based on a Hertzian dipole model, to calculate the radiated emissions from a cable harness in vehicles. This method divided the common mode path into a set of short, elemental, segments and used the frequency domain measurements of common mode currents to calculate, by superposition, the overall resulting field. This method is called the *multi-dipole model*. The same authors, in [5], proposed an improvement to the multi-dipole model with measurements in the frequency domain. The advantage of this method is that they can obtain the radiated emission only from common mode currents and do not require the use the semi-anechoic chamber: providing a test approach with greater utility for development teams without specialist resources.

Using similar logic, [6] presents a method (in accordance with CISPR 25) based on Multiple Segment Transfer Functions (MSTF). This method uses Transfer

Submitted On: December 28, 2015
Accepted On: July 14, 2016

Functions (TF) which represent the correlation between the common mode current in a specific setup environment and the radiated electric field strength.

The chief advantage of the MSTF method is that it helps to minimize the number of test cycles in the anechoic chamber. In fact, it allows the anechoic chamber to be used only once: in order to obtain the TF. Afterwards, the common mode current measurements can be taken for each component in any ordinary laboratory. Combining the last current measurements with the TF, previously obtained, the radiated electric field can be obtained.

Within this study, the MSTF method presented in [6], is replicated without using an anechoic facility. It approximates this by using an electromagnetically shielded room with a small number of radiation absorbing panels around the test system as a simple analogue of a semi anechoic chamber.

II. PRE-COMPLIANCE TEST METHOD FOR RADIATED EMISSION OF AUTOMOTIVE COMPONENT

The setup for radiated emission for components, presented in CISPR 25, comprises a line-over-ground-plane. The ground plane is a flat conductive surface whose potential is used as a common reference. The test harness is placed on a non-conductive material at 50 ± 5 mm above the ground plane.

The wiring type is defined by the actual system application and requirement. The length of the test harness is 1500 ± 75 mm and the antenna is positioned 1000 ± 10 mm from the wiring harness.

The test method relies on the common mode currents and the Transfer Functions to predict the electric field while differential mode currents are neglected due to the closely spaced geometry of the harness [7], [8]. In this work the harness used is a twisted pair cable. For convenience the line over ground plane, according to CISPR 25, is called *big line*.

Transfer functions (TFs) give the correlation, in the frequency domain, between the common mode currents along the harness and the radiated emissions. TFs are calculated with measurements made in the ALSE, thus the proprieties of the test setup are contained in the TFs.

The transfer function is defined by [1]:

$$TF(f) = \frac{E}{I_{CM}}, \tag{1}$$

where the I_{CM} is the common mode current along the cable harness and E is the electric field strength.

The TF can be obtained either by using an antenna connected to the test receiver and signal generator or by using measurements of the scattering parameters performed with a Vector Network Analyzer (VNA). The latter is the approach used in this work.

The line is fed by port 1 of the VNA and it is terminated with a load to simulate the equipment under test (EUT).

The measurements can be performed in two steps. Figure 1 shows the setup block diagram of the first step, where the scattering parameters ($S_{21\_antenna}$) is measured with the VNA. To measure the $S_{21\_antenna}$ the line is fed by port 1 of the VNA and the port 2 is connected to the antenna.

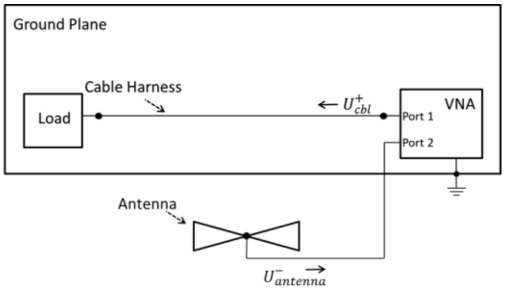

Fig. 1. Setup block diagram for $S_{21\_antenna}$, to obtain TF.

In the second step port 1 of VNA feeds the line, whilst port 2 is connected to the current probe, which is located around the cable. In this step the scattering parameter (S_{21_CP}) is measured. This is illustrated in Fig. 2.

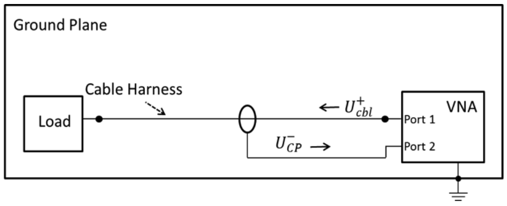

Fig. 2. Setup block diagram for S_{21_CP}, to obtain TF.

The transfer function can be calculated by Equation (2) [8]:

$$TF(f) = \left| \frac{S_{21\_antenna}(f)}{S_{21\_CP}(f)} \right| AF(f) Z_T(f), \tag{2}$$

where:

- AF is the antenna factor.
- Z_T is the transfer impedance of the current probe.

III. MULTIPLE SEGMENTS TRANSFER FUNCTIONS (MSTF)

The method presented in [8] considers the cable harness of the EUT as single segment, thus uses only one current probe measurement of the common mode currents. This method is limited, because it needs an identical current distribution of the EUT setup and the TF generation setup [3].

The MSTF approach divides the cable harness representing the radiation source in segments, for each of them the contribution of electric field is calculated. To obtain the predicted electric field, a union of the contributions for each segment is made taking into account the phase due to the different distance of each segment from the antenna.

A. Small line segmentation

The segmentation of the line is made by building a *small line* with the same type of the cable harness.

The length of the *small line* should be electrically small compared to the wavelength of the upper limit of the frequency range. This ensures a constant current distribution along the segment. Figure 3 shows the electrical scheme of the line.

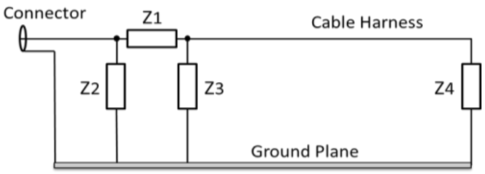

Fig. 3. Electrical scheme of the *small line*.

The line is terminated with an impedance (Z4) whose value is as close as possible to the characteristic impedance of the line and at the near end a network of impedances with π scheme is connected in order to provide an impedance match.

B. TF in the MSTF

For each *small line* the TFs are calculated according to Equation (2). S-parameter measurements, needed to calculate the TF, have to be made in the ALSE according to CISPR 25.

$S_{21\_antenna}$ needs to be measured using the *small line* positioned on the ground plane of the *big line* (see Fig. 4): port 1 feeds the *small line* and port 2 is connected to the antenna.

To measure S_{21_CP} the current probe is positioned around the wire in the middle of the *small line*. The VNA is used connecting port 1 to the *small line* and port 2 to the current probe.

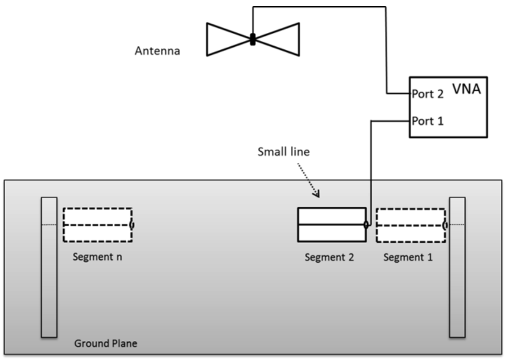

Fig. 4. Measurement setup for $S_{21\_antenna}$.

C. Common mode current determination

The knowledge of the common mode current distribution along the cable is needed for the radiated emission calculation.

The distribution of common mode current can be obtained through measurements of the current envelopes. Those measurements are made along the cable with the current probe and a test receiver in peak mode, illustrated in Fig. 5.

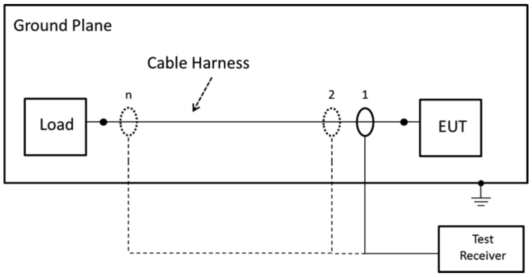

Fig. 5. Measurement setup for common mode current envelopes.

The current distribution from the envelope measurements can be obtained from a cable that is (ideally) longer than half the wavelength of frequency of test. However, for a shorter cable length, it is still an appropriate approximation and the procedure is the one reported in [6].

D. Phase determination

In the MSTF method, phase shift information between the segments is needed. This can be obtained with the current probe measurements along the cable of the EUT test setup. The measurements have to be made in the same positions where the TFs are generated. Using the VNA, the *big line* is fed at port 1 and port 2 is connected to current probe, see Fig. 6.

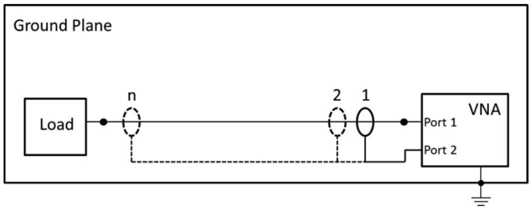

Fig. 6. Measurements of currents phase shifts, with current probe.

The phase shift is equivalent to the angle of S_{21}, see Equation (3):

$$\varphi_{I,i}(f) = \measuredangle S_{21,i} . \tag{3}$$

Each segment has different distance r_i from the antenna. This causes phase shift of the electric field $\varphi_{E,i}(f)$.

As shown in Equation (4), $\varphi_{E,i}(f)$ is equivalent to the angle of $S_{21\_antenna}$ parameter, which is measured using the *small line* and the antenna, see Fig. 4:

$$\varphi_{E,i}(f) = \measuredangle S_{21\_antenna,i} \,. \quad (4)$$

D. Prediction of the electric field

The calculation of the electric field can be performed with the previous information of each segment. As can be seen in the Equation (5), the electric field is given by superposition of each segment's field:

$$E_{pred}(f) = \left| \sum_i TF_i(f,y) I_{EUT,i}(f) e^{j[\varphi_{I,i}(f)+\varphi_{E,i}(f)]} \right| \,. \quad (5)$$

IV. MEASUREMENTS

The measurements are divided in two parts: one is dedicated to the implementation of the MSTF as described in the previous sections (measurements on the *small line* and of common mode currents) while the second part simply consists of a direct measurement of the E field produced by the *big line*.

The cable was a common twisted pair technology (category 5E cable). The diameter of each wire was 0.51 mm and the length of the line was 1.5 m. Measurements were made with the VNA in a screened room with a number of RAM panels used to provide a crude analogue of the ALSE.

The frequency range of the measurements was 30 to 200 MHz, representing a compromise between the emissions spectrum and acceptable dynamic range of the measurement systems. However, it should be noted that the system noise floor was high below 60 MHz so results at these frequencies are not to be regarded as reliable but they are included here to provide a fuller representation of the experimental results for validation by simulation.

Measurements on the *small line* are performed to calculate S_{21_CP} and $S_{21\_antenna}$ as previously described; Fig. 7 shows the current probe around the *small line*'s cable.

As for the common mode currents, the setup was made with the VNA, acting as a broadband source, which fed the *big line* that was terminated with a 50 Ω Load. The currents were measured with the current probe around the *big line*'s cable and connected to the spectrum analyser configured as a peak detector.

In the second part a radiated emission measurements serving as reference to validate the E- field predictions were made. These were made using the same setup used in the common mode measurements, but the current probe was taken off and the spectrum analyser was connected to the antenna. Measurements in the range of 1 MHz to 200 MHz were made to see how the noise floor could affect the tests at the low frequencies.

The measurement, with antenna and spectrum analyzer, was made while the line was fed from the VNA. Then, the measurement was made with the line disconnected, but leaving the VNA turned on inside the chamber.

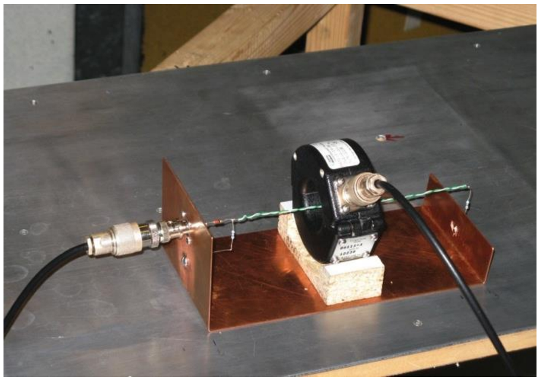

Fig. 7. Measurements with *small line* and current probe.

V. SIMULATION

Computer Simulation Technology CST Studio Suite (CST) was used to generate the reference data used to evaluate the measurements. The measurement systems were replicated as closely as possible. However, ideal free space characteristics were used. This was to allow the representation of what could be expected from the measurements if they were to be undertaken in a theoretically ideal facility. It was previously noted that only the common mode currents were to be considered, so it would have been possible to represent the Category 5 twisted pair with a single conductor in the model (which would have been computationally simpler). However, it was decided to replicate the EUTs as closely as possible so a twisted pair, of the correct dimensions and lay length was created, as illustrated in Fig. 8.

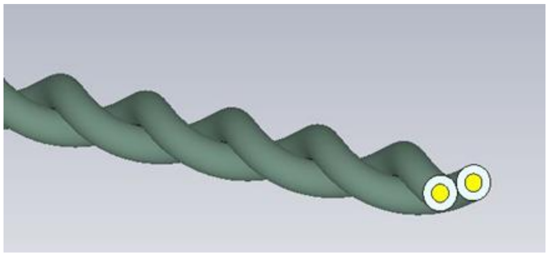

Fig. 8. Model of the twisted pair.

This cable was terminated in the test fixture using a coaxial connector. The simulated version of this is shown in Fig. 9.

The overall simulation configuration is illustrated in Fig. 10, which shows the line being simulated and the E-field probe location, which provides further 'idealised' measurements by removing the effect of the measuring antenna on the results.

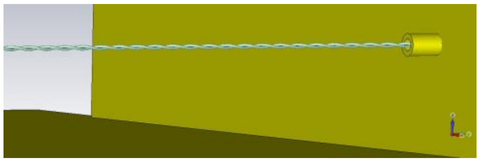

Fig. 9. Termination of the twisted pair.

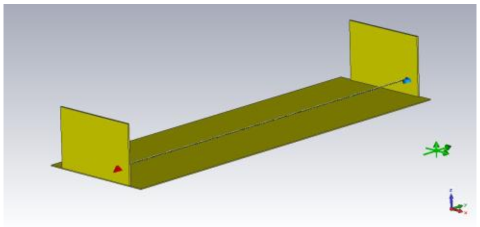

Fig. 10. Simulation configuration.

VI. POST PROCESSING AND RESULTS

This section presents the measurement results, showing how the electric field can be retrieved from the common mode currents and these are compared with the simulations.

The measurements were performed using the biconical antenna and the spectrum analyser. Using the antenna factor, the E field was retrieved in vertical and horizontal polarization. Remembering that the equipment was in the chamber during the tests, Fig. 11 shows how the noise floor could affect the measurements in low frequency.

Figures 12 and 13 show the comparisons between the electromagnetic simulations, the measured E field and the predicted E field, both in the horizontal polarization (Y) and in the vertical polarization (Z).

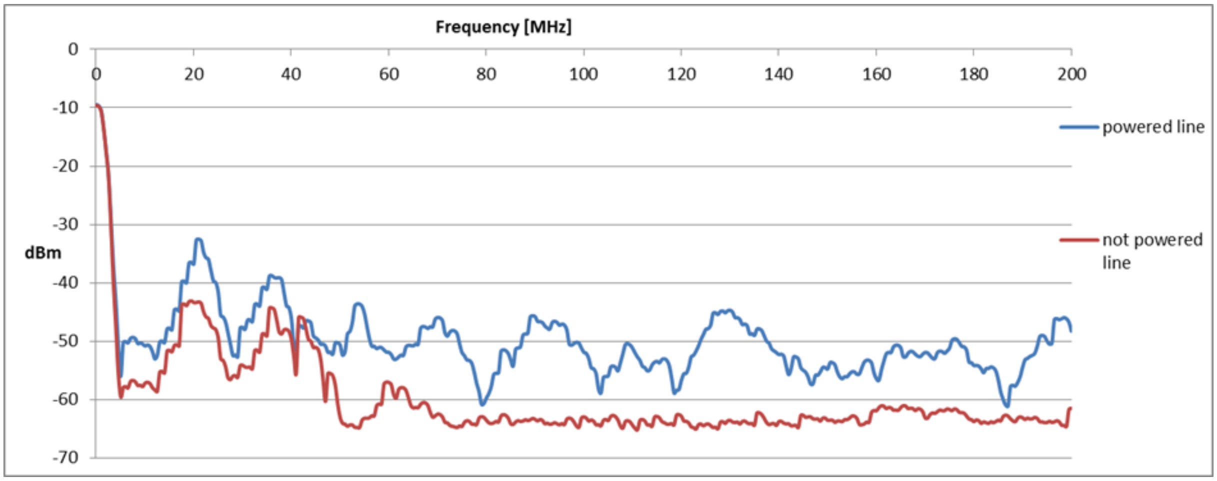

Fig. 11. Comparison, between the measurements with the big line powered and the big line not powered, to see how the noise floor affects the measurements in low frequency.

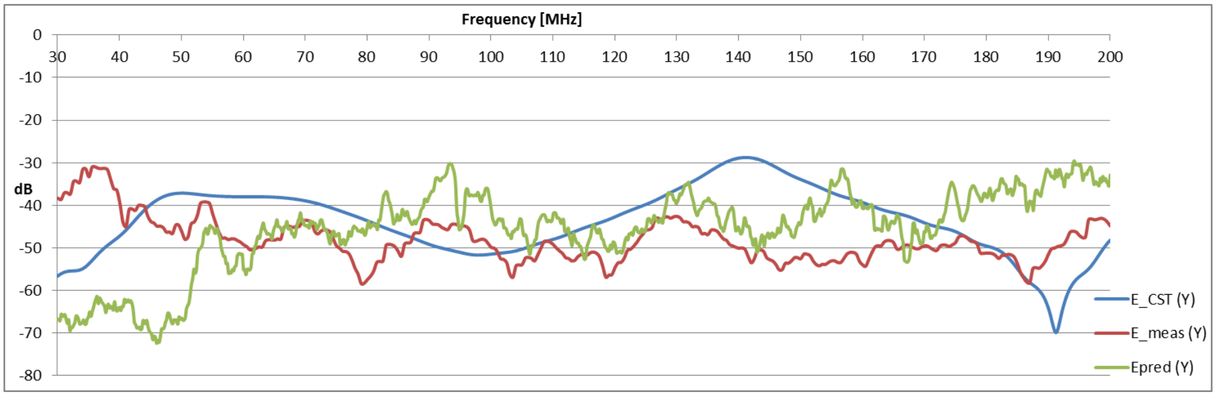

Fig. 12. Comparison for horizontal polarization (Y) of the predicted E field, measured E field and E field CST simulated.

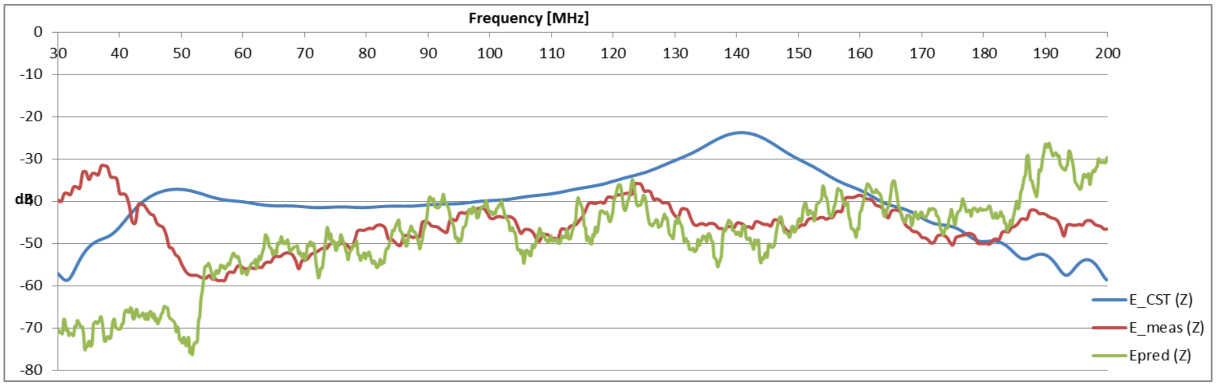

Fig. 13. Comparison for vertical polarization (Z) of the predicted E field, the measured E field and the simulated E field in CST.

At low frequencies (up to 60 MHz) a large difference between the measured E-field and the predicted E field can be seen, the cause of this difference is likely to be the noise floor, because the absorbent materials do not work well at those lower frequencies.

The CST simulations traces are close to the predicted and measured field with an average deviation lower than 10 dB in the most of the frequency range. It is important to underline that in CST the chamber environment is not considered (metal walls, absorbing materials and antenna) and is, therefore, an ‘ideal’ configuration: this explains the big differences between the blue curves (CST) and the red/green curves in some frequency bands.

In the horizontal polarization (Fig. 12) above 50 MHz the predicted E-field and the measured E-field are in good agreement. In the frequency ranges 150 to 160 MHz and 180 to 200 MHz a difference of about 10 dB can be seen.

In the vertical polarization (Fig. 13) above 50 MHz, the predicted E-field and the measured E-field are in good agreement. Only in the frequency range 190 to 200 MHz the difference is about 10 dB.

The comparison has to be made taking into account that an approximation of a semi anechoic chamber was used. Therefore the absorbent materials were located around the setup but they did not cover all walls. Also the measurement equipment was located in the chamber, thus the equipment supply could produce signals that affect the measurements. This was to investigate how well a low cost general laboratory configuration would behave.

Furthermore, in the test configuration, the antenna is in the near field of the line, while the antenna factor from manufacturers is calibrated in far field in an open area test site [9]. This is likely to have an affect the prediction of electric field.

VI. CONCLUSION

One of the principal interests of this paper has been to identify how accurate radiation emissions measurements can be if they are performed in a general laboratory setting. An important aspect of this work has been the use of 3-D full-wave simulations to validate the measurements

The simulations show general agreement with the experiments, giving an indication of the deviation that can be expected from a theoretically ideal configuration. There is clearly some difference in the fine detail, but the general shapes and amplitudes demonstrate reasonable overall agreement.

This work shows that with good measurement practice, a possible test methodology is suitable to be used by a range of interested parties: from automotive components manufacturers to academic teaching and research laboratories can be obtained. This proposed methodology can give results with an accuracy of few dB. It also shows the benefit of the use of simulation to validate measurements. In the case of the results presented here, a shielded room was used. However, it may be possible to use a less isolated environment provided that the initial ‘site survey’ identifies the noise floor characteristics (as was shown in Fig. 9) and results are not relied on where the noise floor (including background radiation) is too high.

ACKNOWLEDGMENT

The authors would like to acknowledge the support of the EU Erasmus scheme that allowed this work to be undertaken.

REFERENCES

[1] W. T. Smith and R. K. Frazier, “Prediction of anechoic chamber radiated emissions measurements through use of empirically-derived transfer functions and laboratory common-mode current measurements,” *Electromagnetic Compatibility, 1998. 1998 IEEE International Symposium on*, vol. 1, pp. 387-392, August 1998.

[2] British Standards Institute, “Radio disturbance

characteristics for the protection of receivers used on board vehicles, boats, and on devices - Limits and methods of measurement," BS EN 55025:2003 CISPR 25:2002, March 2003.

[3] D. Schneider, M. Bottcher, S. Tenbohlen, and W. Kohler, "Pre-compliance test method for radiated emissions with multiple segment transfer functions," International *Symposium on Electromagnetic Compatibility (EMC EUROPE 2013)*, pp. 605-610, August 2013.

[4] J. Jia, D. Rinas, and S. Frei, "Prediction of radiated fields from cable bundles based on current distribution measurements," *International Symposium on Electromagnetic Compatibility (EMC EUROPE 2012)*, pp. 1-7, September 2012.

[5] J. Jia, D. Rinas, and S. Frei, "An alternative method for measurement of radiated emissions according to CISPR 25," *International Symposium on Electromagnetic Compatibility (EMC EUROPE 2013)*, pp. 304-309, September 2013.

[6] D. Schneider, et al., "Transfer functions and current distribution algorithm for the calculation of radiated emissions of automotive components," *International Symposium on Electromagnetic Compatibility (EMC EUROPE 2013)*, pp. 443-448, September 2013.

[7] Clayton R. Paul, "A comparison of the contributions of common-mode and differential-mode currents in radiated emissions," *Electromagnetic Compatibility, IEEE Transactions on*, vol. 31, no. 2, pp. 189-193, May 1989.

[8] D. Schneider, S. Tenbohlen, and W. Kohler, "Pre-compliance test method for radiated emissions of automotive components using scattering parameter transfer functions," *International Symposium on Electromagnetic Compatibility (EMC EUROPE 2012)*, pp. 1-6, September 2012.

[9] D. Rinas, J. Jia, A. Zeichner, and S. Frei, "Substituting EMC emission measurement by field and cable scan method using measured transfer function," *Advances in Radio Science*, vol. 11, pp. 183-188, July 2013.

Giacomo Braglia received the M.S. degree in Electrical Engineering at the University of Pisa in year 2014 and he received the Rohde & Shwartz Prize for Best Project for his Master's thesis. He is currently Project Quality Manager on for GE Oil & Gas (SubSea systems).

Alistair Duffy is Professor of Electromagnetics at De Montfort University, Leicester, UK, having joined from the University of Nottingham in 1994 where he obtained his Ph.D. in 1993. He holds a Bachelors and Masters degree from the University of Wales (University College Cardiff) and an MBA from the Open University. He is a Fellow of the IEEE and a past Board of Directors member of both the Applied Computational Electromagnetics Society and the IEEE EMC Society. His research interests are in computational and experimental electromagnetics, particularly focusing on EMC and validation problems.

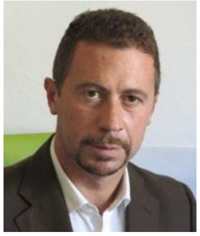

Sami Barmada received the M.S. and Ph.D. degrees in Electrical Engineering from the University of Pisa, Italy, in 1995 and 2001, respectively. He currently is an Associate Professor with the Department of Energy and System Engineering (DESTEC), University of Pisa. His teaching activity is related to circuit theory and electromagnetics. His research activity is mainly dedicated to numerical computation of electromagnetic fields and EMC problems, power line communications, non-destructive testing and signal processing. He is author and co-author of approximately 100 papers in international journals and refereed conferences. Barmada was the General Chair of the ACES 2007 Conference and Technical Chairman of the PIERS 2004 ACES 2013 and ACES 2014 conferences. He is currently President of the ACES Society.

A Novel Asterisk-Shaped Circularly Polarized RFID Tag for On-Metal Applications

Umar H. Khan [1], Bilal Aslam [1], Javaria Khan [1], Misha Nadeem [1], Humayun Shahid [1], Muhammad Awais Azam [1], Yasar Amin [1,2], and Hannu Tenhunen [2]

[1] ACTSENA Research Group
University of Engineering and Technology, 47050-Taxila, Pakistan
umar.hasan@uettaxila.edu.pk

[2] iPack VINN Excellence Center
Royal Institute of Technology, SE-16440, Stockholm, Sweden
{yasr, hannu}@kth.se

Abstract ─ An asterisk-shaped, metal-mountable RFID tag with a minuscule footprint is presented. The proposed design makes use of multiple asymmetric slots patterned in a cross-shaped fashion to achieve circular polarization. The structure is excited capacitively using a terminally-grounded, T-shaped feed line positioned within the slots. This peculiar arrangement permits the attainment of circular polarized radiation characteristics over a wide band of operation. Impedance matching, antenna size reduction and read range enhancement are the additional advantages offered by the embedded feed line. The final design is realized on a commercially available FR-4 substrate over dimensions of 40 x 40 mm^2 yielding an impedance bandwidth and an axial ratio bandwidth of 37 MHz and 20 MHz, respectively. Improvement in antenna gain (and consequently in the read range) is reported upon mounting the tag on metallic surfaces.

Index Terms ─ Circular polarization, impedance matching, Radio Frequency Identification (RFID).

I. INTRODUCTION

Applications built upon radio frequency identification (RFID) technology, particularly the ones in the ultra high frequency (UHF) band of operation (860-960 MHz), have increased in number dramatically over the last decade [1-4]. This primarily is due to a number of advantages associated with RFID tags operating in the UHF band including enhanced read range, high data transfer rate, and small tag footprint [5-8]. For most practical applications, a hefty majority of the RFID reader antennas that exist today incorporate circularly polarized radiation characteristics. Doing so offers a multitude of benefits such as an increase in orientation diversity and reduction in polarization mismatch loss. Most of the commercially available tag antennas, however, are linearly polarized, causing a stark mismatch in polarization between the reader and the tag antenna. This polarization mismatch translates to an undesirable decrease in the tag's read range, limiting the overall performance of any application-specific RFID system within which the tag is deployed [9, 10]. Doing away with the polarization mismatch is bound to result in enhanced read range and tag-orientation independence, making it a highly sought feature. Owing to these advantages, designing RFID tag antennas with circularly polarized radiation characteristics that persist over a wide band of operation has been the prime focus of recent research effort [11, 12].

Yet another sought-after feature for RFID tags is the capability of being readily mountable on metallic surfaces. The majority of metal-mountable RFID tags are linearly polarized in nature [13-17], falling prey to polarization mismatch loss and depriving the RFID system of orientation-independence characteristics. There are but only a few RFID tag antennas reported in literature that both operate in the UHF band and possess circularly polarized radiation characteristics [18, 19]. Moreover, for RFID tags that incorporate circularly polarized radiation characteristics, are metal-mountable, and operate in the UHF band, the structures deployed for providing the feed are essentially located outside the radiating components [20, 21]. This arrangement results in an overall increase in the tag antenna's size. In addition, feeding networks realized external to the radiators generally translate to structural asymmetries that are manifested in the design of the tag antenna. This, in turn, leads to a decrease in the antenna's boresight gain. Lin et al. [22] have presented a RFID reader antenna that incorporates a feeding network embedded within the radiating elements, operates in the circularly

Submitted On: May 25, 2016
Accepted On: July 27, 2016

polarized mode, and offers a wide axial ratio bandwidth equal to 12 MHz. The antenna, however, has been tuned to match an impedance of 50Ω and has its thickness exceeding 10 mm. These drawbacks render an antenna of this type unfit for deployment in modern-day, unobtrusive RFID applications

In this paper, a compact RFID tag operating in the UHF band with circularly polarized radiation characteristics. Opting in for a peculiar asterisk-shaped patch design offers advantages such as miniscule tag footprint and an appreciably wide 3 dB axial ratio bandwidth. The tag not only offers benefits such as orientation independence and enhanced read range, but also boasts the sought-after feature of being readily mountable on metallic surfaces. The tag antenna is fabricated on readily available substrate and the simulated electromagnetic characteristics are juxtaposed with the experimental findings.

II. ANTENNA DESIGN

The flowchart in Fig. 1 elaborates the systematic approach that has been adhered to during the antenna design process.

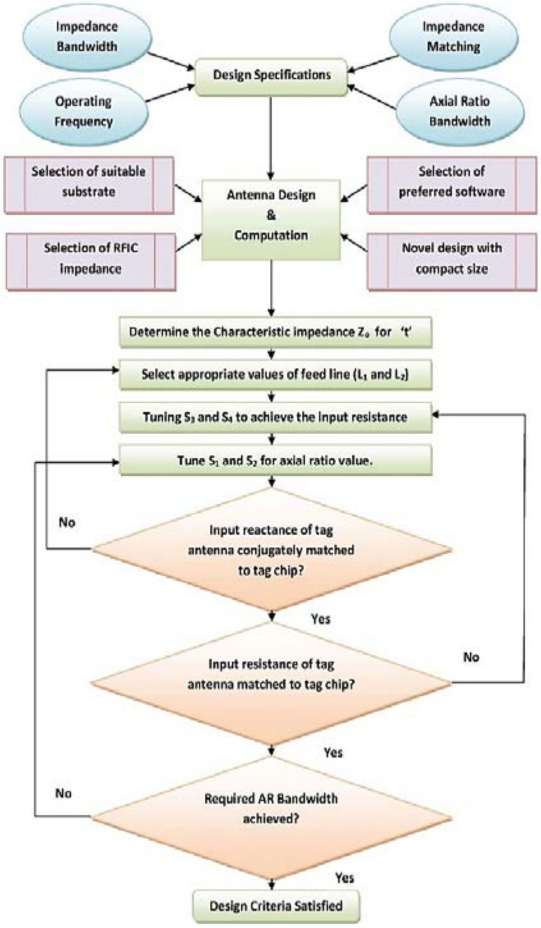

Fig. 1. Flow chart of the proposed antenna design.

The detailed layout of the formulated RFID tag boasting circular polarized radiation characteristics is depicted in Fig. 2. An asterisk-shaped patch antenna of dimensions 40 x 40 mm^2 is realized on an FR-4 substrate that has a thickness of 1.6 mm. Selecting this particular patch design allows for reduction in tag antenna size and also facilitates in maintaining the desired axial ratio over a wide band of operation. Four asymmetric slots, labeled as S_1 through S_4, are meticulously etched within the asterisk-shaped patch to not only achieve circularly polarized radiation characteristics, but also to ensure impedance match between the antenna structure and the Radio Frequency Integrated Circuit (RF IC). In particular, slots S_1 and S_2 patterned in a cross-like fashion, are responsible for the attainment of circularly polarized radiation characteristics. Slots S_3 and S_4, patterned in a plus-shaped manner and provided with feeding lines, allow for the impedance match to take place. The width of the asymmetric slots, with and without the feeding lines, are $S_{w2=}$4 mm and S_{w1}=3.5 mm, respectively. The L-shaped microstrip feed line is oriented at a coupling distance, D, around 1 mm from the radiating patch. The width of the main feed line, t, is 2 mm and is further divided into two unequal feed lines of lengths L_1 and L_2 with the RF IC in between. The formulated design, in its entirety, is fabricated on a ground plane having a size of 60 x 60 mm^2.

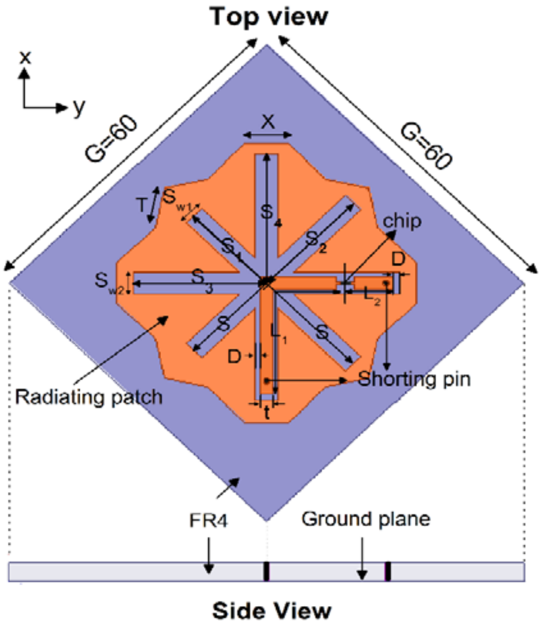

Fig. 2. Geometry of the proposed CP RFID antenna design (Units: mm).

Designing for circularly polarized radiation characteristics involves varying the lengths of both the cross and plus-shaped slots incrementally and concurrently, such that the surface current density is equally distributed over the entire patch, resulting in the generation of two orthogonal degenerated modes. The next step involves controlling the phase difference between the two degenerated modes. This is done by appropriate tuning of the length of S_1 and length of S_2. When the length of S_1 is less than that of S_2, the path of current in the x-direction will be longer than that for the y-direction. This difference in the lengths of S_1 and S_2 leads to the formation of lower and higher resonant modes. Careful selection of lengths of both S_1 and S_2 results in the two degenerate modes being out of phase by 90^0, achieving right-hand circular polarization radiation. Similarly, rendering the length of S_2 great than the length of S_1 generates left-hand circular polarization radiation. The embedded nature of the slotted design allows for the overall antenna size to become minuscule.

The impedance matching phase lies at the core of the tag design process. The RF IC chosen for deployment in the formulated tag antenna is Alien Higgs that operates in the FCC band (902-928 MHz). The RF IC is connected between two feed lines as shown in Fig. 2, and has an associated value of impedance mounting to 13 - j111 Ω at an operating frequency of 915 MHz. In order to ensure that maximum amount of power gets transferred across from the tag antenna to the chip, the value of impedance for the tag antenna is tuned to be around 13 + j111 Ω at 915 MHz. The real part of the antenna's impedance is adjusted by varying the lengths of S_1 and S_2, whereas the required value of inductive reactance is achieved by dint of a pair of short-circuited microstrip transmission lines oriented in the etched slots.

The calculation for length of the short-circuited microstrip lines L_1 and L_2 follows from transmission line theory [23, 24]:

$$111 = Z_o \tan[\frac{2\pi}{\lambda}(L_1 + L_2)], \tag{1}$$

$$Z_o = \frac{120}{\sqrt{\varepsilon_{eff}}} \frac{1}{\{\left(\frac{w}{h}\right)+1.393+0.677\}\{ln\left(\frac{w}{h}\right)+1.444\}}, \tag{2}$$

$$\varepsilon_{eff} = \frac{\varepsilon_r+1}{2} + \frac{\varepsilon_r-1}{2} \times \{\frac{1}{\sqrt{1+\frac{12h}{w}}}\}, \tag{3}$$

where Z_o equals the characteristic impedance of a short-circuited line and λ represents the guided wavelength at 915 MHz. Plugging in the relevant values for Z_o and λ, the total length of the transmission line, $L_1 + L_2$, turns out to be 36 mm. While many solutions exist for solving the equation $L_1 + L_2 = 36$ mm, the values are chosen such that L_1 approximately equals to $L_2 + \lambda/6$. Owing to slight drift in the impedance value of the RF IC as compared to the one quoted on the datasheet, the best impedance match is attained when total length $L_1 + L_2$ equals 37.7 mm. In addition to impedance matching, this peculiar arrangement also offers the advantage of tag miniaturization. The design parameters are optimized using full-wave simulation tool HFSS^{TM}, and are shown in Table 1.

Table 1: Optimized design parameters (length) of the tag

Parameters	S_1	S_2	S_3	S_4	S_5
(λ)	0.052	0.062	0.067	0.069	0.011
Parameters	L_1	L_2	T	X	S
(λ)	0.095	0.019	0.022	0.021	0.113

III. RESULTS AND DISCUSSION

The design of the formulated RFID tag antenna has been fine-tuned by thoroughly examining various key electromagnetic descriptors in an iterative fashion. The investigation is orchestrated using full wave electromagnetic design tool HFSS^{TM}. The meticulously refined design is realized on an FR-4 substrate as shown in Fig. 3.

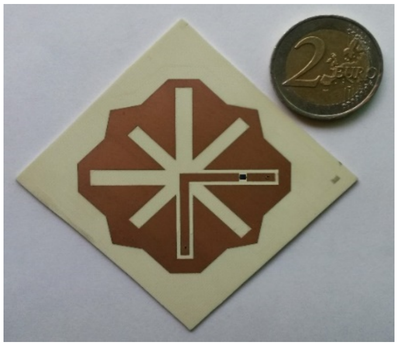

Fig. 3. Fabricated RFID tag antenna.

The fabricated tag prototype is scrutinized for its performance experimentally. The input impedance of the tag antenna is measured by two-port differential probe measurement method, as in [25, 26], using Vector Network Analyzer (MS2026B, Anritsu). The findings for the impedance measurement are depicted in Fig. 4.

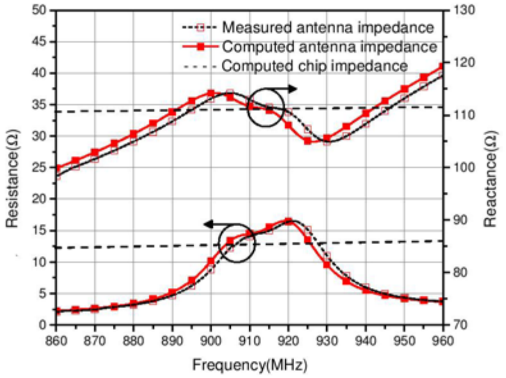

Fig. 4. Measured and computed impedances of the proposed antenna.

It can be observed that the impedance of the RF IC varies only slightly with a change in the frequency. The resistance and reactance of the tag antenna exhibit a close conjugate match with the RF IC's impedance at 915 MHz. The computed and measured return loss is illustrated in Fig. 5. The measured return loss is calculated using the measured antenna impedance. A 10 dB return loss bandwidth equal to 37 MHz (897–934 MHz) has been reported experimentally, making the proposed RFID tag compliant with the North American frequency band. The computed values and measured results for impedance measurement and return loss are, principally, in good accord with one another.

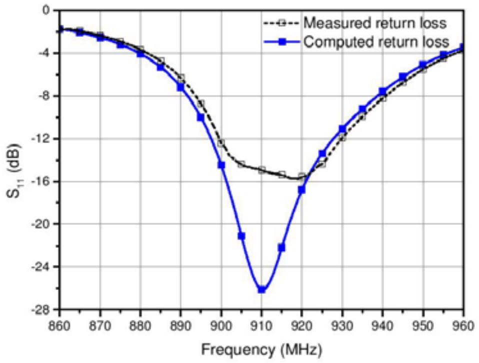

Fig. 5. Measured and computed return loss of the proposed antenna.

The effect of varying the length of the feedline and the asterisk-shaped slot on circular polarization bandwidth is investigated. Embedding the capacitively coupled feed lines, namely L_1 and L_2, within the asterisk-shaped slots translates to a significant phase delay being induced that contributes towards cross-polarized excitation. To ensure resonant modes centered about 915 MHz, appropriate slot lengths have been chosen after exhaustive comparison of two scenarios: length of S_1<length of S_2 (condition 1) and length of S_1>length of S_2 (condition 2).

After optimizing the design iteratively the associated axial ratio bandwidth of condition 1 (length of S_1=17 mm, length of S_2=20.1 mm) and condition 2 (length of S_1=21.8 mm, length of S_2=15.7 mm), as shown in Fig. 6, turns out to be 20 MHz for both the scenarios. The range of the axial ratio bandwidth for condition 1 is (899–919 MHz), and for condition 2 is (896–916 MHz).

The default choice, however, is the case where length of S_1<length of S_2 because, here, the axial ratio bandwidth lies within the FCC band of operation. The results for amplitude and phase along the boresight direction are illustrated in Figs. 7 (a) and (b), respectively.

From Fig. 7 (a), it can be observed that the |Ex| and |Ey| are equal in amplitude. Figure 7 (b) shows that for condition 1, a phase difference $\Phi x - \Phi y = 90^0$ is observed at 915 MHz, which depicts right hand circular polarization. For condition 2, phase difference $\Phi y - \Phi x = 90^0$ is noted at around 900 MHz, which signifies left hand circular polarization. This validates the existence of appreciable circular polarization radiation characteristics at 915 MHz which is within the band of interest.

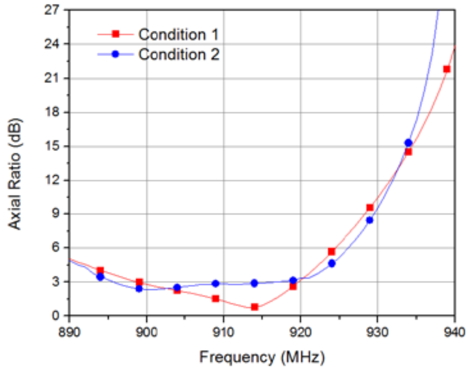

Fig. 6. Axial ratio of the proposed antenna design.

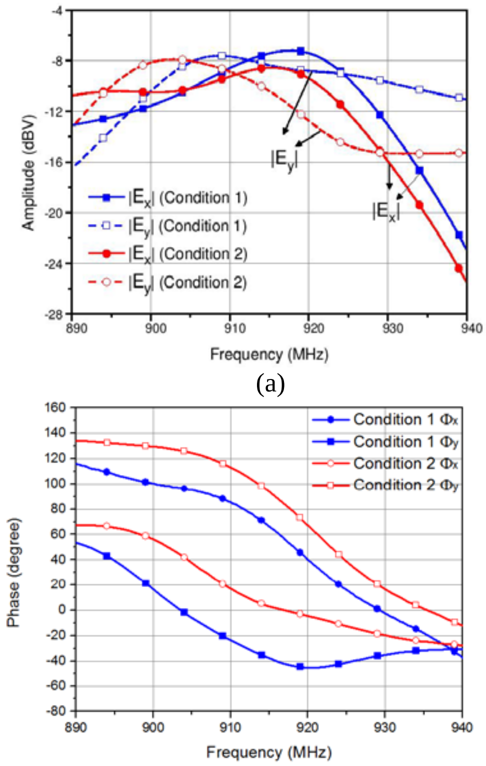

(a)

(b)

Fig. 7. Amplitude (a) and phase (b) diagrams of boresight radiation field E_x and E_y.

Circularly polarized radiation characteristics inherent with the tag antenna design are demonstrated by plotting the simulated surface current distribution at 915 MHz in Fig. 8. The figure depicts the changes in the surface current distribution and the direction of the distributed current at incremental time phases of 0^0, 45^0, 90^0 and 135^0. The counterclockwise direction of the current accompanied by an increase in the intensity of the same solidifies the existence of an RHCP-excited radiation in the design.

Since the input impedance of the formulated tag antenna has been conjugately matched with the impedance of the chip (and not to a 50Ω co-axial feedline) measuring the radiation pattern of the designed tag using conventional anechoic chamber setup is not possible. The results are delimited to the computed scenario only for both free-space and on-metal scenarios. Figure 9 shows the radiation pattern at 915 MHz.

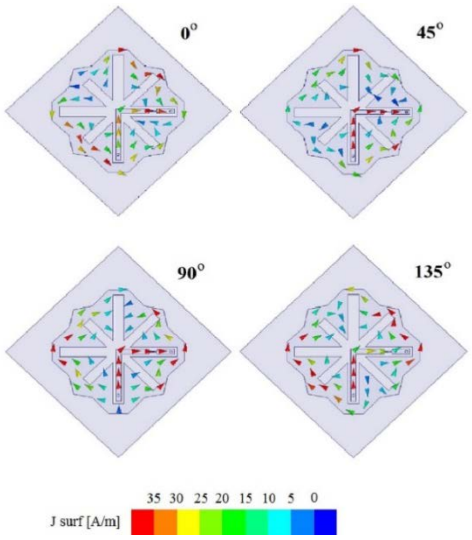

Fig. 8. Current distribution at 915 MHz.

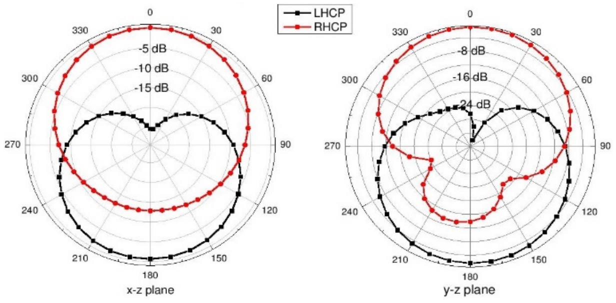

Fig. 9. Normalized CP gain radiation pattern at 915 MHz.

It is evident from Fig. 9 that, the formulated antenna boasts a 3-dB beam width of around 74^0 and an appreciable front-to-back radiation ratio in the order of 22 dB for both x-z and y-z planes. The appreciable front-to-back radiation ratio validates the existence of pure right-hand circularly polarized radiation characteristics exhibited in free space.

Figure 10 depicts the values of electric filed strength in the azimuth and elevation plane obtained upon mounting the tag on a uniform metallic sheet of 400 x 400 mm^2. The results show that the values of E-theta and E-phi are almost identical, verifying the existence of circularly polarized radiation characteristics associated with the formulated tag even when the tag is mounted on the metal surface.

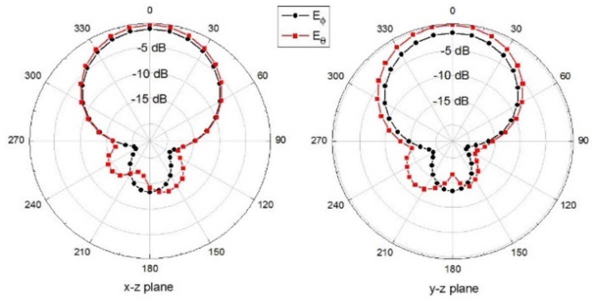

Fig. 10. Antenna realized gain radiation pattern on 400 x 400 mm^2 metallic plate.

The change in gain of the tag antenna upon deployment free space and metallic surfaces is computed. The gain is improved by a factor of 5 dB when the tag antenna is moved from free space on to a metallic surface. A larger metallic surface yields a larger area over which the antenna's current is distributed, resulting in a larger overall gain. As seen in Fig. 11, for ground plane, sizes more than 100 x 100 mm^2, the antenna gain remains well above -10.4 dBic. The calculated and measured read range of the proposed tag in free space and on metal plate sized 400 x 400 mm^2 is shown in Table 2 and measurement setup with Impinj^{TM} RFID reader (xPortal) is shown in Fig. 12.

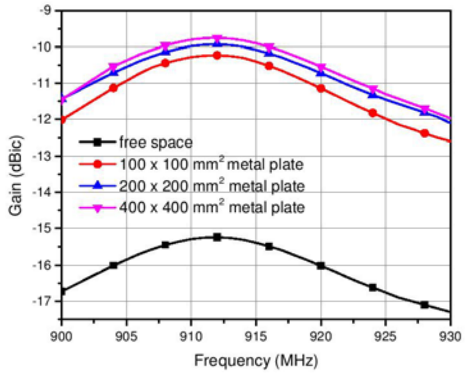

Fig. 11. Computed gain for different metal plate sizes at 915 MHz.

Table 2: Readrange of the proposed antenna with and without metal plate

Condition	Computed Gain (dBi)	Readrange Calculated	Readrange Measured
Free space	-15.3	1.94m	1.52m
On metal, 400x400mm^2	-9.7	3.69m	3.36m

Fig. 12. Measurement setup for readrange.

From Table 3, it is evident that the proposed RFID tag antenna offers a significantly smaller footprint when stacked against designs presented in [20] and [21]. The decrease in size has been achieved without compromising on the gain of the tag antenna which, being -15.3 dBic, is still comparable to competing designs. That said, the proposed tag offers an appreciably wide axial ratio bandwidth of 20 MHz, which is a clear improvement over designs reported in [20] and [21]. Similarly, the overall radiating size of 40 x 40 mm^2 has also been observed as being the minimum among the compared designs.

Table 3: Comparison of different antenna parameters

Antenna Ground Plane (mm^2)	Computed Gain (dBi)	AR Bandwidth (MHz)	Radiating Size (mm^2)
60x60 [pro]	-15.3	20	40x40
70x70 [21]	-14.4	6	50.5x50.5
80x80 [20]	-11.4	6	55.7x55.7

IV. CONCLUSION

A novel, compact, chip-based RFID tag antenna boasting circularly polarized radiation characteristics has been designed, fabricated and measured for its performance. A peculiarly-fashioned, asymmetrical, asterisk-shaped design provisioned with an embedded feed line paves the way for achieving an appreciable axial ratio bandwidth of 20 MHz, as well as a minuscule footprint of 40 x 40 mm^2, within the FCC band. Higher gain and enhanced read range have also been demonstrated when juxtaposed with other circularly polarized RFID antenna. Upon mounting on metallic surfaces, the designed tag exhibits accentuated read range making it a prime candidate for on-metal deployment.

ACKNOWLEDGMENT

This work was financially supported by Vinnova (The Swedish Governmental Agency for Innovation Systems) and University of Engineering and Technology Taxila, Pakistan through the Vinn Excellence Centers Program and ACTSENA Research Group Funding, respectively.

REFERENCES

[1] G. Marrocco, "The art of UHF RFID antenna design: impedance-matching and size-reduction techniques," *IEEE Antennas and Propagation Magazine*, vol. 50, no. 1, pp. 66-69, 2008.

[2] K. V. S. Rao, P. V. Nikitin, and S. F. Lam, "Antenna design for UHF RFID tags: A review and a practical application," *IEEE Transactions on Antennas and Propagation*, vol. 53, no. 12, pp. 3870-3876, 2005.

[3] M. S. R. Bashri, M. Ibrahimy, and S. M. A. Motakabber, "Design of a wideband inductively coupled loop feed patch antenna for UHF RFID tag," *Radio Engineering*, vol. 24, no. 1, pp. 38-44, 2015.

[4] Y. Amin, Q. Chen, L. R. Zheng, and H. Tenhunen, "Development and analysis of flexible UHF RFID antennas for "Green" electronics," *Progress in Electromagnetics Research*, vol. 130, no. 14, pp. 302-307, 2012.

[5] E. A. Soliman, M. O. Sallam, W. L. De Raedt, and G. A. E. Vandenbosch, "Miniaturized RFID tag antenna operating in 915 MHz," *IEEE Trans. Antennas Propagat.*, vol. 11, no. 5, pp. 1068-1071, 2012.

[6] H. W. Lui, C. F. Yang and C. H. Ku, "Novel miniature monopole tag antenna for UHF RFID applications," *IEEE Antennas and Wireless Propagation Letters*, vol. 9, pp. 363-366, 2010.

[7] H. K. Ryu and J. M. Woo, "Miniaturisation of rectangular loop antenna using meander line for RFID tags," *IET Electronics Letters*, vol. 43, no. 7, pp. 372-374, 2007.

[8] M. Dhaouadi, M. Mabrouk, T. P. Vuong, and A. Ghazel, "A broadband UHF tag antenna for near-field and far-field RFID communications," *Radio Engineering*, vol. 23, no. 4, pp. 1026-1032, 2014.

[9] K. H. Lin, et al., "A loop bow-tie RFID tag antenna design for metallic objects," *IEEE Transactions on Antennas and Propagation*, vol. 61, no. 2, pp. 499-505, 2013.

[10] S. Genovesi and A. Monorchio, "Low-profile three-arm folded dipole antenna for UHF band RFID tag mountable on metallic objects," *IEEE Antennas and Wireless Propagation Letters*, vol. 9, no. 12, pp. 1225-1228, 2010.

[11] X. Y. Lui, Y. Liu, and M. Tentzeris, "A novel circularly polarized antenna with coin-shaped patches and a ring-shaped strip for worldwide UHF RFID applications," *IEEE Antennas and Wireless Propagation Letters*, vol. 14, pp. 574-581, 2016.

[12] J. Shi, X. Wu, Q. Xianming, and Z. N. Chen "An omni-directional circularly polarized antenna array," *IEEE Transactions on Antennas and Propagation*, vol. 64, no. 2, pp. 574-581, 2016.

[13] E. S. Yang, "Dual-polarized metal-mountable UHF

RFID tag antenna for polarised diversity," *IET Electronic Letter*, vol. 52, no. 7, pp. 496-498, 2016.

[14] W. Choi, J. Kim, J. H. Bae, and G. Choi, "A small RFID tag antenna using proximity-coupling to identify metallic objects," *Microwave and Optical Technology Letters*, vol. 50, no. 11, pp. 2978-2981, 2008.

[15] P. H. Yang, Y. Li, L. J. Jiang, and T. T. Ye, "Compact metallic RFID tag antennas with a loop-fed method," *IEEE Transactions on Antennas and Propagation*, vol. 59, no. 12, pp. 4454-4462, 2011.

[16] T. V. Koskinen, "A thin multislotted dual patch UHF-band metal-mountable RFID tag antenna," *Microwave and Optical Technology Letters*, vol. 53, no. 1, pp. 40-47, 2011.

[17] T. Bjorninen, "Compact metal mountable UHF RFID tag on a barium titanate based substrate," *Progress In Electromagnetics Research C*, vol. 26, no. 11, pp. 43-57, 2012.

[18] Z. Wang, S. Fang, S. Fu, and S. Jia, "Single-fed broadband circularly polarized stacked patch antenna with horizontally meandered strip for universal UHF RFID applications," *IEEE Transactions on Microwave Theory and Techniques*, vol. 59, no. 4, pp. 1066-1073, 2011.

[19] J. Garcia, A. Arriola, F. Casado, and D. Valderas, "Coverage and readrange comparison of linearly and circularly polarised radio frequency identification ultra-high frequency tag antennas," *IET Microwave, Antennas & Propagation*, vol. 6, no. 9, pp. 1070-1078, 2012.

[20] H. D. Chen, S. H. Kuo, and J. L. Jheng, "Design of compact circularly polarized radio frequency identification tag antenna for metallic object application," *Microwave and Optical Technology Letters*, vol. 55, no. 7, pp. 1481-1485, 2013.

[21] H. D. Chen, S. H. Kuo, C. Y. D. Sim, and C. H. Tsai, "Coupling-feed circularly polarized RFID tag antenna mountable on metallic surface," *IEEE Transactions on Antennas and Propagation*, vol. 60, no. 5, pp. 2166-2174, 2012.

[22] Y. F. Lin, C. H. Lee, S. C. Pan, and H. M. Chen, "Proximity-fed circularly polarized slotted patch antenna for RFID handheld reader," *IEEE Transactions on Antennas and Propagation*, vol. 61, no. 10, pp. 5283-5286, 2013.

[23] D. M. Pozar, *Microwave Engineering*. 3rd ed., New York, NY, USA: Wiley, 2005.

[24] G. Gonzalez, *Microwave Transistor Amplifiers: Analysis and Design*. 2nd ed., New Jersey, NJ, USA: Wiley, 1996.

[25] S. K. Kuo, S. L. Chen, and C. T. Lin, "An accurate method for impedance measurement of RFID tag antenna," *Progress In Electromagnetics Research*, vol. 83, pp. 93-106, 2008.

[26] Y. Amin, Q. Chen, H. Tenhunan, and L. R. Zheng, "Evolutionary versatile printable RFID antennas for "Green" electronics," *Journal of Electromagnetic Waves and Applications*, vol. 26, pp. 264-273, 2012.

Umar Hasan Khan received his B.S. degree in Electrical Engineering from Centre for Advancement Studies in Engineering, Islamabad in the year 2009, and his M.S. degree is in Electrical Engineering from National University of Science and Technology in the year 2013. He joined the University of Engineering and Technology, Taxila the same year as a full-time Ph.D. Researcher, where he is working towards his doctoral degree focused on miniaturized RFID antennas for IoT.

Bilal Aslam received his B.S. degree in Electrical Engineering from the University of Engineering and Technology, Taxila in the year 2007, and his M.S. degree in Electrical Engineering from National University of Science and Technology in the 2013. The same year, he joined the University of Engineering and Technology, Taxila as a full-time Ph.D. Researcher, where he is pursuing his doctoral degree focused on RFID antennas for biomedical applications.

Humayun Shahid received his B.S. degree in Communication Systems Engineering from Institute of Space Technology, Islamabad in the year 2008, and his M.S. degree in Signal Processing from Nanyang Technological University, Singapore in the year 2011. His current research interests include antenna design, microwave engineering and RFID technology. He currently serves as an Assistant Professor and Director of Postgraduate Studies at the Telecommunication Engineering Department, University of Engineering and Technology, Taxila.

Muhammad Awais Azam received his Ph.D. degree in Pervasive and Ubiquitous Computing from London, UK in 2012. He is working as an Assistant Professor at the Department of Computer Engineering, UET Taxila, Pakistan. He leads a research team of M.S. and Ph.D.

students in the area of Pervasive and Ubiquitous Computing. His research interest includes network architecture, communication protocols, network security, embedded systems, ambient intelligence, wireless communications, opportunistic networks and recommender systems.

Yasar Amin is Chairman and Associate Professor of Telecommunication Engineering Department, University of Engineering and Technology Taxila, Pakistan. He is founder of ACTSENA Research Group at UET Taxila, Pakistan. He has done his B.Sc. in Electrical Engineering in 2001 with specialization in Telecommunication and M.Sc. in Electrical Engineering in 2003 with specialization in System-on Chip Design from Royal Institute of Technology (KTH), Sweden. His Ph.D. is in Electronic and Computer Systems from Royal Institute of Technology (KTH), Sweden, with research focus on printable green RFID antennas for embedded sensors, while has MBA in Innovation and Growth from Turku School of Economics, University of Turku, Finland. He has done several specialized courses from Stanford University, California, USA and Massachusetts Institute of Technology (MIT), USA. He has supervised over 15 M.Sc. thesis, and presently supervising 8 doctoral thesis. He is presently serving as leading Guest Editor at two International Journals and an active Reviewer of more than a dozen well reputed International journals. He has contributed to over 20 journal papers, over 30 reviewed international conference papers. Yasar is a Member of IEEE, IET, ACM and ACES.

Hannu Tenhunen is Chair Professor of Electronic Systems at Royal Institute of Technology (KTH), Stockholm, Sweden. Tenhunen has held Professor positions as Full Professor, Invited Professor or Visiting Honorary Professor in Finland (TUT, UTU), Sweden (KTH), USA (Cornel U), France (INPG), China (Fudan and Beijing Jiatong Universities), and Hong Kong (Chinese University of Hong Kong), and has an Honorary Doctorate from Tallinn Technical University. He has been Director of multiple national large scale research programs or being an Initiator and Director of national or European graduate schools. He has actively contributed on VLSI and SoC design in Finland and Sweden via creating new educational programs and research directions, most lately at European level as being the EU-level Education Director of the new European flagship initiative European Institute of Technology and Innovations (EIT), and its Knowledge and Innovation Community EIT ICT Labs.

Tenhunen has been active in promoting the innovation system and innovation support mechanism in research and education both at national and European level. Tenhunen has been a board member in science parks, start-up companies, and has served as Advisor or Expert for high technology companies and venture capitalists, as well as Evaluator for EU and national programs and research institutes. He has supervised over 70 M.Sc. thesis, 39 doctoral thesis, and 8 post-doc. From his doctoral students and post-docs, as of today, 21 are currently professors and associate professors. Tenhunen has served in Technical Program Committees of all major conferences in his area, have been General Chairman or Vice-Chairman or Member of Steering Committee of multiple conferences in his core competence areas. He has been one of the founding editorial board member of 3 scientific journal, have been Guest Editor for multiple special issues of scientific journals or books, and have contributed numerous invited papers to journals. He has contributed to over 110 journal papers, over 625 reviewed international conference papers, over 170 non-reviewed papers, local conference papers, or other publications, and 9 international patents granted in multiple countries. Tenhunen is Member of Academy of Engineering Science of Finland.

Area Spectral Efficiency of a Macro-Femto Heterogeneous Network for Cell-Edge Users under Shadowing and Fading Effects

Mfonobong C. Uko [1], Ubong S. Ukommi [2], Sunday C. Ekpo [3], and Rupak Kharel [3]

[1] Department of Electrical/Electronic Engineering
University of Manchester, Manchester, M60 1QD, UK
mfonuko12@gmail.com

[2] Department of Electrical & Electronic Engineering
Akwa-Ibom State University, Uyo, Akwa-Ibom State, Nigeria
uukommi@yahoo.com

[3] Department of Electrical & Electronic Engineering
Manchester Metropolitan University, Manchester, M1 5GD, UK
scekpo@theiet.org, R.Kharel@mmu.ac.uk

Abstract **–** The traditional macro-only network is not effective, especially when communication signal is required for users far away from the macrocell base station and located in the cell edge. The signal strength reaching these users is excessively attenuated due to fading and shadowing. The deployment of femtocells around the cell edge of this macrocell helps to reduce the effect of fading and shadowing thereby increasing the overall efficiency of the cellular network. This holds a great promise for adaptive space-based wireless sensor networks, formation-flying satellites and constellations.

Index Terms **–** Femtocells, heterogeneous networks, macrocells, spectral efficiency, uplink.

I. INTRODUCTION

Spectral efficiency is an important measure of the performance of a communication system that deals with the effective transmission of data. This efficiency must be optimized to match the available radio spectrum for mobile users to achieve a seamless communication. As the number of mobile users increases, the pressure on the available communication spectrum increases, leaving users in the cell-edge with extremely poor reception of the signal from the base station. The increase in mobile users is fast becoming higher than the spectral efficiency enhancements available to meet the required increase in the teledensity traffic.

To meet these challenging necessities in terms of coverage, capacity and deployment costs, heterogeneous network transmission techniques [1-3] are regarded to be one of the most promising solutions. A crucial part of these techniques will be how to significantly improve the capacity of users in the cell edge, coverage in rural areas due to the long distance between the traditional base stations and the mobile users in these areas as well as underground locations due to wall attenuation. One of the current heterogeneous network approaches is the deployment of low-power and low-cost femtocells within and around the main macro cellular infrastructure. This is referred to as two-tier heterogeneous network [4-6].

This paper considers the effect of shadowing and fading on the area spectral efficiency (ASE) of this two-tier heterogeneous network in uplink called the Macro-Femto Heterogeneous Network (MFHN).

From Fig. 1, the first tier of the case study heterogeneous network comprises of the macro-only network in which the carrier frequency is re-used at a minimum distance D[m]. This first tier comprises of a circular macrocell of radius R_m [m] with a base station made up of an omnidirectional antenna. The user is considered to be randomly located within the macro-cell bounded by R_0 and R_m, where R_0 is the minimum distance a user can be with reference to the macrocell base station.

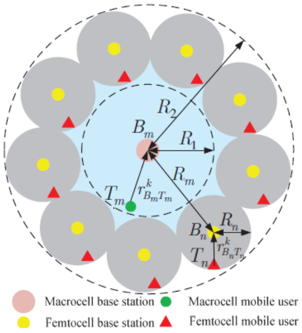

Fig. 1. Femtocells distribution at the cell edge in the Macro-Femto network [7].

Submitted On: January 3, 2014
Accepted On: July 4, 2016

II. SYSTEM MODEL AND ANALYSIS

The second tier heterogeneous network is made up of N circular femtocells each of radius R_n [m] with low-powered low-cost user deployed femto base station at the center. The femtocells are deployed round the edge of the reference macrocell. This is also referred to as the femto-on-edge (FOE) configuration in [7]. For the simulation, the number of femtocells per macrocell, N, is given as:

$$N = \mu \frac{A_m}{A_n}, \tag{1}$$

where A_m is the area of the macrocell, A_n, the area of each of the femtocells and μ the femto population factor (FPF) [7] which controls the number of femtocells per macrocell. Simplifying this further, we obtain the following relationship:

$$N = \mu \frac{4 \times c}{R_n}. \tag{2}$$

A. Bandwidth allocation

In this paper, the co-channel allocation of the bandwidth is utilized where the users all share the same frequency channel without any partitioning. Hence the bandwidth for the macrocell and femtocell users are thus:

$$W_m = W_f = W, \tag{3}$$

where, W_m is the bandwidth for the macrocell users, W_f is the bandwidth for the femtocell users and W is the total available bandwidth. The macrocell and the femtocells share all the communication resources available. For simplicity, the channel is assumed to be serving only one user at a time for the both tier. The bandwidth is re-used throughout the macrocell network at a distance $D = R_u(R_m + R_n)$, where R_u is the network traffic load which has a value of 2 for a fully loaded cellular network [7].

B. Mobile user distribution

The mobile users in the macrocell, femtocell and interfering cells are assumed to be independent and uniformly distributed in their cells. The joint probability density function (PDF) of the macrocell users at any location (r, θ) from its serving macrocell base station is given by [7]:

$$p(r, \theta) = \frac{r - R_0}{\pi (R_1 - R_0)^2}, \tag{4}$$

where $R_0 \leq r \leq R_1$, $0 \leq \theta \leq 2\pi$ and $R_1 = R_m - R_n$.

For the femtocell users at any location $(\tilde{r}, \theta)$ from its serving femtocell base station, the PDF is given as:

$$p(\tilde{r}, \theta) = \frac{\tilde{r}}{\pi {R_n}^2}, \tag{5}$$

where $0 \leq \tilde{r} \leq R_n$ and $0 \leq \theta \leq 2\pi$.

C. Shadowing

The shadowing is modelled as a lognormal distribution with the probability density function (PDF) of the slowly varying received signal power given as [7]:

$$ps(P) = \frac{\varepsilon}{\sqrt{2\pi}\sigma P} exp(-\frac{(\varepsilon \, ln(P) - \mu)^2)}{2\sigma^2}), \tag{6}$$

where ε=10/ln 10, $\mu = \varepsilon \ln(\bar{P})$ is the logarithmic mean power in dB, σ is the shadow standard deviation in dB.

D. Fading

This is modelled using the slow varying flat fading channel. It is assumed that the fading environment is characterized by a Nakagami-m distribution with the probability density function (PDF) of the received signal power given as [7]:

$$ps(P) = (\frac{m}{\Omega})^m \frac{P^{m-1}}{r(m)} \exp\left(-m \frac{P}{\Omega}\right), \tag{7}$$

where m is the Nakagami fading parameter, Ω is the mean received power related to path-loss and shadowing, $r(.)$ is the gamma function.

E. Area spectral efficiency

The area spectral efficiency is defined as the sum of the maximum available rates per bandwidth per unit macro-cell area. For the two tier network being considered, mathematically the ASE can be expressed as:

$$ASE = \frac{4(W_m C_m + N W_f C_f)}{\pi W {R_u}^2 (R_m + R_n)^2}, \tag{8}$$

W_m is the bandwidth of the macrocell, W_f is the bandwidth of the femtocell, C_m is the spectral efficiency (Capacity) of the macrocell, C_f is the capacity of the femtocell and N is the number of femtocell deployed.

From the earlier assumption in Equation (1), this equation reduces to:

$$ASE = \frac{4(C_m + N C_f)}{\pi {R_u}^2 (R_m + R_n)^2}. \tag{9}$$

III. SIMULATION PARAMETERS

A Monte-Carlo simulation procedure is established for the given system parameters in Table 1.

Table 1: Simulation parameters values

Simulation Parameters	Femtocell	Macrocell
System bandwidth	20 MHz	
Cell radius	30 m	100-600 m
Path-loss exponent	2	2
Additional path-loss exponent	2	2
BS antenna height	5 m	25 m
Mobile user antenna height	1.5 m	1.5 m
Femto population factor, μ	1	
Reference distance	100	
Path-loss constant, K	1	
Maximum transmit power	10 Watt	
Reference distance, Ro	-	100 m

A. Area spectral efficiency with shadowing

In this section, the effect of shadowing is investigated. Shadowing occurs due to objects obstructing the relative propagation path between the transmitter and receiver. For a long distance propagation, the received signal is modelled as a log-normal distribution with values in dB. A case of light shadowing (σ_d = 4 dB) and heavy shadowing (σ_d = 6 dB) are considered [8].

Figure 2 shows the effect on the area spectral efficiency for a shadowing parameter of 4 dB. From Fig. 2, a lognormal shadowing parameter of 4 dB reduces the ASE for the macro only. For the macro-femto network, shadowing effect is negligible. In Fig. 3, the increase in the shadowing parameter to 6 dB further reduces the area spectral efficiency of the macro-only network. The area spectral efficiency of the macro-femto network is minimally affected.

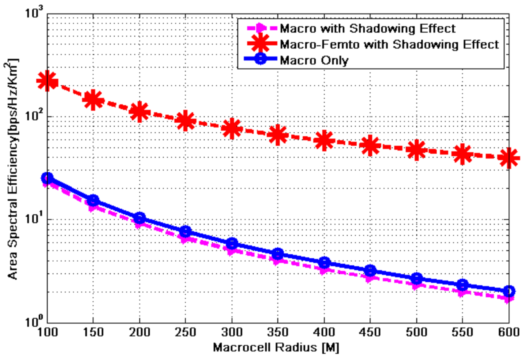

Fig. 2. Effect of shadowing on the area spectral efficiency for $\boldsymbol{\sigma_d}$ = 4 dB.

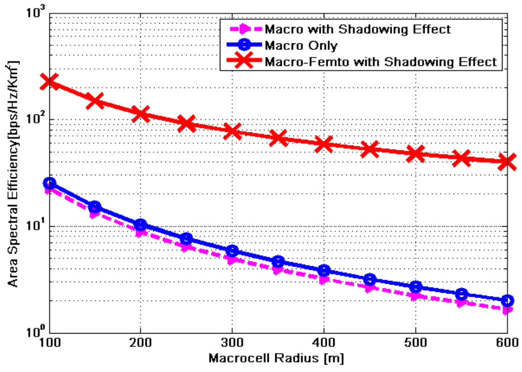

Fig. 3. Effect of shadowing on the area spectral efficiency for $\boldsymbol{\sigma_d}$ = 6 dB.

Comparing Figs. 2 and 3, the lower effect of shadowing on the macro-femto network can be attributed to the deployment of the low powered femtocells at the cell edge which provides the platform of signal reception for the cell-edge user rather than receiving communication signal directly from the traditional macro base station which is subject to more shadowing effect.

Furthermore, the deployment of the femtocells provides the medium for cell-edge users' connection to the network reducing the traffic on the traditional microcell network. This leads to less shadowing experienced over the macro-only distance; hence, improving the quality of the over-all macro-femto network.

The reported area spectral analysis of terrestrial macro-femto heterogeneous network can be extended to design and deploy small satellite missions operating as constellations, clusters and formation flying nodes in space. The categories for this application would span highly adaptive attosatellites, femtosatellites, picosatellites, nanosatellites and microsatellites in low Earth orbit [8, 9]. The feasible modes of operation are explained in [9], while [10] examines the operational times analysis of the payload subsystem for cost-effective mission, optimal operational margins and efficient power budgeting. This is an emerging trend for space-based macro-femto heterogeneous sensor networks.

B. Area spectral efficiency with fading

Fading is the distortion to communication signal as it is being propagated through certain propagation medium. This distortion may be as a result of multiple reflection of transmitted signal from various surfaces leading to a multipath propagation of the transmitted signal. This effect is considered for mobile users situated in the cell edge where they are prone to excessive fading on the communication signal from the traditional macrocell base station.

From Figs. 4 and 5, as the interfering mobile user increases from m_I=1 to m_I=3, the degradation on a Macro-only network reduces the spectral efficiency when compared with the macro-femto heterogeneous network. There is a negligible effect of the fading on the macro-femto heterogeneous network. In a deep fade scenario, the macro-femto network performs better than the Macro-only network as the radius of the macrocell is increased.

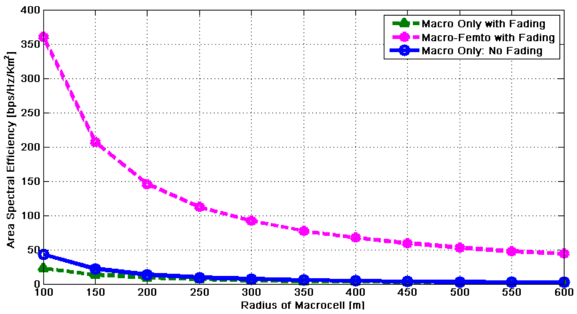

Fig. 4. Effect of fading on the area spectral efficiency for $\boldsymbol{m_I}$ = 1.

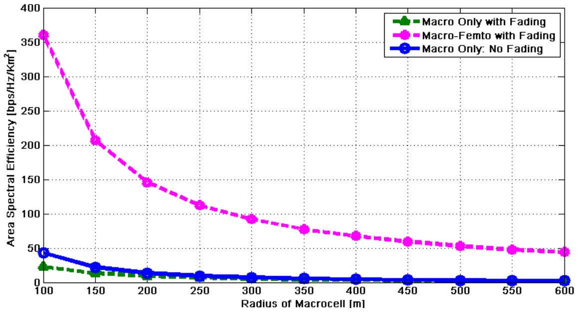

Fig. 5. Effect of fading on the area spectral efficiency for $\boldsymbol{m_I} = 3$.

IV. CONCLUSION

A Monte-Carlo simulation process has been carried out to investigate the effect of fading and shadowing on the area spectral efficiency of a Macro-Femto Heterogeneous Network. This effect is compared with a macro-only network. The simulation result shows that the fading and shadowing effect in the macro-femto network is minimal when compared with the macro-only network. The immediate future works bordering on this research span the terrestrial and space communications networks. Firstly, the investigation of the effect of fading and shadowing between femto and femto cells located in the macro cell-edge is a core research area. Secondly, the energy efficiency of the macro-femto scheme discussed in this paper can be investigated further. Heterogeneous network hybrids such as a three-tier heterogeneous network form a key study niche that next-generation networks will depend on for a reliable seamless global communication. Furthermore, the study can be extended to validate the area spectral efficiency of space-based sensor nodes and small satellite constellations links in Earth orbits.

REFERENCES

[1] R. Pabst, "Relay-based deployment concepts for wireless and mobile broadband radio," *IEEE Commun. Mag.*, vol. 42, pp. 80-89, Sept. 2004.

[2] D. Soldani and S. Dixit, "Wireless relays for broadband access," *IEEE Commun. Mag.*, vol. 46, pp. 58-66, Mar. 2008.

[3] A. Sendonaris, E. Erkip, and B. Aazhang, "User cooperation diversity. Part I and II," *IEEE Trans. Commun.*, vol. 51, pp. 1927-1948, Nov. 2003.

[4] P. Lin, J. Zhang, Y. Chen, and Q. Zhang, "Macro-femto heterogeneous network deployment and management: from business models to technical solutions," *IEEE Wireless Communs. Mag.*, vol. 18, no. 3, pp. 64-70, June 2011.

[5] S. Landstrom, A. Furuskar, K. Johansson, L. Falconetti, and F. Kronestedt, "Heterogeneous networks increasing cellular capacity," *Jour. Ericson Review*, vol. 89, pp. 4-9, Jan. 2011.

[6] Femto Forum, "An overview of the femtocell concept." [Online]. Available: www.femtoforum.org.

[7] M. Z. Shakir and M.-S. Alouini, "On the area spectral efficiency improvement of heterogeneous network by exploiting the integration of macro-femto cellular networks," *in Proc. IEEE Intl. Conf. Communs., (ICC'12)*, Ottawa, Canada, pp. 1-6, June 2012.

[8] Iti Saha Misra, *Wireless Communications and Networks: 3G and Beyond*. McGraw Hill Education, Second Edition, pp. 92-93, 2013.

[9] S. Ekpo and D. George, "Reconfigurable cooperative intelligent control design for space missions," *Recent Patents on Space Technology*, vol. 2, no. 1, pp. 2-11, Apr. 2012.

[10] S. C. Ekpo, B. Adebisi, D. George, R. Kharel, and M. Uko, "A system-level multicriteria modelling of payload operational times for communication satellite missions in LEO," *Recent Progress in Space Technology*, vol. 4, no. 1, pp. 67-77, June 2014.

Mfonobong C. Uko is a graduate of M.Sc. Communication Engineering from the University of Manchester, United Kingdom. He has a B.Sc. in Electrical/Electronic Engineering from the University of Uyo, Uyo, Nigeria. His research interests include Wireless Communication Systems, Cognitive Radios, and Small Satellite research. He is a currently a Lecturer in the Department of Electrical/Electronic Engineering, University of Uyo.

Ubong S. Ukommi, obtained his M.Sc. in Mobile and Satellite Communications, and Ph.D. in Communication Engineering from Univ. of Surrey, UK respectively. He has made contributions to the advancement of engineering and technology through presentations and publications of research findings in reputable journals and conferences in London, UK, California, USA, and Abuja, Nigeria. He is an active member of international and national professional organisations including Institution of Electrical and Electronics Engineers, New York, USA, Institution of Engineering and Technology, UK, Nigerian Society of Engineers, Nigeria. Having completed his Masters, he worked for Viewsat Limited, as a team member consulting, developing, supporting and reviewing engineering designs, project implementation and upgrading of infrastructure and facilities for improved quality of experience. Ukommi also led the design of "Ground Station" project at the University of Surrey, UK, a project jointly funded by the University of Surrey and Surrey Satellite Technology Limited, UK. Ukommi has interest in contributing to the global development and poverty eradication by translating acquired engineering knowledge, skills and experiences into problem solving activities and industrialisation for sustainable development.

Sunday C. Ekpo (M'07) obtained his Bachelor of Engineering (B.Eng. (Hons.)) in Electrical & Electronic Engineering at the Federal University of Uyo, Nigeria in 2001. In Sept. 2008, he graduated with a M.Sc. in Communication Engineering at The University of Manchester, United Kingdom and proceeded for a Ph.D. in Electrical & Electronic Engineering at the same institution.

He joined the Manchester Metropolitan University, UK in 2012 and is a Lecturer in the Department of Electrical & Electronic Engineering, United Kingdom. He has successfully developed the regulated-element Frost beamformer for array signal processing and applied the technique to an industry-sponsored real-time sensor project; it won the Best University Research & Knowledge Exchange; and the Best Faculty of Science & Engineering Knowledge Transfer Partnership Awards in 2014. He has published over 40 internationally peer-reviewed and refereed technical papers in the fields of communication and space systems engineering. His research interests include multiphysics modelling and characterisation of RF/microwave/millimeter wave transceivers; multipurpose space missions modelling; spacecraft payload design; adaptive space-based sensor networks modelling; integrated RF/microwave-fibre/ free space optics satellite signal reception and distribution systems characterisation; antennas and propagation engineering; and multicriteria optimisation of engineering systems. He is a regular peer-reviewer of technical publications for peer-reviewed journals and refereed conferences in his area of expertise and allied fields.

Ekpo is a Member of the IET, AIAA, Applied Computational Electromagnetics Society and a Fellow of the Higher Education Academy, UK. He has served as a Member of several International Technical Programme Committees of refereed conferences (including the Annual International IEEE Systems Conference – effective 2013). He is also a regular chair and organizer of technical sessions at conferences including CSNDSP 2014, ACES 2014 and 2015; and an Invited Speaker at the IEICE ICTF 2015, Manchester, UK (where he spoke on "Space-enabled Future Smart Cities").

Rupak Kharel obtained his B.Eng. degree in Computer Engineering from Institute of Engineering, Pulchowk Campus, Tribhuvan University, Nepal in 2004. He received his M.Sc. degree in Optoelectronic and Communication Systems from Northumbria University in 2007. He received his Ph.D. in Secure Communication Using Chaotic Systems in 2011 from Northumbria University Recently, he has also finished his teaching qualification, Postgraduate Certificate in Academic Practice (PGCAP) from Manchester Metropolitan University.

He was awarded P. O. Byrne prize for outstanding achievement in his M.Sc. and the best Ph.D. student in 2009 and 2010. He has worked on several commercial projects and have provided consultancy in software design and architecture. His current research interests are in the field of security and cryptography, smart m-health applications, IoT, wireless sensor networks and cyber security challenges in distributed systems mainly cloud computing and smart grids.

He is currently working as a Senior Lecturer in the School of Engineering, Manchester Metropolitan University. He joined the school in July 2011. He has over 10 years of experience in the field of academics, R&D and software design. Kharel has served as a local organizing committee member for CSNDSP2014, CSNDSP2010, NOC/OC&I2011, EFEA2012 as well as Reviewer for several leading publications and international conferences.

A Simple UWB Tapered Monopole Antenna with Dual Wideband-Notched Performance by Using Single SRR-Slot and Single SRR-Shaped Conductor-Backed Plane

A. Naghar [1,3], F. Falcone [2], A. Alejos [1], O. Aghzout [3,4], and D. Alvarez [1]

[1] Department of Teoría de la Señal y Comunicación
University of Vigo, Pontevedra, Vigo, 36310, Spain
azzeddin.naghar@uvigo.es, analejos@uvigo.es

[2] Department of Electrical and Electronic Engineering
Public University of Navarre, Pamplona, 31500, Spain
francisco.falcone@unavarra.es

[3] Department of Physics, Faculty of Science
[4] Department of TITM, National School of Applied Science
Abdelmalek Essaadi University, Tetouan, 93000, Morocco
o.aghzout@gmail.com, azz.naghar@gmail.com

Abstract **─** This paper presents the design of a compact UWB antenna with dual band-notch characteristics in the 5 GHz band and X-band satellite communications. The proposed antenna consists of a tapered antenna fed by a microstip feed-line presenting a modified ground plane to achieve a wide impedance bandwidth, in the interval 2.8-12 GHz, with VSWR<2. The electromagnetic coupling of the tapered patch with the rectangular split ring resonator shaped parasitic conductor placed in the ground plane yields the first frequency notch which ranges from 5.05 to 5.95 GHz, in order to eliminate the dedicated short-range communications and wireless local area network interferences. The rejection of the X-band from 7.25 to 8.4 GHz, is achieved by etching a single rectangular split ring resonator slot in the radiator patch. Prototypes of the proposed antenna design were measured and compared to simulations, and good agreement was obtained.

Index Terms **─** Antenna, filter, complementary split ring resonator, notch, rectangular single split-ring resonators, ultrawideband, X-band.

I. INTRODUCTION

In the last decades the ultrawideband (UWB) technology has attracted a great interest both in the industry and academia research field especially since the Federal Communication Commission (FCC) allocated the spectrum portion from 3.1 to 10.6 GHz to be used for commercial purpose of the UWB technology [1]. An enormous attention has taken place for designing UWB microstrip antenna due to its attractive characteristics of low profile, miniaturization, capability to be integrated with the design of other devices, and low cost. Mitigating interference between UWB antennas and co-existing narrow band systems have prompted the design of UWB antennas doted of frequency notch filtering characteristics. Different configurations can be found in the scientific literature proposing the use of planar monopole printed antennas with modified radiator and/or ground plane in order to achieve a frequency notch characteristic [2-14]. Single, dual or triple notched frequencies can be obtained by using parasitic elements [2], [3], inserting rod-shaped parasitic structures [4], utilizing a small resonant patch [5], embedding a slot in the feed line, or cutting different shapes of slots in both the radiation patch and the ground plane [6-8]. Other designs include split ring resonators (SRR), and its complementary structure (CSRR), as shaped-slot and/or shaped-conductor, to produce a desired frequency notch filtering property [9-16].

This paper describes a novel and simple design of a UWB tapered monopole antenna doted of a dual wideband frequency notch feature. The first notch is generated at 5.5 GHz by introducing a single SRR-shaped parasitic conductor in the ground plane to reject the interference due to the dedicated short-range communications (DSRC) and wireless local area network (WLAN) systems that operate within the range from 5.15 to 5.925 GHz. A single rectangular SSR-slot is etched in the tapered radiator to eliminate the wideband interference (7.25-8.4 GHz) corresponding to the uplink and downlink

Submitted On: March 12, 2015
Accepted On: July 7, 2016

signals of the X-band satellite communication systems.

The modified ground plane is responsible of achieving the desired wider impedance bandwidth matching over the entire UWB frequency range. This technique implemented in our design can be employed on any UWB monopole antenna design doted of a partial ground plane to obtain any frequency notch requisite with a necessary stopband impedance bandwidth.

In the following sections we describe the experimental validation with discussion of measurement results in order to demonstrate the performance of the proposed antenna design.

II. ANTENNA CONFIGURATION

The geometrical configuration of the proposed UWB tapered monopole antenna is shown in Fig. 1. It consists of a tapered radiation patch with modified ground plane to achieve the impedance bandwidth matching requisite over the UWB range. The tapered patch was connected to the microstrip line providing a characteristic impedance of 50 Ω. The antenna was printed on the Rogers ULTRALAM 2000 high performances substrate with dielectric permittivity of 2.5, thickness of 0.762 mm and loss tangent of 0.0019.

In order to obtain the frequency notch filtering function and eliminate the undesired frequencies so avoiding possible interference within the UWB band (3.1 GHz to 10.6 GHz), this design introduces two additional simple structures in the basic antenna geometry. By loading the SRR-shaped conductor in the ground plane, we achieve the lower notched-band at 5-6 GHz. The suppression of the radiation at this notch frequency is due to the effect of the electromagnetic coupling between the tapered radiator and the single SRR embedded on the radiator backside. The higher notched-band 7.25-8.4 GHz is obtained by embedding a single rectangular SRR-slot in the tapered patch. Moreover the stop-band property can be controlled by adjusting the width and the length of the SRR element for both cases [18,19]. Simulation results have been obtained with the CST MW Studio^{TM}.

Figure 2 illustrates the three stages of the antenna design. Initially, a reference UWB tapered monopole antenna is designed without notch band characteristics (antenna#1). Later this configuration is modified to introduce the rejection of a single band by loading a SRR-shaped parasitic conductor in the ground plane (antenna#2). Finally, the dual-band notched UWB antenna is achieved loading the SRR-shaped parasitic conductor in the ground plane and etching the SRR-slot in the tapered patch, and it is presented as antenna#3.

The SRR and CSRR elements embedded within the antenna are designed by considering the corresponding resonant frequency derived from their respective quasi-static resonance [17]. The specific geometrical details of each element are provided in the following section.

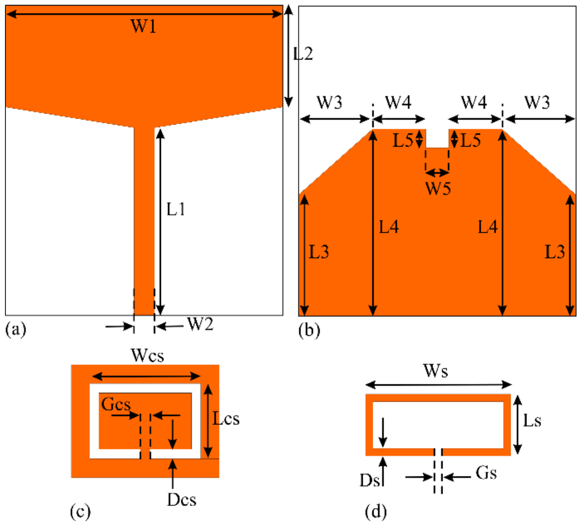

Fig. 1. Schematic of the proposed antenna design: (a) radiator tapered element, (b) modified ground plane, (c) rectangular CSRR-shaped slot, and (d) rectangular SRR-shaped parasitic conductor.

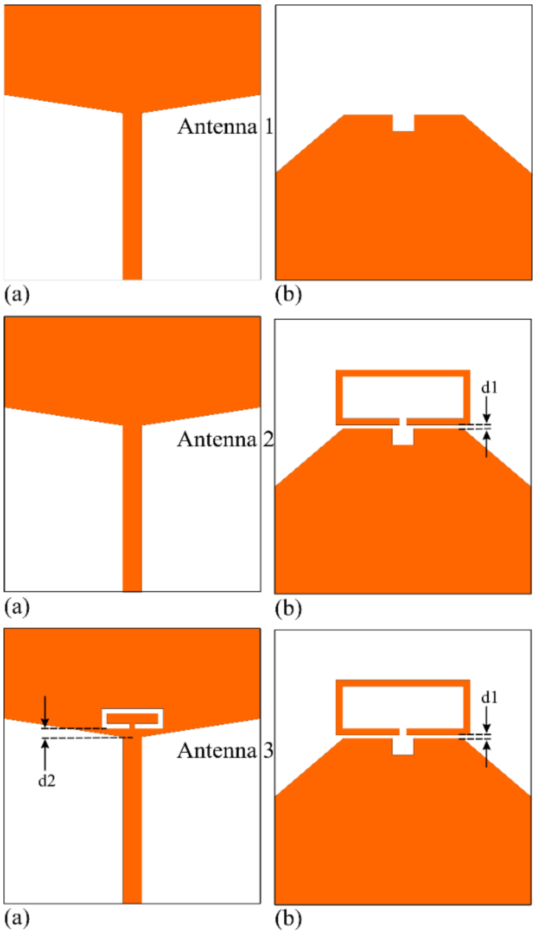

Fig. 2. Configuration of the antennas used for our study: top and bottom layers.

III. MEASUREMENT RESULTS

Following we compare the performance of the three stages of the antenna design: the reference design case (antenna#1), single notched band case (antenna#2), and the dual-band notched case (antenna#3).

A. UWB tapered monopole antenna

Figure 3 shows the VSWR performance of the basic UWB tapered monopole antenna without any embedded notch filtering element. As can be seen in the plot, the UWB antenna operates from 2.8 to 12 GHz with a voltage standing wave ratio (VSWR) lower than 2. Good agreement between the measured and simulated plots is inferred from the comparison. The parameters of the UWB reference antenna without notch function are as follows, in mm: L_1=20, L_2=10.8, L_3=13, L_4=20, L_5=2, W_1=30, W_2=2.2, W_3=8, W_4=6 and W_5=2.5.

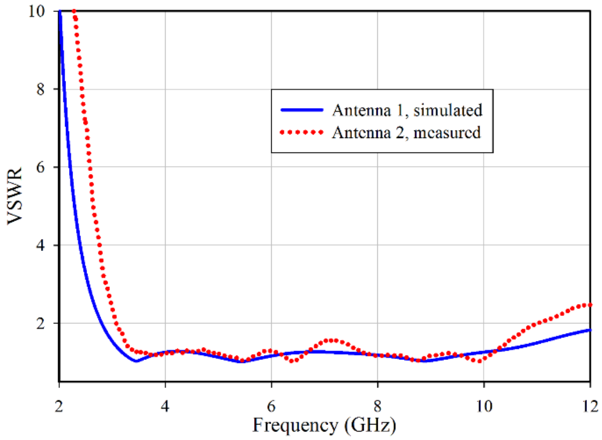

Fig. 3. Simulated and measured VSWR for antenna#1.

B. UWB tapered monopole antenna with single band-notch

In order to reject the WLAN/DSRC frequencies (5.05-5.95 GHz), we loaded a single SRR-shaped parasitic on the backside of the tapered patch, so obtaining the namely antenna#2 case. This notch filtering property is due to the electromagnetic coupling occurring between the radiating patch element and the resonant SRR-shaped parasitic element. The selection of critical parameters of the SRR structure is related to important effects arising on the antenna performance.

Figure 4 shows the VSWR of antenna#2 obtained for different values of the total length of the SRR-shaped parasitic, given by $L_t = L_s + W_s$. It can be observed that when the total length of the SRR structure increases, the center of the notch frequency decreases without affecting the stop-band impedance bandwidth. Then, the notch frequency is controllable by varying the total length L_t of the embedded SRR-shaped parasitic.

Furthermore, the band rejection is influenced by the width of the SRR-shaped parasitic, D_s. This effect was investigated and shown in Fig. 5. We observe that the notched frequency depends of the SRR-shaped parasitic width D_s, in a similar way to that one due to the influence of the total length L_t, as previously described.

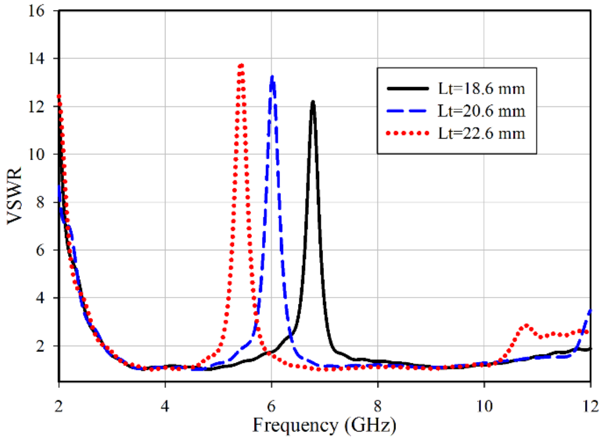

Fig. 4. Simulated VSWR for antenna#2 with different values of L_t.

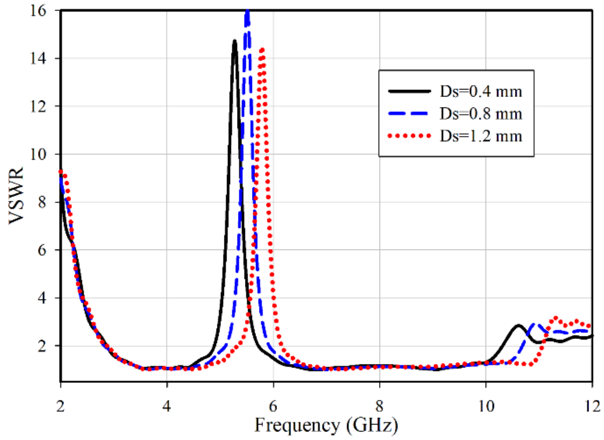

Fig. 5. Simulated VSWR of antenna#2 for different values of D_s with L_t = 22.3 mm.

The capacitive coupling between the introduced SRR-shaped parasitic and the modified ground plane also affects the stop-band performance, as illustrated in Fig. 6. We can deduce that the impedance bandwidth of the stop-band increases as the distance d_1 between the ground plane and the SRR-shaped parasitic element decreases. Rejection levels are enhanced when distance d_1 decreases, corresponding to an intensification in the effective capacitive value provided by the gap between the antenna and the SRR loading element [17]. Thus, the variation of the distance d1 introduces an easy way for controlling both the stop-band impedance bandwidth and the corresponding maximum value of VSWR.

The values of the design parameters selected for the SRR-shaped parasitic conductor backed-plane are as follows, in mm: W_s=15.7, L_s=6.6, G_s=0.8, D_s=0.8 and d_1=0.3.

Figure 7 shows comparison between the simulated and measured VSWR characteristics of the single-band-notched UWB antenna (antenna#2) and the reference antenna (antenna#1). This plot clarifies that the achieved notched frequency bandwidth is achieved from 5.05 to 5.95 GHz with a maximum VSWR higher than 10. Obviously, the achieved notched bandwidth can suppress the DSRC and WLAN bands for UWB communications.

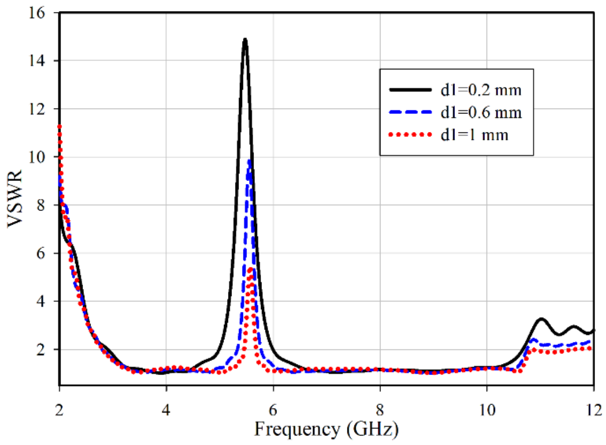

Fig. 6. Simulated VSWR for antenna 2 with different values of d_1 (L_t = 22.3 mm, D_s = 0.8 mm).

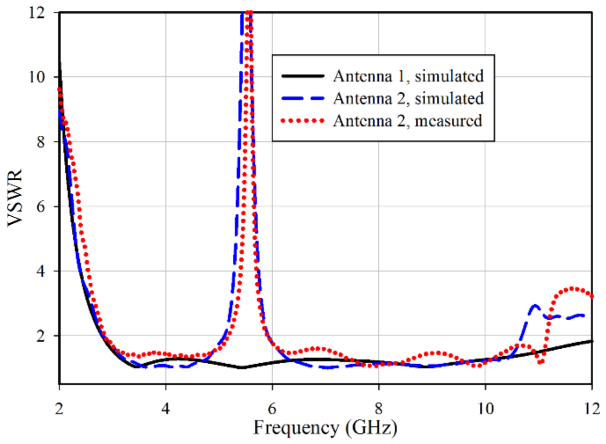

Fig. 7. Simulated and measured VSWR of the proposed UWB antenna with single frequency notch.

C. Dual band-notched UWB tapered monopole antenna

The next step was to achieve a dual band notched feature to reject the uplink and downlink signals of the X-band satellite communications. Then, a SRR-slot was etched in the tapered patch, as shown in Fig. 2, so obtaining the namely antenna#3 case.

The proposed dual band-notched UWB antenna with was fabricated and tested. The measured and simulated VSWR of the antenna#3 are illustrated in Fig. 8. It can be seen that for this case the impedance bandwidth is 8.2 GHz, covering the band 2.8-11 GHz along to achieving the required dual band-notched performance. The simulated notched frequency bandwidth of the proposed antenna is achieved from 4.95 GHz to 6.05 GHz and from 7.25 GHz to 8.45 GHz, while the measured stop-band frequency ranges are from 4.95 GHz to 5.95 GHz and from 7.5 GHz to 8.9 GHz for VSWR>2 with maximum VSWR of more than 10 and 4 respectively. The suppression of the WLAN/DSRC and X-band narrow band systems was completely obtained. The frequency shifting observed in the second frequency notch of measurement results is due to the fabrication tolerance limit when etching the SRR-slot.

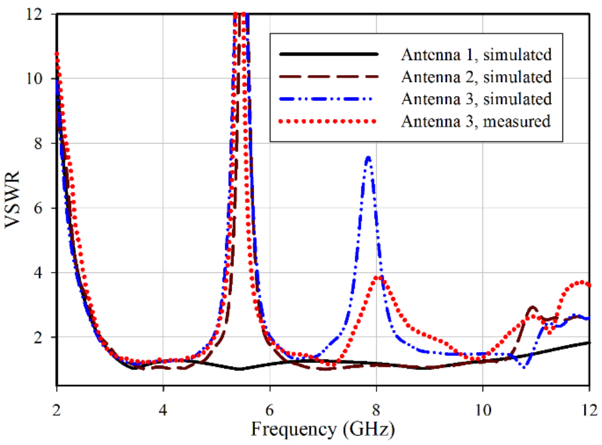

Fig. 8. Simulated and measured VSWR of the proposed dual bad-notched UWB antenna.

The design parameters of the etched SRR-slot are as follows, in mm: W_s=7.2, L_{cs}=2.4, G_{cs}=0.6, D_{cs}=0.6 and d_2=1.

For the case of antenna#3, we analyzed the surface current distribution. In Fig. 9, we depicted at two frequencies of operation, (5.5 and 7.85 GHz, corresponding to the center frequencies of the notched bands. It is visible that the quasi-static resonance frequencies of the SRR/CSRR elements are located precisely at 5.5 GHz and 7.85 GHz. For those frequencies the tapered monopole is then not excited and so resulting in the radiation suppression.

The radiation pattern of the proposed antenna#3 is presented in Fig. 10. The figure shows good directive pattern in the E-plane and omnidirectional pattern for the H-plane. General good agreement is observed between measured and simulated results.

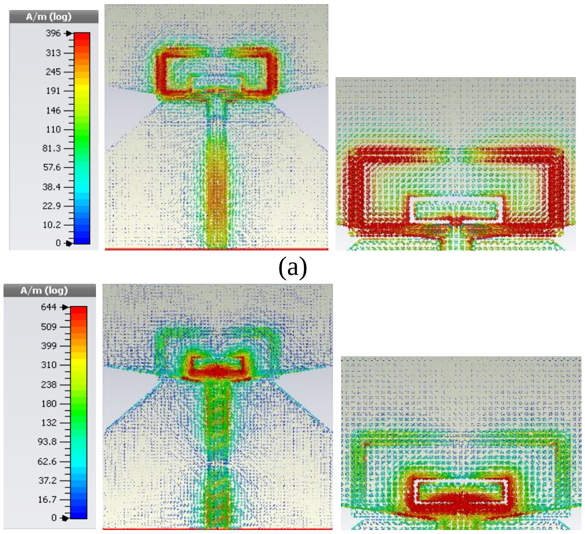

(a)

(b)

Fig. 9. Simulated surface current distribution of the dual band-notched case (antenna#3): (a) at 5.5 GHz and (b) at 7.85 GHz.

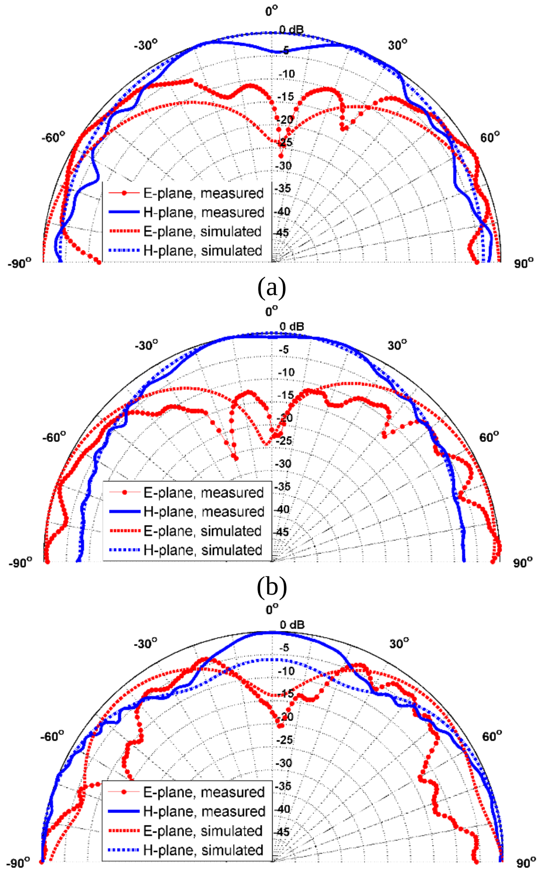

(a)

(b)

(c)

Fig. 10. Simulated and measured radiation patterns of the proposed antenna#3 case for E- and H-planes: (a) 4.5 GHz, (b) 6.5 GHz, and (c) 9.5 GHz.

In Fig. 11 we illustrate the variation of the peak gain with the frequency for the single and dual frequency notched antennas#2 and #3 over the frequency range (2-12 GHz) along to the reference case (antenna#1). Sharp dips in the value of the far-field peak gain are observed in the two desired notched bands, confirming the fact that loading the basic antenna with single SRR-shaped parasitic and SRR-slot provides excellent intrinsic notch filtering.

Furthermore, it can be checked that, in the radiating band, the gain variation is almost the same for the three antennas. Photographs of fabricated antenna prototypes are shown in Fig. 12.

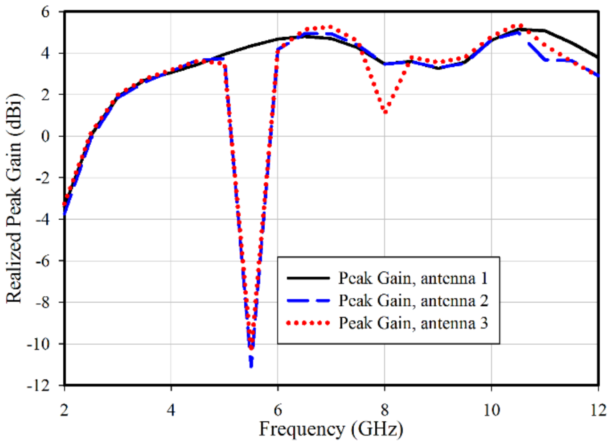

Fig. 11. Peak gain for the three cases of UWB tapered antennas.

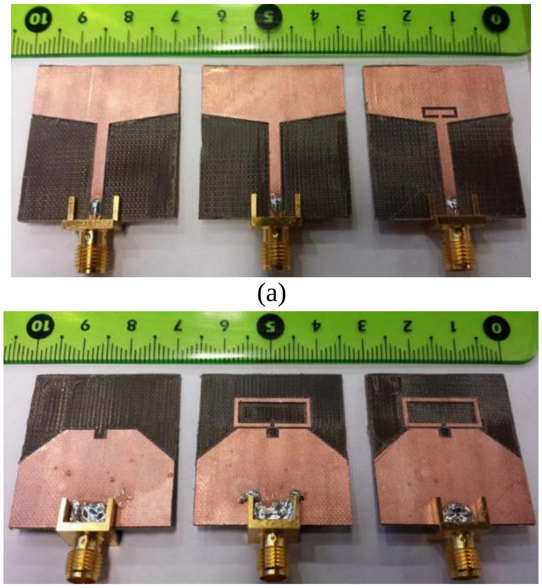

(a)

(b)

Fig. 12. Photograph of prototyped antennas: (a) top later and (b) bottom layer. Left: Antenna1. Center: Antenna 2. Right: Antenna 3.

VI. CONCLUSION

A simple and symmetric tapered monopole UWB antenna with a single SRR-shaped parasitic and single SRR-slot etched in the tapered patch, exhibiting dual-frequency notch performance is presented in this paper. The electromagnetic coupling between the tapered patch and the SRR-shaped parasitic introduced on the back side of the tapered element, yields the first notch at 5.5 GHz, with a large bandwidth, filtering the interferences due to the co-existence of DSRC/WLAN systems. Moreover, the uplink and downlink signals of the X-band satellite communication systems are rejected by embedding a single SRR-slot on the radiation patch. The notched frequencies can be easy controlled by modifying the dimensions of the SRR structures. Fabricated antennas demonstrate overall good match between simulated and measured results. In summary, a simple design procedure, valid to obtain a good omnidirectional radiation pattern, with relative stable gain and low profile, as well as manufacturable at low cost make the proposed antenna a suitable candidate for UWB systems needed of multiple frequencies notches.

ACKNOWLEDGMENT

The authors would like to thank the support given under projects EMR2012/138 and GRC1015/019 funded by Xunta de Galicia, and Erasmus Mundus Green IT (Grant 2012-2625/001-001-EMA2).

REFERENCES

[1] Federal Communications Commission, "Federal Communications Commission revision of Part 15 of the commission's rules regarding ultra-wideband transmission system from 3.1 to 10.6 GHz," Washington, DC, USA, 2002.

[2] M. Rostamzadeh, S. Mohamadi, J. Nourinia, C. Ghobadi, and M. Ojaroudi, "Square monopole antenna for UWB applications with novel rod-shaped parasitic structures and novel V-shaped slots in the ground plane," *IEEE Antennas and Wireless Propagation Letters*, vol. 11, pp. 446-449, 2012.

[3] N.-I. Jo, C.-Y. Kim, D.-O. Kim, and H.-A. Jang, "Compact ultrawideband antenna with quadruple-band rejection characteristics using SRR/CSRR structure," *Journal of Electromagnetic Waves and Applications*, vol. 26, no. 5-6, pp. 583-592, 2012.

[4] M. Rostamzadeh, S. Mohamadi, J. Nourinia, C. Ghobadi, and M. Ojaroudi, "Square monopole antenna for UWB applications with novel rod-shaped parasitic structures and novel V-shaped slots in the ground plane," *IEEE Antennas and Wireless Propagation Letters*, vol. 11, pp. 446-449, 2012.

[5] K. G. Thomas and M. A. Sreenivasan, "A simple ultrawideband planar rectangular printed antenna with band dispensation," *IEEE Transactions on Antennas and Propagation*, vol. 58, no. 1, pp. 27-34, 2010.

[6] R. Azim, M. T. Islam, J. S. Mandeep, and A. T. Mobashsher, "A planar circular ring ultra-wideband antenna with dual bandnotched characteristics," *Journal of Electromagnetic Waves and Applications*, vol. 26, no. 14-15, pp. 2022-2032, 2012.

[7] S. Mohammadi, J. Nourinia, C. Ghobadi, and M. Majidzadeh, "Compact CPW-fed rotated square-shaped patch slot antenna with band-notched function for UWB applications," *Electronics Letters*, vol. 47, no. 24, pp. 1307-1308, 2011.

[8] H.-W. Liu, C.-H. Ku, T.-S. Wang, and C.-F. Yang, "Compact monopole antenna with band-notched characteristic for UWB applications," *IEEE Antennas and Wireless Propagation Letters*, vol. 9, pp. 397-400, 2010.

[9] M. C. Tang, et al., "Compact UWB antenna with multiple band-notches for WiMAX and WLAN," *IEEE Trans. Antennas Propagation*, vol. 59, no. 4, pp. 1372-1376, Apr. 2001.

[10] J. Y. Siddiqui, C. Saha, and Y. M. M. Antar, "Compact dual-SRR-loaded UWB monopole antenna with dual frequency and wideband notch characteristics," *IEEE Antennas and Wireless Propagation Letters*, vol. 14, pp. 100-103, 2015.

[11] D. Sarkar, K. V. Srivastava, and K. Saurav, "A compact microstrip-fed triple band-notched ultra-wideband monopole antenna," *IEEE Antennas and Wireless Propagation Letters*, vol. 13, pp. 396-399, 2014.

[12] M. S. A. Rani, S. K. A. Rahim, M. R. Kamarudin, T. Peter, S. W. Cheung, and B. M. Saad, "Electromagnetic behaviors of thin film CPW-fed CSRR loaded on UWB transparent antenna," *IEEE Antennas and Wireless Propagation Letters*, vol. 13, pp. 1239-1242, 2014.

[13] M. M. Islam, M. R. I. Faruque, and M. T. Islam, "A compact 5.5 GHz band-rejected UWB antenna using complementary split ring resonators," *The Scientific World Journal*, vol. 2014.

[14] Q. Wang and Y. Zhang, "Design of a compact UWB antenna with triple band-notched characteristics," *International Journal of Antennas and Propagation*, vol. 2014.

[15] M. C. Tang, "Compact UWB antenna with multiple band-notches for WiMAX and WLAN," *IEEE Trans. Antennas Propagation*, vol. 59, no. 4, pp. 1372-1376, 2001.

[16] T. Yuan, C.-W. Qiu, L. W. Li, M. S. Leong, and Q. Zhang, "Elliptically shaped ultra-wideband patch antenna with band-notch features," *Microw. Opt. Tech. Lett.*, vol. 50, no. 3, pp. 736-738, 2008.

[17] J. Baena, J. Bonache, F. Martín, R. Marqués, F. Falcone, T. Lopetegi, M. Laso, J. Gil, M. Flores,

and M. Sorolla, "Equivalent circuit models for split ring resonators and complementary split ring resonators coupled to planar transmission lines," *IEEE Trans. Microwave Theory and Techniques*, vol. 53, no. 4, pp. 1451-1461, Apr. 2005.

[18] P. Wang, "Compact dual band-reject monopole antenna for UWB applications," *Applied Computational Electromagnetics Society ACES*, vol. 28, no. 8, pp. 725-730, 2013.

[19] J. Y. Siddiqui, C. Saha, and Y. M. M. Antar, "Compact SRR-loaded UWB circular monopole antenna with frequency notch characteristics," *IEEE Antennas and Wireless Propagation Letters*, vol. 62, no. 8, pp. 4015-4020, 2014.

Azzeddin Naghar was born in Tetouan, Morroco. He received the Engineer Degree in Telecommunication Engineering at the National School of Applied Sciences from Abdelmalek Essaadi University, Tetouan, Morocco 2011. He is currently working toward the Ph.D. degree in Electrical Engineering with the Department of Teoría de la Señal y Comunicación, University of Vigo, Pontevedra, Vigo, Spain. His research interests include UWB antenna design and RF filters.

Otman Aghzout was born in Tétouan, Morocco. He received the Electronics degree from Abdelmalek Essaadi University, Tétouan, Morocco, in 1995, M. and Ph.D. degrees in Telecommunications Engineering at the High School of Telecommunications Engineering (ETSITGC) of Canary University, Spain in 2000 and January 2002, respectively. He has also been a Researcher Student at the Microwave Group of the Dept. of Electronics and Electromagnetism, University of Seville (Seville, Spain) from 1996 till 1999. In January 2002, he joined the Medical Technology Center (CTM) of the University Hospital of GC, where he worked in Medical Engineering applications for two years. (2002-2004) has been a Teacher Assistant on Telecommunications Engineering and Postdoctoral Researcher at the Department of the Signal Processing Engineering, High School of TE (ETSITGC). Since 2009 he joined the Dept. Of Engineering Technologies: Telecommunications and Mecatronics (TITM) as an Associate Professor of Telecommunications Engineering, National School of applied Sciences, UAE, Tétouan, Morocco. Currently he is interested on printed microwave passive and active circuits, filters and antenna designs.

Ana Vazquez Alejos has been working with the Department of Signal Theory and Communications, University of Vigo, as Research and Teaching staff. She completed her Ph.D. thesis on the radio channel characterization for the millimeter wave frequencies. In 2009 she was granted with the Marie Curie International Outgoing Fellowship, carrying out the outgoing phase in the New Mexico State University (NM, USA), with a research focused on propagation through dispersive media, and radar waveform generation. In 2002, her M.S. thesis received the Ericcson Award by the Spanish Association of Electrical Engineers, as the best Multimedia Wireless Project. Her research work includes radio propagation, communication electronics, wideband radio channel modeling, multimedia wireless systems, waveform and noise code design, and radar.

Alejos is a Reviewer for several IEEE and IET journals, and works for the IEEE TMC Spain Chapter.

Francisco Falcone received the Telecomunication Engineering degree and Ph.D. degrees from the Universidad Publica de Navarra (UPNA), Pamplona, Spain, in 1999 and 2005, respectively.

From 1999 to 2000, he was a Microwave Commissioning Engineer with Siemens–Italtel. From 2000 to 2008, he was a Radio Network Engineer with Telefonica Moviles. In 2009, he cofounded the spinoff Tafco Metawireless. From 2003 to 2009, he was an Assistant Lecturer with UPNA, and since June 2009, has been an Associate Professor with the same university. From 2005 to 2008, he was Internal Instructor with Telefonica Moviles.

His research areas cover complex and artificial electromagnetic media, EBG, metamaterials, enhanced transmission and plasmonic guiding, as well mobile system design and analysis.

Falcone works for the IEEE MTT-11 Committee, IEEE ES Spain Chapter, and IEEE TMC Spain Chapter. He was recipient of the CST Best Paper Award in 2003 and 2005, a Ph.D. Award in 2006 from the Colegio Oficial de Ingenieros de Telecomunicacion, and a Ph.D. Award at UPNA, in 2010.

David Alvarez was born in Vigo, Spain. He received the Engineer degree in Telecommunication Systems and Master in Industrial Mathematics at the Higher Technical School of Telecommunications Engineering from University of Vigo, Vigo, Morocco 2014. He is currently Researcher with the Department of Teoría de la Señal y Comunicación, University of Vigo, Pontevedra, Vigo, Spain. His research interests include antenna and sensor designs.

Tunable Metasurfaces for Filtering the Electromagnetic Waves Under Different Excitations

Sultan Can[1], Emrullah Karakaya [2], Fulya Bagci[2], Asim E. Yilmaz[1], and Baris Akaoglu[2]

[1] Department of Electrical and Electronics Engineering
Ankara University, Ankara, 06830, Turkey
sultancan@ankara.edu.tr, aeyilmaz@eng.ankara.edu.tr

[2] Department of Engineering Physics
Ankara University, Ankara, 06100, Turkey
emrullah.fizik@gmail.com, fbagci@eng.ankara.edu.tr, akaoglu@eng.ankara.edu.tr

Abstract **─** In this study a tunable metasurface has been presented and evaluated for different excitation types. Tunability has been achieved by changing the substrate and geometrical properties. In order to obtain uniqueness, a parameter retrieval for the effective permittivity and permeability is performed using a version of the Nicholson-Ross-Weir (NRW) algorithm that is improved by implementing the Kramers-Kronig relationship. The results regarding the parametric and retrieval analysis are presented.

Index Terms **─** Double negative materials, electronic band gap, ε-negative materials, frequency selective surfaces, metamaterials, single negative materials.

I. INTRODUCTION

Electronic devices, which incredibly penetrate our daily life, make the electromagnetic pollution problem more critical and the researchers pay significant attention in order to cope with those problems. The protection of electromagnetic waves are necessary not only in terms of human health but also to prevent the devices to interact with each other. Several methods are used for shielding including designing frequency selective surfaces (FSS), left handed materials, double negative materials (DNG), single negative materials (SNG), plasmons, electronic band gap structures (EBG) and artificial magnetic conductors (AMC).

Metamaterials are artificial materials, which can satisfy having simultaneously negative values of permeability (μ) and permittivity (ε). The theory of the metamaterials goes back to 1968 in which Veselago claimed that such materials have extra-ordinary properties unlike the ordinary right-handed materials [1]. Metamaterials are referred to as left-handed materials and can have double or single negative values of permittivity and permeability. Those materials can achieve reverse Doppler Effect, reverse Vavilov-Cerenkov effect and negative index of refraction. The realization of metamaterials is first handled by Pendry *et al.* by achieving ε-negative values by using the thin-wire array structures, based on the plasma theory [2-4]. Although the realization of the ε-negative materials could be accomplished since, free electric charges exist in nature, the μ-negative materials were still a problem due to the absence of magnetic charges. This handicap is overcome by the invention of the split-ring resonators (SRRs). Smith and his group realized μ-negative materials by exciting the SRRs magnetically and afterwards Shelby experimentally showed that double negative materials could be achieved by combining conductor rods and SRRs [5,6]. Some modifications are introduced thereafter in SRRs and SRR-type structures such as edge- and broadside-coupled SRRs, complementary SRRs (CSRRs) or spiral resonators are developed [7-9]. Electric-*LC* (ELC) resonators are later proposed, offering more practicality in realization [10].

Engineered-surfaces are required for filtering the electromagnetic waves and having single or double negative properties. The most familiar example of the μ-negative material can be regarded as the SRR structure. A band of frequencies where the effective permeability is negative is shown to cause attenuation of scattering for the 3D arrangement of SRR arrays when illuminated by an incident electromagnetic wave with a magnetic field vector axial to the rings [4]. Similarly, the negative image structure of the SRR, so-called the complementary SRR is demonstrated to exhibit an ε-negative behavior [8]. Another approach to obtain an ε-negative metamaterial is to use ELC resonator [10]. These resonators can be combined with microstrip technology and compact stop band filters can be designed, thanks to the sharp change of ε from positive to negative in the vicinity of resonance [8,9]. ε-negative and μ-negative materials can also find applications in the design of miniaturized antennas [11-14]. A miniaturized dual band antenna is designed by

Submitted On: September 29, 2015
Accepted On: June 17, 2016

embedding an ε-negative and a DNG inclusion in a single dipole antenna [12]. By combining the double negative property with conventional right-handedness, compact metamaterial antennas with omni-directional radiation patterns are demonstrated [13,14]. Continuous scanning of radiation angle can be realized in these antennas by loading the structure with varactors and tuning the bias voltage [14]. SNG materials can also be used in the reduction of the specific absorption rate values of portable electronic devices, such as cell phones and for this purpose there are several studies conducted in the literature [15,16].

In this study, a window-like shaped novel metasurface structure is proposed and evaluated in terms of permittivity and permeability for both electrical and magnetic excitation types. The proposed structure is a promising metasurface, which can be modified easily to be as either a single band or dual band filter by opening or closing the aperture on the conductor part of the FSS. It also satisfies the tunability feature.

In addition to tuning of aperture length, the frequency tunability can also be achieved by changing the FSS copper strip width or substrate properties. It is noteworthy to mention that these changes do not affect the attenuation of the filter while tuning the operation frequency. The proposed structure with gap has double band characteristics for C-band and K_u-band. C-band can be used for applications such as satellite transponders and K_u-band for application areas such as high-resolution imaging and for satellite transponders.

An improved algorithm for extracting the effective constitutive parameters of a metamaterial is proposed by Szabo *et al.* [17] and achieved satisfactory results for the sparse unit cell models with the proper periodicity. The procedure presented in the mentioned paper invokes the Kramers–Kronig relations to ensure the uniqueness of the solution. The accuracy of the mentioned method is demonstrated by retrieving the effective material parameters of a homogeneous slab [17].

Due to the approved accuracy, we used the corresponding algorithm for retrieving the permittivity and permeability values. The results obtained from the algorithm are presented in the following sections as well as the parametric analysis results of the proposed structure. Impact of substrate thickness, permittivity, copper strip width, gap length, and excitation types are evaluated regarding the parametric analysis.

II. PROPOSED FSS GEOMETRY AND BOUNDARY CONDITIONS

The proposed geometry is presented in Fig. 1 where the parameter g is assumed zero at the beginning of the design, which corresponds to the case of "no gap" in the structure. The substrate thickness and the conductor thickness are denoted by h and h_c, respectively. The conductor part is etched to the dielectric layer. As it is seen on the Fig. 1 (a), c denotes the gap between the edge and the conductor, x denotes the width of the side gratings, and also the width of the mid-strips are equal to x.

The scattering parameters are calculated and the electric field, magnetic field and surface current properties of the structure under resonance are evaluated using the CST Microwave Studio full-wave software with unit cell boundary conditions. Besides a detailed parametric analysis, the impacts of different types of excitations are investigated in this study. For this reason, the proposed structure is excited by a plane wave perpendicular to the FSS plane with its E-field along the gap for the analyses in Section III (Fig. 1 (b)). For the analyses in Section IV, the structure is excited from one side with an H-field perpendicular to the FSS plane (Fig. 1 (c)).

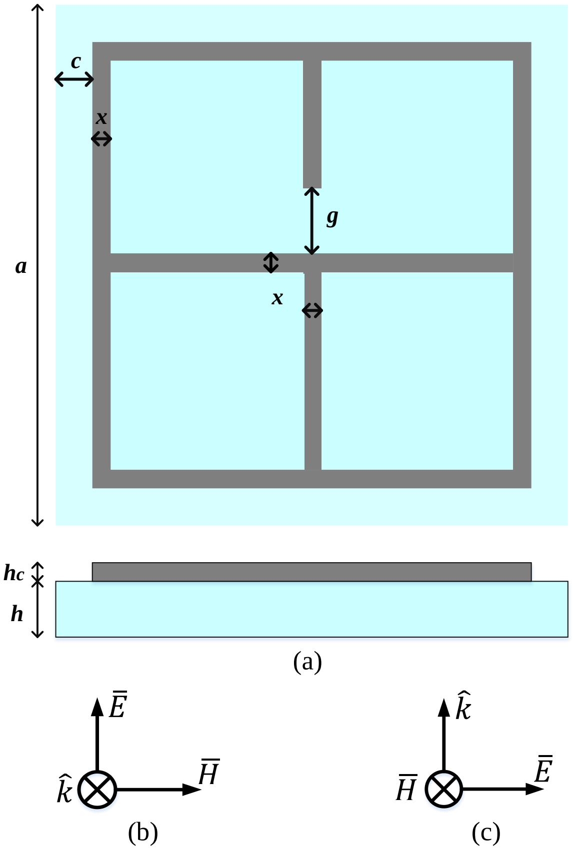

Fig. 1. (a) Geometry of the proposed FSS structure, (b) electric excitation, and (c) magnetic excitation.

III. ELECTRICALLY EXCITED FSS GEOMETRY

A. Impact of substrate thickness

Thickness of the substrate has a significant effect on scattering parameters and bandwidth. The resonance characteristics of S_{11} parameter is affected from the change of the thickness of the substrate. Resonance frequency of the S_{11} is 12.8 GHz for a thickness value of 0.2 mm and reduces to 12.24 GHz for a thickness value of 0.4 mm. S_{11} resonance occurs at 11.7 GHz, 11.6 GHz and 11.52 GHz for thickness values of 0.6 mm, 0.8 mm and 1 mm, respectively. The change of the value of the resonance frequency is in a much less amount for thicker substrates. S_{11} bandwidth, which is considered as the 10 dB bandwidth, also reduces from 2.67 GHz to 2.19 GHz for the thickness values 0.2 mm to 1 mm. The results regarding the thickness effect to S_{11} parameter is presented in Fig. 2 (a) and that to S_{21} parameter is demonstrated in Fig. 2 (b).

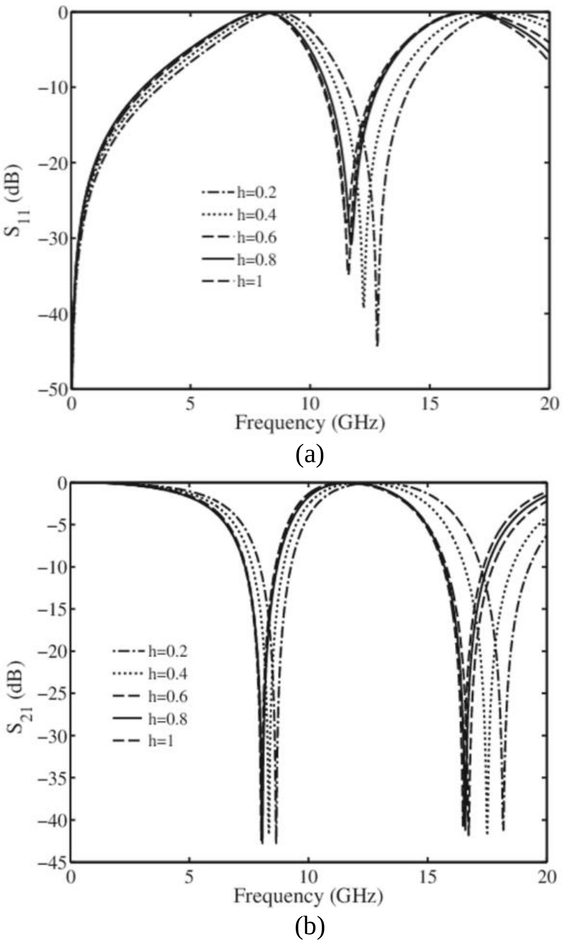

(a)

(b)

Fig. 2. Impact of substrate thickness to: (a) S_{11} and (b) S_{21} parameter. a=10 mm, x=0.1 mm, g=1 mm, c=1 mm, h=1 mm, h_c=0.035 mm, ε_r=2.2.

As seen in Fig. 2 (b) dual resonance is observed for S_{21} parameter. Lower S_{21} resonance frequency is decreased from 8.64 to 8.02 GHz with the increment of the thickness value from 0.2 mm to 1 mm. As a similar characteristic, the higher S_{21} resonance frequency is decreased from 18.18 GHz to 16.4 GHz for the aforementioned thickness values. S_{21} bandwidth is varied between 1.28 GHz to 1.39 GHz for the lower frequency and 2.74 to 1.71 GHz for the higher frequency. As expected, the thicker substrates caused wider band values.

B. Impact of substrate permittivity

In order to evaluate the impact of the substrate properties, Rogers RT5880, Arlon350and FR4 are considered as substrates of the proposed structure since they are the most used substrates in most of the applications including periodic structures and antennas, having a permittivity value of ε_r=2.2, ε_r=3.5 and ε_r=4.3, respectively. The corresponding results are demonstrated in Fig. 3.

S_{11} characteristics of the proposed structure with respect to the varied parameter, the permittivity, is demonstrated in Fig. 3 (a) and the S_{21} parameter is shown in Fig. 3 (b). As shown in Fig. 3 (a), the S_{11} resonances are at 11.5 GHz, 9.58 GHz and 8.74 GHz for the permittivity values of 2.2, 3.5 and 4.3, respectively.

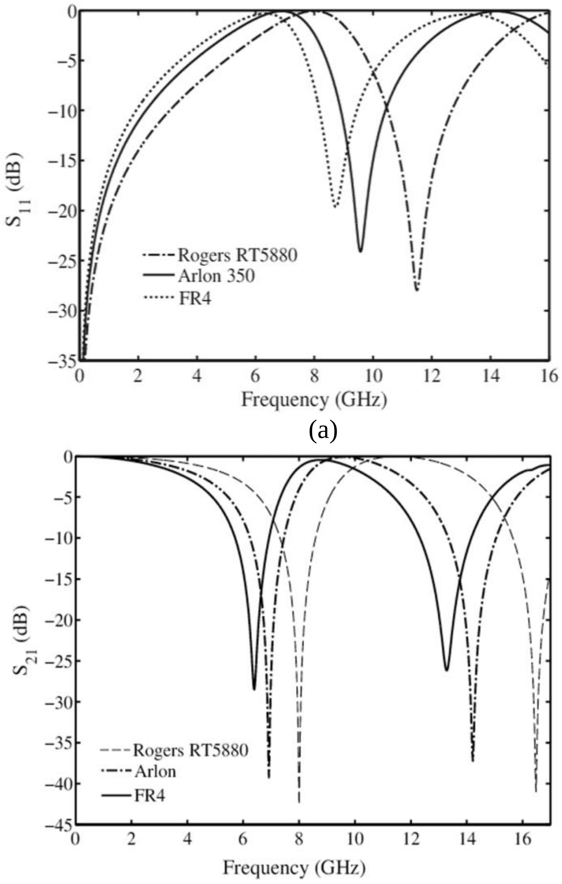

(a)

(b)

Fig. 3. Effect of substrate to: (a) S_{11} and (b) S_{21}. a=10 mm, x=0.1 mm, g=1 mm, c=1 mm, h=1 mm, h_c=0.035 mm, ε_r=2.2 (Rogers RT5880), ε_r=4.3 (FR4), ε_r=3.5 (Arlon350).

The higher permittivity values caused lower resonance values, as expected. The bandwidth values are observed as 2.22 GHz, 1.51 GHz and 1.3 GHz for the increasing value of permittivity. S_{21} resonance values are observed at 8 GHz, 6.92 GHz and 6.4 GHz for the lower frequency band and at 16.48 GHz, 14.22 GHz and 13.28 GHz for the upper resonance frequencies, for the permittivity values of 2.2, 3.5 and 4.3, respectively. The change in bandwidth values for the lower S_{21} resonance was negligible and around 1.22GHz and around 1.7 GHz for the lower and upper resonance bands, respectively.

C. Impact of copper strip width (*x*)

Impact of the copper strip width is also worth to evaluate since it directly affects the mutual impedance and changes the resonance frequency and bandwidth. For that purpose, the copper width *x* is varied between 0.1 mm to 0.5 mm and the effects of the parameter to S_{11} and S_{21} are presented in Figs. 4 (a) and 4 (b), respectively.

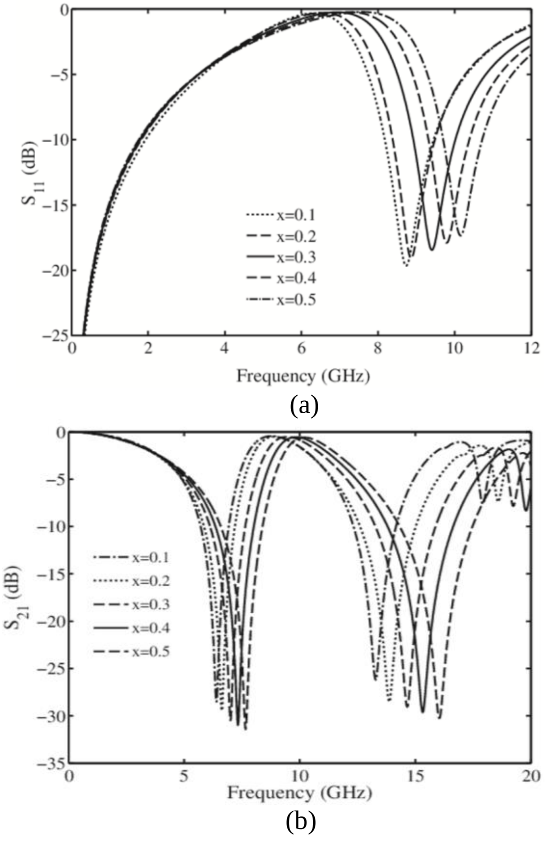

(a)

(b)

Fig. 4. Effect of *x* size to: (a) S_{11} and (b) S_{21}. *a*=10 mm, *x*=0.1 mm, *g*=1 mm, c=1 mm, *h*=1 mm, h_c=0.035 mm, ε_r=2.2.

S_{11} resonance frequencies are found to be 8.73 GHz, 8.86 GHz, 9.42 GHz, 9.79 GHz and 10.157 GHz for *x* values of 0.1, 0.2, 0.3, 0.4 and 0.5 mm, respectively. The increment of the copper width causes an increment in resonance frequency; however, it causes a decrement in bandwidth. The bandwidth is decreased from 1.28 GHz to 1.002 GHz when the copper width is increased to 0.5 from 0.1 mm. As the *x* increases, the inductance decreases and therefore the decrement of the resonance frequency confirms our expectations.

S_{21} resonances for the aforementioned copper thicknesses are observed as 6.4 GHz, 6.62 GHz, 7 GHz, 7.32 GHz and 7.66 GHz for lower band frequencies with a bandwidth value of 1.19 GHz, 1.37 GHz, 1.5 GHz, 1.65 GHz and 1.8 GHz respectively. The upper band S_{21} resonances occur at 13.28 GHz, 13.88 GHz, 14.64 GHz, 15.32 GHz and 16.04 GHz with a bandwidth value of 1.84 GHz, 2.43 GHz, 2.59 GHz, 2.85 GHz and 3.159 GHz, respectively.

D. Impact of gap length (*g*)

The proposed structure has an aperture on the conductor part of the FSS from the center and this gap has a significant effect on resonance frequencies. Inserting this gap automatically increases the number of resonances when compared with the structure without gap. The impact of the gap is also evaluated and the results are presented in Fig. 5.

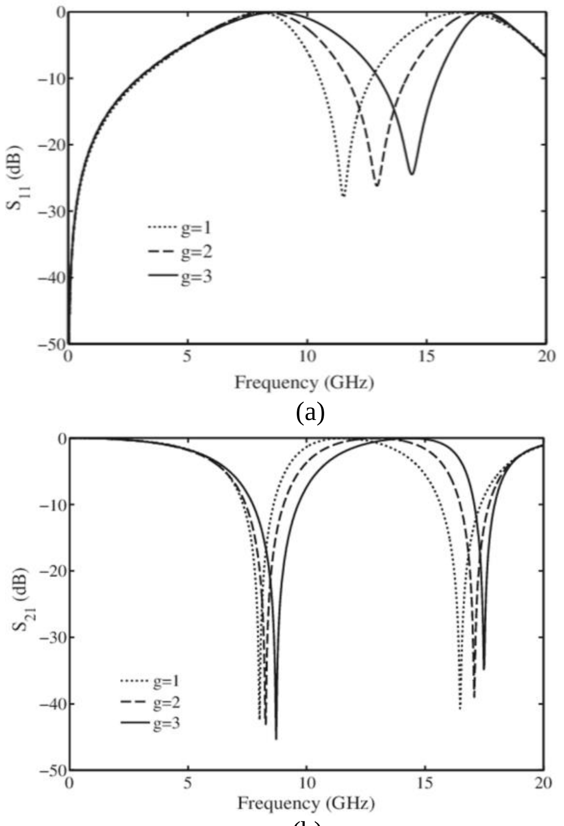

(a)

(b)

Fig. 5. Effect of gap width to: (a) S_{11} and (b) S_{21}. *a*=10 mm, *x*=0.1 mm, *g*=1 mm, c=1 mm, *h*=1 mm, h_c=0.035 mm, ε_r=2.2.

S_{11} resonance values increase to 14.98 GHz from 11.52 GHz with the increment of the gap from 1 mm to 3 mm. The increase of the resonance frequency can be explained with the decrease of the capacitance by the increase of the gap length. Bandwidth for the gap values 1 mm, 2 mm and 3 mm are 2.17 GHz, 2.49 GHz and 2.44 GHz, respectively.

Tunability is obtained not only in resonance values of S_{21} but also in bandwidth values of S_{21} for both upper (at K_u band around 16 GHz) and lower frequency bands (at X-band, around 8 GHz). Bandwidth of the S_{21} lower resonance frequency band is increased to 1.89 GHz from 1.28 GHz and the bandwidth of the S_{21} upper resonance frequency band is reduced to 0.89 GHz from 1.73 GHz.

E. Parameter retrieval results of electrically excited FSS geometry for "with" and "without gap"

The structures with and without gap are considered and the retrieval algorithm is applied in order to obtain the permittivity and permeability values.

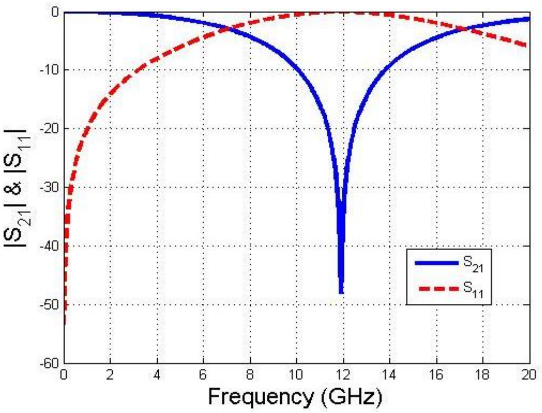

Fig. 6. Scattering parameters of a structure without gap (*a*=10 mm, *x*=0.1 mm, *g*=0 mm, c=1 mm, *h*=1 mm, h_c=0.035 mm, Rogers RT 5880).

The structure without gap has a single S_{21} resonance as expected due to the surface current distribution and the scattering characteristics are presented in Fig. 6.

Permittivity and permeability values are retrieved by using the magnitude and the phase information of the structure over a particular period and the results are presented in Fig. 7. As seen in the Fig. 7 (a), permittivity has negative values between 10.8 GHz and 17 GHz with a center frequency at 12 GHz. Since the structure is electrically excited, it was expected to have a negative permittivity value over a frequency region around resonance, but not a negative value of permeability value over the band of evaluation. The results presented in Fig. 7 (b) approves this expectation. The real permeability value is observed positive for the entire band.

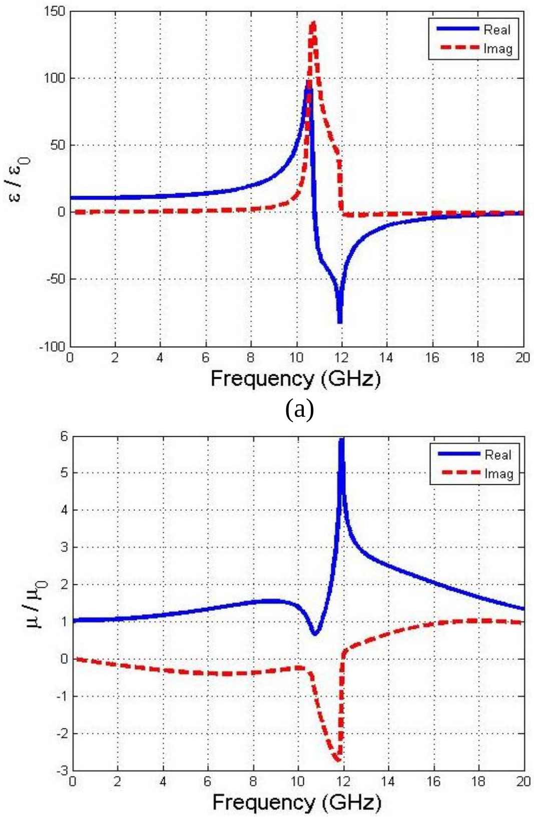

(a)

(b)

Fig. 7. Retrieved permittivity and permeability values (*a*=10 mm, *x*=0.1 mm, *g*=0 mm, c=1 mm, *h*=1 mm, h_c=0.035 mm, Rogers RT 5880).

The algorithm confirms well the expected negative permittivity behavior around the resonance frequency of the gap (see Fig. 6), although there exists a small inconsistency of the algorithm which accounts for the negative imaginary permeability in a narrow frequency region.

As aforementioned, the gap value (*g*) is one of the important parameters, which changes the surface currents and even increasing the number of the resonances of the structure. For that purpose, a gap having 1mm length is inserted to the structure and the structure is excited with a plane wave, which has an electrical field vector in parallel to this gap. The resulting scattering parameters are presented in Fig. 8.

As shown in Fig. 8 the structure has two S_{21} resonances, lower resonance is at 8.02 GHz and the upper resonance is at 16.5 GHz. The S_{11} resonance is occurred at 11.5 GHz with a bandwidth of 2.14 GHz.

The results regarding the permittivity and permeability retrieval are presented in Figs. 9 (a) and (b). The permittivity is negative around the resonance frequencies of 8.02 GHz and 16.5 GHz. When compared with the “no-gap” case, the opening of the gap creates two negative-permittivity regions in the [0, 20 GHz] frequency interval. This can be explained by the occurrence of an additional resonance for the “with gap” structure.

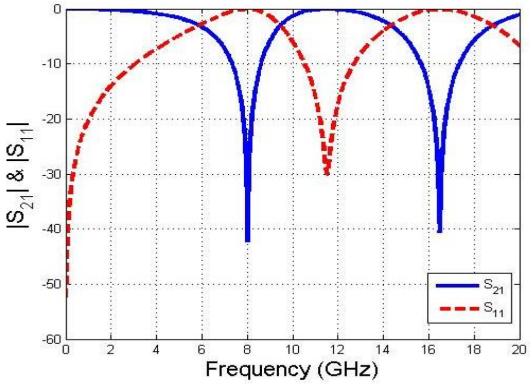

Fig. 8. Scattering parameters of the structure with gap for which the parametric retrieval algorithm is conducted (a=10 mm, x=0.1 mm, g=1 mm, c=1 mm, h=1 mm, h_c=0.035 mm, Rogers RT 5880).

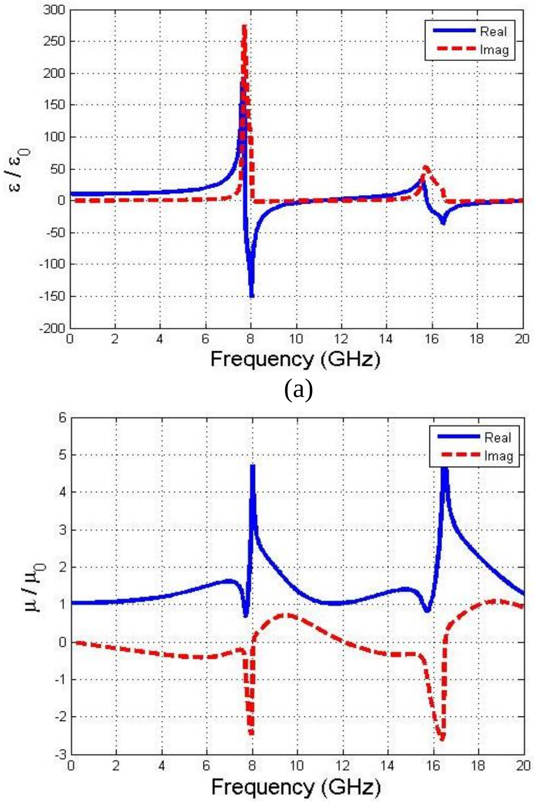

(a)

(b)

Fig. 9. (a) Retrieved permittivity and (b) permeability values of the structure with gap (a=10 mm, x=0.1 mm, g=1 mm, c=1 mm, h=1 mm, h_c=0.035 mm, Rogers RT 5880).

IV. MAGNETICALLY EXCITED FSS

Excitation type is another parameter that affects the resonance characteristics of the structure. Around resonance, a structure may show single or double negative properties when excited electrically, or magnetically. The magnetic excitation causes surface currents on the conductor part of the structure and resonance can occur due to this surface current. In order to show the difference between electric and magnetic excitation types for the proposed structure, several simulations are performed including the impact of the substrate thickness, substrate permittivity, gap length, copper strip width and the results are demonstrated.

A. Impact of substrate thickness

Impact of substrate thickness is evaluated and the scattering parameter results are presented in Fig. 10. The thickness values are varied between 0.2 mm to 1 mm and a resonance has been obtained in the S_{11} parameter. However, no resonance is occurred for S_{21}. Unlike the electric excitation case, changing the thickness value exhibits a negligible effect on the scattering characteristics of the magnetically excited structure.

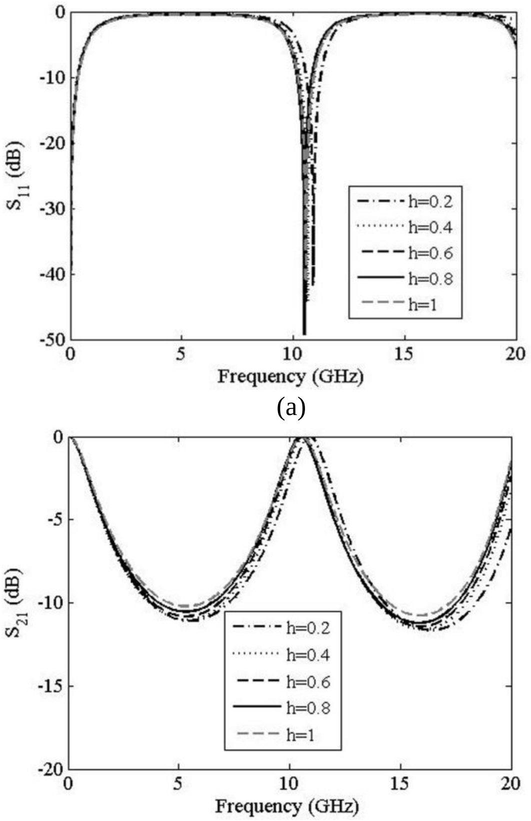

(a)

(b)

Fig. 10 Effect of substrate thickness of a magnetically excited structure to: (a) S_{11} and (b) S_{21} (a=10 mm, x=0.1 mm, g=1 mm, c=1 mm, h=1 mm, h_c=0.035 mm, ε_r=2.2).

B. Impact of substrate permittivity

The effect of using different substrates is also evaluated by considering FR4 (ε_r=4.3), Arlon350 (ε_r=3.5) and Rogers RT5880 (ε_r=2.2) as substrate materials. Similar to the electrically excited metasurface structure, as the permittivity of the substrate decreases, the resonance bands shift to higher frequencies, as shown in Fig. 11.

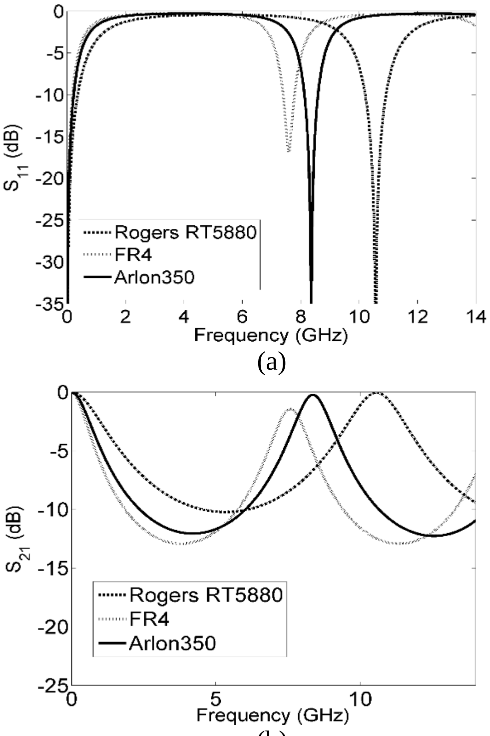

(a)

(b)

Fig. 11. Effect of substrate to: (a) S_{11} and (b) S_{21}. (a=10 mm, x=0.1 mm, g=1 mm, c=1 mm, h=1 mm, h_c=0.035 mm, ε_r=2.2 (Rogers RT5880), ε_r=4.3 (FR4), ε_r=3.5 (Arlon350)).

C. Impact of the copper strip width (x)

Similar to the thickness effect, the width of the copper strip does not affect the scattering characteristics as shown in Fig. 12 (a) for S_{11} and Fig. 12 (b) for S_{21}.

The magnetic field and surface current distribution of the structure are investigated at the resonance frequency of 10.56 GHz in order to clarify the underlying physics for the invariance of the resonance frequency against x change.

The magnetic field and surface current distribution are shown in Figs. 13 (a) and (b), respectively for the structure with g=1 mm, x=1 mm and ε_r=2.2. Magnetic field strength is primarily distributed in the outer sides of the outer metal strips and most of the current circulates on the outer side of the metal strip and in opposite directions for adjacent cells, as can be seen in Figs. 13 (a) and (b), respectively. Therefore the change of the metal strip width, x, does not affect the resonance characteristics, even for thicker strip values.

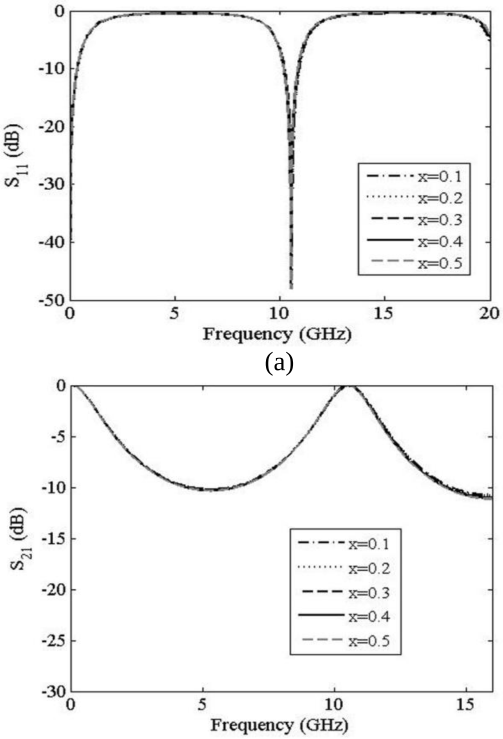

(a)

(b)

Fig. 12. Effect of copper width of a magnetically excited structure to: (a) S_{11} and (b) S_{21} (a=10 mm, g=1 mm, c= 1 mm, h=1 mm, h_c=0.035 mm, ε_r=2.2).

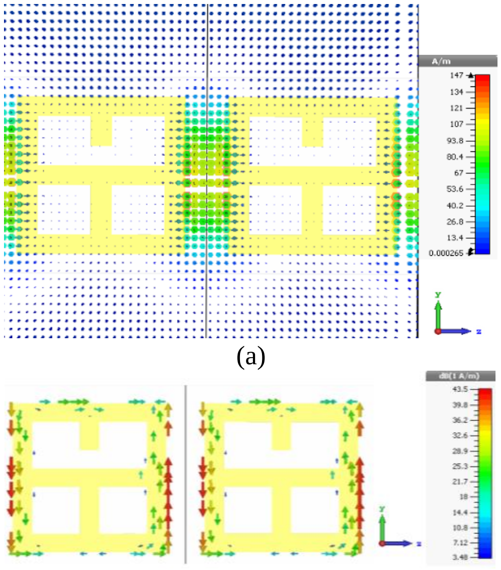

(a)

(b)

Fig. 13. (a) Magnetic field distribution and (b) surface current distribution of the structure with a=10 mm, x=1 mm, g=1 mm, c=1 mm, h=1 mm, h_c=0.035 mm, and ε_r=2.2, is shown in yz-plane. Since the structure is periodic in x and y directions, the adjacent metal strip can also be seen.

D. Impact of gap length (*g*)

Similarly, the length of the gap does not affect the scattering characteristics as shown in Figs. 14 (a) and (b) for S_{11} and S_{21}, respectively. The reason of this finding lies in the fact that there is no surface current circulation in the interior part of the metallic structure. Therefore, the existence of the gap does not affect the resonance frequency. In addition, no resonance condition is obtained for the S_{21}.

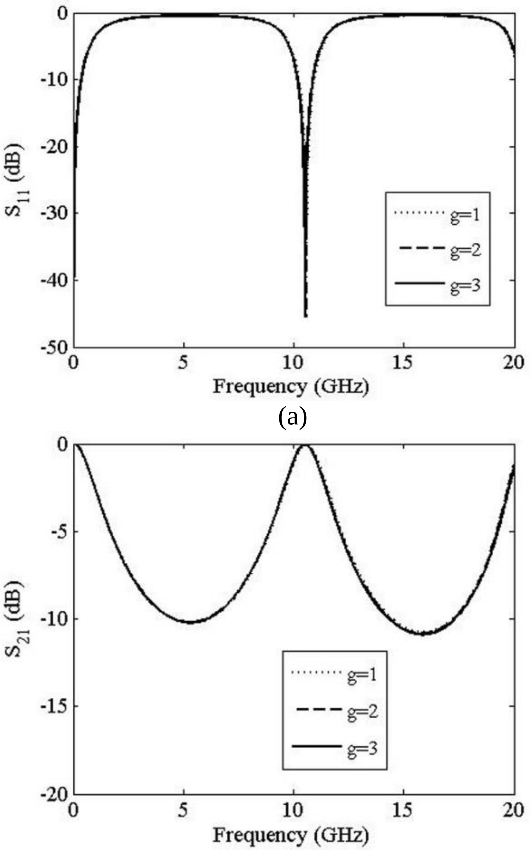

(a)

(b)

Fig. 14. Effect of gap length of a magnetically excited structure to: (a) S_{11} and (b) S_{21}. (a=10 mm, x=1 mm, g=1 mm, c=1 mm, h=1 mm, h_c=0.035 mm, and ε_r=2.2).

As shown in the corresponding results of the magnetically excited metasurface structure tunability could not be achieved since the structure parameters change the scattering characteristics negligibly or not at all.

Retrieval analysis is also conducted for the metasurface structure with magnetic excitation. Since no transmission resonance is observed for this structure, the proposed structure did not achieve to have negative region either in permittivity or permeability through the Nicholson-Ross-Weir (NRW) algorithm based on Kramers-Kronig relationship.

V. CONCLUSION

In this study, a window-like shaped novel tunable metasurface is proposed in order to be used for X and K_u band applications. The proposed structure is achieved to have dual-frequency resonance when a gap is inserted on the conductor side of the metamaterial and for each resonance frequency a single epsilon-negative region is obtained for the electrically excited structure. The structure is also evaluated under magnetic excitation conditions. However, it is observed that tunability could not be achieved; besides no single negative region is obtained for this case.

ACKNOWLEDGEMENT

We gratefully acknowledge the financial support by Scientific Research Projects of Ankara University (BAP) under Grant No. 13B4343015 and 16B0443005.

F. B. also acknowledges “The Scientific and Technological Research Council of Turkey (Tubitak)” through BIDEB-2219 Postdoctoral Research Fellowship.

REFERENCES

[1] V. G. Veselago, “The electrodynamics of substances with simultaneously negative values of ε and μ,” *Soviet Physics Uspekhi*, vol. 10, no. 4, pp. 509-514, 1968.

[2] J. B. Pendry, A. J. Holden, W. J. Stewart, and I. Youngs, “Extremely low frequency plasmons in metallic mesostructures,” *Phys. Rev. Lett.*, vol. 76, no. 25, pp. 4773-4776, 1996.

[3] J. B. Pendry, A. J. Holden, D. J. Robbins, and W. J. Steward, “Low frequency plasmons in thin-wire structures,” *J. Phys.: Condens. Matter*, vol. 10, pp. 4785-4809, 1998.

[4] J. B. Pendry, A. J. Holden, D. J. Robbins, and W. J. Stewart, “Magnetism from conductors and enhanced nonlinear phenomena,” *IEEE Trans. Microw. Theory Techn.*, vol. 47, no. 11, pp. 2075-2084, 1999.

[5] D. R. Smith, W. J. Padilla, D. C. Vier, S. C. Nemat-Nasser, and S. Schultz, “Composite medium with simultaneously negative permeability and permittivity,” *Phys. Rev. Lett.*, vol. 84, no. 18, pp. 4184-4187, 2000

[6] R. Shelby, D. R Smith, and S. Schultz, “Experimental verification of a negative index of refraction,” *Science*, vol. 292, no. 5514, pp. 77-79, 2001.

[7] R. Marqués, F. Mesa, J. Martel, and F. Medina, “Comparative analysis of edge- and broadside-coupled split ring resonators for metamaterial design-Theory and experiments,” *IEEE Transac. Antennas Propag.*, vol. 51, no. 10, pp. 2572-2581, 2003.

[8] F. Falcone, T. Lopetegi, J. D. Baena, R. Marqués, F. Martin, and M. Sorolla, “Effective negative-

epsilon stopband microstrip lines based on complementary split ring resonators," *IEEE Microw. Wireless Compon. Lett*., vol. 14, no. 6, pp. 280-282, 2004.

[9] J. D. Baena, R. Marqués, F. Medina, and J. Martel, "Artificial magnetic metamaterial design by using spiral resonators," *Phys. Rev. B*, vol. 69, pp. 014402-1-5, 2004.

[10] D. Schurig, J. J. Mock, and D. R. Smith, "Electric-field-coupled resonators for negative permittivity metamaterials," *Appl. Phys. Lett*., vol. 88, pp. 041109, 2006.

[11] E. Çelenk, E. Unal, D. Kapusuz, and C. Sabah, "Microstrip patch antenna covered with left handed metamaterial," *ACES Journal*, vol. 28, no. 10, pp. 999-1004, 2013.

[12] A. Jafargholi and M. Kamyab, "Dipole antenna miniaturization using single-cell metamaterial," *ACES Journal*, vol. 27, no. 3, pp. 261-270, 2012.

[13] S. Lim, C. Caloz, and T. Itoh, "Metamaterial based electronically controlled transmission-like structure as a novel-leaky wave antenna with tunable radiation angle and beamwidth," *IEEE Transac. Microw. Theory Techn*., vol. 53, no. 1, pp. 161-173, 2005.

[14] K. L. Sheeja, P. K. Sahu, S. K. Behera, and N. Dakhli, "Compact tri-band metamaterial antenna for wireless applications," *ACES Journal*, vol. 27, no. 11, pp. 947-955, 2012.

[15] M. T. Islam, M. R. I. Faruque, and N. Bisran, "Reduction of specific absorption rate (SAR) in human head with ferrite material and metamaterial," *PIER C*, vol. 9, pp. 47-58, 2009.

[16] M. R. I. Faruque, M. T. Islam, and N. Misran, "Evaluation of EM absorption in human head with metamaterial attachment," *ACES Journal*, vol. 25, no. 12, pp. 1097-1107, 2010.

[17] Z. Szabo, G.-H. Park, R. Hedge, and E.-P. Li, "A unique extraction of metamaterial parameters based on Kramers-Kronig relationship," *IEEE Trans. Microw. Theory and Techn*., vol. 58, no. 10, pp. 2646-2653, 2010.

Sultan Can received her B.Sc. degree in Electrical-Electronics Engineering from the Atilim University in 2008. She received her M.Sc. Degree from the same university in 2011. She is currently with the Dept. of Electrical-Electronics Engineering in Ankara University since 2013, where she is a Research Assistant and a Ph.D. Candidate. Her research interests include electromagnetism, metamaterials and antennas.

Emrullah Karakaya obtained his B.Sc. degree in Department of Engineering Physics in Ankara University, graduating in 2015. He is currently pursuing his master degree at the same department. His research interests include the analysis of frequency selective surfaces and metamaterials.

Fulya Bagci obtained her first degree in Engineering Physics from Ankara University, graduating in 2005. She received her M.Sc. and Ph.D. degrees from the same department in 2008 and 2013, respectively. Bagci is a Research Assistant in the Department of Engineering Physics, Ankara University since 2005. She has conducted postdoctoral researches at the Microwave Group in University of Sevilla (Spain), during 01.03.2015-01.03.2016. Her research interests include the analysis of frequency selective surfaces and metamaterials for photonic and microwave device applications.

A. Egemen Yilmaz received his B.Sc. degrees in Electrical-Electronics Engineering and Mathematics from the Middle East Technical University in 1997. He received his M.Sc. and Ph.D. degrees in Electrical-Electronics Engineering from the same university in 2000 and 2007, respectively. He is currently with the Dept. of Electrical-Electronics Engineering in Ankara University, where he is an Associated Professor. His research interests include computational electromagnetics, nature-inspired optimization algorithms, knowledge-based systems; more generally software development processes and methodologies.

Baris Akaoglu received his B.Sc. degree in Physics from the Middle East Technical University in 1996. He received his M.Sc. and Ph.D. degrees in Physics from the same university in 1998 and 2004, respectively. He is currently with Department of Engineering Physics in Ankara University, where he is a Professor. He did experimental research on semiconductors. His current research interests include photonic crystals and metamaterials.

Design of Compact Novel Dual-Band BPF Using Open-Loop Dumbbell Shaped Defected Ground Structure and Step Impedance Cross-Shaped Lines with Independently Controllable Frequencies and Bandwidths

R. Khosravi [1], Ch. Ghobadi [2], J. Nourinia [2], M. Abbasilayegh [2], and B. Mohammadi [2]

[1] Department of Electrical Engineering, Science and Research Branch
Islamic Azad University, West Azerbaijan, Iran
ronak62@gmail.com

[2] Department of Electrical Engineering
Urmia University, Urmia, Iran
ch.ghobadi@urmia.ac.ir, j.nourinia@urmia.ac.ir, m.abbasilayegh@urmia.ac.ir, b.mohammadi@urmia.ac.ir

Abstract **─** In this paper a compact novel dual-band bandpass filter (DB-BPF) with independently controllable frequencies and bandwidths is presented and the procedure of its design is discussed. The proposed filter consists of an open-loop dumbbell shaped (OLDS) defected ground structure (DGS) and step impedance cross-shaped lines (SICSLs). To generate the first band, the authors used a pair of end-coupled uniform transmission lines with equal-length on the top and an OLDS outline symmetrically was etched in the ground plane. In addition, by introducing cross-shaped lines, a dual band function is achieved. In the proposed structure, in order to reject the unwanted harmonic pass bands, step impedance transmission lines are implemented along the ports of the filter. The fabricated filter has the merits of simple topology, compact size, good return loss, low insertion loss and high isolation. The measurement agrees well with the simulation.

Index Terms **─** Defected Ground Structure (DGS), Dual-band Bandpass Filter (DB-BPF), Step Impedance Cross-Shaped Lines (SICSLs).

I. INTRODUCTION

Microstrip BPFs have been extensively studied and developed for a long time to meet various requirements in many modern communication systems. Among these designs, planar types of narrow and wide BPFs are highly promising in size compactness, large out-of-band rejection, low fabrication cost, and so on [1]–[18]. DB-BPFs are highly desired in modern dual-band wireless communication systems. Therefore, they have been extensively investigated and various design approaches have been proposed [1]–[14]. Among them, there are three typical methods. The first approach is using the cascade connection of a BPF and a bandstop filter. However, it occupies large size. The second method is utilizing stepped-impedance resonators (SIRs) as multi-mode resonators (MMRs), by controlling impedance and the length ratios of the SIRs, the desired operating frequencies can be obtained, the two resonant frequencies of which can be controlled by the impedance ratio and electrical length of two sections [1]–[5]. The third approach is using dual-mode DB-BPF [6]–[11]. [2] presents a compact DB-BPF based on mixed electric and magnetic coupling. SIR is utilized to construct mixed electric and magnetic coupling by placing the low impedance stubs and the high-impedance stubs closely, respectively. A transmission zero (TZ) can be generated and its location is determined by the dominant coupling.

In [4], compact dual-wideband function is achieved based on a novel penta-mode resonator (PMR). The first two modes are employed to generate the first passband, and the other three modes are used to form the second one. In [5], a compact dual-wideband BPF with two MMRs is proposed. The first MMR is a quad-mode resonator (QMR) which consists of a main transmission line loaded with a short-ended stub and two open-ended stubs, and the second MMR is a triple-mode resonator (TMR) which is composed of a main transmission line loaded with a square ring and a short-ended stub. In [3], a compact and high selectivity dual-band dual-mode microstrip BPF with the source-load coupling is proposed using the single short-circuited stub-loaded SIR. The resonator can generate two resonant modes in each band.

In general, dual-mode characteristics are excited by adding corner cut or corner patch perturbations to loop resonator. This pair of degenerate modes is coupled with each other and its coupling strength can be adjusted by the perturbation's size with respect to the

Submitted On: March 26, 2015
Accepted On: July 24, 2016

reference element. Patch perturbation with capacitive coupling is often adopted in dual-mode resonator filter because it can provide TZs for high selectivity design [6]–[11]. In [6], two microstrip perturbed ring resonators are employed to obtain dual-mode dual-band responses. [7] proposes a single slotted circular patch resonator for a dual-mode DB-BPF design. The arc- and radial-oriented slots are used to bring down the TM_{01}-like mode and to split the TM_{11}-like mode and its degenerate mode, respectively. [8] Presented a novel multilayer dual-mode DB-BPF using two identical microstrip cross-slotted patch resonators placed back-to-back. The lengths of the slots on the patch resonator are designed to be different, which can be used to control the two degenerate modes. Another class of dual-mode DB-BPFs can be realized by open-loop resonators and center-loaded resonators [9] or open-loop slotline resonators [10]. A perturbation technique using simple loading stub is investigated in [10], which is applied to produce the non-degenerate mode for open-loop slotline resonator and to improve the operating band selectivity. The distinct characteristics of this dual-mode resonator are studied by using even–odd mode analysis. Likewise, equivalent circuit models at non-degenerate modes are given to determine the resonance frequencies and TZs. In [11] a simple microstrip ring-resonator is presented for novel design of dual-band dual-mode BPFs. By increasing the length of the loaded open-circuited stub, the two first-order degenerate modes are excited and slit for the use of the first passband. Moreover, other strategies to improve the impedance bandwidth which do involve a modification of the geometry of the planar DB- BPFs have been investigated in [12]-[14].

In this paper, a compact novel DB-BPF with independently controllable frequencies and bandwidths has been presented. The proposed DB-BPF consists of OLDS DGS and SICSLs. By inserting an OLDS slot in the ground plane and a pair of end-coupled uniform transmission lines with equal-length on the top, the first band can be produced.

The OLDS slot consists of two identical circle loops having open-loop edge length (W_{10}-W_{11}) together with open ends W_9 and a slot-line L_8 which forms connection between them. In this configuration, the dumbbell-arm is aligned with the microstrip line on the top. Placing OLDS slot in the ground plane is used for miniaturizing the size of proposed structure and also improving the mutual coupling between the end-coupled transmission lines. In addition, by introducing cross-shaped lines, a dual band function is achieved. By step impedance transmission lines, significant improvement in isolation between dual-band is observed. Also by using OLDS DGS, much wider bandwidth can be produced. In addition, a parametric study is carried out in detail to provide filter engineers with essential design information. The experimental data show that the DB-BPF can provide two band-widths of 920 MHz centered at 3 GHz and 830 MHz centered at 8 GHz.

II. DB-BPF DESIGN AND CONFIGURATION

The compact novel DB-BPF with independently controllable frequencies and bandwidths fed by a 50Ω microstrip lines is shown in Fig. 1, which is printed on a Rogers (RO4003) substrate of thickness 0.8 mm, permittivity 3.55, and loss tangent 0.0027. The basic DB-BPF structure consists of OLDS DGS and SICSLs. The transmission lines are connected to a feed line of width W_1 and length L_1, as shown in Fig. 1. The proposed DB-BPF is connected to a 50Ω SMA connector for signal transmission. A single band function is provided by inserting an OLDS slot in the ground plane and a pair of end-coupled uniform transmission lines with equal-length on the top and a dual band characteristic is obtained by introducing cross-shaped lines. The end-coupled transmission lines provide one TZ at DC. The first passband is further bounded by two finite TZs at frequencies lower TZ (1.06 GHz) and upper TZ (3.91 GHz) because of OLDS DGS. The first passband of the measured results is centered at 3 GHz with a low insertion loss of 1 dB and an FBW of 31%. The second passband of the measured results has a center frequency of 8 GHz with a low insertion loss of 2 dB, and an FBW of 11%. The planar DB-BPF with various design parameters is constructed, and the numerical and experimental results of the input impedance and transmission characteristics are presented and discussed. The parameters of this proposed DB-BPF are studied by changing one parameter at a time and fixing the others. The simulated results are obtained using Ansoft simulation software high-frequency structure simulator (HFSS). The final values of the presented DB-BPF design parameters are specified in Table 1.

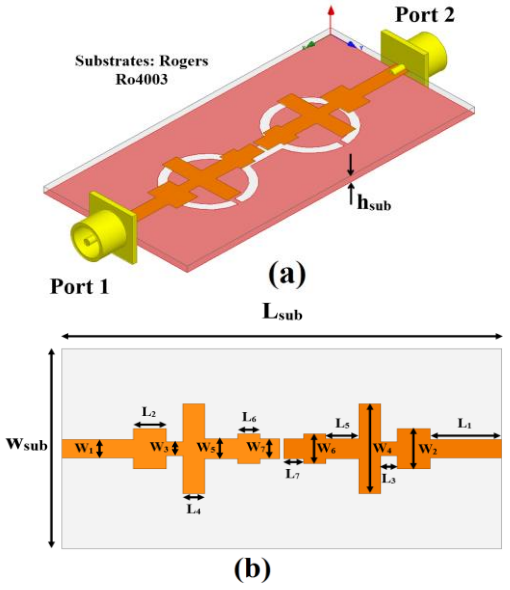

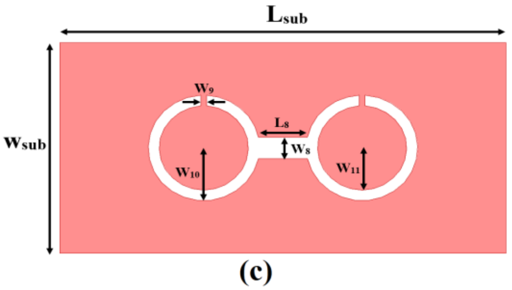

Fig. 1. The Geometry of the proposed DB-BPF using OLDS and SICSLs: (a) side view, (b) top view, and (c) bottom view.

Table 1: The final values of design parameters

Param.	mm	Param.	mm	Param.	mm
W_{sub}	20	W_7	2	L_2	3
W_1	1.8	W_8	2	L_3	1.5
W_2	4	W_9	0.5	L_4	2
W_3	1.4	W_{10}	5	L_5	3
W_4	9	W_{11}	4	L_6	2
W_5	2	L_{sub}	40	L_7	1.8
W_6	3	L_1	6.5	L_8	4.2

Figure 2 shows the structure of various microstrip filters which are used for simulation studies. Frequency responses for filter with OLDS DGS and a pair of end-coupled uniform transmission lines (Fig. 2 (a)), with a pair of end-coupled uniform transmission lines and cross-shaped lines (Fig. 2 (b)), and the proposed structure are compared in Fig. 3. As shown in Fig. 3, for the proposed DB-BPF configuration, in order to generate the first band characteristics, an OLDS slot is used in the ground plane and a pair of end-coupled uniform transmission lines with equal-length on the top and by introducing cross-shaped lines; a dual band function is achieved that covers all the 2.61-3.53 GHz and 7.82-8.65 GHz for WLAN/WiMAX and satellite communications, respectively.

As illustrated in Fig. 3, the passband is bounded by two TZs. One is at DC and the other at some higher frequency. The zero at DC is imposed by the end-coupled line (gap width= 0.4 mm) whilst the higher-frequency TZ is generated by the above DGS pattern. To improve the stopband performance of the above filter using OLDS DGS, step impedance transmission lines can be considered. In general, the OLDS DGS perturbs the current distribution on the ground plane of the microstrip line and as a result the equivalent inductance and capacitance are increased. The dimensions of the OLDS DGS have influence on its frequency behavior as by increasing the area of the DGS the cutoff frequency decreases and the attenuation pole moves toward lower frequencies. In order to explain the movement of the attenuation pole toward the lower frequencies, it can be said that by increasing the area of the defect structure the length of the looping path around the OLDS DGS for the returning current on the ground plane is increased and as a result the effective inductance of the transmission line is increased which in turn leads to an increase in equivalent inductance of the overall structure and consequently the cutoff frequency is decreased and the attenuation pole is moved toward lower frequencies [15]–[17].

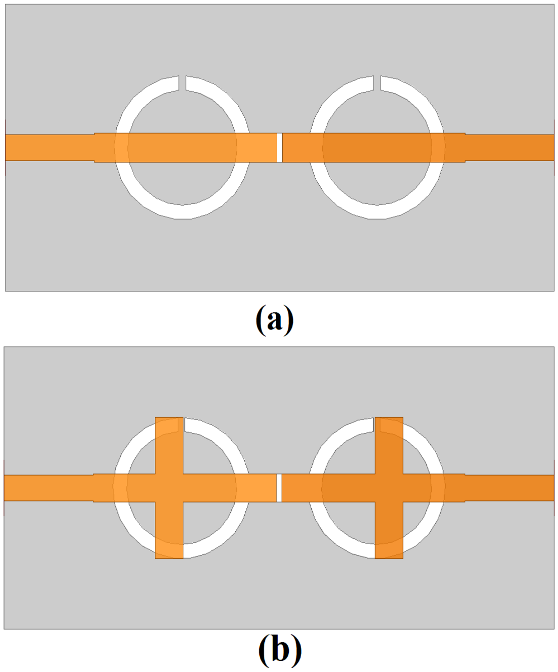

Fig. 2. Filter with OLDS DGS and (a) a pair of end-coupled uniform transmission lines, (b) a pair of end-coupled uniform transmission lines and cross-shaped lines.

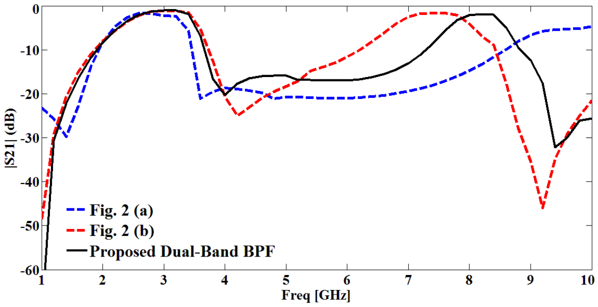

Fig. 3. The insertion loss characteristics for filter structures shown in Fig. 2 and proposed DB-BPF.

In order to modify the design parameters of the proposed DB-BPF, a parametric study was performed. As examples of the aforementioned parametric study, the effect of five design parameters are presented and discussed here. Figure 4 shows the effect of variation in inner radius length of the OLDS DGS (W_{11} in Fig. 1 (c)) on the frequency responses of the proposed DB-BPF for different cases. It is found that by changing the inner radius length of the OLDS DGS from 3.0 mm to 4.5 mm, the position of the attenuation pole is shifted from 4.2 GHz to 3.7 GHz, respectively. Fig. 5 shows the effect of variation in outer radius length of the OLDS DGS (W_{10} in Fig. 1 (c)) on return loss characteristic of the proposed DB-BPF for different cases. As can be observed from this figure, the impedance bandwidth can be fine-tuned effectively by modifying this parameter. Another effective way to tune the proposed DB-BPF is the replacement of uniform transmission by SICSLs.

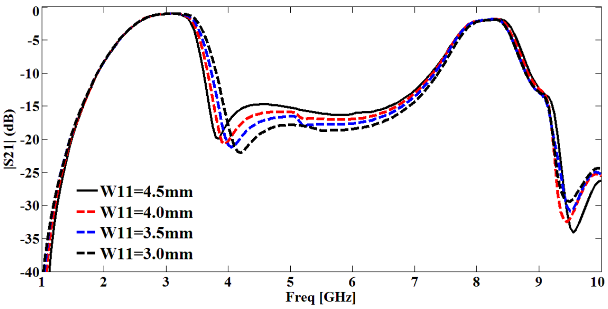

Fig. 4. The effect of variation in inner radius length of the OLDS DGS (W_{11} in Fig. 1 (c)) on insertion loss.

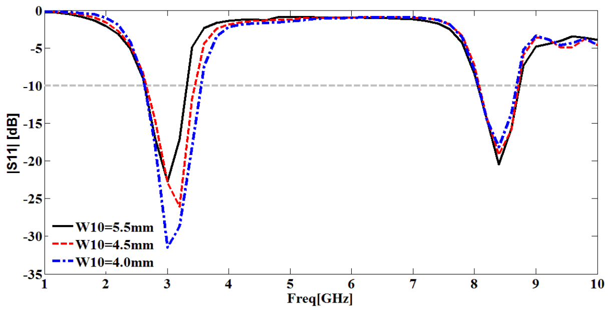

Fig. 5. The effect of variation in outer radius length of the OLDS DGS (W_{10} in Fig. 1 (c)) on return loss.

Figure 6 shows the effect of variation in the width of the arm of the SICSLs (L_6 in Fig. 1 (b)) on return loss. From the simulation results in Fig. 6, it can be seen in the figure that the impedance bandwidth and return loss characteristics of the upper frequency band are slightly changed when L_6 is varied. The simulated return loss curves with different values of the proposed DB-BPF are plotted in Fig. 7. From the simulation results in Fig. 7, it is found that the upper frequency band is significantly affected by the variation of the W_4.

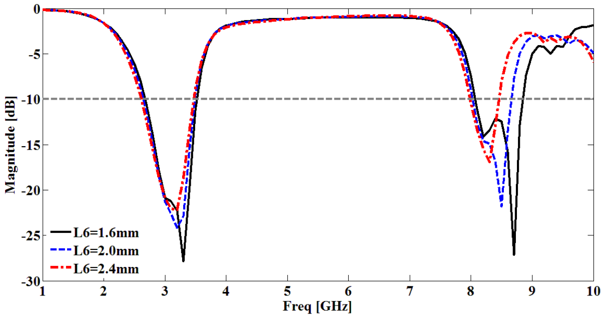

Fig. 6. The effect of variation in the width of the arm of the SICSLs (L_6 in Fig. 1 (b)) on return loss.

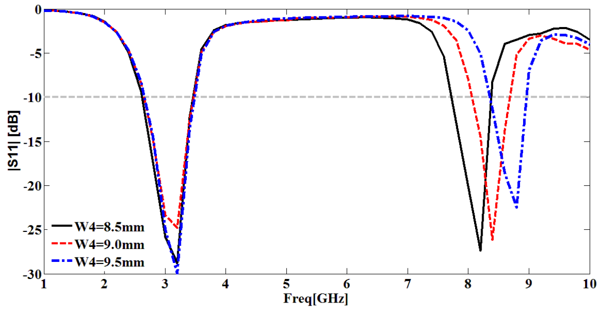

Fig. 7. The effect of variation in the finger length of the vertical arm of the cross-shaped lines (W_4 in Fig. 1 (b)) on return loss.

As illustrated in Fig. 8, the upper passband is bounded by a TZ at upward 9 GHz that is imposed by the cross-shaped lines. To improve the stopband performance of the upper passband, step impedance transmission lines can be considered. It is found that by changing the finger width of the vertical arm of the cross-shaped lines (L_4 in Fig. 1 (b)) from 1.4 mm to 2.4 mm, the position of the proposed TZ is shifted from 9.85 GHz to 9.07 GHz, respectively.

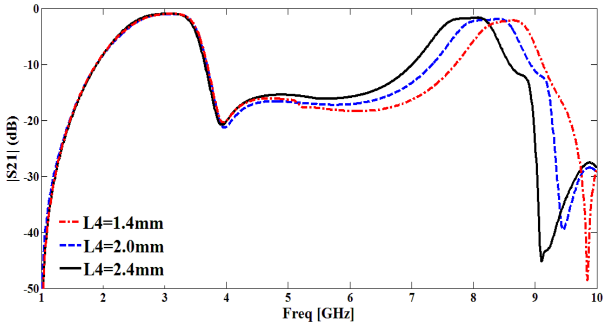

Fig. 8. The effect of variation in the finger width of the vertical arm of the cross-shaped lines (L_4 in Fig. 1 (b)) on insertion loss.

III. RESULTS AND DISCUSSIONS

The proposed DB-BPF with final design parameters, as shown in Fig. 9, was fabricated and tested. All measured and simulated results of the fabricated DB-BPF are shown in Fig. 10. The first passband of the measured results is centered at 3.07 GHz (2.61-3.53 GHz) with a low insertion loss of 1 dB, a return loss of 20 dB, and an FBW of 31%. The second passband of the measured results has a central frequency of 8.23 GHz (7.82-8.65 GHz) with a low insertion loss of 2 dB, a return loss of 16 dB and a FBW of 11%. The three TZs are located at 1.06, 3.91, and 9.74 GHz with attenuation levels of 40, 21, and 35 dB, respectively.

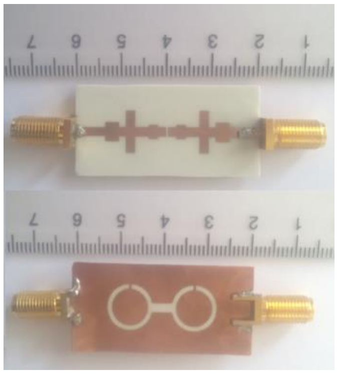

Fig. 9. Photograph of the fabricated DB-BPF prototype with OLDS and SICSLs.

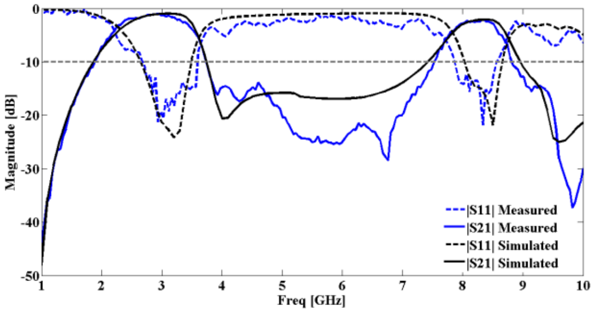

Fig. 10. Measured and simulated frequency responses of the fabricated DB-BPF using OLDS and SICSLs shown in Fig. 1.

The measured results show a good performance, which verifies the design concepts. As shown in the measured results, there exists a discrepancy between the measured data and the simulated results. The discrepancy is mostly due to a number of parameters such as the fabricated DB-BPF dimensions as well as the thickness and dielectric constant of the substrate, on which the DB-BPF is fabricated. In order to confirm the accurate return loss characteristics for the designed DB-BPF, it is recommended that the manufacturing and measurement process need to be performed carefully; besides, SMA soldering accuracy and substrate quality need to be taken into consideration [18]-[20]. In summary it can be said that a fine agreement between measured and simulated results is obtained in the frequency band of operation. Finally, a comparison between the proposed DB-BPF and other filter structures which have been published in literature and used here as references is presented in Table 2. From this table it can be concluded that the proposed DB-BPF has improved in-band and out-of-band performances as well as size miniaturization. In comparison with [3, 10, 11] and [13], the proposed DB-BPF has a smaller size, with respect to the operating frequency band and substrate relative dielectric constant. The presented DB-BPF has a wider bandwidth in comparison with the DB-BPFs in [1], [3] and [10]-[11]. The transmission loss performance of the presented DB-BPF is better than the ones in [1] and [10]. The in-band performance of the presented DB-BPF is better than the ones in [3], [5]. Moreover, the realization of the proposed DB-BPF is simpler than the ones in [1, 4, 5, 13].

IV. CONCLUSION

A compact novel DB-BPF with independently controllable frequencies and bandwidths are presented and discussed. The proposed DB-BPF consists of OLDS DGS and SICSLs. By inserting an OLDS slot in the ground plane and a pair of end-coupled uniform transmission lines with equal-length on the top, the first band can be produced. In addition, by introducing cross-shaped lines, a dual band function is achieved. In the proposed structure, in order to reject the unwanted harmonic pass bands, step impedance transmission lines are implemented along the ports of the filter. The DB-BPF exhibits low insertion loss over the desired passbands, and a sufficient isolation level at the frequency bands of interest.

Table 2: A comparison among the proposed DB-BPF using OLDS and SICSLs and the previous works

Ref.	f_0 (GHz)	IL (dB)	FBW (%)	ε_r/h (mm)	Size (mm^2)
[1]	2.37/3.43	2.85/2.94	7/1	3.5/0.508	137
[2]	2.58/6.79	0.54/1.18	44.7/18.3	2.2/0.508	132
[3]	1.58/5.2	1.6/1.42	4/3	2.2/0.508	470
[4]	3.32/5.32	0.62/0.91	28/20	3.55/0.508	218
[5]	2.34/3.46	0.84/1.2	26/21	3.38/0.508	258
[9]	3.88/5.35	0.38/1.03	12.4/8.6	2.54/0.54	276
[10]	3.34/3.93	1.8/1.9	5.2/7.7	4.5/0.8	232
[11]	2.3/4.1	0.65/1.0	11/8	10.8/1.27	339
[13]	1.03/2.85	0.65/0.45	94.8/35.8	10.8/1.27	306
This Work	3.07/8.23	0.8/1.8	31/11	3.55/0.8	480

f_0: Centre frequency of operation bands; IL: Insertion Loss over the whole pass-bands; ε_r: substrate relative dielectric constant; h: substrate thickness.

ACKNOWLEDGMENT

The authors thank the northwest antenna and microwave research laboratory (NAMRL) for their beneficial and professional help.

REFERENCES

[1] Y. Mo, K. Song, and Y. Fan, "Compact dual-band bandpass filter based on mixed electric and magnetic coupling," *Microwave and Optical Technology Letters*, vol. 56, pp. 1903-1907, August 2014.

[2] H. J. Xu and W. Wu, "Miniaturised dual-wideband bandpass filter using novel dual-band coupled-line sections," *Electronics Letters*, vol. 49, no. 18, pp. 1162-1163, August 2013.

[3] J. Li, Sh. Huang, and J. Z. Zhao, "Compact dual-wideband bandpass filter using a novel penta-mode resonator (PMR)," *IEEE Microw. Wireless Compon. Lett.*, vol. 24, no. 10, pp. 668-670, October 2010.

[4] J. Li, Sh. Huang, H. Wang, and J. Z. Zhao, "A novel compact dual-wideband bandpass filter with multi-mode resonators," *Progress In Electromagnetics Research Letters*, vol. 51, pp. 79-85, 2015.

[5] X. S. Zhang, B. Liu, Y. J. Zhao, J. K. Wang, and W. Chen, "Compact and high selectivity dual-band dual-mode microstrip BPF with five transmission zeros," *Microwave and Optical Technology Letters*, vol. 54, pp. 79-81, January 2012.

[6] X. Y. Zhang and Q. Xue, "Novel dual-mode dual-band filters using coplanar-waveguide-fed ring resonators," *IEEE Trans. Microw. Theory Tech.*, vol. 55, no. 10, pp. 2183-2190, October 2007.

[7] R. Zhang, L. Zhu, and S. Luo, "Dual-mode dual-band bandpass filter using a single slotted circular patch resonator," *IEEE Microw. Wireless Compon. Lett.*, vol. 22, no. 5, pp. 233-235, May 2012.

[8] J.-X. Chen, C. Shao, J. Shi, and Z.-H. Bao, "Multilayer independently controllable dual band bandpass filter using dual-mode slotted-patch resonator," *Electronics Letters*, vol. 49, no. 9, pp. 605-607, April 2013.

[9] Z. Yao, C. Wang, and N. Y. Kim, "A compact dual-mode dual-band bandpass filter using stepped impedance open-loop resonators and center-loaded resonators," *Microwave and Optical Technology Letters*, vol. 55, pp. 3000-3005, December 2013.

[10] H. Liu, L. Shen, L. Y. Shi, Y. Jiang, X. Guan, and T. Wu, "Dual-mode dual-band bandpass filters design using open-loop slotline resonators," *IET Microwave and Antenna Propagation*, vol. 7, no. 12, pp. 1027-1034, July 2011.

[11] S. Sun, "A dual-band bandpass filter using a single dual-mode ring resonator," *IEEE Microw. Wireless Compon. Lett.*, vol. 21, no. 6, pp. 298-300, June 2011.

[12] X. Y. Zhang, C. H. Chan, Q. Xue, and B. J. Hu, "Dual-band bandpass filter with controllable bandwidths using two coupling paths," *IEEE Microw. Wireless Compon. Lett.*, vol. 20, no. 11, pp. 616-618, November 2010.

[13] R. Zhang and L. Zhu, "Synthesis and design of dual-wideband bandpass filters with internally-coupled microstrip lines," *IET Microwave and Antenna Propagation*, vol. 8, no. 8, pp. 556-563, August 2014.

[14] Y. Wu, S. Zhou, W. Zhang, M. Liao, and Y. Liu, "Coupled-line dual-band bandpass filter with compact structure and wide stopband," *Electronics Letters*, vol. 50, no. 3, pp. 187-189, January 2014.

[15] S. Nouri, J. Nourinia, N. Valizade, B. Mohammadi, and A. Valizade, "Novel compact branch-line coupler using non-uniform folded transmission line and shunt step impedance stub with harmonics suppressions," *Applied Computational Electromagnetic Society (ACES) Journal*, vol. 31, no. 4, pp. 401-409, April 2016.

[16] B. Mohammadi, A. Valizade, J. Nourinia, and P. Rezaei, "Design of a compact dual-band-notch UWB bandpass filter based on wave cansellation method," *IET Microwave and Antenna Propagation*, vol. 9, no. 1, pp. 1-9, January 2015.

[17] B. Mohammadi, A. Valizade, P. Rezaei, and J. Nourinia, "A new design of compact dual band-notch UWB BPF based on coupled wave canceller inverted T-shaped stubs," *IET Microwave and Antenna Propagation*, vol. 9, no. 1, pp. 64-72, January 2015.

[18] B. Mohammadi, J. Nourinia, C. Ghobadi, and A. Valizade, "Design and analysis of the stub and radial-stub loaded resonator bandpass filter with cross-shaped coupled feed-lines for UWB applications," *Applied Computational Electromagnetic Society (ACES) Journal*, vol. 28, no. 9, pp. 851-857, September 2013.

[19] P. Beigi, J. Nourinia, B. Mohammadi, and A. Valizade, "Bandwidth enhancement of small square monopole antenna with dual band notch characteristics using U-shaped slot and butterfly shape parasitic element on backplane for UWB applications," *Applied Computational Electromagnetic Society (ACES) Journal*, vol. 30, no. 1, pp. 78-85, January 2015.

[20] S. Hoseyni, J. Nourinia, C. Ghobadi, S. Masumina, and B. Mohammadi, "A compact design and new structure of monopole antenna with dual band notch characteristic for UWB applications," *Applied Computational Electromagnetics Society Journal (ACES)*, vol. 31, no. 7, pp. 797-805, July 2016.

Ronak Khosravi received the B.Sc. degree in Electronic Engineering from Azad university of Tabriz in 2011 and M.Sc. degree in Telecommunications Engineering in Science and Research University of Urmia in 2014. Her interest include in wideband passive microwave devices and metamaterial antennas.

Changiz Ghobadi received his B.Sc. in Electrical Engineering-Electronics and M.Sc. degrees in Electrical Engineering from Isfahan University of Technology, Isfahan, Iran and Ph.D. degree in Electrical-Telecommunication from University of Bath, Bath, UK in 1998. From 1998 he was an Assistant Professor and now he is a Professor in the Department of Electrical Engineering of Urmia University, Urmia, Iran. His primary research interests are in antenna design, radar and adaptive filters.

Javad Nourinia received his B.Sc. in Electrical and Electronic Engineering from Shiraz University, M.Sc. degree in Electrical and Telecommunication Engineering from Iran University of Science and Technology, and Ph.D. degree in Electrical and Telecommunication from University of Science and Technology, Tehran Iran in 2000. From 2000 he was an Assistant Professor and now he is a Professor in the Department of Electrical Engineering of Urmia University, Urmia, Iran. His primary research interests are in antenna design, numerical methods in electromagnetic, microwave circuits.

Bahman Mohammadi received the B.Sc. degree in Electrical Engineering - Telecommunication from Tabriz University, Tabriz, Iran, in 2011 and M.Sc. degree in Electrical Engineering-Microwave, Antenna and Propagation from Urmia University, Urmia, Iran, in 2013 (1 honor or award). He is with Northwest Antenna and Microwave Research Laboratory (NAMRL) as a Microwave Engineering since March 2011. He has authored and co-authored more than 32 journal and conference papers. His research interests include Floquet Analysis and Periodic Structures, Microwave Components, Optimization Methods, MIMO and Measurements.

Dual High-Selectivity Band-Notched Ultra-Wideband Filter with Improved Out-of-Band Rejection

Ying Jiang Guo [1], Xiao Hong Tang [1], and Kai Da Xu [2,3]

[1] EHF Key Lab of Science, University of Electronic Science and Technology of China, Chengdu, 611731, China

[2] Department of Electronic Science, Xiamen University, Xiamen, 361005, China

[3] Shenzhen Research Institute of Xiamen University, Shenzhen 518057, China
kaidaxu@xmu.edu.cn

Abstract **─** A novel microstrip ultra-wideband (UWB) filter with dual notched bands is presented. By placing a simple dual-mode resonator having two symmetrical outer high-impedance lines beside the UWB filter, two controllable rejection bands are created, each of which features two resonant modes and high frequency selectivity. Defected ground structure techniques (DGS) is applied to realize wide out-of-band attenuation. To explain band-notched operating mechanism, the parametric studies and equivalent circuit of the proposed structure are presented. The experimental results agree well with the predicted results declaring the advantages of the proposed structure with high-selectivity wide-bandwidth notched bands and improved out-of-band rejection.

Index Terms **─** Band-notched filter, high frequency selectivity, improved out-of-band rejection, ultra-wideband filter.

I. INTRODUCTION

Research on design and development of ultra-wideband (UWB) bandpass filters (BPF) have attracted great attention as the release of unlicensed UWB spectrum (3.1–10.6 GHz) by the Federal Communications Commission (FCC) for hand held devices in indoor environment [1]. There have existed various structures for UWB generation [2-14]. One common method for the design of an UWB-BPF is the use of multiple-mode resonators (MMRs), which possesses the flexibility of placing resonant modes at frequencies of interest in the passband [2-5]. Other methods were also presented to achieve UWB response, such as back-to-back broadside coupled structure [6], cascading lowpass and highpass filter [7], etc. However, many critical issues still puzzle researchers. One such challenge is to eliminate the frequency interference between UWB system and other wireless systems which have already occupied some operating bands of UWB system, especially like IEEE 802.11a (5.15 ~ 5.35 GHz & 5.725 ~ 5.825 GHz) and X-band military radar. Moreover, to achieve higher data rates, many systems including LTE Carrier Aggregation manage to increase their spectrum bandwidths, which, in turn, requires wider rejection band for the UWB design. Therefore, it is significantly necessary to introduce more than one wide-bandwidth notched-band responses into UWB filters.

Several methods to introduce notched bands in UWB filters were reported, such as etching slots on the ground [8], [9], embedding spurlines or stubs on the transmission line [10-12], and loading a resonator beside the original structure [13-15]. However, most structures in these filters can only generate one notched frequency band, which means that more complex structures are required when it comes to multiple notched bands, i.e., more than one resonators/stubs, MMRs, etc. Although some MMRs have been adopted for more than one band-notched generation [16-18], they show narrow rejection bandwidth and unsatisfactory frequency selectivity.

In this paper, by using only one simple dual-mode resonator and two high-impedance lines, a novel dual wideband band-notched UWB filter has been realized. With the help of two symmetrical outer high-impedance lines beside the microstrip feed line, the proposed resonators can produce two stopbands with higher rejection level and better frequency selectivity than that of only one stopband using the same resonator without outer lines. Moreover, the dumbbell-shape DGS helps to realize wide out-of-band rejection band. In Section II, the proposed resonator and its design evolution are demonstrated. Comparison between the proposed resonator and the conventional ones is made, showing clearly the advantage of the proposed structure. Parametric analysis and mathematical explanation provide guidelines to facilitate design process. In Section III, a UWB filter is designed and then the proposed resonator is loaded on this UWB filter for dual high-selectivity notched bands generation. Finally, a short

Submitted On: April 9, 2016
Accepted On: July 12, 2016

conclusion is given in Section IV.

II. BAND-NOTCHED RESONATOR ANALYSIS

The conventional resonator and modified structure as shown in Fig. 1 are used to evoke notched bands for the UWB filters. The conventional resonator is a folded half-wavelength resonator with a grounding via in the center, while the modified structure is developed with two additional symmetrical high-impedance outer lines connecting the conventional resonator to feed line. For size reduction, the outer lines are meandered. Figure 1 (c) illustrates the corresponding circuit model of Fig. 1 (b). The outer high-impedance lines can be equivalent to a series inductor-capacitor tank (L_2 and C_2), and the broad side coupling between two open stubs in Fig. 1 (b) is modeled as a capacitor C_1. Additionally, the via hole acts as an inductor L_1. The physical dimensions of the proposed resonator can be determined by using this model.

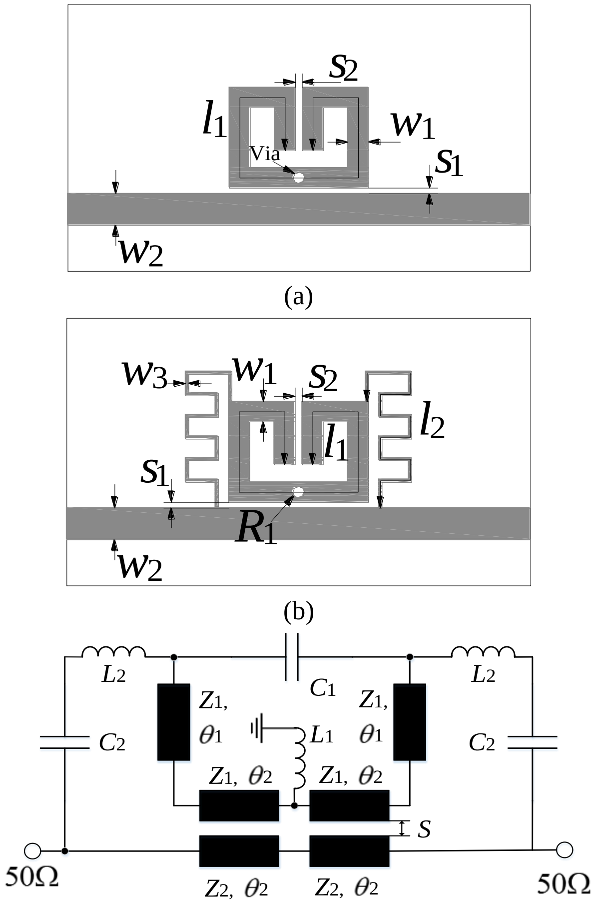

(a)

(b)

(c)

Fig. 1. (a) Layout of the conventional resonator, (b) the proposed structure, and (c) corresponding circuit model.

To analyze the characteristics of this proposed resonator, the resonators depicted in Fig. 1 are modeled with the help of full-wave electromagnetic simulation. All the structures in this paper are designed on a RT/Duorid 4350 substrate with a dielectric constant 3.48, thickness of 0.508 mm, and dielectric loss tangent value of 0.004. Figure 2 shows the simulated S_{21} and S_{11} magnitudes of the three resonators types under weak coupling which have the same physical dimensions. Dual-resonance characteristics are obtained for Fig. 1 (a), while the one without via has only one resonant mode. This feature can be applied to create a wideband notched band. The resonant frequency of the conventional resonator f_r can be approximately calculated by:

$$f_r = \frac{c}{\lambda_g \sqrt{\varepsilon_{eff}}} \approx \frac{c}{2l_1\sqrt{(\varepsilon_r + 1)/2}}, \qquad (1)$$

where λ_g denotes the guided wavelength, c is the velocity of light in free space, and ε_{eff} denotes the effective dielectric constant of the substrate. Once two symmetrical outer high-impedance lines are added as shown in Fig. 1 (b), the center frequency of one notched band is almost the same with that of Fig. 1 (a), and interestingly an extra stopband is generated. Compared to the conventional resonator, both of these two notched bands exhibit higher rejection level and satisfactory frequency selectivity. Additionally, multiple reflection zeros are located at each side of the stopbands enhancing the passband impedance matching.

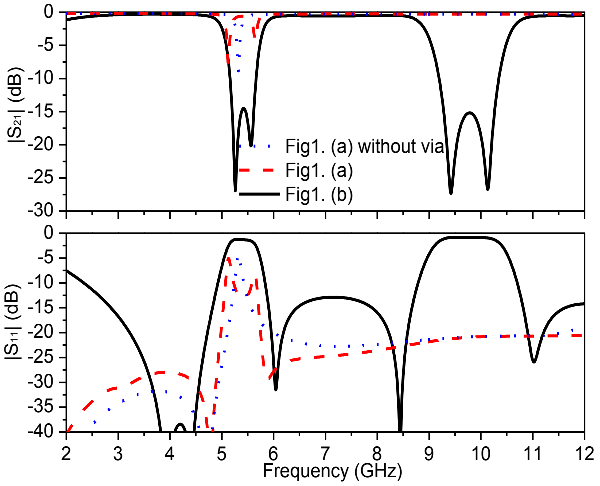

Fig. 2. Simulated results of the three resonators types ($l_1 = 16.4$, $l_2 = 12.2$, $w_1 = 0.7$, $w_2 = 1.1$, $w_3 = 0.1$, $S_1 = 0.3$, $S_2 = 0.2$, and the radius of via R_1=0.2, all in mm).

The center frequency of the extra stopband f_{r2} is primarily determined by the outer high-impedance lines equivalent to a series L_2-C_2 tank, which is approximately calculated by:

$$f_{r2} \approx \frac{1}{2\pi\sqrt{L_2 C_2}}. \tag{2}$$

Here, L_2 and C_2 in this case equals to 3.48 nH and 0.08 pF, respectively, and the corresponding calculated f_{r2} is around 9.6 GHz, where the value is in order to make good agreement with the simulated center frequency of the higher stopband shown in Fig. 2. Due to the inductance much more than capacitance of the high-impedance lines equivalent circuit, adjusting the inductance L_2 is observed as shown in Fig. 3. When L_2 increases from 3.28 to 3.68 nH, the resonant frequency for the higher stopband will decrease gradually but the lower stopband almost keeps fixed.

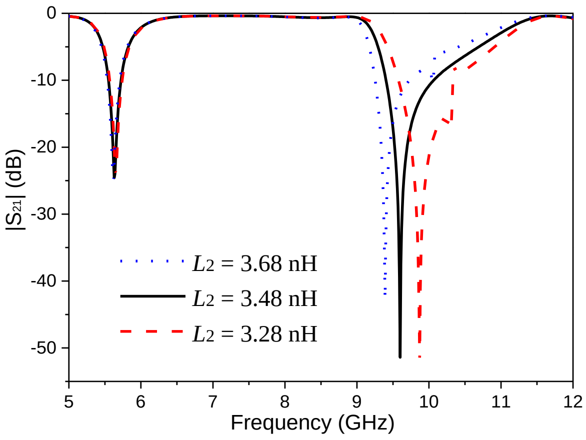

Fig. 3. Simulated $|S_{21}|$ variations with different L_2.

Furthermore, as the three important physical parameters (l_1, S_1, and S_2) have significant influence on the proposed resonator's frequency response, the proposed resonator having the same dimensions with discussed above are modeled and studied. Figure 4 demonstrates the predicted magnitude of S_{21} against frequency with different l_1, S_1, and S_2. As observed in Fig. 4 (a), the center frequencies of two stopbands both increase as l_1 changes from 16.9 to 15.9 mm, showing the length of the folded half-wavelength resonator l_1 affects both two stopbands. Obviously, l_1 is mainly determined by Equation (1) when the substrate material is chosen. When the gap between the resonator and feed line S_1 varies from 0.2 to 1.2 mm as seen in Fig. 4 (b), the center frequencies of the higher stopband experience an obvious drop, while the lower-frequency stopband changes slightly. Thus, the center frequencies of the two stopbands can be designed by tuning l_1, l_2, and S_1. In addition, the coupling gap S_2 can be used to adjust the bandwidth of the two stopbands (see Fig. 4 (c)). These graphs can be applied to simplify the proposed resonator design.

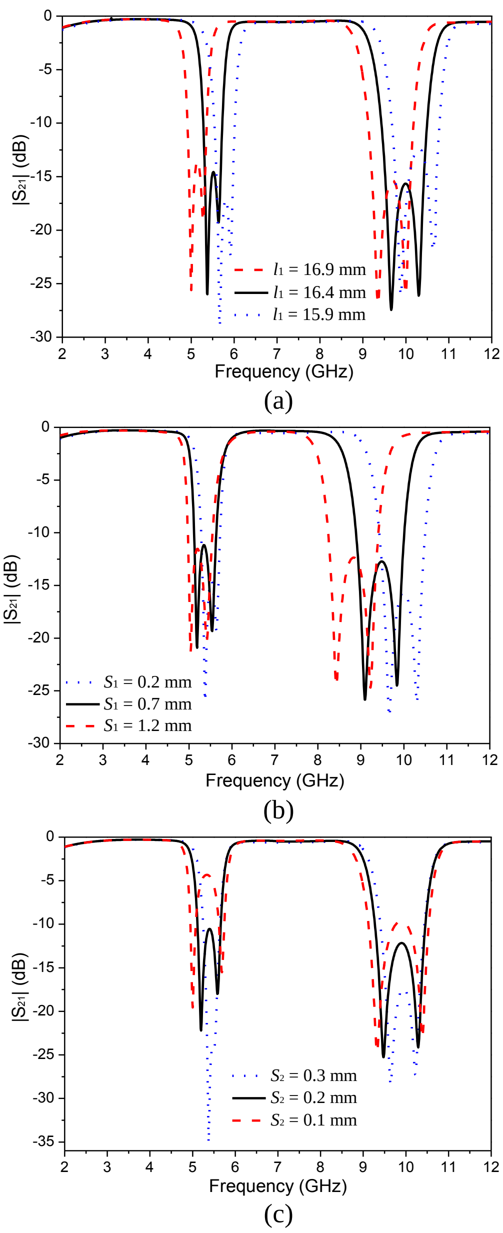

(a)

(b)

(c)

Fig. 4. Simulated $|S_{21}|$ variations with different: (a) l_1, (b) S_1, and (c) S_2.

III. DESIGN OF UWB FILTER WITH NOTCHED BANDS

A. UWB filter

Figure 5 depicts the layout and physical dimensions of the proposed basic UWB filter. The UWB response is developed based on the MMR which consists of a stepped-impedance resonator (SIR) loaded with one short-circuited stub and two symmetrical open-circuited folded stubs. Two interdigital coupled line sections are directly coupled to the two sides of the SIR. On the bottom layer of the filter, two tapered dumbbell-shaped

DGS units are designed to suppress the harmonic passband, since they can produce the transmission zeroes in the high frequency out-of-band range [19].

The frequency characteristics of the proposed MMR is presented in Fig. 6. Compared with previous MMR without DGS, open- and short-circuited stub, the proposed MMR can produce more resonant modes in UWB band improving the in-band impedance matching, and higher skirt selectivity is also achieved because the transmission zeros can be positioned close to the edge of UWB band.

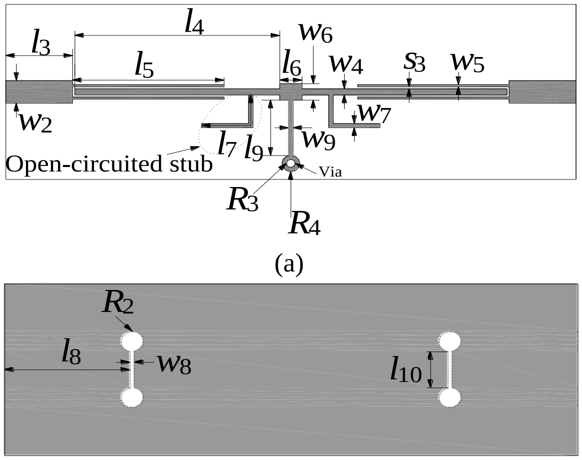

(a)

(b)

Fig. 5. Configuration of the basic UWB filter: (a) top layer and (b) bottom layer (w_2 = 1.1, w_4 = 0.3, w_5 = 0.1, w_7 = 0.2, w_8 = 0.2, w_9 =0.2, l_3 = 3, l_4 = 9.2, l_5 = 6.8, l_6 = 1, l_7 = 3.7, l_8 = 5.6, l_9 = 2.7, l_{10} = 1.8, w_6 = 0.8, R_1=0.2, and R_2 = 0.5, all in mm).

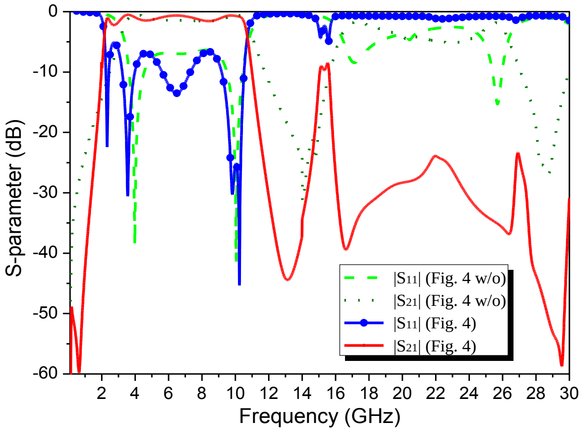

Fig. 6. Comparison between the basic UWB filter (Fig. 4) and its corresponding structure w/o (w/o: without DGS, open- and short-circuited stubs).

Figure 7 shows the simulated S_{21}-magnitudes of the proposed UWB structure under tight coupling case (interdigital coupled lines, S_3 = 0.1 mm) and weak coupling case (one coupled line, S_3 = 0.3 mm), respectively, where the other physical dimensions are the same. Four resonant modes are evoked in UWB band due to the proposed structure. Moreover, four resonant modes all increase as l_4 decreases, showing they are all affected by the length of the high-impedance line of SIR (see Fig. 8 (a)). Interestingly, only the first resonant mode are sensitive to l_9 (see Fig. 8 (b)), while as l_7 drops only the third and fourth resonant frequencies increase (see Fig. 8 (c)). It means that lengths of the short- and open-circuited stubs (i.e., l_9 and l_7) can be used to independently adjust the low- and high-frequency edge of the UWB band, respectively. Therefore, by carefully tuning the physical dimensions of the proposed resonator, the four resonant modes can be allocated properly to create the UWB response.

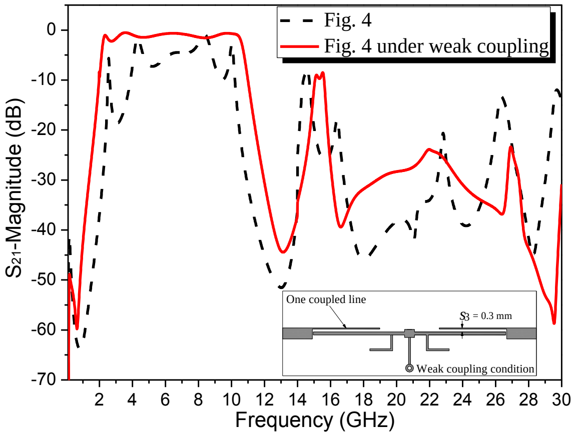

Fig. 7. Simulated S_{21}-magnitudes of the basic UWB filter and the same structure under weak coupling.

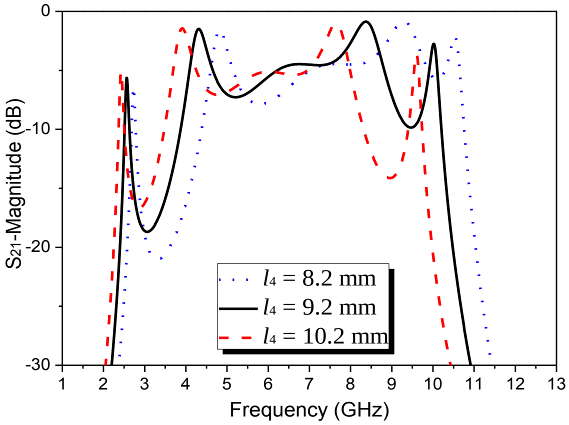

(a)

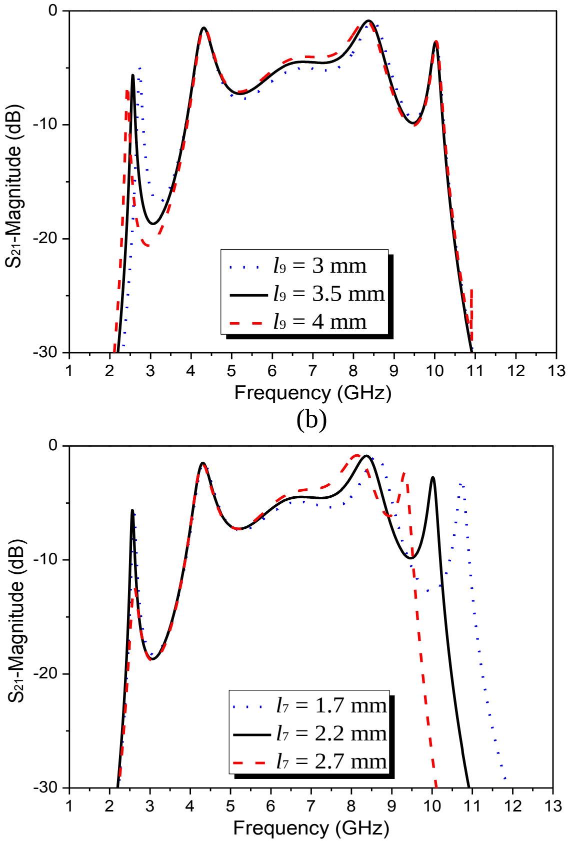

(b)

(c)

Fig. 8. Simulated S_{21} variations of the proposed MMR structure under weak coupling case with: (a) l_4, (b) l_9, and (c) l_7.

B. UWB filter loaded with the proposed resonator

In order to obtain notched band UWB response, the proposed band-notched resonator is added to the proposed basic UWB filter, as depicted in Fig. 9. The physical parameters of the loading notch resonator and basic UWB filter are assumed the same with those mentioned above. The whole structure is fabricated and its photograph is displayed in Fig. 10.

Figure 11 illustrates the simulated and measured S_{21}- and S_{11}-magnitudes as well as the group delays for the proposed band-notched UWB filter. They are found in good agreement with each other. The 3-dB passband covers the range of approximately 2.5–10.8 GHz (relative bandwidth: 124.8%) with the in-band measured insertion loss less than 2 dB except for the dual notched band (3-dB bandwidth: 4.95-5.85 GHz and 8.81-10.05 GHz). Each notched band has two resonant modes achieving wider bandwidth, while high frequency selectivity is also realized due to the intrinsic features of the proposed resonator. The measured upper-stopband is dramatically extended up to 30 GHz with an insertion loss larger than 20 dB due to the introduction of the out-of-band zeros caused by DGS units. In addition, the group delay varies between 0.2–1.4 ns within the UWB passband showing a good linearity, and significant drops are observed in the two stopbands.

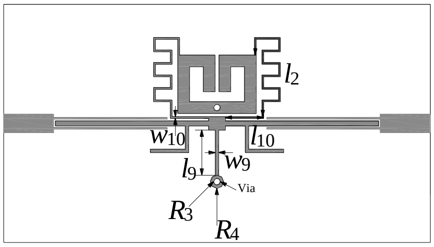

Fig. 9. Configuration of the proposed notched-band UWB filter.

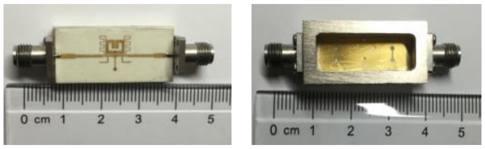

(a) (b)

Fig. 10. Photograph of the fabricated dual band-notched UWB filter: (a) top view and (b) bottom view.

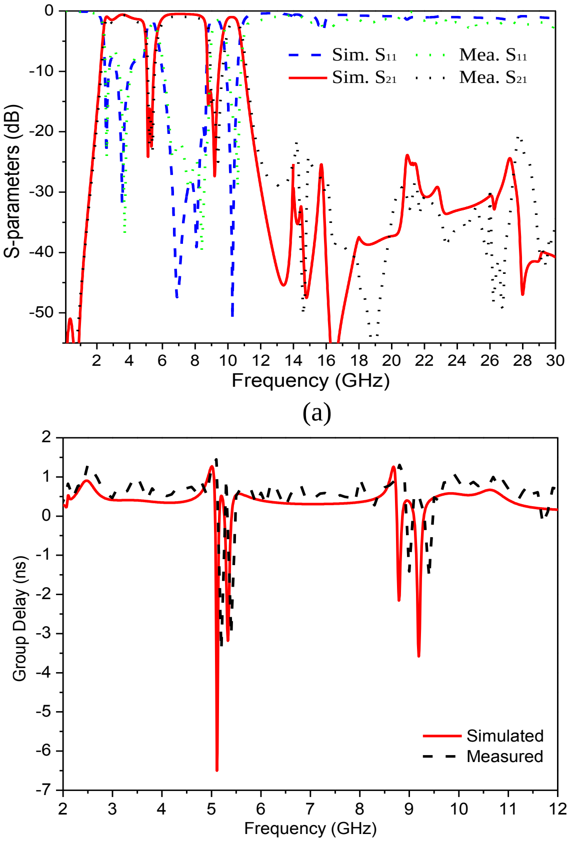

(a)

(b)

Fig. 11. Simulated and measured results of the proposed filter: (a) S-parameters and (b) group delays.

IV. CONCLUSION

To obtain dual notched bands with high frequency selectivity and wide bandwidth, a simple resonator with two symmetrical outer high-impedance lines connecting to the basic UWB filter has been proposed. Wide out-of-band attenuation is achieved by adopting DGS. Due to its simple structure and excellent performance, the proposed filters are expected to be good candidates for use in various UWB systems.

ACKNOWLEDGMENT

This work was supported in part by the Natural Science Foundation of Fujian Province of China (No. 2016J05164), and Guangdong Natural Science Foundation (No. 2016A030310375).

REFERENCES

[1] Federal Communications Commission, "First report and order in the matter of revision of part 15 of the Commission's Rules Regarding Ultra-Wideband Transmission Systems," ET-Docket 98-153, Apr. 22, 2002.

[2] L. Zhu, S. Sun, and W. Menzel, "Ultra-wideband (UWB) bandpass filters using multiple-mode resonator," *IEEE Microwave Wireless Comp. Lett.*, vol. 15, no. 11, pp. 796-798, 2005.

[3] R. Li and L. Zhu, "Compact UWB bandpass filter using stub-loaded multiple-mode resonator," *IEEE Microwave Wireless Comp. Lett.*, vol. 7, no. 1, pp. 40-42, 2007.

[4] Z. Zhang and F. Xiao, "An UWB bandpass filter based on a novel type of multi-mode resonator," *IEEE Microwave Wireless Comp. Lett.*, vol. 22, no. 10, pp. 506-508, 2012.

[5] K. D. Xu, Y. H. Zhang, J. L. Li, W. T. Joines, and Q. H. Liu, "Compact ultra-wideband bandpass filter using quad-T-stub-loaded ring structure," *Microwave Opt. Technol. Lett.*, vol. 56, no. 9, pp. 1988-1991, 2014.

[6] H. Wang and L. Zhu, "Ultra-wideband bandpass filter using back-to-back microstrip-to-CPW transition structure," *Electron. Lett.*, vol. 41, no. 24, pp. 1337-1338, 2005.

[7] C. W. Tang and M.-G. Chen, "A microstrip ultra-wideband bandpass filter with cascaded broadband bandpass and bandstop filters," *IEEE Trans. Microwave Theory Tech.*, vol. 55, no. 11, pp. 2412-2418, 2007.

[8] J. Q. Huang, Q. X. Chu, and C. Y. Liu, "Compact UWB filter based on surface-coupled structure with dual notched bands," *Progress in Electromagnetics Research*, vol. 106, pp. 311-319, 2010.

[9] S. G. Mao, Y. Z. Chueh, C. H. Chen, and M. C. Hsieh, "Compact ultra-wideband conductor-backed coplanar waveguide bandpass filter with a dual band-notched response," *IEEE Microwave Wireless Comp. Lett.*, vol. 19, no. 3, pp. 149-151, 2009.

[10] F. Wei, L. Chen, Q. Y. Wu, X. W. Shi, and C. J. Gao, "Compact UWB bandpass filter with narrow notch-band and wide stop-band," *Journal of Electromagnetic Waves & Applications*, vol. 24, no. 7 pp. 911-920, 2010.

[11] C.-Y. Liu, T. Jiang, and Y.-S. Li, "A novel UWB filter with notch-band characteristic using radial-UIR/SIR loaded stub resonators," *Journal of Electromagnetic Waves & Applications*, vol. 25, no. 2, pp. 233-245 2011.

[12] Y. H. Chun, H. Shaman, and J. S. Hong, "Switchable embedded notch structure for UWB bandpass filter," *IEEE Microwave Wireless Comp. Lett.*, vol. 18.no. 9, pp. 590-592, 2008.

[13] R. Ghatak, P. Sarkar, R. K. Mishra, and D. R. Poddar, "A compact UWB bandpass filter with embedded SIR as band notch structure," *IEEE Microwave Wireless Comp. Lett.*, vol. 21, no. 5, pp. 261-263, 2011.

[14] J. Xu, W. Wu, W. Kang, and C. Miao, "Compact UWB bandpass filter with a notched band using radial stub loaded resonator," *IEEE Microwave Wireless Comp. Lett.*, vol. 22, no. 7, pp. 351-353, 2012.

[15] M. J. Gao, L. S. Wu, and J. F. Mao, "Compact notched ultra-wideband bandpass filter with improved out-of-band performance using quasi electromagnetic bandgap structure," *Progress in Electromagnetics Research*, vol. 125, no. 17, pp. 137-150, 2012.

[16] F. Wei, W. T. Li, X. W. Shi, and Q. L. Huang, "Compact UWB bandpass filter with triple-notched bands using triple-mode stepped impedance resonator," *IEEE Microwave Wireless Comp. Lett.*, vol. 22, no. 10, pp. 512-514, 2012.

[17] F. Wei, Q. Y. Wu, X. W. Shi, and L. Chen, "Compact UWB bandpass filter with dual notched bands based on SCRLH resonator," *IEEE Microwave Wireless Comp. Lett.*, vol. 21, no. 1, pp. 28-30, 2011.

[18] Y. Li, W. Li, C. Liu, and Q. Ye, "A compact UWB band-pass filter with ultra-narrow tri-notch-band characteristic," *Applied Computational Electromagnetics Society Journal*, vol. 29, no. 2, pp. 170-177, 2014.

[19] G. M. Yang, R. Jin, C. Vittoria, V. G. Harris, and N. X. Sun, "Small ultra-wideband (UWB) bandpass filter with notched band," *IEEE Microwave Wireless Comp. Lett.*, vol. 18, no. 3, pp. 176-178, 2008.

Ying Jiang Guo received the B.E. degree in Electronic Engineering from the Sichuan University (SCU), Chengdu, China in 2008, and received M.E. in Electromagnetic Field and Microwave Technology from the University of Electronic Science and Technology of China (UESTC), Chengdu, China in 2011, where he is currently working toward the Ph.D. degree in Electromagnetic Field and Microwave Technology. From 2011 to 2013, he was with the Chengdu Research Institute of Huawei Technology Ltd., where he was involved in the pre-research of ultra-wideband power amplifier, high frequency clock for AD and 5G communication prototype design. From 2013 to 2014, he was with the Sichuan Normal University, where he was a Lecturer. He has filed/granted a number of China patents in microwave circuit and internet of vehicle. His research interests include RF/microwave/mm-wave circuits design, antennas design, and monolithic-microwave integrated circuit applications.

Xiao Hong Tang was born in Chongqing, China, in 1962. He received the M.S. and Ph.D. degrees in Electromagnetism and Microwave Technology from the University of Electronic Science and Technology of China (UESTC), Chengdu, China, in 1983 and 1990, respectively. In 1990, he joined the School of Electronic Engineering, UESTC, as an Associate Professor, and became a Professor in 1998. He has authored or co-authored over 80 technical papers. His current research interests are microwave and millimeter-wave circuits and systems, microwave integrated circuits, and computational electromagnetism.

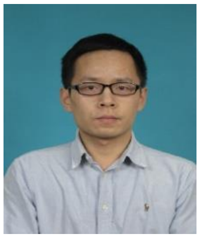

Kai Da Xu received the B.S. and Ph.D. degrees in Electromagnetic Field and Microwave Technology from University of Electronic Science and Technology of China (UESTC), Chengdu, China, in 2009 and 2015, respectively. He is now an Assistant Professor with Institute of Electromagnetics and Acoustics, and Department of Electronic Science, Xiamen University, Xiamen, China.

From September 2012 to August 2014, he was a Visiting Researcher in the Department of Electrical and Computer Engineering, Duke University, Durham, NC, under the financial support from the China Scholarship Council (CSC). He received the UESTC Outstanding Graduate Awards in 2009 and 2015. He was the recipient of National Graduate Student Scholarship in 2012, 2013, and 2014 from Ministry of Education, China. He has authored and co-authored over 40 papers in peer-reviewed journals and conference proceedings. Since 2014, he has served as a Reviewer for some journals including IEEE Transactions on Microwave Theory and Techniques, IEEE Transactions on Electron Devices, IEEE Transactions on Computer-Aided Design of Integrated Circuits and Systems, IEEE Transactions on Applied Superconductivity, International Journal of RF and Microwave Computer-Aided Engineering, ACES Journal, PIER, JEMWA and Journal of Engineering. His research interests include RF/microwave and mm-wave circuits, antennas, and nanoscale memristors.

Design of a Compact Wideband Filtering Power Divider with Improved Isolation

Yijing Deng [1], Yixuan He [2], and Jianpeng Wang [1]

[1] Nanjing University of Science and Technology, Nanjing 210094, China
lillian-deng.y.j@outlook.com, eejpwang@gmail.com

[2] School of Information and Electronics
Beijing Institute of Technology, China
xuandd1995@126.com

Abstract **─** A novel design of wideband filtering power divider (FPD) with high selectivity, good isolation and widen upper stopband is presented in this paper. A new topology is proposed by adding an isolation resistor between two tri-mode resonators to guarantee the isolation. Besides, owing to the intrinsic characteristics of tri-mode resonators and coupled lines with one of them terminated by an open-circuited stub, four transmission zeros (*TZ*s) can be generated outside the operating band to improve the signal selectivity. For demonstration, a FPD operating at 2.35 GHz with 3-dB fractional bandwidth of 25.6% is designed, fabricated and measured. The measured isolation is better than 15.5 dB and the upper stopband is extended to 7.6 GHz (3.23f_0) with a rejection level of 20 dB.

Index Terms **─** Filtering power divider, synthesis design, tri-mode resonator, wide bandwidth.

I. INTRODUCTION

Nowadays, power dividers (PDs) and bandpass filters (BPFs) are frequently used in various microwave and millimeter-wave systems for power splitting/ combining and signal selection. These two components typically occupy an excessive area apiece, especially at low gigahertz frequency region. In order to obtain dual functions simultaneously with a relatively small area, it is beneficial to integrate the PD and BPF together.

Over the past few years, much effort has been focused on improving the performance of FPD based on compact size, high selectivity, good isolation, widen upper stopband, and etc. Embedded dual-mode resonator [1] and inductors with low impedance transmission lines [2] are introduced for compact size. Subsequently, short-circuited stub along with coupled lines [3] and open-ended transmission line [4] are utilized for high passband selectivity. Moreover, the isolation performance is a main consideration in FPD design. Isolation resistor added between two filters [5], net-type resonator [6] and distributed isolation network (DINW) [7] are proposed to provide improved isolation performance. Finally, widen upper stopband is achieved by replacing quarter-wavelength section with stepped impedance interdigital coupling element [8] and by creating TZ at the second harmonic frequency [9]. Although these studies presented satisfactory bandpass responses and power splitting properties, few of them have demonstrated wide stopband along with good isolation performance within the entire passband simultaneously.

The primary motivation of this paper is to design a wideband FPD with compact size, high selectivity, widen upper stopband and improved isolation. To achieve good isolation within not only the entire passband but also frequency region out of the operating band, a novel topology is proposed by adding an isolation resistor between the high-impedance stubs of two tri-mode resonators. Theoretical analysis is described to design the proposed FPD with prescribed performance. For demonstration, the proposed wideband FPD is designed, fabricated, and measured. Ultimately, both simulated and measured results validate the theoretical ones well.

II. CIRCUIT DESIGN OF THE PROPOSED FPD

Figure 1 shows the configuration of the proposed FPD. Owing to the intrinsic characteristic of tri-mode resonator and coupled lines with one of them terminated by an open-circuited stub, four transmission zeros (TZs) are generated to achieve high passband selectivity as well as deep stopband rejection. Besides, by adding an isolation resistor between high-impedance stubs of two tri-mode resonators, a novel topology is proposed for isolation improvement.

Submitted On: May 18, 2016
Accepted On: July 17, 2016

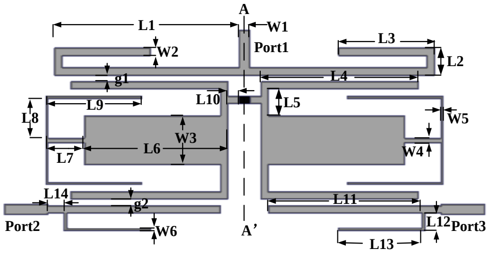

Fig. 1. Configuration of the proposed FPD.

A. Tri-mode resonator

When a signal is launched into the T-junction at Port 1, it will be equally split and delivered to the tri-mode resonators via coupling, thus engendering wideband filtering response as well as sharp roll-off skirt. The proposed tri-mode resonator shown in Fig. 2 (a) is symmetrical and can be analyzed by using odd- and even-mode methods. Under each resonance conditions, the input admittance can be derived as:

$$Y_{\text{int}\,rio} = Y_1/(j\tan\theta_1) = 0, \tag{1}$$

$$Y_{\text{int}\,rie} = Y_1\frac{Y_{\text{int}\,ri2} + jY_1\tan\theta_1}{Y_1 + jY_{\text{int}\,ri2}\tan\theta_1} = 0, \tag{2}$$

where the input admittance Y_{intri2} of stepped-impedance resonator in Fig. 2 (c) yields:

$$Y_{\text{int}\,ri2} = jY_2\frac{Y_2\tan\theta_2 + Y_3\tan\theta_3}{2Y_2 - 2Y_3\tan\theta_2\tan\theta_3}. \tag{3}$$

To simplify the analysis, here we set $\theta_1=\theta_2=\theta_3$, $2Y_3=Y_1$ and $M=Y_2/Y_3$, then the resonance conditions can be written as:

$$1/j\tan\theta_1 = 0, \tag{4}$$

$$M^2 + 5M - 4\tan^2\theta_1 = 0. \tag{5}$$

The first three resonant modes of the tri-mode resonator are expected as even-/odd-/even-modes with their resonant frequencies defined as f_o, f_{e1} and f_{e2} respectively. Specifically, with geometrical parameters listed in Table 1, the frequency response properties of the resonator are provided in Fig. 3. As shown in Fig. 3, two even-mode resonant frequencies can be observed at both sides of the odd-mode one under weak coupling situation ($g_1=g_2=0.5$ mm), while under strong coupling ($g_1=g_2=0.15$ mm), a wideband filtering response with a fractional bandwidth of 25.6% can be achieved, which verify the feasibility of proposed tri-mode resonator in wideband performance design.

Table 1: Dimension values of the proposed FPD (unit: mm)

W1	W2	W3	W4	W5	W6	L1	L2
1.11	0.5	7	0.2	0.1	0.1	22	2.5
L3	L4	L5	L6	L7	L8	L9	L10
15.6	15.7	2	19.8	4	4.5	8.8	0.9
L11	L12	L13	L14	g1	g2		
22	1.5	9.2	2	0.14	0.16		

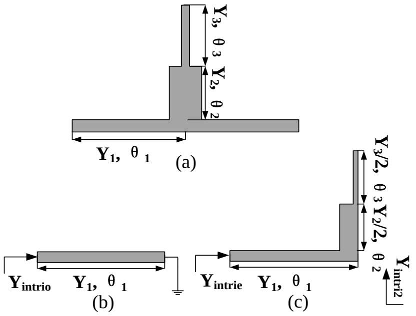

Fig. 2. Configuration of the proposed tri-mode resonator: (a) proposed tri-mode resonator, (b) odd-mode excitation, and (c) even-mode excitation.

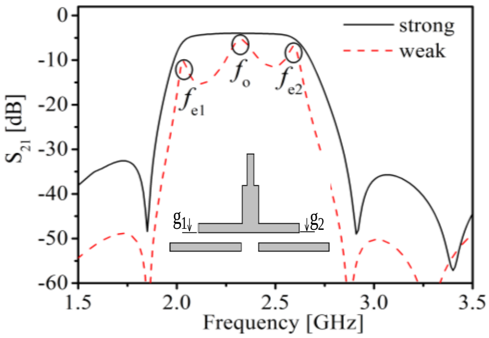

Fig. 3. Response performances under weak and strong coupling schemes.

B. Operating frequency, bandwidth and isolation

Due to the symmetrical topology of proposed FPD, it can be bisected into two identical parts along its symmetrical plane AA' and only half a bisection is considered which is classified into five distinctive sections as illustrated in Fig. 4, so as to simplify our analysis.

According to the power divider's design principle, Port 2 needs to be matched to 50 Ω. Since tuning the coupling lengths of resonator will change the resonance frequency, here the impedance matching is mainly realized by altering Z_r. Figure 5 shows the return loss at Port 2 versus various values of Z_r, including when $Z_r=0$. Therefore, for a better impedance matching, here we choose Z_r as 65 Ω.

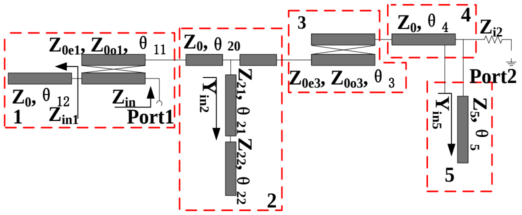

Fig. 4. Half a bisection of equivalent circuit of the proposed FPD in five sections.

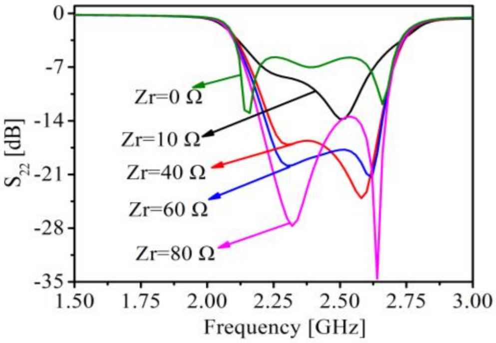

Fig. 5. S_{22} at Port 2 versus various values of Z_r.

Assuming that the electrical lengths of the coupled line section under even- and odd-modes are equal, the transmission matrix of each section can be extracted as:

$$[ABCD_1]= \begin{bmatrix} \dfrac{-d_1(a_1Z_{in1}+b_1)}{a_1e_1Z_{in1}-c_1d_1} & \dfrac{-a_1(a_1Z_{in1}+b_1)}{a_1e_1Z_{in1}-c_1d_1} \\ \dfrac{e_1^{\,2}Z_{in1}-d_1^{\,2}Z_{in1}-a_1d_1}{a_1e_1Z_{in1}-c_1d_1} & \dfrac{-(a_1d_1Z_{in1}+a_1^{\,2}-c_1e_1)}{a_1e_1Z_{in1}-c_1d_1} \end{bmatrix}, \tag{6}$$

$$[ABCD_2]=\begin{bmatrix} \cos\theta_{20} & jZ_0\sin\theta_{20} \\ jY_0\sin\theta_{20} & \cos\theta_{20} \end{bmatrix}\times\begin{bmatrix} 1 & 0 \\ Y_{in2} & 1 \end{bmatrix} \times\begin{bmatrix} \cos\theta_{20} & jZ_0\sin\theta_{20} \\ jY_0\sin\theta_{20} & \cos\theta_{20} \end{bmatrix}, \tag{7}$$

$$[ABCD_3]=\begin{bmatrix} -a_3d_3/c_3e_3 & -a_3^{\,2}/e_3 \\ -d_3^{\,2}/e_3+e_3 & -a_3d_3/e_3 \end{bmatrix}, \tag{8}$$

$$[ABCD_4]=\begin{bmatrix} \cos\theta_4 & jZ_0\sin\theta_4 \\ j\sin\theta_4/Z_0 & \cos\theta_4 \end{bmatrix}, \tag{9}$$

$$[ABCD_5]=\begin{bmatrix} 1 & 0 \\ \text{-}\,jZ_7\cot\theta_7 & 1 \end{bmatrix}, \tag{10}$$

where $a_{1/3}=\cos\theta_{11/3}$, $b_1=j(Z_{0e1}+Z_{0o1})\sin\theta_{11/2}$, $c_{1/3}=j(Z_{0e1/3}-Z_{0o1/3})\sin\theta_{11/3}/2$, $d_{1/3}=j(1/Z_{0e1/3}+1/Z_{0o1/3})\sin\theta_{11/3}/2$, $e_{1/3}=j(1/Z_{0e1/3}-1/Z_{0o1/3})\sin\theta_{11/3}/2$, $Z_{in1}=-jZ_0\cot\theta_{12}$, $Y_{in2}=-j(Z_{21}+Z_{22}\cot\theta_{22}\tan\theta_{21})/(Z_{21}(Z_{21}\tan\theta_{21}-Z_{22}\cot\theta_{22}))$.

Then, the transmission matrix of the equivalent circuit in Fig. 4 can be expressed as a multiplication of five matrixes of each section:

$$\left[ABCD\right]=\left[ABCD_1\right]\times\left[ABCD_2\right]\times\left[ABCD_3\right] \times\left[ABCD_4\right]\times\left[ABCD_5\right]. \tag{11}$$

The synthesis method based on the transmission matrix [10] is elucidated to initially determine the operating central frequency and its respective bandwidth. In this context, the input impedance at Port 1 is calculated under the perfect impedance matching at both Port 2 and Port 3:

$$Z_{in}=(Z_{i2}A+B)/(Z_{i2}C+D), \tag{12}$$

where Z_{i2}=50 Ω is the image impedance at Port 2. Subsequently, the reflection and transmission coefficient of Port1 can be elucidated by:

$$S_{11}=(Z_{in}-Z_0)/(Z_{in}+Z_0), \tag{13}$$

$$S_{21}=(0.5-0.5S_{11}^{\;2})^{\frac{1}{2}}. \tag{14}$$

The isolation between Port 2 and 3 can be analyzed through the equivalent circuits under the even-/odd-mode excitations as depicted in Figs. 6 (a) and (b), respectively. When the even-/odd-mode signal is applied to Port 2 and 3, the transmission matrix of the even-/odd-mode equivalent circuit can be derived as:

$$\left[ABCD_{e/o}\right]=\left[ABCD_5\right]\times\left[ABCD_4\right] \times\left[ABCD_3\right]\times\left[ABCD_{2e/o}\right]\times\left[ABCD_{1e/o}\right], \tag{15}$$

where

$$[ABCD_{1e}]=[ABCD_{1o}] =\begin{bmatrix} \dfrac{ce-a^2-adZ_{in1}}{be+aeZ_{in1}} & -a/e \\ \dfrac{e^2Z_{in1}-d^2Z_{in1}-ad}{be+aeZ_{in1}} & -d/e \end{bmatrix}, \tag{16}$$

$$[ABCD_{2o}]=[ABCD_{2e}]\times\begin{bmatrix} 1 & 0 \\ 2/Z_r & 1 \end{bmatrix} =[ABCD_2]\times\begin{bmatrix} 1 & 0 \\ 2/Z_r & 1 \end{bmatrix}. \tag{17}$$

Thus, the input impedance at Port 2 under even-/odd-mode excitation and the transmission coefficient between Port 2 and Port 3 can be elucidated as

$$Z_{ine/o}=\frac{Z_{i1e/o}A_{e/o}+B_{e/o}}{Z_{i1e/o}C_{e/o}+D_{e/o}}, \tag{18}$$

$$S_{23}=Z_0\frac{Z_{ine}-Z_{ino}}{(Z_{ine}+Z_0)(Z_{ino}+Z_0)}, \tag{19}$$

where the image impedance at Port 1 under even-/odd-excitation is 100 Ω and 0 Ω, respectively.

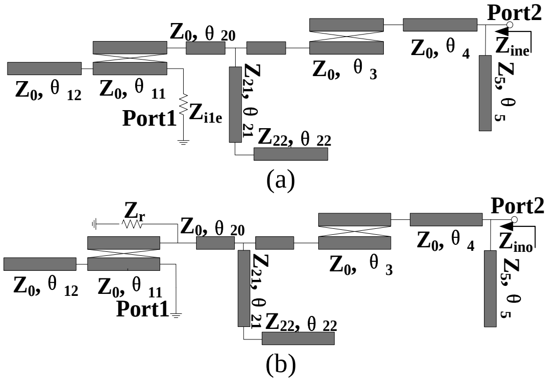

(a)

(b)

Fig. 6. Equivalent circuit of the proposed FPD under even-/odd-mode excitations: (a) even-mode excitation and (b) odd-mode excitation.

Till now, the analysis method has been described to predict the *S*-matrix of the proposed FPD. Based on this method, a FPD circuit is analyzed and its predicted performance is attained with 3-dB fractional bandwidth of 29.2% at central frequency of 2.18 GHz. As illustrated in Fig. 7, the isolation between Port 2 and 3 is better than 17.0 dB. It should be mentioned that owing to inevasible distinctions caused by the modeling simplification, slight differences are adopted between the geometrical parameters in theoretical analysis and those as denoted in Fig. 1 during circuit design.

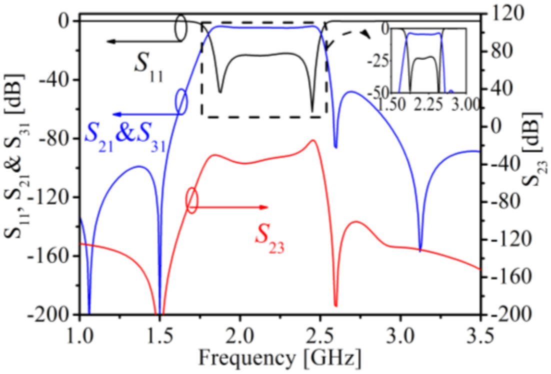

Fig. 7. Calculated results of S-parameters.

III. SIMULATION AND MEASUREMENT RESULTS

For verification, the proposed FPD with an overall size of 0.29 λ_0×0.89 λ_0 has been fabricated on a 0.508 mm thick RO4003C substrate with a dielectric constant of 3.38 and its photograph is shown in the inset of Fig. 8.

The diameter of via hole is 0.6 mm, and the dimensions of proposed FPD are presented in Table 1. Simulation was accomplished by the EM simulator HFSS while the measurement was carried out on the Agilent N5244A network analyzer.

The simulated and measured results are shown in Fig. 8. As can be seen from Fig. 8 (a), the FPD operates from 2.04 GHz to 2.64 GHz with a 3-dB bandwidth of 25.6%. Inside the passband, the measured minimum insertion loss is 0.9 dB with a maximum return loss of 25 dB. Besides, the minimum in-band isolation is 15.5 dB and the out-of-band rejection bandwidth is extended to 7.6 GHz ($3.23f_0$) with a rejection level of 20 dB. It can be found in Fig. 8 (b) that better than 0.12 dB amplitude imbalance and 0°±3.8° phase difference are both achieved, while at the frequency band of 1.5-2 GHz, the phase imbalance is slightly larger than that at higher frequency but still within the rational range. It should be mentioned that the small discrepancy between measured and simulated results are mainly due to the fabrication tolerance. A comparison between the proposed FPD and other recent designs is tabulated in Table 2. It is seen that the 3-dB bandwidth of this work is wider than those of counterparts in [1], [6] and [9], with an extended isolation bandwidth as well as upper stopband.

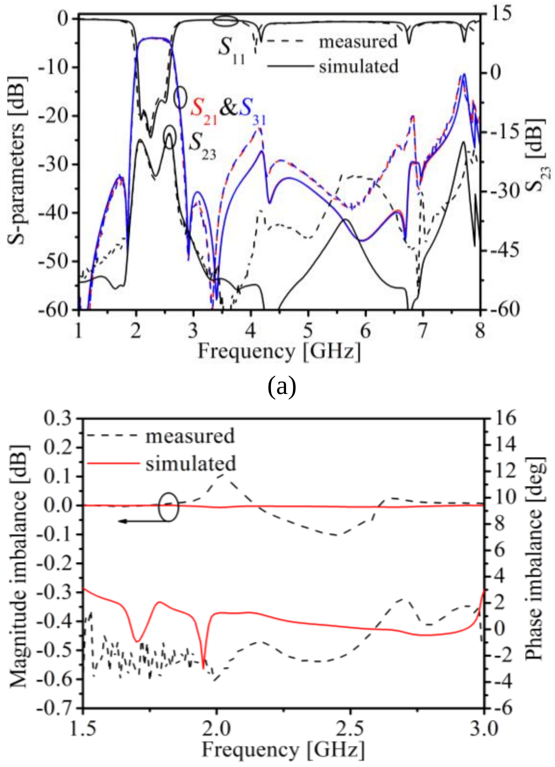

(a)

(b)

Fig. 8. Measured and simulated results: (a) S11, S21, S31 & S23, and (b) amplitude and phase imbalance.

Table 2: Comparisons among the proposed and previously reported filtering power dividers

	3-dB Bandwidth	Isolation <-15 dB within entire Passband	Harmonic Suppression	Roll Off
[1]	7.1%	No	2.9 f_0	Yes
[6]	3.5%	Yes	Not mentioned	No
[9]	6.5%	Yes	2.6 f_0	Yes
This work	25.6%	Yes	3.23 f_0	Yes

IV. CONCLUSION

In this paper, a new design of compact wideband FPD has been presented. A novel topology is introduced by adding an isolation resistor between two high-impedance stubs of tri-mode resonators for good isolation. Synthesis method and calculative verification have been presented to predict or initially determine its performance. To verify the feasibility of the design concept, a FPD has been then designed, fabricated and measured. Simulated and measured results agree well in the entire design frequency band, which verify the feasibility of the proposed design method to a great extent. We believe the proposed wideband FPD will be very promising in wireless communication.

REFERENCES

[1] R. Mirzavand, M. Honari, A. Abdipour, and G. Moradi, "Compact microstrip Wilkinson power dividers with harmonic suppression and arbitrary power division ratios," *IEEE Trans. Microw. Theory Tech.*, vol. 61, no. 1, pp. 61-68, Jan. 2013.

[2] K. J. Song, "Compact filtering power divider with high frequency selectivity and wide stopband using embedded dual-mode resonator," *Electron. Lett.*, vol. 51, no. 6, pp. 495-497, Mar. 2015.

[3] S. W. Wong and L. Zhu, "Ultra-wideband power dividers with good isolation and improved sharp roll-off skirt," *IET Microw. Antennas Propag.*, vol. 3, no. 8, pp.1157-1163, Feb. 2009.

[4] B. Zhang and Y. A. Liu, "Wideband filtering power divider with high selectivity," *Electron. Lett.*, vol. 51, no. 23, pp. 1950-1952, Nov. 2015.

[5] J. Y. Shao, S. C. Huang, and Y. H. Pang, "Wilkinson power divider incorporating quasi-elliptic filters for improved out-of-band rejection," *Electron. Lett.*, vol. 59, no. 11, pp. 2848-2855, Nov. 2011.

[6] C. F. Chen and C. Y. Lin, "Compact microstrip filtering power dividers with good in-band isolation performance," *IEEE Microw. Wireless Compon. Lett.*, vol. 24, no. 1, pp. 17-19, Jan. 2014.

[7] S. F. Chao and W. C. Lin, "Filtering power divider with good isolation performance," *Electron. Lett.*, vol. 50, no. 11, pp. 815-817, May 2014.

[8] P. Cheong, K. I. Lai, and K. W. Tam, "Compact Wilkinson power divider with simultaneous bandpass response and harmonic suppression," *IEEE MTT-S International Microwave Symposium Digest*, vol. 23, no. 3, pp. 1588-1591, May 2010.

[9] X. Y. Zhang, K. X. Wang, and B. J. Hu, "Compact filtering power divider with enhanced second-harmonic suppression," *IEEE Microw. Wireless Compon. Lett.*, vol. 23, no. 9, pp. 483-485, Sep. 2013.

[10] D. M. Pozar, *Microwave Engineering*. 3rd ed., New York: Wiley, 2005.

Yijing Deng, received the B.S. degree in Information Countermeasures Engineering from NJUST, Nangjing, China, in 2014. She is currently working toward the Ph.D. degree in Electromagnetic Field and Microwave Technology in NJUST. Her research interest is the design of miniaturized high performance microwave/millimeter-wave passive device and numerical methods in electromagnetics.

Yixuan He is with the Beijing Institute of Technology (BIT), Beijing, China. His research interest is the design of high performance microwave passive components on PCB.

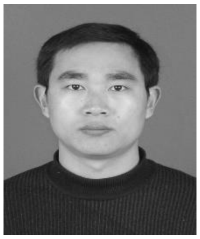

Jianpeng Wang received the M.Sc. and Ph.D. degrees from UESTC, Chengdu, China, in 2004, and 2007, respectively. Since Jan. 2008, he has been with the Ministerial Key Laboratory of JGMT, School of Electronic and Optical Engineering, NJUST. His research interests include the high performance microwave/ millimeter-wave passive components, circuits and systems realized on PCB, LTCC, etc.

Integrated RFIC On-Chip and GPS Antenna with Human Body for Wrist and Wearable Communication Applications

Wen Cheng Lai and Jhin Fang Huang

Department of Electronic Engineering
National Taiwan University of Science and Technology
wenlai@mail.ntust.edu.tw

Abstract **─** A GPS and Miracast RFIC-on-chip antenna in 0.18 um CMOS 1p6M process is presented. The HFSS 3-D EM simulator is employed for design simulation. A printed 1.575 GHz and 2.4 GHz antenna has been realized by using the CMOS RFIC-on-chip. The measured VSWR is less than 2 from 1.575 GHz and 2.4- to 2.483-GHz. This propose super quadric combo antenna in free space, electromagnetic coupling between super quadric antenna and human body and rectangular antenna for wrist watch type wireless communication applications. The measured phase distribution of the input impedance is quite linear and the H-plane patterns are almost omnidirectional and field tried GPS integration. In addition, in order to improve the way controlling this provide switch by software, a novel circuit structure which will control antenna pattern switching automatically by hardware is also developed for wireless healthcare and mobile biomedical application. RFIC-on-chip GPS and Miracast antenna also merger T/R-Switch design on single chip solution for 2.4GHz CMOS transceiver RF front-end. The old man can monitor healthcare and transfer to health center or passive devices by Miracast with software and show GPS location for wearable ambulatory application.

Index Terms **─** Chip antenna, GPS, wearable communication, wrist and wireless application.

I. INTRODUCTION

Wrist wearable ambulatory healthcare and mobile biomedical application for old man demand. The 1.575 GHz and 2.4 GHz CMOS RFIC on-Chip antenna and T/R-Switch for wireless application [1] silicon-germanium (SiGe) HBT processing 1.575 GHz and 2.4 GHz band antenna and merger T/R-Switch design as shown in Fig. 1, [2], [3]. This analysis has including super quadric combo antenna in free space, electromagnetic coupling between super quadric antenna and human body and rectangular antenna for wrist watch type wireless communication applications. CMOS standard processing FET based T/R switch that insertion loss more large and power handing capability performance low. But now low power transceiver develop insertion loss low and FET based T/R switch is more importance [4], [5]. This flexible proximate d antenna has switch by software, and develop a novel circuit structure controlling antenna pattern switching automatically by hardware.

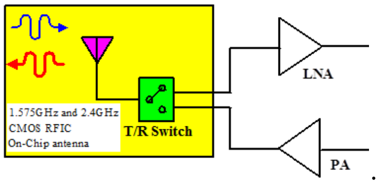

Fig. 1. The structure of 1.575 GHz and 2.4 GHz CMOS transceiver front –end Antenna and T/R-Switch.

II. GPS AND MIRACAST RFIC-ON-CHIP ANTENNA

The proposed 1.575 GHz and 2.4-GHz RFIC-on-chip antenna with T/R-Switch in 0.18 um CMOS 1p6M process is designed and based on the mender line by loop type. The chip area is 1.21 (1.1mm×1.1mm) mm^2 as shown in Fig. 2. The simulated VSWR of the single RFIC-on-chip antenna is less than 2 from 1.575 GHz and 2.4- to 2.483-GHz as shown in Fig. 3 and Fig. 4. At antenna part of M6 layer the trace width is 30mm on 0.75mm x 1.1mm area. M1~M6 metal layer are grounding to M3~M6 layer by via. The antenna paths are M1 and M2 including area 0.27mm x 0.94mm and extend 0.07mm trace to meet VSWR is less than 2 from 1.575 GHz and 2.4- to 2.483-GHz. M5 layer is shielding area 0.47mm x 0.67mm to metal grounding. The distance is 30μm between pad area 0.2mm x 0.1mm and grounding can support measured VSWR on wafer measurement by GS testing finger as pad used multi-layers and multi-via. The T/R-switch is expected to be integrated with the front-end circuits into the chip that area is 0.15mm x 1.1mm as shown in Fig. 5 [6].

In the monolithic switching system, this device can operate two switching status by controlling with a low

Submitted On: September 29, 2015
Accepted On: October 1, 2015

forward voltage drop and a very fast switching action. Switching radiation pattern is demonstrated such that the fading effect due to multipath propagations could be avoided [7].

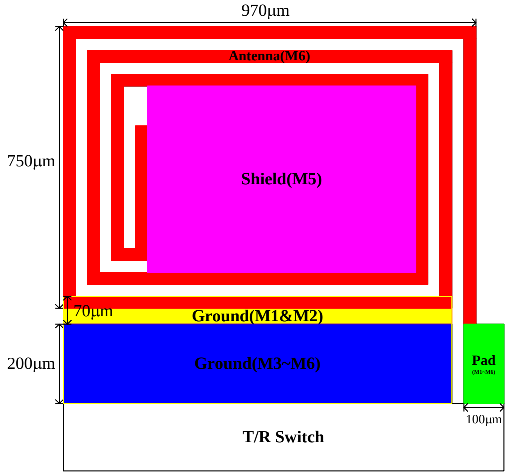

Fig. 2. Layout of 1.575 GHz and 2.4 GHz CMOS RFIC On-Chip Antenna and T/R-Switch.

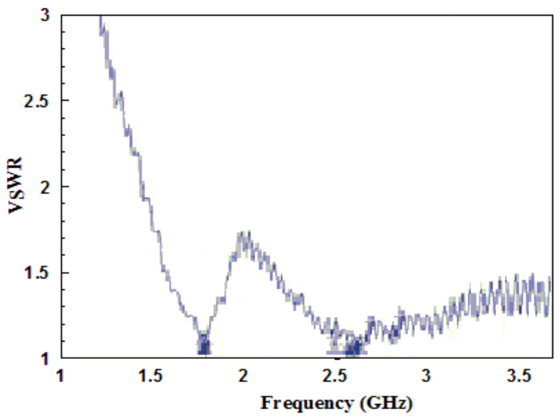

Fig. 3. Measured RFIC-on-Chip combo antenna VSWR.

Radiation Patterns of XY-Plane @ 2.45 GHz

XY plane	*Max*	*Min*	*Average*
E_ϕ gain (dBi)	-43.2	-38.7	-53.2
E_θ gain (dBi)	-61.4	-89.8	-67.4

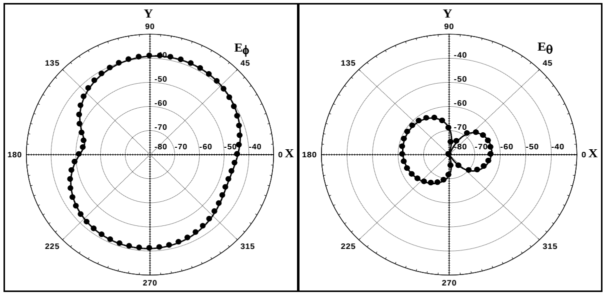

(a) E_ϕ -field (cross-polarization) (b) E_θ -field

Radiation Patterns of XZ-Plane @ 2.45 GHz

Xz plane	*Max*	*Min*	*Average*
E_ϕ gain (dBi)	-44.4	-53.0	-49.4
E_θ gain (dBi)	-40.9	-66.9	-46.1

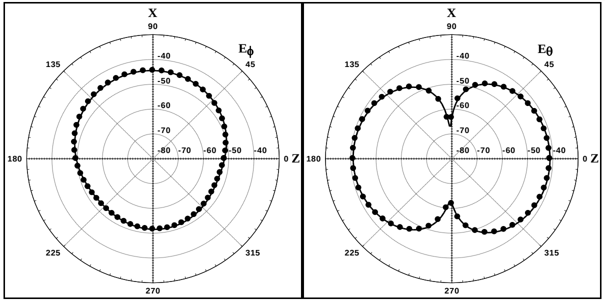

(a) E_ϕ -field (cross-polarization) (b) E_θ -field

Radiation Patterns of YZ-Plane @ 2.45 GHz

Xz plane	*Max*	*Min*	*Average*
E_ϕ gain (dBi)	-39.1	-41.4	-40.5
E_θ gain (dBi)	-49.6	-80.0	-56.1

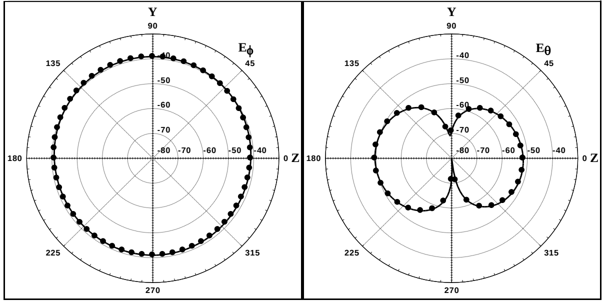

(a) E_ϕ -field (cross-polarization) (b) E_θ -field

Fig. 4. Measured antenna gain patterns.

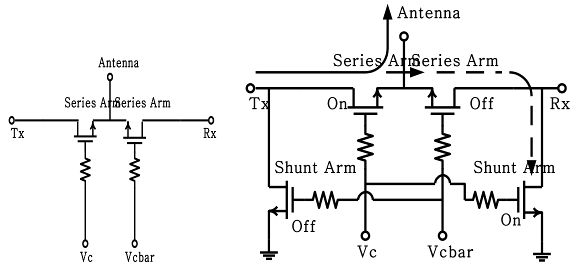

Fig. 5 T/R Switch architecture diagram and schematic.

III. T/R-SWITCH DESIGN

Regarding series type T/R Switch theory, this proposed voltage control series arm gate on transistors. The shunt/series type T/R Switch phase in shunt arm when shunt arm transistors switching on. Transistor gate width related on T/R switch phase in lost and isolation that means width increase and on-state resistance reduce then phase in lost as less. But opposite off-state capacitance increase and isolation go to bad. Base on TSMC support model design, series arm select 90/0.24um NMOS transistor, the control voltage V_c is

1.8V. After design simulation T/R-Switch circuit as shown in Fig. 6 and characteristics as shown in Table 1. R_1 connect to grounding means define DC voltage. R_2, R_3 is gate-level bias resistor. R_1, R_2 and R_3 are 20kΩ.

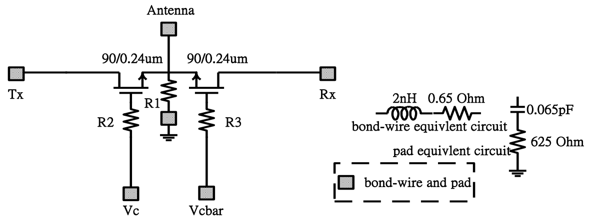

Fig. 6. T/R Switch circuit and layout.

Table 1: T/R Switch characteristics table

T/R Switch: Characteristics	
Control Voltage	1.8V
Insertion loss	<1.0dB
Input return loss (Tx and Rx modes)	>12dB
Input P_{1dB} (Tx and Rx modes)	>21dBm
Isolation (Tx-Rx in Tx mode)	>24dB
Isolation (ANT-Tx in Rx mode)	>18dB

IV. ELECTROMAGNETIC COUPLING BETWEEN ANTENNA AND HUMAN BODY

EM interaction between combo antenna and body are mutual coupling as shown in Fig. 7.

Expression of E field outside and inside a lossy body have confirm as shown in Fig. 8.

The EM interaction between antenna and body are B.C. and source model. Boundary condition on the perfectly conducting surface of the antenna as:

$$\hat{s}\cdot[\vec{E}^a(s)+\vec{E}^b(s)+\vec{E}^i(s)]=0, \tag{1}$$

$\vec{E}^a$ = electric field radiated from the combo antenna $\vec{E}^b$ = electric field scattered from the induced current in the human body $\vec{E}^i$ = impressed field from the voltage source.

(1) Delta-gap voltage source as shown in Fig. 9 (a):

$$E^i = V_o\delta(s)\cdot \tag{2}$$

(2) Magnetic frill source as shown in Fig. 9 (b):

$$\vec{M}_s=-\frac{2V_o}{\rho\ln(r_o/r_i)}\hat{\varphi}\,,\qquad \vec{E}^i=-\int_s \vec{M}_s\times\nabla'\frac{e^{-jk_oR}}{4\pi R}ds'. \tag{3}$$

According coupled integral equations (CIE), this proposed have calculated antenna IE and VEFIE with mutual coupling terms as shown in Fig. 10.

$$\frac{-1}{j\omega\varepsilon_o}\int_{ant}\left[\hat{s}\cdot\hat{s}'k_o^2 I(s')+\frac{\partial I(s')}{\partial s'}\cdot\frac{\partial}{\partial s}\right]G(s,s')ds' - \int_{V_b}\hat{s}\cdot\vec{\vec{G}}(s,\vec{r}')\cdot\tau(\vec{r}')\vec{E}(\vec{r}')dv'=\hat{s}\cdot\vec{E}^i(s)$$

$$\int_{ant}I(s')\hat{s}'\cdot\vec{\vec{G}}(\vec{r},s')ds'+\mathrm{PV}\int_{V_b}\tau(\vec{r}')\vec{E}(\vec{r}')\cdot\vec{\vec{G}}(\vec{r},\vec{r}')dv' - \left[1+\frac{\tau(\vec{r})}{3j\omega\varepsilon_o}\right]\vec{E}(\vec{r})=0 \qquad .(4)$$

(1) Induced Equivalent Current Density as:

$$\vec{J}_{eq}(\vec{r})=\left[\sigma+j\omega(\varepsilon-\varepsilon_o)\right]\vec{E}(\vec{r})=\tau\vec{E}(\vec{r}). \tag{5}$$

(2) Dyadic Green's Function as:

$$\vec{\vec{G}}(\vec{r},\vec{r}')=-j\omega\mu_o[\vec{\vec{I}}+\frac{1}{k_o^2}\nabla\nabla]G(\vec{r},\vec{r}')$$

$$G(\vec{r},\vec{r}')=\frac{e^{-jk_o|\vec{r}-\vec{r}'|}}{4\pi|\vec{r}-\vec{r}'|}\cdot \tag{6}$$

The proposed antenna with arbitrary orientation and wrist body are present as shown in Fig. 11 and Fig. 12 [8]-[12]. Regarding moment method (MoM) solution, the combo antenna current is expanded in terms of piecewise sinusoidal basis functions: (N_a segments) as:

$$I(\phi^*)=\sum_{n=1}^{Na}I_n f_n(\phi^*)$$

$$f_n(\phi^*)=\begin{cases}\dfrac{\sin(\phi^*-\phi^*_{n-1})}{\sin(\phi^*_n-\phi^*_{n-1})} & \text{if } \phi^*_{n-1}\le\phi^*\le\phi^*_n\\ \dfrac{\sin(\phi^*_{n+1}-\phi^*)}{\sin(\phi^*_{n+1}-\phi^*_n)} & \text{if } \phi^*_n\le\phi^*\le\phi^*_{n+1}\\ 0 & \text{otherwise}\end{cases} \qquad . \tag{7}$$

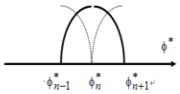

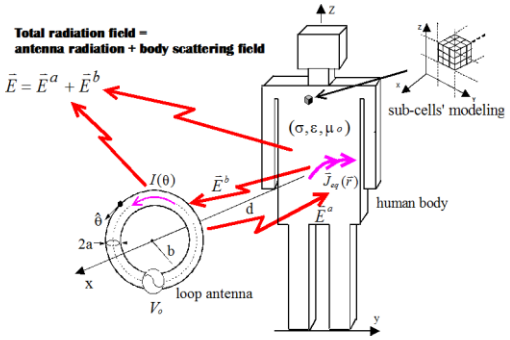

Fig. 7. EM interaction between antenna and body are mutual coupling.

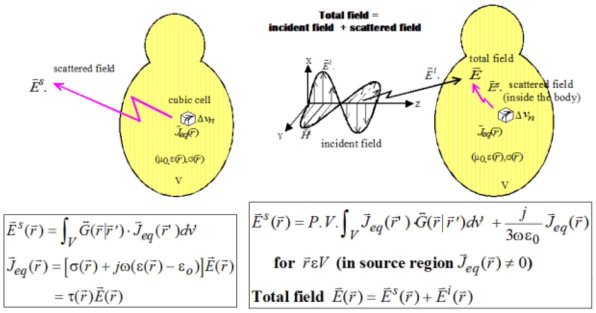

$$\vec{E}^s(\vec{r})=\int_V\vec{\vec{G}}(\vec{r}|\vec{r}')\cdot\vec{J}_{eq}(\vec{r}')dv'$$

$$\vec{J}_{eq}(\vec{r})=[\sigma(\vec{r})+j\omega(\varepsilon(\vec{r})-\varepsilon_o)]\vec{E}(\vec{r}) =\tau(\vec{r})\vec{E}(\vec{r})$$

$$\vec{E}^s(\vec{r})=P.V.\int_V\vec{J}_{eq}(\vec{r}')\cdot\vec{\vec{G}}(\vec{r}|\vec{r}')dv'+\frac{j}{3\omega\varepsilon_0}\vec{J}_{eq}(\vec{r})$$

for $\vec{r}\varepsilon V$ **(in source region** $\vec{J}_{eq}(\vec{r})\neq 0$**)**

Total field $\vec{E}(\vec{r})=\vec{E}^s(\vec{r})+\vec{E}^i(\vec{r})$

Fig. 8. Dyadic green's function technique.

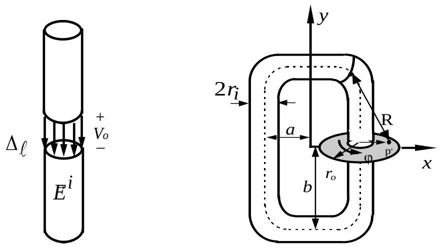

Fig. 9. (a) Delta-gap voltage source, and (b) Magnetic frill source.

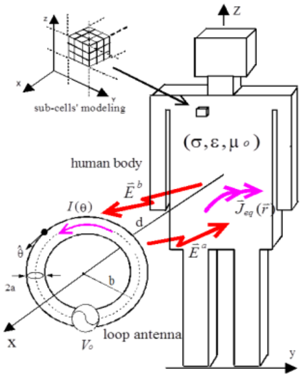

Fig. 10. Antenna IE and VEFIE with mutual coupling terms.

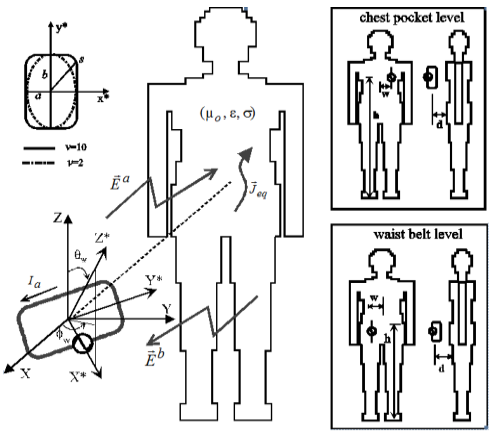

Fig. 11. Antenna with arbitrary orientation and wrist body.

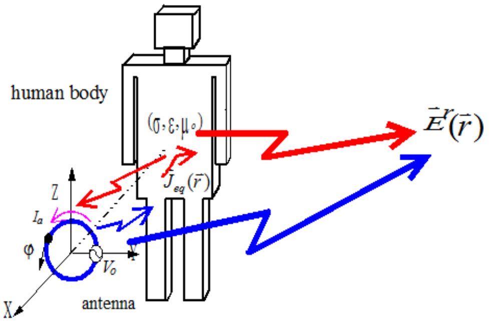

Fig. 12. Total radiation field from antenna and human body.

The induced electric field in the body is expressed in terms of pulse basis functions: (N_b cells) as:

$$\vec{E}(\vec{r}) = \hat{x}\sum_{n=1}^{N_b} E_x^n p_n(\vec{r}) + \hat{y}\sum_{n=1}^{N_b} E_y^n p_n(\vec{r}) + \hat{z}\sum_{n=1}^{N_b} E_z^n p_n(\vec{r}). \quad (8)$$

Moment Method Solution: Galerkin & point-matching as:

$$\frac{-1}{j\omega\varepsilon_o}\sum_{n=1}^{Na} I_n \int_{\phi^*_{m-1}}^{\phi^*_{m+1}}\int_{\phi^*_{n-1}}^{\phi^*_{n+1}}\Big\{(s_{x^*}s'_{x^*} + s_{y^*}s'_{y^*})k_o^2 f_n(\phi^{*\prime})\Delta(\phi^{*\prime}) - \frac{(jk_oR+1)}{R^2}\left[s_{x^*}(x^* - x^{*\prime}) + s_{y^*}(y^* - y^{*\prime})\right]$$

$$\frac{\partial f_n(\phi^{*\prime})}{\partial\phi^{*\prime}}\Big\}\frac{e^{-jk_oR}}{4\pi R} f_m(\phi^*)\Delta(\phi^*)d\phi^{*\prime}\, d\phi^* \quad ,$$

$$-\sum_{n=1}^{N_b}\sum_{p=1}^{3} E_{x_p}^n \int_{V_b} \tau_n \int_{\phi^*_{m-1}}^{\phi^*_{m+1}}\left[s_x G_{xx_p}(s,r') + s_y G_{yx_p}(s,r') + s_z G_{zx_p}(s,r')\right] f_m(\phi^*)\Delta(\phi^*)d\phi^*\, dv'$$

$$= \int_{\phi^*_{m-1}}^{\phi^*_{m+1}} (s_{x^*}\hat{x}^* + s_{y^*}\hat{y}^*)\cdot\vec{E}^i(\phi^*) f_m(\phi^*)\Delta(\phi^*)d\phi^* \quad (9)$$

$$\sum_{p=1}^{3}\hat{x}_p\Bigg\{\sum_{n=1}^{N_a} I_n \int_{\phi^*_{n-1}}^{\phi^*_{n+1}}\left[G_{x_px}(\vec{r}_i,s')s_x + G_{x_py}(\vec{r}_i,s')s_y + G_{x_pz}(\vec{r}_i,s')s_z\right] f_n(\phi^{*\prime})\Delta(\phi^{*\prime})d\phi^{*\prime}$$

$$+\sum_{n=1}^{N_b}\sum_{q=1}^{3} E_{x_q}^n\left[\tau_n \mathrm{PV.}\int_{(\Delta v)_n} G_{x_px_q}(\vec{r}_i,\vec{r}\,')dv' - \delta_{pq}\delta_{\vec{r}_i\vec{r}_n}\Big(1+\frac{\tau_i}{j3\omega\varepsilon_o}\Big)\right]\Bigg\} = 0 \quad . \quad (10)$$

Finally moment method solution is transformation of CIEs to matrix equation as:

$(N_a + 3N_b)\times(N_a + 3N_b)$ matrix equation:

$$\begin{bmatrix} [AA] & | & [AB^x] & [AB^y] & [AB^z] \\ \text{-----} & | & \text{-----} & \text{-----} & \text{-----} \\ [BA^x] & | & [BB^{xx}] & [BB^{xy}] & [BB^{xz}] \\ [BA^y] & | & [BB^{yx}] & [BB^{yy}] & [BB^{yz}] \\ [BA^z] & | & [BB^{zx}] & [BB^{zy}] & [BB^{zz}] \end{bmatrix}\begin{bmatrix} [I_a] \\ \text{---} \\ [E_b^x] \\ [E_b^y] \\ [E_b^z] \end{bmatrix} = \begin{bmatrix} [V^i] \\ \text{---} \\ [0] \\ [0] \\ [0] \end{bmatrix}, \quad (11)$$

[AA]: $N_a \times N_a$ submatrix (antenna to antenna),
[AB]: $N_a \times 3N_b$ submatrix (body to antenna),
[BA]: $3N_b \times N_a$ submatrix (body to antenna),
[BB]: $3N_b \times 3N_b$ submatrix (body to body),
$[I_a]$: N_a column-vector (antenna current),
$[E_b^\alpha]$: N_b column-vector (a component of the induced field in the body).

Total radiation field from antenna and human body as:

$$\vec{E}^r(\vec{r}) = -j\eta_o k_o \frac{e^{-jk_or}}{4\pi r}\int_{-\pi}^{\pi}\left\{\hat{\theta}[-I(\theta')\sin\theta'\cos\theta\sin\phi - I(\theta')\cos\theta'\sin\theta] + \hat{\phi}[-I(\theta')\sin\theta'\cos\phi]\right\}$$

$$e^{jk_o(x'\sin\theta\cos\phi + y'\sin\theta\sin\phi + z'\cos\theta)}\, b\,d\theta' \quad \textbf{loop antenna radiation field}$$

$$-j\eta_o k_o \frac{e^{-jk_or}}{4\pi r}\int_{V_b}\Big\{\hat{\theta}[J_{eq}^x(\vec{r}\,')\cos\theta\cos\phi + J_{eq}^y(\vec{r}\,')\cos\theta\sin\phi - J_{eq}^z(\vec{r}\,')\sin\theta] +$$

$$\hat{\phi}[-J_{eq}^x(\vec{r}\,')\sin\phi + J_{eq}^y(\vec{r}\,')]\cos\phi\Big\} e^{jk_o(x'\sin\theta\cos\phi + y'\sin\theta\sin\phi + z'\cos\theta)}\, dv' \quad .$$

$$\textbf{body-induced current radiation field} \quad (12)$$

The antenna parameters (affected by body) as shown in Fig. 14 and below:

(1) Input power & input impedance:

$$P_i = \tfrac{1}{2}\mathrm{Re}\left[V_o I_o^*\right], \quad Z_i = V_o / I_o .$$

(2) Power absorbed by body:

$$P_{abs} = \int_{V_b} \tfrac{1}{2}\sigma|\vec{E}|^2\, dv .$$

(3) Power radiated to free space:

$$P_{rad} = \oint_s \tfrac{1}{2}[\vec{E}^r \times \vec{H}^{r*}]\cdot d\vec{s} .$$

(4) Directive gain:

$$G(\theta,\phi) = \frac{\tfrac{1}{2}\mathrm{Re}[\vec{E}^r \times \vec{H}^{r*}]}{P_{rad}/(4\pi r^2)} .$$

(5) Radiation efficiency:

$$\eta_{rb} = \frac{P_{rad}}{P_{rad}+P_{abs}} \text{(body absoption)} \quad \eta_{r\Omega} = \frac{R_r}{R_r+R_{ohm}} \text{(ohmic loss)}.$$

(6) Power gain:

$$G_p = \eta_{rb} \times \eta_{r\Omega} \times G.$$

(7) Average G_{p}:

$$G_{avg} = \tfrac{1}{8}\sum_{i=1}^{8} G_p(\theta = \tfrac{\pi}{2}, \phi_i).$$

(8) Receiving system noise temperature:

$$T_{sys} = T_A + T_{REC}.$$

(9) Antenna noise temperature: T_A,

(T_b: **background noise temperature**),

$$T_A = \eta_{r\Omega}T_b + (1-\eta_{r\Omega})T_P,$$

only $\eta_{r\Omega}$ (not η_{rb}) appear in T_A.

Rectangular combo antennas of y-orientation at 2.4 to 2.483 GHz measured results as shown in Fig. 13 and below Table 2. The 3D patterns of rectangular combo antennas as shown in Fig. 14-Fig. 18 [8]-[12].

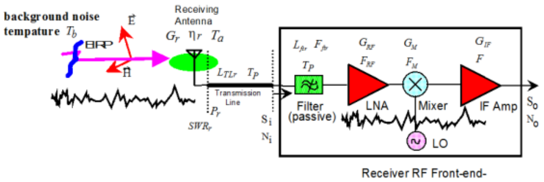

Fig. 13. Antenna and receiving system S/N Ratio (affected by body).

Table 2: Rectangular combo antennas of y-orientation at 2.4 GHz

Antenna Position	in free space	chest pocket level	waist belt level
E_θ Max. Power Gain (dB)	-12.4	-7.4	-8.6
E_θ Min. Power Gain (dB)	-22.3	-56.8	-34.0
E_θ Ave. Power Gain (dB)	-15.0	-13.4	-13.6
E_ϕ Max. Power Gain (dB)	<-100	-20.8	-21.3
E_ϕ Min. Power Gain (dB)	<-100	-38.5	-41.3
E_ϕ Ave. Power Gain (dB)	<-100	-23.7	-25.7

Antenna Position	Free Space	Chest Pocket Level			Waist Belt Level
Antenna Orientation	Y	X	Y	Z	Y
Radiation Efficiency $\eta_{r\Omega}$	4	33	17	26	14
Radiation Efficiency η_{rb}	100	13	40	27	45
Total Efficiency (%)	4	4.29	6.8	7	6.3
Nosie Temperature(K)**	296	267	283	274	286

* **Total Radiation Efficiency** $\eta_r = \eta_{r\Omega} \times \eta_{rb}$

** $T_A = \eta_{r\Omega}T_b + (1-\eta_{rr\Omega})T_p$,

assuming T_b=200 K & T_p=300 K

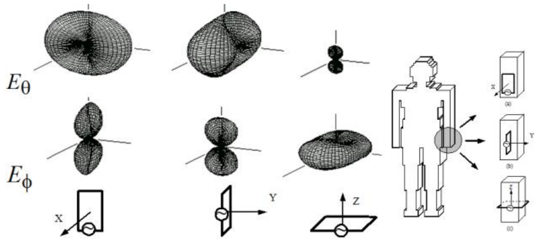

Fig. 14. 3D patterns of rectangular combo antennas in free space (1.575 GHz).

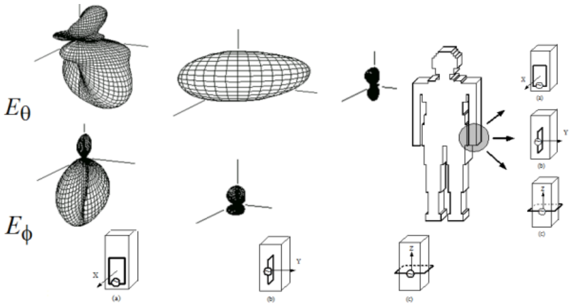

Fig. 15. 3D patterns of rectangular combo antennas at the Wrist (1.575 GHz).

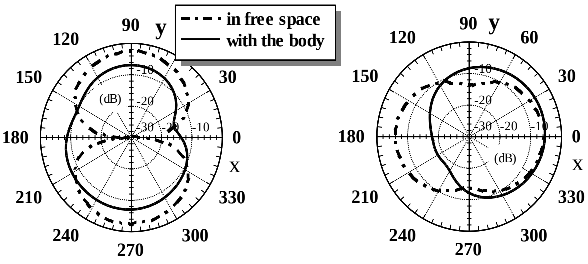

Fig. 16. 2D power patterns in the H-plane at wrist level (1.575 GHz).

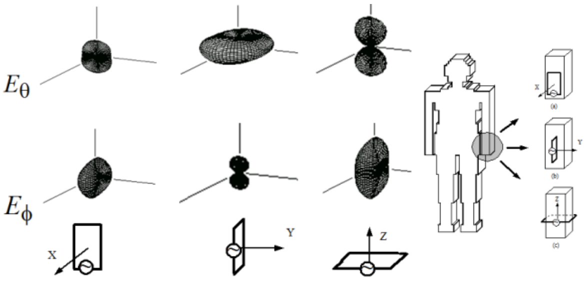

Fig. 17. 3D patterns of rectangular antennas in free Space (2.45 GHz).

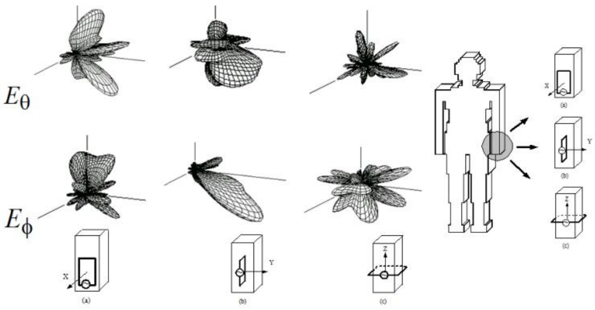

Fig. 18. 3D patterns of rectangular combo antennas at the wrist (2.45 GHz).

Detailed analysis and extensive numerical simulations of the influence of a human body model on combo antennas with arbitrary orientations for personal wireless communications has been conducted. Coupled integral equations (CIE), which consist of a Pocklington-type integral equation (PIE) and a volume electric field integral equation (VEFIE) with mutual coupling terms, and the method of moments (MoM) are used to numerically solve this antenna-body coupling problem. The proximate human body absorbs a large part of the antenna radiated power and reduces the antenna radiation efficiency. For the circular combo antenna: (2.45 GHz) as:

x- : body-absorption & ohmic-loss efficiency $\eta_{rb}=5\%$, $\eta_{r\Omega}=69\%$, $\eta_r=3.5\%$
y- : body-absorption & ohmic-loss efficiency $\eta_{rb}=62\%$, $\eta_{r\Omega}=44\%$, $\eta_r=27.5\%$
z- : body-absorption & ohmic-loss efficiency $\eta_{rb}=25\%$, $\eta_{r\Omega}=58\%$, $\eta_r=14.6\%$.

For the rectangular combo antenna: (2.45 GHz) as:

x- : body-absorption & ohmic-loss efficiency $\eta_{rb}=13\%$, $\eta_{r\Omega}=33\%$, $\eta_r=4.3\%$
y- : body-absorption & ohmic-loss efficiency $\eta_{rb}=40\%$, $\eta_{r\Omega}=17\%$, $\eta_r=6.8\%$
z- : body-absorption & ohmic-loss efficiency $\eta_{rb}=27\%$, $\eta_{r\Omega}=26\%$, $\eta_r=7.0\%$.

The EM coupling effects of the human body increase the radiation resistance (rectangular part of input impedance) for 4 to 10 times for different orientations, and hence, enhance the antenna ohmic-loss efficiency. The average power gain in the H-plane for the y-oriented combo antenna, a preferred choice for general pager usage, is enhanced about 2 dB by the human body**.** For watch-type communicator applications, the (z-oriented) combo antenna encircling the wrist may be a preferred choice. Numerical results of the antenna input impedance, radiation patterns, cross-polarization field level, radiation efficiencies, and maximum/minimum/average power gains are important for the pager or wireless communicator antenna/RF design and communication link budget consideration. Numerical simulation of complicated antenna parameter variations is important for the pager antenna/RF design and communication link budget consideration. For watch-type communicator applications, the (z-oriented) combo antenna encircling the wrist may be preferred choice. Numerical results of the antenna input impedance, radiation patterns, cross-polarization field level, radiation efficiencies, and maximum/minimum/average power gains are important for the pager or wireless communicator antenna/RF design and communication link budget consideration. Detailed near-zone behavior of the E-field distribution of the combo antenna is also studied for EMC application. The superquadric antenna is used to model the signal trace on the FPC board. The radiation efficiency of higher-order harmonic frequencies from a rectangular antenna to free space is not necessarily higher than that of lower frequencies. The proximate human body absorbs a large part of the radiated power from the combo antenna and reduces the antenna radiation efficiency:

x- : absoption = 87% radiation efficiency $\eta_{rb}=13\%$
y- : absoption = 60% radiation efficiency $\eta_{rb}=40\%$
z- : absoption = 73% radiation efficiency $\eta_{rb}=27\%$.

The EM coupling effects of the human body increase the radiation resistance (real part of input impedance) for 5 to 10 times for different orientations and hence enhance the antenna ohmic-loss efficiency. The average power gain in the H-plane for the y-oriented combo antenna is enhanced about 2 dB by the human body. For watch-type communicator applications, the (z-oriented) combo antenna encircling the wrist may be preferred choice. Numerical results of the antenna input impedance, radiation patterns, cross-polarization field level, radiation efficiencies, and maximum/minimum/ average power gains are important for the pager or wireless communicator antenna/RF design and communication link budget consideration. Detailed near-zone behavior of the E-field distribution of the combo antenna is also studied for EMC application. The superquadric antenna is used to model the signal trace on the FPC board. The radiation efficiency of higher-order harmonic frequencies from a rectangular antenna to free space is not necessarily higher than that of lower frequencies. Analysis and extensive numerical computation of EM interaction between a human body model and a circular combo antenna with arbitrary orientation for radio paging communications has been performed. The proximate human body absorbs a large part of the antenna radiated power and reduces the antenna radiation efficiency, but enhance the radiation resistance (real part of input impedance), and hence, increase the antenna ohmic-loss efficiency:

x- : body-absoption & ohmic-loss efficiency $\eta_{rb}=6\%$ $\eta_{r\Omega}=70\%$
y- : body-absoption & ohmic-loss efficiency $\eta_{rb}=61\%$ $\eta_{r\Omega}=46\%$
z- : body-absoption & ohmic-loss efficiency $\eta_{rb}=26\%$ $\eta_{r\Omega}=60\%$.

As the electromagnetic spectrum becomes more crowded and the digital hardware is widely used, it is important for engineers to take electromagnetic interference into account in the circuit design process. Because EMC equipment operate normally in proximity to other electronic devices, it is important that the near field distribution of the antenna must be carefully quantified. In EMC analysis, radiated emissions from signal traces in FPC boards are an important topic. In some situation, the signal trace encloses to an antenna. It is known that an antenna having small perimeter compared to a wavelength is an inefficient radiating element. However, when the signal frequency is high enough, the electrical perimeter of the antenna may then be comparable to a wavelength. The antenna will become an efficient radiator. In addition, detailed near-zone behavior of the E-field distribution of the combo antennas is studied for electromagnetic compatibility (EMC) application. The superquadric antenna is used to model the signal trace on the FPC board. A circular, rectangular, and elliptical antennas have are studied. The E-field distribution of the rectangular antenna in the near-zone region, which corresponded to the fundamental frequency, 2^{nd} and 3^{rd} harmonics of a clock rate, are computed. It is found that the radiation efficiency of higher-order harmonic frequencies from a rectangular antenna to free space is not necessarily higher than that of lower frequencies. Numerical results may be useful for the analysis of radiated emission of the signal trace on a FPC board.

V. GPS FIELD TRIED MEASURED RESULTS

For GPS static and dynamic evaluation, this antenna performance criteria are carry per noise ratio more than 40 (C/N >= 40) and TTFF less than 45 seconds under signal generator by antenna with wireless device. This wearable ambulatory application also provide GPS field trial test at multi-difficult conditions such as high building, high tree, high bridge, alley, underground tunnel by dead reckoning for mobile biomedical application. Normally the old man can monitor healthcare and transfer to health center by Miracast with software and show GPS location. Even ambulance goes to hospital on the way also can simulations such as freeway shown as in Fig. 19.

Fig. 19. GPS antenna filed tried measurement at freeway.

VI. CONCLUSION

This paper has provided COMS RFIC On-Chip combo antenna with T/R Switch design to support wrist wearable ambulatory technological performance and mobile biomedical healthcare application.

REFERENCES

[1] E. Ojefors, F. Bouchriha, K. Grenier, and A. Rydberg, "24 GHz ISM-Band Antennas on Surface Micro-machined Substrates for Integration with a Commercial SiGe Process," Department of Engineering Sciences, Uppsala University, Uppsala, Sweden.

[2] http://www.eettaiwan.com

[3] Electronic Engineering Times-Taiwan, pp. 3, Nov. 15, 2003.

[4] F.-J. Huang and O. Kenneth, "A 0.5-um CMOS T/R switch for 900-MHz wireless applications," *IEEE Journal of Solid-State Circuits*, vol. 36, no. 3, pp. 486-492, Mar. 2001.

[5] K. Yamamoto, T. Heima, A. Furukawa, et al., "A 2.4-GHz-band 1.8-V operation single-chip Si-CMOS T/R-MMIC front-end with a Low insertion loss switch," *IEEE Journal of Solid-State Circuits*, vol. 36, no. 8, pp. 1186-1197, Aug. 2001.

[6] M. R. Kamarudin, Y. I. Nechayev, and P. S. Hall, "Antenna for on-body communication systems," *IEEE IWAT*, pp. 17-20, Mar. 2005.

[7] J.-F. Huang, J.-Y. Wen, and W.-C. Lai, "Design of a printed dipole array antenna with wideband power divider and RF switches," *Microwave and Optical Technology Letters*, vol. 55, no 10, pp. 2410-2413, Oct. 2013.

[8] J.-F. Huang and W.-C. Lai, "Design of a compact printed double-sided dual-band dipole antenna by Fdtd for Wifi application," *Microwave and Optical Technology Letters*, vol. 55, pp. 1845-1851, Aug. 2013.

[9] W.-C. Lai and J.-F. Huang, "Numerical modeling of electromagnetic coupling electronic device with proximity-based radio power control for LTE/ WWAN SAR," *IEEE Fifth International Conference on Advanced Computational Intelligence (ICACI)*, pp. 142-147, Oct. 18-20, 2012.

[10] J.-F. Huang, W.-C. Lai, and P.-G. Yang, "An automatically tuneable antenna design with GPS dead reckoning switch for multiband laptop and mobile cellular phone applications to the human body," *The 2013 6th International Conference on BioMedical Engineering and Informatics (BMEI)*, pp. 306-311, Dec. 16-18, 2013.

[11] "A 2.4-GHz RFIC-on-chip antenna on flexible surface proximate to the human body for miracast and wireless application," *International Workshop on Microwave and Millimeter Wave Circuits and System Technology (MMWCST)*, pp. 165-169, Oct. 24-25, 2013.

[12] "Long term evolution antenna design by FDTD for Femto communication on tablet application," *International Microwave Workshop Series on RF and Wireless Technologies for Biomedical and Healthcare Applications (IMWS-Bio 2015)*, pp. 120-121, Sep. 21-23, 2015.

Wen-Cheng Lai received Ph.D. degrees in Electronic Engineering from National Taiwan University of Science and Technology in 2015. He is Hardware Director in ASUSTek Computer Inc. Taiwan.

Jhin-Fang Huang received Ph.D. degrees in Electrical Engineering from University of Kansas, U.S.A. From 1989-Now he is Associate Professor in Department of Electronic Engineering National Taiwan University of Science and Technology.

ACES JOURNAL, Vol. 31, No.9, September 2016

Mutual Coupling Reduction of Dual-Frequency Patch Antenna Arrays

Yantao Yu, Lijun Yi, Xiaoya Liu, and Zhaokai Gu

College of Communication Engineering
Chongqing University, Chongqing, 400044, China
yantaoyu@cqu.edu.cn, yiljcqu@163.com

Abstract **─** In this paper, a compact patch antenna array with dual resonant frequencies is presented. The mutual coupling between array elements can be reduced simultaneously at two frequencies by inserting a simple C-shaped resonator between the radiating patches and etching an inverted C-shaped slot defected ground structure (DGS) on the ground plane. The characteristics of the DGS and the resonator are investigated, respectively. The measured results show that the isolation between the antenna ports has been enhanced about 10 dB and 18 dB at the two operation frequencies with the presence of the proposed DGS and resonator structure.

Index Terms **─** Defected ground structure (DGS), dual frequency, mutual coupling, patch array, resonator.

I. INTRODUCTION

In order to accommodate higher data rates and provide increased capacity, the multi-port antenna arrays are widely used in new generation of wireless communication systems. However, it is very difficult to realize multiple antennas in a small size wireless device while keeping a high level of isolation between antenna elements [1], especially for dual-frequency arrays. In such a case, surface waves and near fields can lead to coupling between the antenna elements. As the separation between array elements becomes smaller, the effect of mutual coupling becomes more severe, which may result in severe degradation to the antenna's radiation properties, e.g., increment of the magnitude of S_{12} and distortion of radiation pattern.

Mutual coupling has attracted a lot of research in past years [2]. Different methods have been proposed in the literature to deal with the mutual coupling while keeping the array with compact design [3,4]. The orientations and feed configurations of antenna elements can be changed to minimize the inter-element mutual coupling [5-7]. Various decoupling networks using reactive components [8] or hybrid couplers [9] have been proposed to increase the isolation between antenna ports. However, the designed networks may be very complicated. There are some other methods for printed antennas, e.g., using parasitic elements [10], defected ground structures (DGS) [11-13] and microstrip sections [14]. Most of the designs in the literature are for arrays with single operating frequency band. However, dual-frequency operation is preferred for many popular communication standards. Mutual coupling reduction for dual-frequency arrays has also attracted many studies. The paper [15] describes a procedure to achieve simultaneous decoupling and matching at two frequencies using decoupling network with series and parallel combination of inductors and capacitors. A reconfigurable dual-band monopole array with high isolation is given in [16], which exploits the neutralization techniques and uses a switch to control the operating frequency band.

In this paper, a compact design utilizing a simple microstrip resonator and a defected ground structure to reduce the mutual coupling between a dual-frequency patch antenna array is proposed. In Section II, the design of compact dual-frequency patch antenna array is presented. In Section III, the characteristics of the DGS and the resonator are analyzed and the mutual coupling reduction of the array is studied both numerically and experimentally. Furthermore, the technique is extended to arrays with four elements. Finally, Section IV concludes the paper.

II. THE DUAL-FREQUENCY ARRAY

The geometrical structure of the proposed dual-frequency patch antenna array is shown in Fig. 1. This antenna array is designed on an FR4 substrate with a relative permittivity of 4.4, a thickness of 1.6 mm and a loss tangent of 0.02. The overall dimension ($W \times L$) of the antenna is 75 mm × 60 mm. The element spacing D is 7 mm. Without the C-shaped resonator, as in Fig. 1 (a), and the inverted C-shaped slot, as in Fig. 1 (b), the original patch array resonates at two frequencies. The antenna array is simulated using the EM software Ansoft HFSS and the S-parameters of the optimized patch array are shown in Fig. 2. Since the array structure is symmetrical, S_{11} equals to S_{22} and only S_{11} is shown in the figure. The optimum dimensions of the patch antenna are W_2 = 18 mm, L_2 = 22 mm, W_3 = 9 mm, L_3 = 14.55 mm, L_4 = 2 mm, H = 1 mm and L_8 = 7 mm. It can be seen from

Submitted On: September 30, 2015
Accepted On: July 27, 2016

Fig. 2 that the array resonates at 2.78 GHz and 4.12 GHz, respectively. It is also noticed that the magnitudes of the transmission coefficients S_{12} are about -11 dB and -22 dB at the two operating frequencies, respectively.

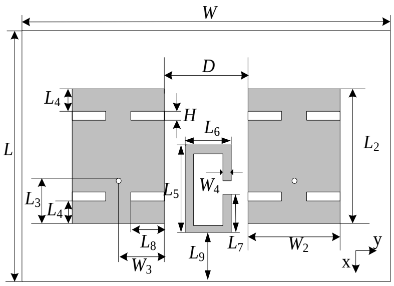

(a) Front view

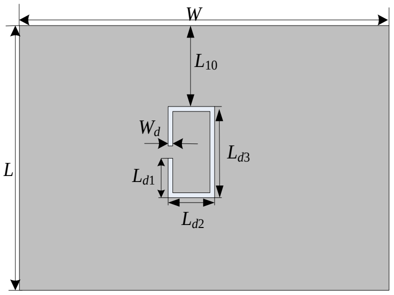

(b) Back view

Fig. 1. The structure of the proposed patch array.

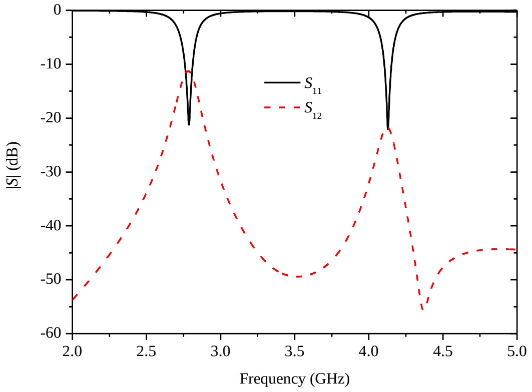

Fig. 2. The S-parameters of the proposed dual-frequency patch antenna array.

III. MUTUAL COUPLING REDUCTION

To reduce the mutual coupling of the dual-frequency patch antenna array, a C-shaped resonator is inserted between the radiating patches and an inverted C-shaped DGS is etched on the ground plane. The effects of the presence of the DGS and the resonator are studied as follows.

A. Inverted C-shaped DGS

The inverted C-shaped DGS, as shown in Fig. 1 (b), is etched from the ground plane of the patch array. The inverted C-shaped slot resonates and creates a stop band. To study the frequency characteristics of the DGS structure, a microstrip filter model as shown in Fig. 3 was built. The performance of the filter is analyzed in the EM simulator Ansoft HFSS by changing the dimensions of the slot. Figure 4 shows the transmission coefficients of the filter with various values of L_{d1}. It can be seen that the stop band frequency decreases as the increase of L_{d1}. Figure 5 shows the transmission coefficients of the filter with various values of L_{d2}. The parameter L_{d2} has a similar effect on the performance of the filter as L_{d1} does because they determine the total size of the slot. In addition, the transmission coefficients of the filter for different slot widths are plotted in Fig. 6. It is noted that the stop band frequency increases as the increase of W_d. The moderate value of W_d = 1 mm is chosen in our design.

By properly choosing the dimensions of the DGS structure, the desired band rejection characteristic can be achieved. Figure 7 shows the simulated and measured S-parameters of the designed filter with the optimized dimensions of W_d = 1 mm, L_{d1} = 4.9 mm, L_{d2} = 9 mm and L_{d3} = 12 mm. The measured results agree well with the simulated ones. It can be seen that the filter has a stop band at 2.78 GHz, which is the lower operating frequency of the patch array. By employing the proposed DGS in the array, the surface wave excited in the substrate can be suppressed and the mutual coupling can be reduced.

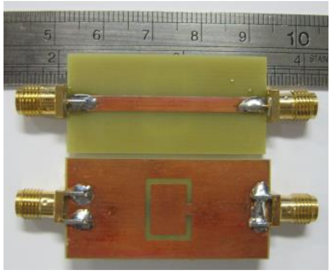

Fig. 3. The fabricated prototype of the DGS section.

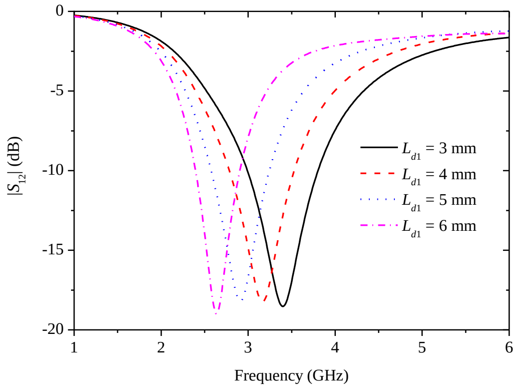

Fig. 4. The transmission coefficients of the filter with various L_{d1}.

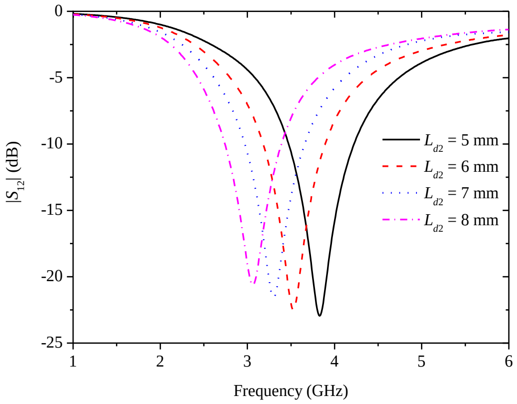

Fig. 5. The transmission coefficients of the filter with various Ld_2.

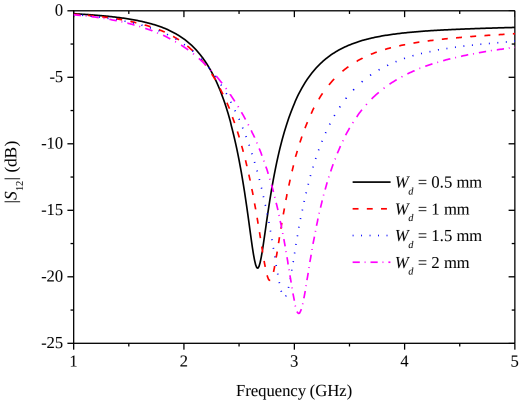

Fig. 6. The transmission coefficients of the filter with various W_d.

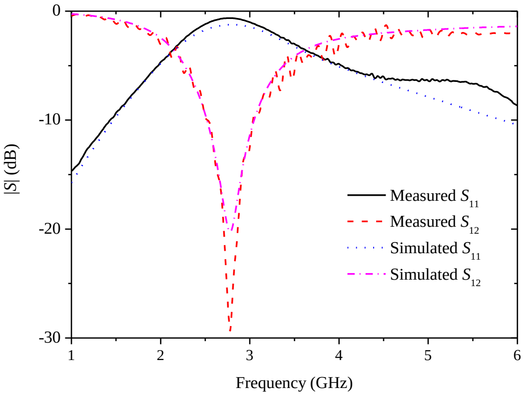

Fig. 7. The S-parameters of the optimized filter.

B. C-shaped resonator

The C-shaped resonator placed between the two radiating patches, as shown in Fig. 1 (a), is strongly involved in the coupling at the upper operation frequency of the array and is a half-wavelength resonator. A similar parametric study as for the DGS can be done here and then the dimensions of the resonator can be optimized to obtain the best result. Figure 8 depicts the fabricated resonator with coupled microstrip lines. The dimensions of the resonator are W_4 = 1 mm, L_5 = 15 mm, L_6 = 5.5 mm and L_7 = 5.8 mm. The simulated and measured S-parameters of the structure are shown in Fig. 9. It can be seen that this structure has a bandpass function at about 4.1 GHz. Therefore, with the C-shaped resonator added, an extra indirect coupling path is introduced, which can cancel out the direct mutual coupling between the two elements.

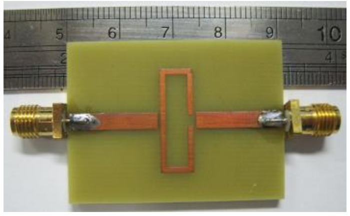

Fig. 8. The fabricated prototype of the resonator.

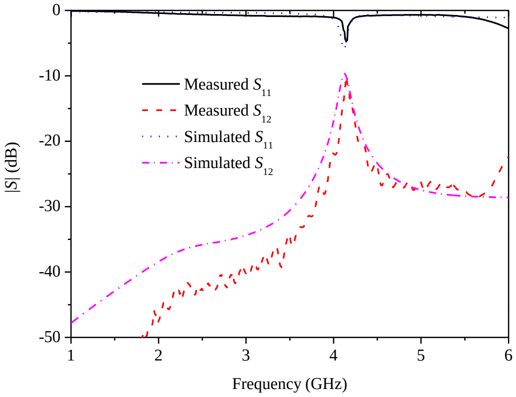

Fig. 9. The S-parameters of the resonator.

C. Mutual coupling reduction of the array

According to the above studies on the proposed DGS and resonator structures, both of them can be involved in the coupling at two different resonant frequencies of the patch array. The DGS reduces the mutual coupling at 2.78 GHz and the resonator does it at 4.12 GHz.

In order to investigate their effects on mutual coupling reduction of the array, different combinations of the DGS and resonator structures are studied. Firstly, the combination of the inverted C-shaped DGS and the C-shaped resonator is investigated. In this case, the openings of the two structures are in the opposite directions, as shown in Fig. 1. L_9 is the distance from the bottom of the resonator to the lower edge of the substrate, while L_{10} is the distance from the top of the DGS to the upper edge of the substrate. The relative positions of the DGS, the resonator and the array change as the values of L_9 and L_{10} vary. Figure 10 and Fig. 11 show the transmission coefficients of the array for different values of L_9 and L_{10}, respectively. It can be seen from the two figures that the relative position of the DGS and the resonator does affect the mutual coupling of the array. When L_9 = 17 mm and L_{10} = 30 mm, the achieved enhancement in port isolation are more than 10 dB and 20 dB at the lower frequency and the higher frequency, respectively.

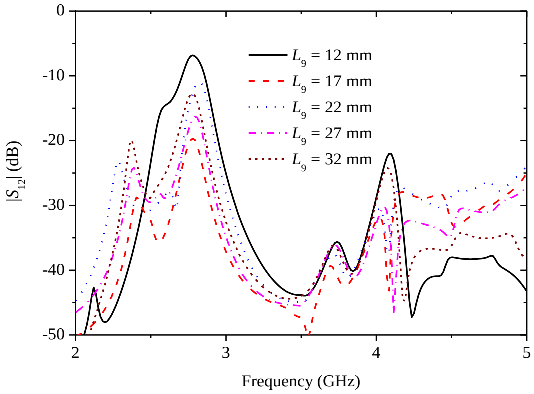

Fig. 10. The transmission coefficients of the array with various L_9.

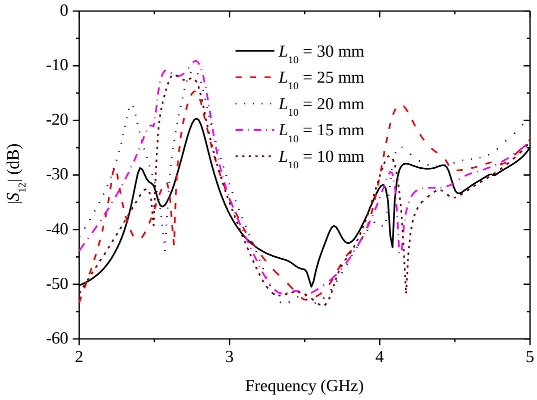

Fig. 11. The transmission coefficients of the array with various L_{10}.

Furthermore, the combination of the C-shaped DGS and the C-shaped resonator is studied. In this case, the openings of the two structures are in the same direction. Figure 12 shows the S-parameters of the array after optimization. It can be seen that the port isolation is increased by 6 dB at the lower frequency and about 20 dB at the higher frequency, which is worse than that of the first one. Therefore, the results of the first design are used in the rest of the paper.

Figure 13 shows the fabricated prototype of the optimized design of the proposed patch array. Figure 14 shows the simulated and the measured reflection coefficients of the patch array with and without the DGS and resonator structures, respectively. With the addition of the DGS and resonator, the array structure is no longer symmetrical, so S_{22} is also shown in Fig. 14. Figure 15 shows the simulated and measured transmission coefficients of the array with and without the DGS and resonator. It can be seen that the simulation results agree well with the measurement results, although with a slight frequency shift. It is also clearly shown in the figures that the measured transmission coefficients have been reduced about 10 dB at 2.78 GHz and 18 dB at 4.12 GHz and the ports of the array are well matched.

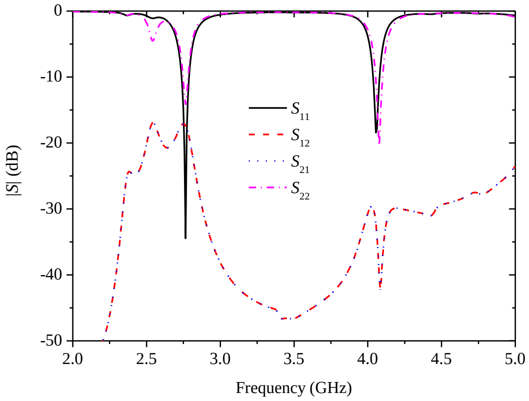

Fig. 12. The S-parameters of the array with the openings of the DGS and resonator in the same direction.

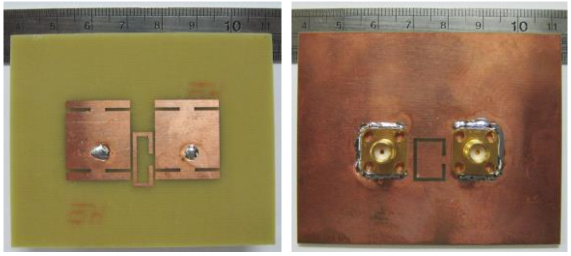

(a) (b)

Fig. 13. The fabricated prototype of the proposed patch array: (a) top view and (b) bottom view.

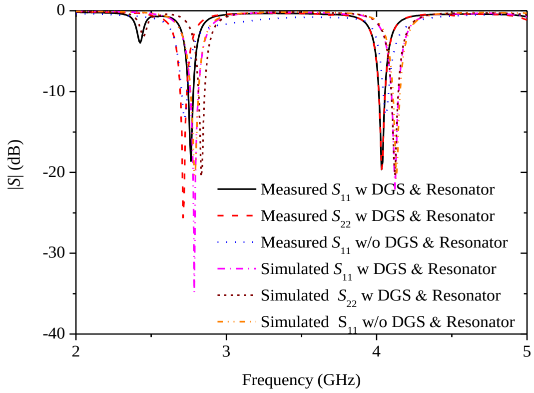

Fig. 14. The simulated and measured reflection coefficients of the array with and without the DGS and resonator.

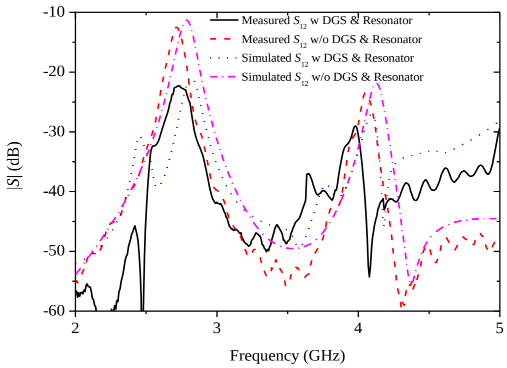

Fig. 15. The simulated and measured transmission coefficients of the array with and without the DGS and resonator.

Figure 16 shows the simulated current distributions at two frequencies 2.78 GHz and 4.12 GHz when the right antenna element is excited while the left one is terminated with a matched load of 50 Ω. It is observed from the figure that without the presence of the DGS and the resonator, a strong mutual coupling exists between the two patches at each resonant frequency. The mutual coupling has been significantly reduced with the implementation of the DGS and the resonator. The calculated radiation efficiency of the proposed array is about 60%. The simulated radiation patterns of the patch array at 2.78 GHz and 4.12 GHz are depicted in Fig. 17. It is obvious that the radiation patterns of the patch array remain their general shapes before and after implementing the DGS and resonator structure.

Correlation coefficient is an important parameter in MIMO applications to evaluate their diversity performance. It is required to minimize the correlation between antenna elements because that the lower the correlation, the higher will be the diversity gain. By assuming uniform external signal source distribution, the envelope correlation coefficient (ECC) can be calculated from the *S*-parameters using [17]:

$$\rho_e(1,2)=\frac{\left|S_{11}^{*}S_{21}+S_{12}^{*}S_{22}\right|^2}{(1-\left|S_{11}\right|^2-\left|S_{21}\right|^2)(1-\left|S_{22}\right|^2-\left|S_{12}\right|^2)}. \qquad (1)$$

Figure 18 shows the envelope correlation of the patch array with and without DGS using the above equation. It can be seen that the envelope correlation in the frequency band of interest is very low, which means that the antenna array has good spatial diversity and is suitable for MIMO applications.

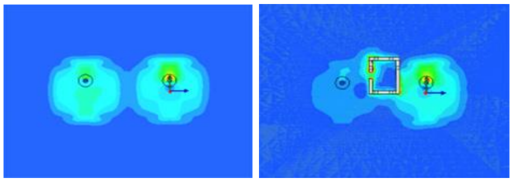
(a) (b)

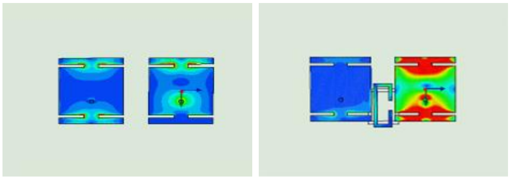
(c) (d)

Fig. 16. Simulated current distributions: within the ground plane at 2.78 GHz: (a) without the DGS and (b) with the DGS. Within the radiating patches at 4.12 GHz: (c) without the resonator and (d) with the resonator.

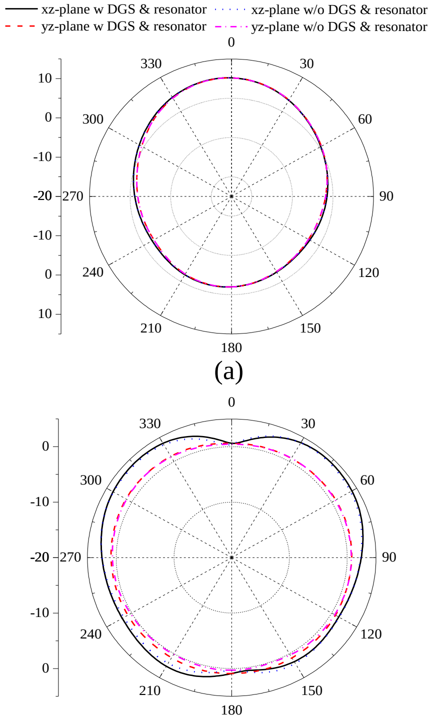

(a)
(b)

Fig. 17. Radiation patterns of the array with and without DGS and resonator: (a) 2.78 GHz and (b) 4.12 GHz.

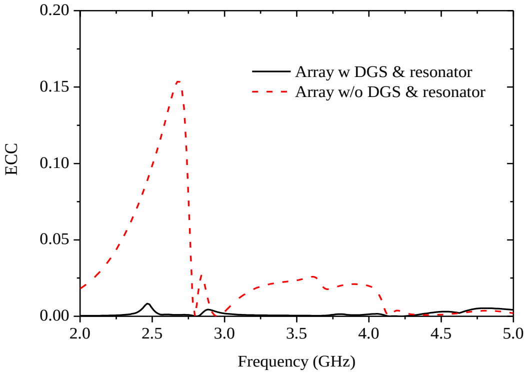

Fig. 18. The calculated envelope correlation coefficient of the patch array with and without DGS and resonator.

The results of the comparison between the proposed array and the other designs in literature are presented in Table 1. It is observed from Table 1 that the proposed DGS and resonator structures help in better isolation enhancement with less edge-to-edge spacing and lower structural complexity.

Table 1: Various comparison between the proposed array and other designs

Paper	Approach	Frequency (f_0) in GHz	Edge to Edge Spacing	Improvement in S_{12} (dB)	Structural Complexity	Size of the Array (mm^2)
[18]	Slotted meander-line resonator	4.8	0.11 λ_0 (7 mm)	6 to 16	Moderate	54×45
[19]	Slotted complementary split-ring resonators	5	0.25 λ_0 (15 mm)	10	High	78×60
[20]	Capacitively loaded loops	0.84 & 2.85	0.067 λ_0 (14 mm)	7 and 9	Very high	50×100
[21]	Meandering slotted high impedance surface	6 & 9.15	3 λ_0 (50 mm)	8 and 13	Very high	100×42
This paper	DGS & resonator	2.78 & 4.12	0.06 λ_0 (7 mm)	10 and 18	Low	75×60

D. Extension to larger array

In this section, we extend the proposed technique to a linear array with four elements. In the new array, the dimensions of the element antenna and the DGS and resonator remain the same as in Section C. The element spacing is still 7 mm. Figure 19 shows the *S*-parameters of the array without the proposed DGS and resonator. It is noticed that the mutual coupling between adjacent elements is highest. The magnitudes of S_{12} at the two operating frequencies are -12 dB and -21 dB, respectively, while $|S_{13}|$ and $|S_{14}|$ are both below -20 dB across the frequency bands. With the addition of the DGS and resonator, the isolation between array elements has been obviously increased. It can be seen from Fig. 20 that $|S_{12}|$ has been reduced to -23 dB at the lower frequency and -30 dB at the higher frequency, while $|S_{13}|$ and $|S_{14}|$ have an averaged reduction of 6-8 dB at the operating frequencies.

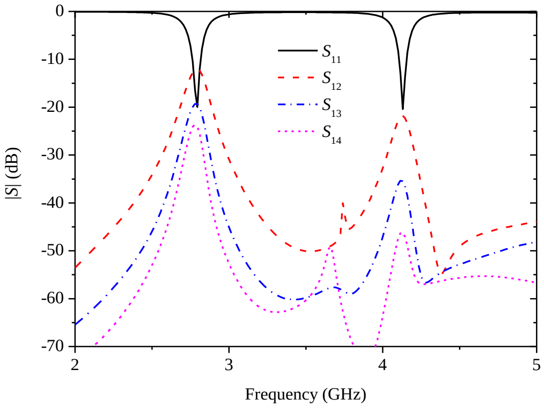

Fig. 19. The *S*-parameters of the four-element array without the proposed DGS and resonator.

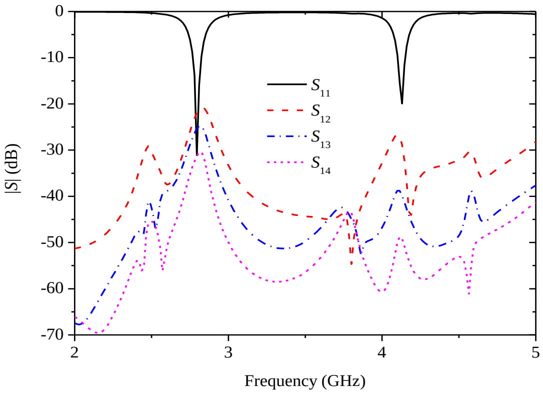

Fig. 20. The *S*-parameters of the four-element array with the proposed DGS and resonator.

IV. CONCLUSION

The mutual coupling reduction of a novel compact patch antenna array with dual resonant frequencies has been presented. Simulations and measurements show that the C-shaped resonator and the inverted C-shaped slot defected ground structure could effectively suppress the mutual coupling of an array at two frequencies simultaneously. The proposed structures are simple and can be easily fabricated together with the printed patches.

ACKNOWLEDGMENT

This work was supported in parts by the National Natural Science Foundation of China (Grant 61101024), the Natural Science Foundation Project of CQ CSTC (Grant CSTC, 2011BB2070), the Fundamental Research Funds for the Central Universities (Grant CDJZR12160013 and 106112014CDJZR165504) and the open research fund of Chongqing Key Laboratory of Emergency Communications.

REFERENCES

[1] A. C. K. Mak, C. R. Rowell, and R. D. Murch, "Isolation enhancement between two closely packed antennas," *IEEE Trans. Antennas Propag.*, vol. 56, no. 11, pp. 3411-3419, 2008.

[2] M. M. Elsewe and D. Chatterjee, "Mutual coupling characterization of ultra-wideband U-slot microstrip patch array antennas," *ACES Express Journal*, vol. 1, no. 1, pp. 36-39, 2016.

[3] A. Diallo, C. Luxey, P. L. Thuc, R. Staraj, and G. Kossiavas, "Study and reduction of the mutual coupling between two mobile phone PIFAs operating in the DCS1800 and UMTS bands," *IEEE Trans. Antennas Propag.*, vol. 54, no. 11, pp. 3063-3073, 2006.

[4] Y. Li, W. Li, and W. Yu, "A multi-band/UWB MIMO/diversity antenna with an enhanced isolation using radial stub loaded resonator," *Appl. Comp. Electro. Society Journal*, vol. 28, no. 1, pp. 8-20, 2013.

[5] K.-L. Wong, J.-H. Chou, S.-W. Su, and C.-M. Su, "Isolation between GSM/DCS and WLAN antennas in a PDA phone," *Microw. Opt. Technol. Lett.*, vol. 45, no. 4, pp. 347-352, 2005.

[6] P. Zibadoost, J. Nourinia, C. Ghobadi, S. Mohammadi, A. Mousazadeh, and B. Mohammadi, "Full band MIMO monopole antenna for LTE systems," *Appl. Comp. Electro. Society Journal*, vol. 29, no. 1, pp. 54-61, 2014.

[7] X.-S. Yang, S.-G. Qiu, and J.-L. Li, "Triangular-arranged planar multiple-antenna for UWB-MIMO applications," *Appl. Comp. Electro. Society Journal*, vol. 29, no. 1, pp. 62-66, 2014.

[8] T. Huang, Y. Yu, and L. Yi, "Design of highly isolated compact antenna array for MIMO applications," *Int. Journal Antennas Propag.*, vol. 2014, Article ID 473063, 5 pages, 2014.

[9] J. C. Coetzee and Y. Yu, "Port decoupling for small arrays by means of an eigenmode feed network," *IEEE Trans. Antennas Propag.*, vol. 56, no. 6, pp. 1587-1593, June 2008.

[10] Z. Li, Z. Du, M. Takahashi, K. Saito, and K. Ito, "Reducing mutual coupling of MIMO antennas with parasitic elements for mobile terminals," *IEEE Trans. Antennas Propag*., vol. 60, no. 2, pp. 473-481, February 2012.

[11] F.-G. Zhu, J.-D. Xu, and Q. Xu, "Reduction of mutual coupling between closely-packed antenna elements using defected ground structures," *Electronic Letters*, vol. 45, no. 12, pp. 601-602, 2009.

[12] A. Farahbakhsh, G. Moradi, and S. Mohanna, "Reduction of mutual coupling in microstrip array antenna using polygonal defected ground structure," *Appl. Comp. Electro. Society Journal*, vol. 26, no. 4, pp. 334-339, 2011.

[13] T. Shabbir, R. Saleem, A. Akram, and F. Shafique, "UWB-MIMO quadruple with FSS-inspired decoupling structures and defected grounds," *Appl. Comp. Electro. Society Journal*, vol. 30, no. 2, pp. 184-109, 2015.

[14] S. Farsi, H. Aliakbarian, D. Schreurs, B. Nauwelaers, and G. A. E. Vandenbosch, "Mutual coupling reduction between planar antennas by using a simple microstrip U-section," *IEEE Antennas Wireless Propag. Lett.*, vol. 11, pp. 1501-1503, 2012.

[15] J. C. Coetzee, "Dual-frequency decoupling networks for compact antenna arrays," *Int. Journal Microwave Science Tech.*, 2011.

[16] Q. Luo, J. R. Pereira, and H. M. Salgado, "Reconfigurable dual-band C-shaped monopole antenna array with high isolation," Electron. Lett., vol. 46, no. 13, pp. 888-889, 2010.

[17] H. Li, X. Lin, B. K. Lau, and S. He, "Equivalent circuit based calculation of signal correlation in lossy MIMO antennas," *IEEE Trans. Antennas Propag.*, vol. 61, no. 10, pp. 5214-5222, 2013.

[18] M. G. N. Alsath, M. Kanagasabai, and B. Balasubramanian, "Implementation of slotted meander-line resonators for isolation enhancement in microstrip patch antenna array," *IEEE Antennas Wireless Propag. Lett.*, vol. 12, pp. 15-18, 2013.

[19] M. M. Bait-Suwailam, O. F. Siddiqui, and O. M. Ramahi, "Mutual coupling reduction between microstrip patch antennas using slotted-complementary split-ring resonators," *IEEE Antennas Wireless Propag. Lett.*, vol. 9, pp. 876-878, 2010.

[20] M. S. Sharawi, A. B. Numan, and D. N. Aloi, "Isolation improvement in a dual-band dual-element MIMO antenna system using capacitively loaded loops," *Progress in Electromagnetics Research*, vol. 134, pp. 247-266, 2013.

[21] X. Chen, L. Li, C. H. Liang, Z. J. Su, and C. Zhu, "Dual-band high impedance surface with mushroom-type cells loaded by symmetric meandered slots," *IEEE Trans. Antennas Propag.*, vol. 60, no. 10, pp. 4677-4687, 2012.

Yantao Yu received the B.Eng. degree (1st class honors) and the Ph.D. degree both from the National University of Singapore, in 2004 and 2009, respectively. From 2008 to 2009, he worked at Motorola Electronics Pte Ltd., Singapore, as an RF Engineer. From 2009 to 2010, he was a Research Fellow with the National University of Singapore. He is currently an Associate Professor in the College of Communication Engineering, Chongqing University, China. His research interests include analysis and design of antennas and compact antenna arrays.

Lijun Yi received the B.Eng. degree from the Chongqing Univesity, China in 2013. He is working toward the Master degree in the same university from 2013. His research interests include mutual coupling of array and wideband antennas.

Xiaoya Liu received the B.Eng. degree from the Northwest Polytechnical University, China in 2014. She is working toward the Master degree in the Chongqing University from 2014. Her research interests include antenna design, decoupling network and microwave circuits.

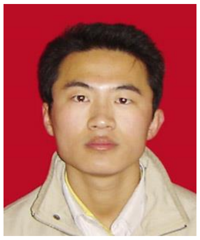

Zhaokai Gu received the B.Eng. degree from the Yantai University, China in 2014. He is working toward the Master degree in the Chongqing University from 2014. His research interests include antenna array and multiband antennas.

DOA Estimation for Unequal Power Sources using Extremely Low Profile Aperture Coupled Microstrip Antenna

Yong Han [1], Qingyuan Fang [*2], Lizhong Song [1], Fenggang Yan [1], Xiaolin Qiao [1], and Shanna Zhuang [2]

[1] School of Electronics and Information Engineering
Harbin Institute of Technology, Weihai, 264209, China

[2] School of Information Science and Technology
Shijiazhuang Tiedao University, Shijiazhuang, 050043, China
fangqingyuanHIT@gmail.com

Abstract **─** In this paper, an aperture coupled microstrip antenna with extremely low profile ($0.022\lambda_c$, λ_c is the wavelength of the center frequency) is proposed and then applied to direction of arrival (DOA) estimation for unequal power sources. Two serial coupling slots resonating at connected frequencies are employed to expand the bandwidth of this microstrip antenna with extremely low profile. Compared with the microstrip antenna fed by a single coupling slot, the bandwidth is increased to 1.37% by using two serial coupling slots. Measurements of the antenna prototype exhibit 6.63% bandwidth ($S_{11} < -10$ dB) and agree well with the simulation results. The measured antenna gain is 5.79 dBi, and the 3 dB beam width is 56° and 112° in the E-plane and H-plane, respectively. In addition, the cross-polarization level of the prototype is −20 dB down from the co-polarization. Finally, the proposed antenna is applied in the DOA estimation for unequal power sources. Simulation results confirmed that the proposed antenna is effective and can be used in passive radar application.

Index Terms **─** Aperture coupled antenna, DOA estimation, H-shaped coupling slot, low profile, passive radar, unequal power sources.

I. INTRODUCTION

Aperture coupled microstrip antennas are extensively used for target estimation, localization, and recognition in radar systems because of their compact structure and low cost [1, 2]. With the growing demands for multi-tasking in the radar system, the space for each electronic device is strictly restricted, including the antenna. However, the compressed space will seriously limit the bandwidth of microstrip antennas, especially for the aperture coupled microstrip antenna, which is sensitive to the profile height [3-5].

For microstrip antennas, various methods have been proposed to achieve wide bandwidth. For example, a thick substrate with low permittivity is applied to expand the bandwidth; however, a thicker substrate suffers from decreased efficiency due to surface wave generation [6]. By employing diverse apertures [7] on the radiating patches, such as quasi-ring aperture [8], E-shaped aperture [9], and U-shaped aperture [10], the bandwidth can be improved. Generally, an aperture-loading technique is applied to probe feed microstrip antenna and will cause decreasing of the front-to-back (F/B) ratio for aperture coupled microstrip antennas [8]. The parasitic [11, 12] and stacked patches [13, 14] resonating at connected frequencies are applied to increase the bandwidth of the aperture coupled microstrip antennas. However, the parasitic and stacked patches will increase the antenna size or height, and such increase is undesirable for electronic devices with very limited space. To decrease the profile, artificial magnetic conductor (AMC) and electromagnetic bandgap (EBG) structures are exploited [15, 16] in the design of microstrip antennas. However, excessive parameters of AMC and EBG structures increase the design complexity and cost of antennas. Hence, concise bandwidth-enhancement methods for aperture coupled microstrip antennas with extremely low profile remain to be investigated.

Antennas working as electromagnetic wave sensors play an important role in subsequent signal processing, such as DOA estimation. Aperture coupled microstrip antennas have been widely used in DOA estimations [17-19]. DOA estimation methods based on array signal processing have been highly developed in the past three decades. One class of method, called subspace method, is very representative, in which the multiple signal classification (MUSIC) is intensively studied for its good performance in resolving adjacent sources [20-22]. However, the performance of the MUSIC method suffers

Submitted On: September 30, 2015
Accepted On: July 4, 2016

from great degradation when confronted with unequal power sources [23, 24]. Moreover, in most DOA estimation literature, the performances of proposed DOA methods for unequal power sources are seldom discussed. Actually, the sources with different power levels are very common in electronic warfare environment. For example, the powers of targets and decoys are usually different, whereas sources with equal power levels seldom exist. Hence, the performance discussion of DOA methods for unequal power sources based on aperture coupled microstrip antennas is of great significance for passive radar.

In this work, two serial H-shaped slots are exploited to expand the bandwidth of a microstrip antenna with extremely low profile ($0.022\lambda c$). The bandwidth is effectively expanded without increasing the antenna profile or fabrication complexity. In addition, the H-shaped coupling slots can move the resonant frequency to a lower band, which is useful in antenna miniaturization. The measurements of the antenna prototype are in good agreement with the simulation results, which exhibit 6.63% bandwidth (from 1.415 GHz to 1.512 GHz), stable antenna gain, broad beam width, and low cross-polarization level. To investigate the performance of the proposed antenna on DOA estimation for unequal power sources, a subspace method that utilizes the noise subspace eigenvalues to estimate the DOAs of unequal power sources [25] is applied to the proposed antenna. The simulation results demonstrate that the proposed antenna can be used for DOA estimation with unequal power sources and show better performance when applied as a method in [25] than the MUSIC method.

II. ANTENNA CONFIGURATION

As shown in Fig. 1, the proposed antenna is a 2 × 1 array (87 mm apart from each other) consisting of two square radiating patches etched on layer A (Rogers 4003C substrate with relative permittivity of 4.5 and thickness 0.508 mm) and a ground plane etched on layer C (Rogers 5880 substrate with relative permittivity of 2.2 and thickness 0.508 mm).

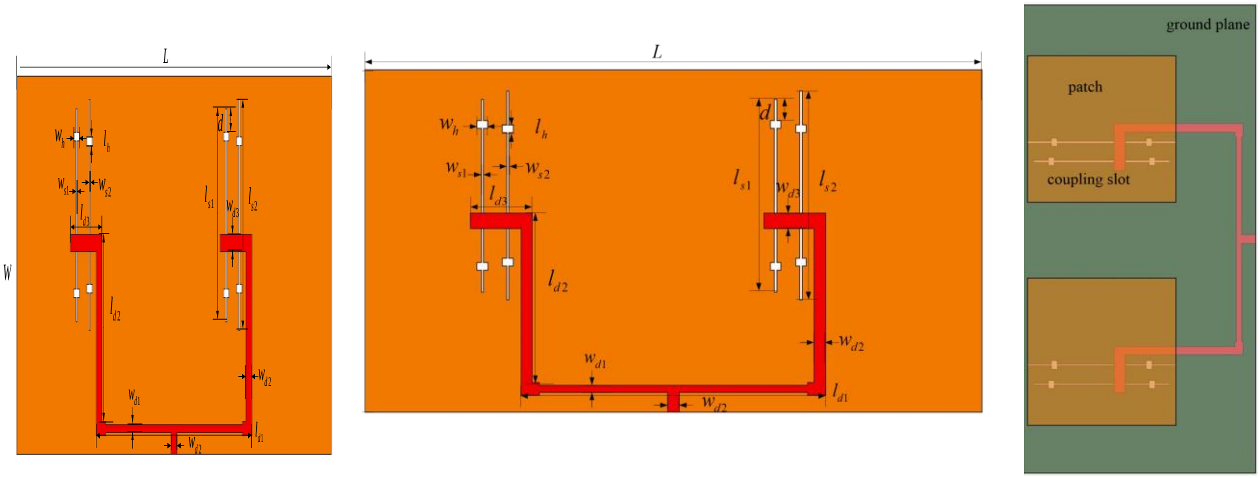

(a) (b) (c)

Fig. 1. Antenna array geometry with key parameters: (a) Side view, (b) ground plane and power divider, and (c) cross views.

Between the radiating patches and the ground plane is an air space (Layer B) with relative dielectric constant 1 and thickness of 4.5 mm ($0.022\lambda_c$). The length of the square radiating patches printed on the bottom side of layer A is 53.20 mm. Two serial H-shaped coupling slots are embedded in the ground plane at the bottom side of layer C. The coupling slots with slightly different lengths resonating at connected working frequencies are exploited to expand the bandwidth of the antenna. The parameters of proposed antenna are optimized by Ansoft HFSS. The final parameters of the proposed antenna are listed in Table 1.

Table 1: Antenna parameters

Parameter	Value (mm)	Parameter	Value (mm)
W	87.00	L	170.00
w_{d1}	2.45	l_{d1}	83.90
w_{d2}	3.13	l_{d2}	43.11
w_{d3}	4.00	l_{d3}	17.00
w_{s1}	0.68	l_{s1}	49.00
w_{s2}	0.70	l_{s2}	53.00
w_h	1.16	l_h	2.00
d	7.50		

III. SIMULATED AND MEASURED RESULTS AND DISCUSSION

The thickness of the air layer is 4.5 mm, which is extremely low ($0.022\lambda_c$@1.46GHz) and will seriously affect the bandwidth of the microstrip antenna. The coaxial probe fed microstrip antennas with such ultralow profile are studied in [7, 10, 26, 27]. In [7], the multi-couple staggered slots on the patch produce a 3.9% bandwidth with substrate thickness of $0.022\lambda_c$. In [26], an E-shaped microstrip patch antenna illustrates a 15.2% bandwidth with a low profile of $0.0583\lambda_c$. In [27], and [28], the U-slot microstrip antennas show 11.3% and 20%–30% bandwidth with $0.0581\lambda_c$ and $0.08\lambda_c$ profiles, respectively. However, little research has been conducted on the aperture coupled microstrip antenna with extremely low profile. In the present work, an effective and concise method employing two H-shaped coupling slots is studied.

A. Bandwidth comparison between antennas with different numbers of coupling slots

The configurations of aperture coupled microstrip antennas with one, two, and three coupling slots are shown in Fig. 2. In Fig. 2 (a), the length of feed line (l_{d3}) is 14 mm, and the length of coupling slot (l_{s2}) is 56 mm, which is optimized to match with the feed network. In Fig. 2 (b), the length of the middle slot is 51 mm, and other parameters are the same as those of the antenna shown in Fig. 1.

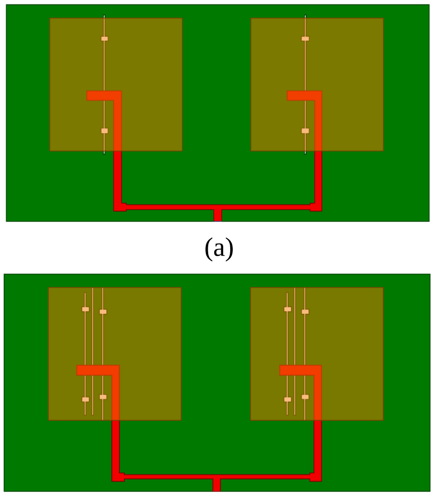
(a)

(b)

Fig. 2. Aperture coupled microstrip antennas with different coupling slots: (a) one coupling slot and (b) three coupling slots.

The simulated results of reflection coefficient (S_{11}) for antennas with different numbers of coupling slots are shown in Fig. 3, in which the bandwidths of antennas with one, two, and three coupling slots are 3.76% (from 1.434 GHz to 1.489 GHz), 5.13% (from 1.424 GHz to 1.499 GHz), and 5.54% (from 1.386 GHz to 1.465 GHz), respectively. Notably, the impendence bandwidth increased to 36.4% by utilizing two serial coupling slots compared with one coupling slot.

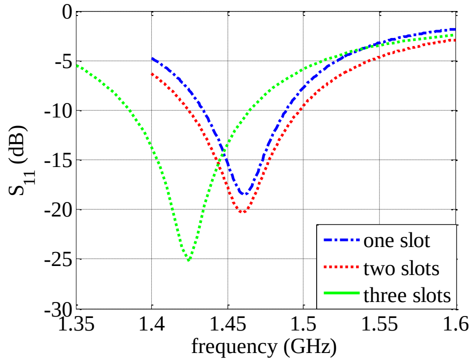

Fig. 3. Simulated S_{11} of antennas with different numbers of coupling slots.

The amplitudes of the surface current distributions at different frequencies on the ground plane are shown in Fig. 4. As shown in Fig. 4 (a), the longer coupling slot is excited more strongly than the shorter coupling slot. This finding indicates that the performance of the antenna at 1.43 GHz (lower working frequency) is mainly determined by the longer coupling slot. As shown in Fig. 4 (b), the shorter slot is excited at 1.5 GHz. However, only one longer coupling slot is available in Fig. 4 (c). Therefore, the working bandwidth will be narrower than that of the antenna with two resonant coupling slots.

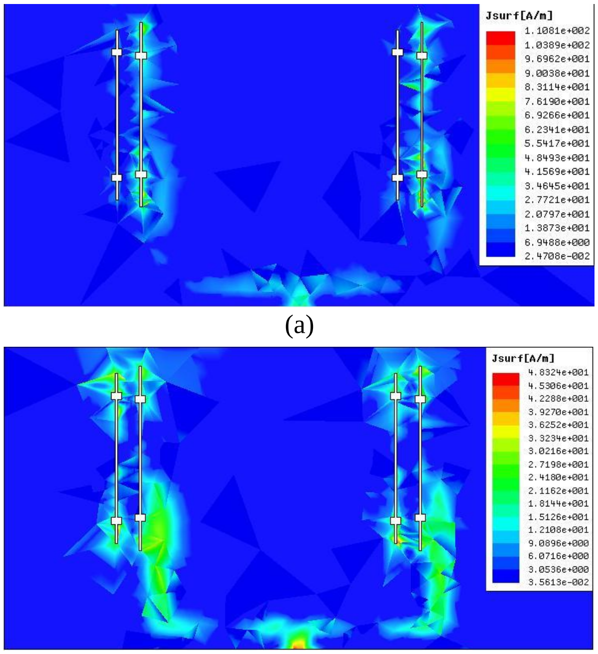

(a)

(b)

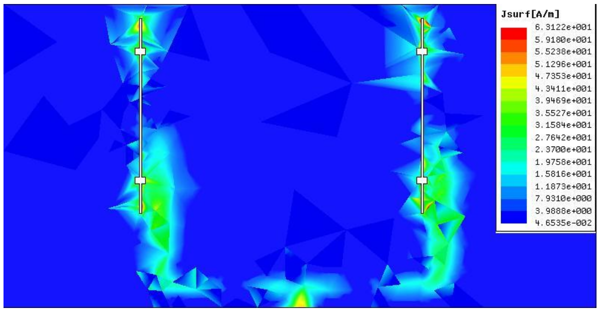

(c)

Fig. 4. Surface current distributions: (a) antenna with two coupling slots at 1.43 GHz, (b) antenna with two coupling slots at 1.5 GHz, and (c) antenna with one coupling slot at 1.5 GHz.

Consequently, an additional serial slot can enhance the working bandwidth of an aperture coupled microstrip antenna, which can also be applied to other aperture coupled antenna designs. Notably, the coupling slots on the ground plane will deteriorate the F/B ratio; thus, a trade-off between the bandwidth and the F/B ratio should be made. In this work, a configuration with two coupling slots is studied and fabricated.

B. Parametric study

Parameters with critical influence on the performance of the proposed antenna are studied. The effects on working frequency introduced by the length of coupling slots (l_{s1} and l_{s2}) are shown in Fig. 5. It is noted that the working frequency is sensitive to the length of coupling slots. Extending l_{s1} will shift the working frequency to a lower band, so does the same of l_{s2}. Comparison of Fig. 5 (a) and Fig. 5 (b) shows that the longer coupling slot exerts a dominant effect in determining the working frequency. Simulation results of S_{11} at different widths of the coupling slot are shown in Fig. 6. The width of coupling slots can slightly influence the resonant frequency; however, this width also influences the impendence matching.

In the proposed antenna, the optimization results of w_{s1} and w_{s2} are 0.68 and 0.70 mm, correspondingly.

The effects of tiny slot parameters, such as length l_h, width w_h, and the position of the tiny slot on the antenna performance are shown in Fig. 7. As illustrated in Figs. 7 (a) and 7 (b), increasing the slot width and length will move the working frequency to the lower band. Compared with the slot length l_h, the antenna is more easily influenced by the slot width w_h.

The influence of tiny slot position on the antenna performance is presented in Fig. 8. The distance of the tiny slot from the top of the long slot is denoted by d. From Fig. 8, we can conclude that the position of the tiny slot also affects the working frequency of the antenna. The operation frequency increases as the tiny slot moves far away from the long slot center.

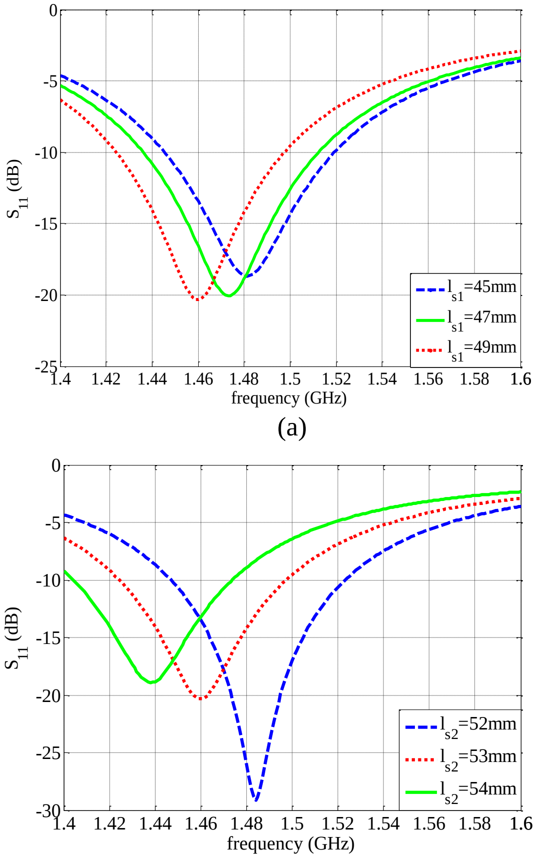

(a)

(b)

Fig. 5. Simulated S_{11} with different lengths of coupling slots: (a) simulated S_{11} under l_{s2} = 53 mm, and (b) simulated S_{11} under l_{s1} = 49 mm.

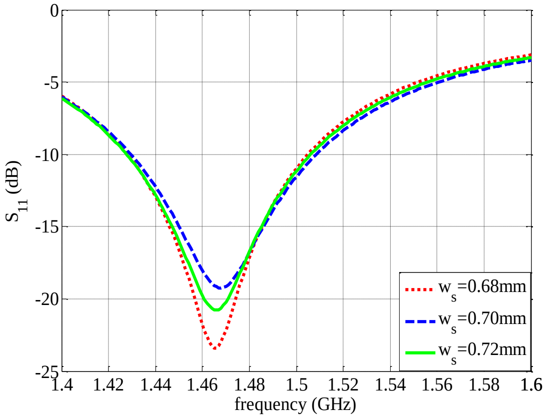

Fig. 6. Simulated S_{11} with different coupling slot widths.

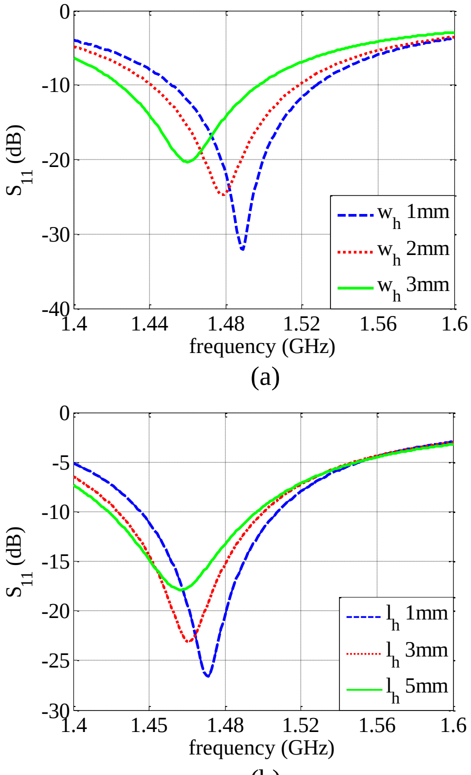

(a)

(b)

Fig. 7. Simulated S_{11} with different parameters of tiny slot perpendicular to the long coupling slot: (a) with different w_h and (b) with different l_h.

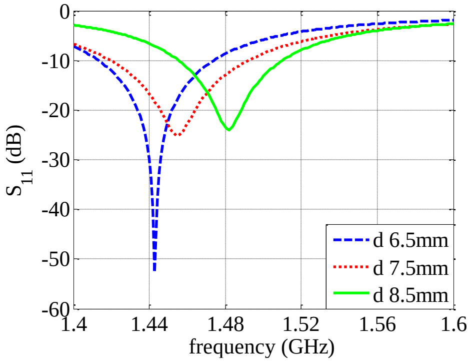

Fig. 8. Simulated S_{11} with different tiny slot positions.

The normalized input impedance as a function of w_h and l_h is shown in Fig. 9. The working frequency is decreased when w_h and l_h are increased. As shown in Fig. 9, increasing the w_h and l_h also increases the normalized input resistance and reactance. Simultaneously, the resonant frequency is shifted to the lower band.

After the parametric studies, the effects of coupling slots on the performance of antenna are clearly understood and can be referred to when we design other aperture coupled microstrip antennas. The tiny slots play an important role in determining the working frequency of the proposed antenna. Simulated results of S_{11} when employing H-shaped coupling slots (with tiny slots) and conventional slots (without tiny slots) are shown in Fig. 10; the resonant frequency of the proposed antenna is shifted to a lower frequency band when the H-shaped coupling slots are employed compared with conventional coupling slots.

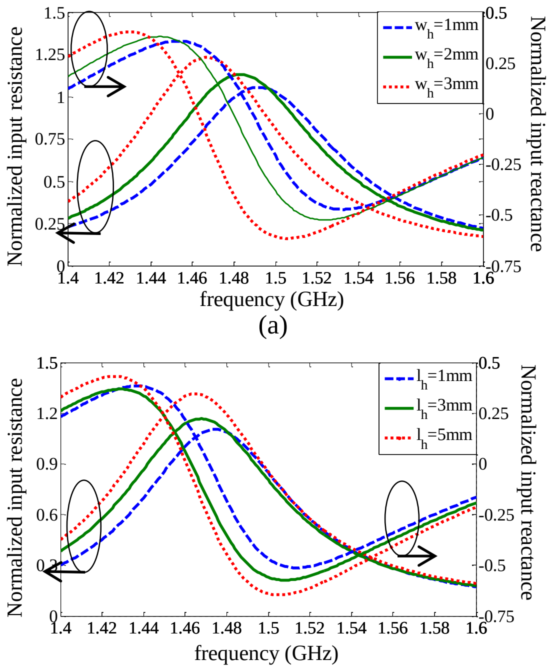

(a)

(b)

Fig. 9. Normalized input impedance of the proposed antenna: (a) with different w_h and (b) with different l_h.

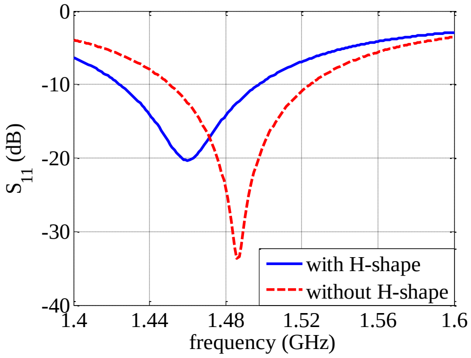

Fig. 10. Simulated S_{11} with H-shaped coupling slots and conventional coupling slots.

C. Experimental results

As shown in Fig. 11, a prototype of the proposed antenna with an overall size of $0.83\lambda_c \times 0.43\lambda_c \times 0.022\lambda_c$ is fabricated and measured with an Agilent E8363B vector network analyzer. The measured S_{11} is shown in Fig. 12, which illustrates a bandwidth of 6.63% (from 1.415 GHz to 1.512 GHz) as $S_{11} < -10$ dB and agrees well with the simulation result.

The simulated and measured antenna gain (Table 2) presents the same tendency as the frequency varies from low to high. The measured antenna gain is lower than the simulation results, which may be caused by the loss of substrate and fabrication errors. The gain of the proposed antenna is not as high as the traditional microstrip antenna because of the apertures in the ground plane leading to back radiation.

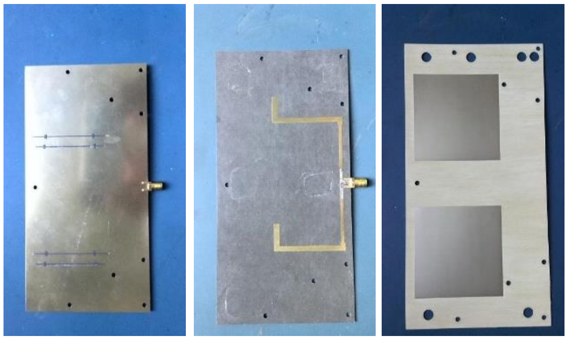

(a) (b) (c)

Fig. 11. Antenna prototype: (a) the ground plane with coupling slots, (b) the feed network, and (c) the radiating patches.

Table 2: Antenna gain

Frequency (GHz)	Simulated Gain (dB)	Measured Gain (dB)
1.42	6.02	4.37
1.45	6.25	5.32
1.48	6.47	5.39
1.51	6.70	5.79

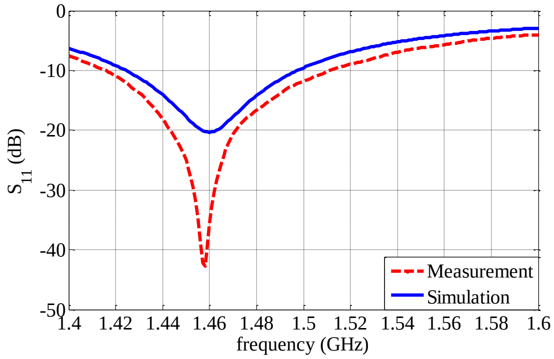

Fig. 12. Measured and simulated results of S_{11} as a function of frequency.

The normalized radiation patterns at 1.45 GHz are measured in both principal planes and are shown in Fig. 13. The half-power beam width (HPBW) of the proposed antenna is 56° and 112° in the E-plane and H-plane, respectively. The measured and simulated radiation patterns show good agreement with each other. The cross-polarization level is approximately −20 dB down from the co-polarization on boresight in both E-plane and H-plane. The F/B ratio is not very high at approximately 10 dB. This can be attributed to the coupling slots in the ground plane leading to the leakage of the electromagnetic wave.

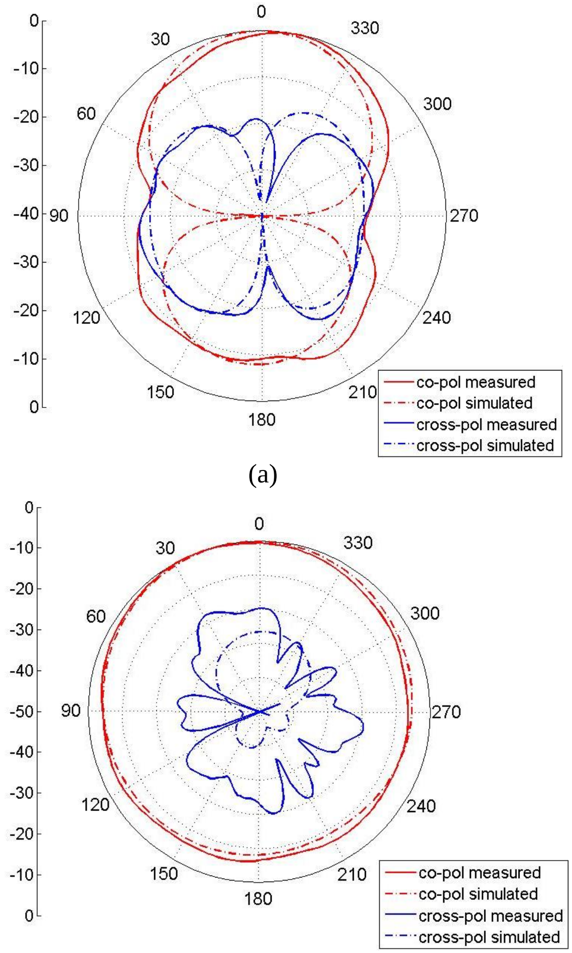

(a)

(b)

Fig. 13. Measured and simulated results of normalized co-polarized and cross-polarized radiation patterns at 1.45 GHz: (a) in xoy plane (E-plane) and (b) in yoz plane (H-plane).

IV. DOA ESTIMATION EXPERIMENT FOR UNEQUAL POWER SOURCES

Aperture coupled microstrip antennas used for DOA estimation are extensively studied [17-19]. DOA estimation is the first step for target detection in passive radar application and can provide target direction to passive radar for target tracking until the target is destroyed. The performance of microstrip antennas when applied in DOA estimation has been investigated extensively by employing the MUSIC method [22, 28]. In those studies, the DOA estimation for sources (targets) with equal power levels is intensively investigated. However, the performance of DOA estimation for unequal power sources when employing microstrip antennas as the receiving antenna array is seldom conducted. Sources with unequal power levels are commonly observed in practical applications, especially in passive radar. In electronic warfare environment, multiple targets exhibit different power levels. For example, decoys are usually disposed around the real target (usually the active radar) to protect it from being attacked. In this case, the decoys and the real target transmit unequal power signals that reach the receiving antenna array of passive radar simultaneously. Therefore, the received signals often present unequal power levels for passive radar. However, the performance of the MUSIC method suffers from great degradation when resolving the unequal power sources. Once the DOA estimation of the target becomes inaccurate, the following target location, recognition, and tracking will deteriorate sharply. In this work, another subspace method [25] is applied to DOA estimation for unequal power sources based on the proposed antenna. Simultaneously, the performance of the MUSIC method for unequal power sources based on the proposed antenna is also simulated to make comparisons with the method in [25].

In [25], the invariance property of the noise subspace (IPNS) is proposed when the powers of the sources are increased. We call the method proposed in [25] as the IPNS method. The invariant noise subspace eigenvalues are then used to estimate the DOAs of the sources. The uniform linear antenna array configuration used for DOA estimation is shown in Fig. 14.

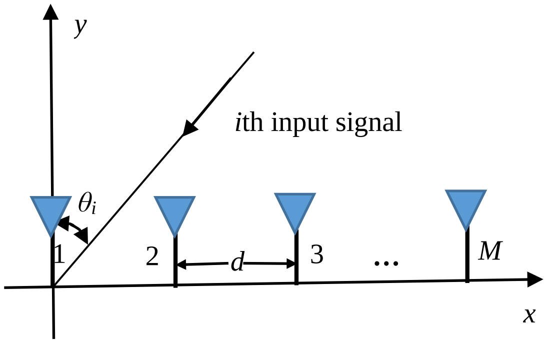

Fig. 14. Configuration of uniform linear array.

The number of antenna element is M, and the distance between each element is d. The total number of input signals is P. The DOA of the ith input signal is θ_i. The covariance matrix of the antenna array output $\mathbf{R}$ can be replaced by a maximum likelihood estimate $\hat{\mathbf{R}}$ expressed as:

$$\hat{\mathbf{R}} = 1/L\sum_{j=1}^{L}\mathbf{X}(t_j)\mathbf{X}(t_j)^{\mathrm{H}}, \tag{1}$$

where $\mathbf{X}(t)=[x_1(t)\cdots x_M(t)]^{\mathrm{T}}$ is the array signal vector, L is the number of snapshots, $(\bullet)^{\mathrm{H}}$ and $(\bullet)^{\mathrm{T}}$ denote the conjugate transpose and the transpose, respectively. The noise subspace eigenvalues $\lambda_i, i = P+1, P+2, \cdots M$ can be obtained through the eigenvalue decomposition (EVD) of $\mathbf{R}$. In the IPNS method, another covariance matrix is constructed as follows:

$$\mathbf{D} = \mathbf{R} + h\mathbf{a}(\theta)\mathbf{a}(\theta)^{\mathrm{H}}, \tag{2}$$

where $\mathbf{a}(\theta)$ is the steering vector of the receiving antenna array. In [25], the noise subspace eigenvalues of $\mathbf{D}$ have been proven to remain the same as $\mathbf{R}$ when only the power of the input signals increased. This invariance property of the noise subspace can be used for DOA estimation. Therefore, the spatial spectrum obtained from the IPNS method is given as

$$P(\theta) = \frac{1}{\sum_{i=P+1}^{M}(\hat{\mu}_i - \hat{\lambda}_i)}, \tag{3}$$

where $\hat{\mu}_i$ and $\hat{\lambda}_i$ are the noise subspace eigenvalues of the sample covariance matrix $\hat{\mathbf{D}}$ and $\hat{\mathbf{R}}$, respectively. The sample covariance matrix $\hat{\mathbf{D}}$ is obtained through $\hat{\mathbf{D}} = \hat{\mathbf{R}} + h\mathbf{a}(\theta)\mathbf{a}(\theta)^{\mathrm{H}}$, where $h = \mathrm{tr}(\hat{\boldsymbol{R}})/M$ and $\mathrm{tr}(\hat{\boldsymbol{R}})$ denote the trace of $\hat{\mathbf{R}}$. The DOAs of the sources are the P maxima of $P(\theta)$.

A uniform linear array comprising five proposed antennas is used to estimate the DOAs of the unequal power sources. The coupling between the antennas is not considered to assess the influence of unequal power levels on the spatial spectrums. Assuming that the strong signal (signal to noise ratio, SNR 25 dB) impinges from −6° and −3°, the weak signal (SNR 5 dB) impinges from 6° and 3°. The spatial spectrums of the MUSIC method and IPNS method when employing the measured and simulated antenna radiation patterns are shown in Figs. 15 (a) and 14 (b).

As shown in Fig. 15, the proposed antenna can be used to perform DOA estimation for unequal power sources; the DOA estimation methods also showed almost the same performance when using the simulated and measured antenna radiation patterns. This finding indicates that the measured radiation pattern of the proposed antenna is in good agreement with the simulation results. Comparison of Figs. 15 (a) and 15 (b) shows that the MUSIC method is insufficient, whereas the IPNS method is valid in resolving the adjacent unequal power sources. The capability of DOA methods in distinguishing the adjacent sources will directly affect their performance when they are applied in engineering applications. The experiment demonstrates that the proposed antenna can be applied to perform DOA estimation for unequal power sources. Sources with unequal powers are commonly observed in an electronic warfare environment. The received signals usually present unequal power levels, especially for passive radar application. The real active radar and decoys of the enemy used as jamming to protect the active radar demonstrate different power levels. The signals with unequal powers transmitted from the active radar and decoys reach the antenna array of the passive radar simultaneously. As shown in Fig. 15, the IPNS method is more efficient in resolving the adjacent sources than the MUSIC method, especially for unequal power sources, when the proposed antenna is used as the receiving antenna array element. Therefore, the IPNS method based on the proposed antenna is more capable in resolving the adjacent real targets and decoys, which are significant for passive radar in anti-jamming application.

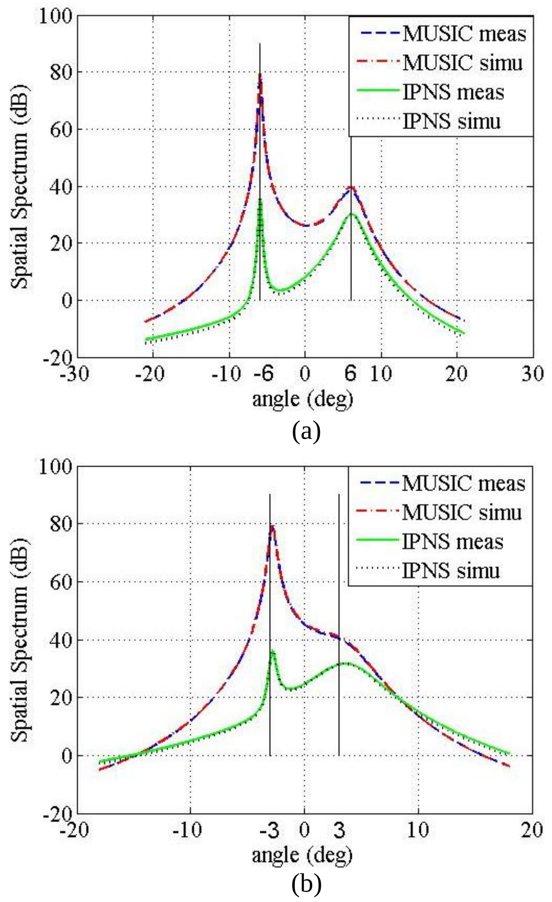

Fig. 15. Spatial spectra of different methods using the measured and simulated antenna radiation patterns: (a) large angle separation, and (b) small angle separation.

V. CONCLUSION

A serial H-shaped aperture coupled microstrip antenna with extremely low profile is investigated and applied in DOA estimation for unequal power sources. The proposed antenna exhibits a bandwidth of 6.63% (from 1.415 GHz to 1.512 GHz) and increases 1.37% bandwidth compared with one coupling slot aperture coupled antenna. Good radiation patterns and low cross-polarization level are also available. The serial coupling slots, which does not increase the design and manufacture complexity, is demonstrated to comprise an effective method to expand the bandwidth of the aperture coupled microstrip antenna. Moreover, the proposed antenna proved to be valid in the DOA estimation for unequal power sources, which is useful in passive radar to estimate the target and decoys.

ACKNOWLEDGMENT

This work was supported by the Natural Science Foundation of China (Grant No. 61571154), Natural Science Foundation of Hebei Province (No. F2014210123), Natural Scientific Research Innovation Foundation in Harbin Institute of Technology (HIT.NSRIF 2013130), Shandong Provincial Natural Science Foundation (ZR2014FQ003), China Postdoctoral Science Foundation (2015M571414), and the Fundamental Research Funds for the Central Universities (HIT.NSRIF.2016102).

REFERENCES

[1] S. Gao, L. W. Li, M. S. Leong, and T. S. Yeo, “A broad-band dual-polarized microstrip patch antenna with aperture coupling,” *IEEE Trans. Antennas Propagat*., vol. 51, no. 4, pp. 898-900, 2003.

[2] C. J. Meagher and S. K. Sharma, “A wideband aperture-coupled microstrip patch antenna employing spaced dielectric cover for enhanced gain performance,” *IEEE Trans. Antennas Propagat*., vol. 58, no. 9, pp. 2802-2810, 2010.

[3] F. Yang, X. X. Zhang, X. Ye, and Y Rahmat-Samii, “Wide-band E-shaped patch antennas for wireless communications,” *IEEE Trans. Antennas Propagat*., vol.49, no. 7, pp. 1094-1100, 2001.

[4] H. S. Shin and N. Kim. “Wideband and high-gain one-patch microstrip antenna coupled with H-shaped aperture,” *Electron. Lett.*, vol.38, no.19, pp. 1072-1073, 2002.

[5] K. L. Wong, H. C. Tung, and T. W. Chiou, “Broadband dual-polarized aperture-coupled patch antennas with modified H-shaped coupling slots,” *IEEE Trans. Antennas Propagat*., vol. 50, no. 2, pp. 188-191, 2002.

[6] K. F. Lee and K. F. Tong, “Microstrip patch antennas-Basic characteristics and some recent advances,” *Proc. IEEE*, vol. 100, no. 7, pp. 2169-2180, 2012.

[7] S. Xiao, Z. Shao, B. Z. Wang, M. T. Zhou, and M. Fujise, “Design of low-profile microstrip antenna with enhanced bandwidth and reduced size,” *IEEE Trans. Antennas Propagat*., vol. 54, no. 5, pp. 1594-1599, 2006.

[8] M. M. Honari, A. Abdipour, and G. Moradi, “Bandwidth and gain enhancement of an aperture antenna with modified ring patch,” *IEEE Antennas Wireless Propag. Lett*., vol. 10, pp. 1413-1416, 2011.

[9] B. K. Ang and B. K. Chung, “A wideband E-shaped microstrip patch antenna for 5-6 GHz wireless communications,” *Prog. Electromagn. Res.*, vol. 75, pp. 397-407, 2007.

[10] A. Khidre, K. F. Lee, A. Z. Elsherbeni, and F. Yang, “Wide band dual-beam U-slot microstrip antenna,” *IEEE Trans. Antennas Propagat*., vol. 61, no. 3, pp. 1415-1418, 2013.

[11] T. Y. Yang, W. Hong, and Y. Zhang, “Wideband high - gain low - profile dual - polarized stacked patch antenna array with parasitic elements,” *Microw. Opt. Techn. Let.*, vol. 57, no. 9, pp. 2012-2016, 2015.

[12] C. Deng, “Wideband microstrip antennas loaded by ring resonators,” *IEEE Antennas Wireless Propag. Lett*., vol. 12, pp. 1665-1668, 2013.

[13] M. Barba, “A high-isolation, wideband and dual-linear polarization patch antenna,” *IEEE Trans. Antennas Propagat*., vol. 56, no. 5, pp. 1472-1476, 2008.

[14] A. A. Serra, P. Nepa, G. Manara, G. Tribellini, and S. Cioci, “A wide-band dual-polarized stacked patch antenna,” *IEEE Antennas Wireless Propag. Lett*., vol. 6, pp. 141-143, 2007.

[15] A. P. Feresidis, G. Goussetis, S. Wang, and J. C. Vardaxoglou, “Artificial magnetic conductor surfaces and their application to low-profile high-gain planar antennas,” *IEEE Trans. Antennas Propagat*., vol. 53, no. 1, pp. 209-215, 2005.

[16] J. Liang and H. Y. D. Yang, “Radiation characteristics of a microstrip patch over an electromagnetic bandgap surface,” *IEEE Trans. Antennas Propagat*., vol. 55, no. 6, pp. 1691-1697, 2007.

[17] K. Gotsis, K. Siakavara, and J. N. Sahalos, “On the direction of arrival (DoA) estimation for a switched-beam antenna system using neural networks,” *IEEE Trans. Antennas Propagat*., vol. 57, no. 5, pp. 1399-1411, 2009.

[18] N. J. G. Fonseca, M. Coudyser, J. J. Laurin, and J. Brault, “On the design of a compact neural network-based DOA estimation system,” *IEEE Trans. Antennas Propagat*., vol. 58, no. 2, pp. 357-366, 2010.

[19] M. Coulombe, S. F. Koodiani, and C. Caloz, “Compact elongated mushroom (EM)-EBG structure for enhancement of patch antenna array performances,” *IEEE Trans. Antennas Propagat*., vol. 58, no. 4, pp. 1076-1086, 2010.

[20] R O. Schmidt. Multiple emitter location and signal parameter estimation [J], *IEEE Trans. Antennas Propagat*., vol. 34, no. 3, pp. 276-280, 1986.

[21] F. G. Yan, M. Jin, S. Liu, and X. L. Qiao, “Real-valued MUSIC for efficient direction estimation with arbitrary array geometries,” *IEEE Trans. Signal Proces*., vol. 62, no. 6, pp. 1548-1560, 2014.

[22] C. H. Niow and H. T. Hui, “Improved noise modeling with mutual coupling in receiving antenna arrays for direction-of-arrival estimation,” *IEEE Trans. Wireless Commu*., vol. 11, no. 4, pp. 1616-1621, 2012.

[23] Q. Fang, Y. Han, M. Jin, and X. L. Qiao, “Joint DOA and polarization estimation for unequal power sources,” *International Antenna. Propagat.*, 2015.

[24] M. L. McCloud and L. L Scharf, “A new subspace identification algorithm for high-resolution DOA estimation,” *IEEE Trans. Antennas Propagat*., vol. 50, no. 10, pp. 1382-1390, 2002.

[25] A. Olfat and S. Nader-Esfahani, “A new signal subspace processing for DOA estimation,” *IEEE Proc. Microwave Antenna Propagat.*, vol. 84, no. 4, pp. 721-728, 2004.

[26] B. K. Ang and B. K. Chung, “A wideband E-shaped microstrip patch antenna for 5-6 GHz wireless communications,” *Prog. Electromagn. Res.*, vol. 75, pp. 397-407, 2007.

[27] K. F. Lee, K. M. Luk, K. F. Tong, S. M. Shum, T. Huynh, and R. Q. Lee, “Experimental and simulation studies of the coaxially fed U-slot rectangular patch antenna,” *Proc. IEEE*, vol. 144, no. 5, pp. 354-358, 1997.

[28] M. Coulombe, S. F. Koodiani, and C. Caloz, “Compact elongated mushroom (EM)-EBG structure for enhancement of patch antenna array performances,” *IEEE Trans. Antennas Propagat*., vol. 58, no.4, pp. 1076-1086, 2010.

Yong Han was born in Heilongjiang Province, China, in 1976. He received his Ph.D. degree from Harbin Institute of Technology, Harbin, China, in 2010. He is now a Lecturer in the School of Information and Electrical Engineering in Harbin Institute of Technology, Weihai, China. His research interests include array signal processing and polarization sensitive array signal processing.

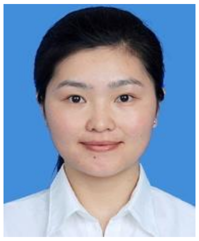

Qingyuan Fang was born in Shandong Province, China, in 1987. She received her M.S. degree and Ph.D. degree from Harbin Institute of Technology in 2010 and 2015, respectively. Now, she is a Lecturer in the School of Information Science and Technology in Shijiazhuang Tiedao University, Shijiazhuan, China. Her research interests include anti-jamming technology in passive radar and antenna technology.

Lizhong Song was born in Liaoning Province, China, in 1975. He received the Master degree and Ph.D. degree from Harbin Institute of Technology in 2001 and 2005, respectively. He is a Professor and Doctoral Supervisor of Harbin Institute of Technology at Weihai. His research interests include antenna design, wireless electromagnetic wave propagation, microwave technology and radar signal processing.

Fenggang Yan was born in ShaXi, China, in 1983. He received the B.E., M.S., and Ph.D. degrees in Information and Communication Engineering from Xi'an Jiaotong University, Xi'an, the Graduate School of Chinese Science of Academic, Beijing, and Harbin Institute of Technology (HIT), Harbin, in 2005, 2008, and 2013, respectively. Since August 2015, he has been an Associate Professor with the Department of Electronics Information Engineering, HIT, Weihai, China. His current research interests include array signal processing and statistical performance analysis

Xiaolin Qiao was born in Inner Mongolia Autonomous Region, China, in June 1948. He received the B.E., M.S., and Ph.D. degrees in Information and Communication Engineering from Harbin Institute of Technology, Harbin, China, in1976, 1983, and 1991, respectively. His research interests are in the areas of signal processing, wireless communication, special radar, parallel signal processing, and radar polarimetry.

Shanna Zhuang was born in Henan Province, China, in 1985. She received the B.Sc. degree in Electrical Information Engineering in 2007 and the Ph.D. degree in Communication and Information System in 2012 from Nanjing University of Science and Technology, Nanjing, China. She is now a Lecturer in the School of Information Science and Technology in Shijiazhuang Tiedao University, Shijiazhuang, China. Her research interests include cognitive radar and adaptive waveform design.

On and Off-Body Radio Channel Performance of a Dual Band and Dual Mode Antenna

Mohammad Monirujjaman Khan [1,2]

[1] Department of Electrical and Computer Engineering
North South University, Bashundhara, Dhaka, 1229, Bangladesh
monirkhan.qmul@gmail.com

[2] School of Electronic Engineering and Computer Science
Queen Mary University of London, Mile End, London E1 4NS, United Kingdom

Abstract ─ In this paper, measurement results of on-body radio propagation channels at 2.45 GHz and off-body radio propagation channels at 1.9 GHz using dual band and dual mode (DBDM) antenna are presented. The proposed antenna works at two different frequencies with different radiation modes. Experiments are performed first in the chamber and then in an indoor environment. The path loss has been characterized for ten different on-body radio channels at 2.45 GHz. Five off-body radio channels are studied at 1.9 GHz. The path loss was modeled as a function of distance for on-body radio propagation at 2.45 GHz and off-body radio propagation at 1.9 GHz. For on-body propagation, the path loss exponent is noticed to be 2.48 and 2.22 in the camber and sensor laboratory, respectively. For off-body radio propagation case, the path loss exponent is noticed to be 1.27. The proposed antenna shows very good on-body and off-body radio propagation channel performance.

Index Terms ─ Body-centric wireless communications, dual band and dual mode antenna, on/off-body communications, path loss.

I. INTRODUCTION

The rapid development of biosensors and wireless communication devices brings new opportunities for Body-Centric Wireless Networks (BCWNs) which has recently received increasing attention due to their promising applications in medical sensor systems and personal entertainment technologies. Body-centric wireless communications (BCWCs) is a central point in the development of fourth generation mobile communications. In body-centric wireless networks, various units/sensors are scattered on/around the human body to measure specified physiological data, as in patient monitoring for healthcare applications [1-5]. A body-worn base station will receive the medical data measured by the sensors located on/around the human body. In BCWCs, communications among on-body devices are required, as well as communications with external base stations.

Antennas are the essential component for wearable devices in body-centric wireless networks and they play a vital role in optimizing the radio system performance. The human body is considered an uninviting and even hostile environment for a wireless signal. The diffraction and scattering from the body parts, in addition to the tissue losses, lead to strong attenuation and distortion of the signal [1]. In order to design power-efficient on-body and off-body communication systems, accurate understanding of the wave propagation, the radio channel characteristics and attenuation around the human body is extremely important.

Researchers have been comprehensively investigating narrow band and ultra wideband on-body radio channels recently. In [6-11], on-body radio channel characterisation was presented at the unlicensed frequency band of 2.45 GHz. In body-centric wireless communications, there is a need of communications among the devices mounted on the body as well as off-body devices. In previous study, researchers have designed the antennas for on-body communications and investigated the on-body radio channel performance both in narrowband and ultra wideband technologies. However, in common healthcare monitoring scenarios, it is very important for the antenna to radiate over the body surface omni-directionally and also directive towards off the body units in order to get the best on body and off-body radio channel performances, i.e., minimise the link loss to ensure power efficiency. Body-centric wireless devices need to offer low power consumption in order to extend the battery life of the body worn devices and also need to provide power-efficient and reliable on-body and off-body communications [12]. Antenna with omni-directional radiation pattern over the body surface improves the path gain for the on-body links while antenna with directive off-body radiation pattern

Submitted On: November 16, 2014
Accepted On: June 4, 2015

improves the path gain for off-body channels.

This paper presents experimental results of on-body and off-body radio propagation channels of dual band and diverse radiation pattern antenna. The antenna used in this study works at two different frequency bands as 2.45 GHz (ISM band) with omnidirectional radiation pattern over the human body surface and 1.9 GHz (PCS band) with off-body radiation mode from the human body. The 2.45 GHz is used for the communication over human body surface (on-body) and 1.9 GHz is used for the communication from body mounted devices to off-body units (off-body communications). Experiments were performed in the Body-Centric Wireless Sensor Laboratory and Anechoic Chamber in Queen Mary University of London. In this study, a frequency-domain measurement set-up was applied. For on-body case, the path loss for ten different on-body radio channels is shown and analysed. For off-body case, the path loss for five different radio propagation channels at 1~6 meter distance locations in indoor environment is investigated.

The rest of the paper is organized as follows; Section II discusses about the antenna, on-body radio channel measurements setting and on-body results, Section III presents off-body radio channels measurement settings and results, and finally Section IV provides the conclusion.

II. ON-BODY RADIO PROPAGATION CHANNEL STUDY AT 2.45 GHz

A. On-body radio channel characterisation at 2.45 GHz

The on-body radio channel performance at 2.45 GHz of the dual band and dual mode (DBDM) antenna has been experimentally investigated. Figure 1 shows the fabricated dual band and dual mode antenna. The antenna was modelled on FR4 substrate with a thickness of 1.57 mm and a relative permittivity of 4.6. There is a full ground plane at the backside of the substrate with the size of 60×60 mm. The antenna contains two radiating elements, a disk loaded Monopole and circular Patch [12].

The antenna was designed using Computer Simulation Technology (CST) Microwave Studio^{TM} and then fabricated in the antenna laboratory in Queen Mary University of London. The antenna is simulated both in free space and on the human phantom (ground plane 4 mm away from right chest) using Computer Simulation Technology (CST) Microwave Studio^{TM}. The human body employed is the commonly available detailed multi-layer model namely the 'visible male model' developed by the US Air Force [13]. The resolution of the model applied is 4 mm with the electrical properties of human tissues defined at 2.45 GHz and 1.9 GHz, respectively, for all organs and tissues used including heart, lungs, muscle, fat, skin, etc. [14-15]. The on-body performances (return loss and radiation pattern) of the antenna were measured on the real human body (4 mm away from right chest). Figure 2 shows the free space and on-body return loss responses of the proposed antenna. The antenna works at 2.45 GHz and 1.9 GHz. The antenna is proposed to use in body-centric wireless communications where communication is necessary both to the devices on body and to the external off body networks nodes. The top loaded disk Monopole structure is to get the resonance at 2.45 GHz with omnidirectional radiation pattern over the body surface to communicate with other body worn devices whereas the lower circular patch on the FR4 board is for 1.9 GHz with off the body directive radiation mode to communicate power-efficiently from on-body device to off-body units. At 2.45 GHz, this dual band dual mode antenna radiates omnidirectionally over the body surface of the human body which is good to set up power-efficient on-body communication with other collocated devices on the body and at 1.9 GHz it produces directional radiation pattern towards off the body which will be good for power-efficient communication from on-body device to off-body units. The free space and on-body radiation patterns of the proposed DBDM antenna are shown in Figs. 3 and 4, respectively. The antenna shows very good bandwidth, radiation efficiency and gain when it is placed on the human body. More details about the free space and on-body performance parameters (radiation pattern, bandwidth, gain and radiation efficiency) of this antenna are available in [12].

Fig. 1. Fabricated version of the dual band and dual mode (DBDM) antenna [12].

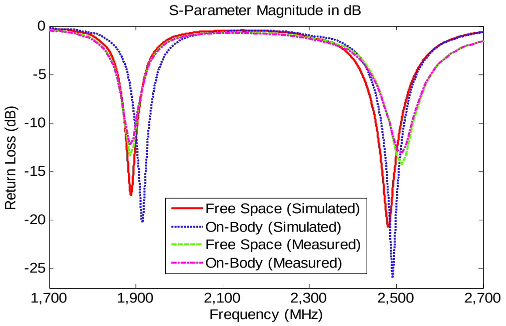

Fig. 2. Simulated and measured free space and on-body return loss responses of the proposed dual band and dual mode antenna [12].

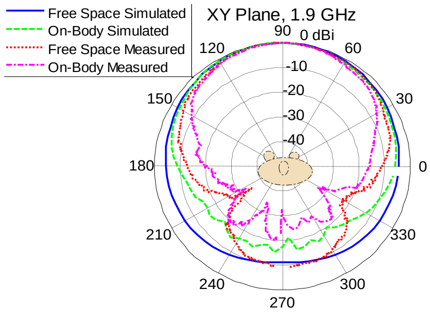

(a) XY plane at 1.9 GHz

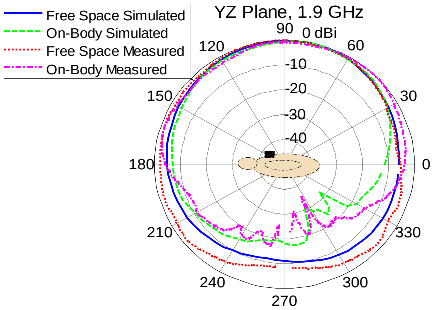

(b) YZ plane at 1.9 GHz

Fig. 3. Simulated and measured free space and on-body radiation patterns of the proposed dual-band and dual mode antenna: (a) XY plane at 1.9 GHz, and (b) YZ plane at 1.9 GHz.

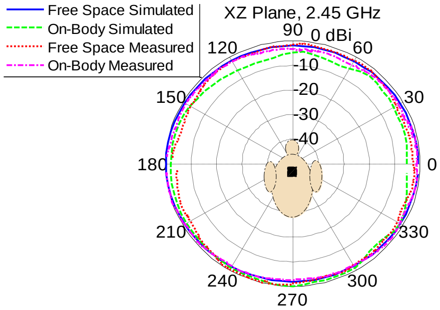

(a) XZ plane at 2.45 GHz

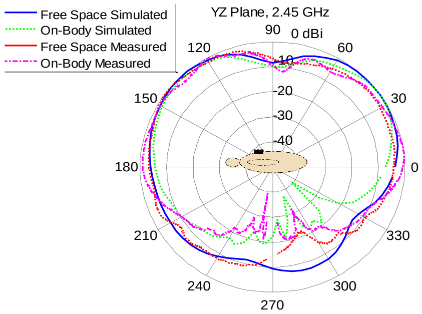

(b) YZ plane at 2.45 GHz

Fig. 4. Simulated and measured free space and on-body radiation patterns of the proposed dual-band and dual mode antenna: (a) XZ plane at 2.45 GHz, and (b) YZ plane at 2.45 GHz.

In this study for on-body radio propagation channel study at 2.45 GHz, the S21 measurements of the proposed DBDM antenna were performed in an anechoic chamber and in the indoor environment. An average-sized real male test subject, with a height of 1.74 m and a weight of 80 kg was used. In this study, a pair of DBDM antenna was used. A HP8720ES vector network analyser was used to measure the transmission response (S21) between two DBDMs placed on the body.

The transmitter antenna connecting with the cable was placed on the left waist, while the receiver antenna connecting with the cable was successively placed on 10 different locations on the front part of the standing human body; as shown in Fig. 5. The test subjects were standing still during the measurements and, for each receiver location and measurement scenario, 10 sweeps were considered. The effects of the cable were calibrated out.

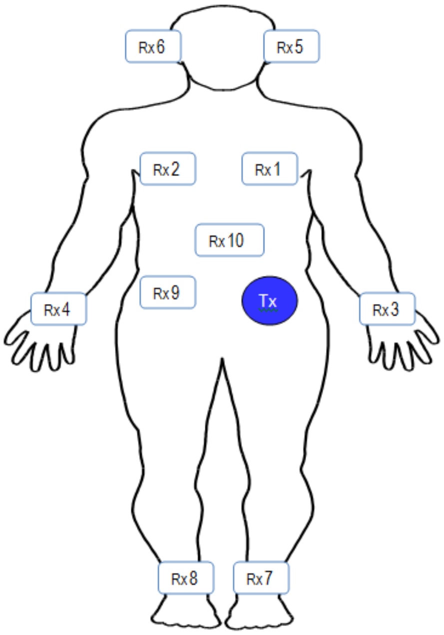

Fig. 5. On-body radio propagation channel measurement settings at 2.45 GHz showing the transmitter antenna is on the left waist while the receiver antenna is on 10 various locations of the body.

The on-body measurements were first performed in the anechoic chamber and then repeated in the Body-Centric Wireless Sensor Laboratory at Queen Mary, University of London. The total area of the laboratory is 45 m^2 which includes a meeting area, treadmill machine, workstations and a hospital bed for healthcare applications [16-17].

The path loss for the different receiver locations was computed directly from the measurement data of S21 (10 sweeps) averaging at 2.45 GHz. Figure 6 shows the comparison of path loss for left waist to ten different on-body links measured in the chamber and in an indoor environment.

Results show that for both in the chamber and in indoor environment cases, the lowest path loss value is observed for the left waist to left chest and left wrist links while the highest is noticed for the right ear and right wrist channels. This is so happened because for left chest left wrist channels, the communication distance between the transmitter antenna and the receiver antenna is less and there is direct Line-Of-Sight (LOS) communication but for the right ear and right wrist the communication distance between the Receiver (Rx) antenna and Transmitter (Tx) antenna is higher moreover the communication is blocked by human body and the presence of Non-Line-Of-Sight (NLOS) communication. The average path loss of ten different on-body channels is noticed to be higher in the chamber than in the sensor laboratory. The higher path loss value for on-body links in the anechoic chamber may be due to the non-reflecting environment. The average of ten different on-body link's path loss in the sensor laboratory is noticed to be 44.48 dB, while in the chamber it is noticed to be 42.05 dB. Based on the results and analysis, it is noticed that this antenna shows very good on-body radio channel performance at 2.45 GHz.

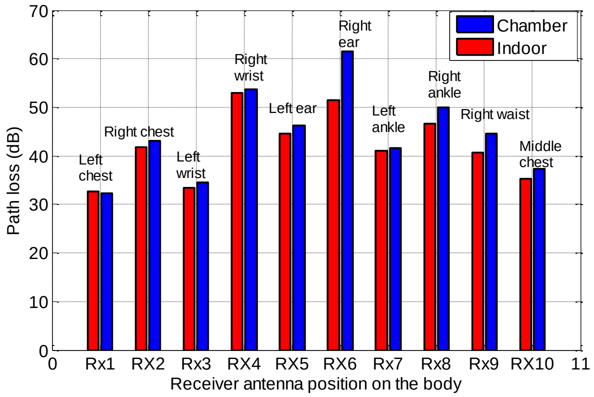

Fig. 6. Comparison of path loss for left waist to 10 different on-body links measured in the chamber and in an indoor environment.

B. Path loss vs. distance

The path loss was modelled as a function of distance for 31 different receiver locations for propagation along the front part of the body. In this case, the transmitter DBDM antenna connecting with cable was placed on the left waist and the receiver DBDM antenna was attached on 31 different locations on the front part of the body; as shown in Fig. 7.

The average received signal decreases logarithmically with distance for both indoor and outdoor environments as explained in [18]:

$$PL_{dB}(d) = PL_{dB}(d_0) + 10\gamma\log(\frac{d}{d_0}) + X_\sigma, \quad (1)$$

where d is the distance between transmitter and receiver, d_0 is a reference distance set in measurement (in this study it is set to 10 cm), $PL_{dB}(d_0)$ is the path loss value at the reference distance, and X_σ is the shadowing fading. The parameter γ is the path loss exponent that indicates the rate at which the path loss increases with distance [15].

In order to extract the path loss exponent a least-square fit technique was performed on the measured path loss for the 31 different receiver locations, (Fig. 7).

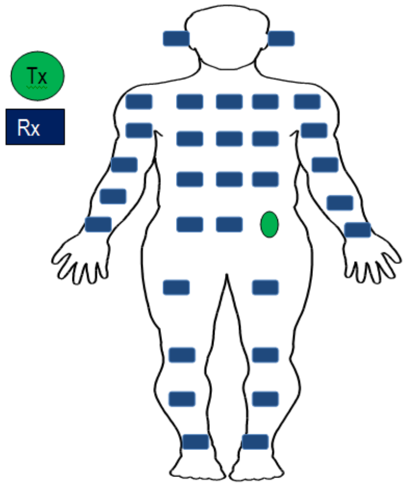

Fig. 7. On-body measurement settings at 2.45 GHz showing the transmitter is on the left waist and the receiver antenna is on 31 different locations of the body.

The measured value and modelled path loss for on-body channels versus logarithmic Tx-Rx separation distance are shown in Fig. 8. The path loss exponent was found to be 2.48 in the chamber and 2.22 in indoor (Table 1). In the indoor environment, the path loss exponent was found to be lower compared to chamber. Results and analysis show that when measurements are performed in indoor, the reflections from surroundings scatters increase the received power, causing reduction in the path loss exponent. A reduction of 10.48% was noticed in indoor compared to the chamber in this case.

X_σ is a zero mean, normal distributed statistical variable, and is introduced to consider the deviation of the measurements from the calculated average path loss. Figure 9 shows the deviation of measurements from the average path loss fitted to a normal distribution for both measurement cases. The standard deviation of the normal distribution value is noticed to be slight smaller in the indoor environment (Table 1).

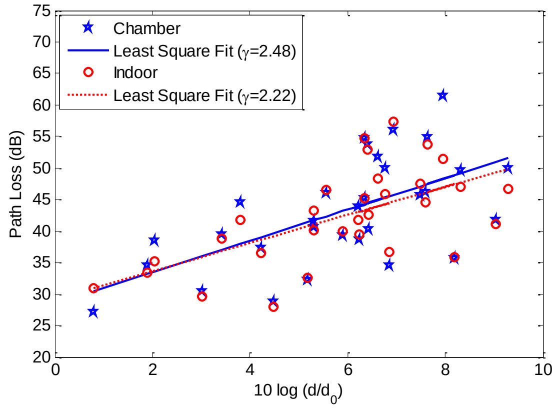

Fig. 8. Measured and modelled path loss for on-body channel versus logarithmic transmitter (Tx) and receiver (Rx) separation distance for the DBDM antenna at 2.45 GHz.

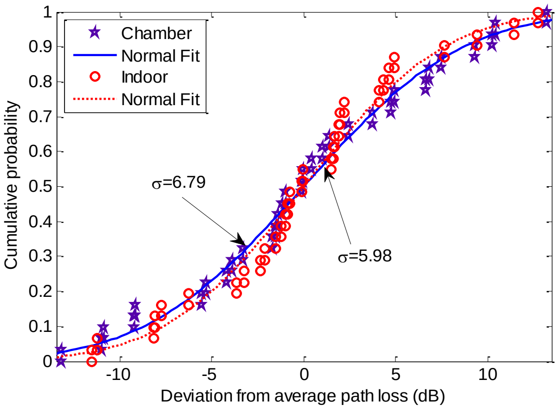

Fig. 9. Deviation of measurement from the average path loss (fitted to normal distribution) for the dual band and dual mode antenna at 2.45 GHz.

Table 1: On-body path loss parameters at 2.45 GHz

Path Loss Parameters	Chamber	Indoor
γ	2.48	2.22
$PL_{dB}(d_0)$ (dB)	28.45	29.22
σ (dB)	6.79	5.98

III. OFF-BODY RADIO PROPAGATION CHANNELS STUDY AT 1.9 GHz

A. Off-body radio channel characterisation at 1.9 GHz

In this section, off-body radio propagation measurement at 1.9 GHz is performed in the Body-Centric Wireless Sensor Laboratory at Queen Mary, University of London using the same dual band dual mode (DBDM) antenna. Five different off-body radio channels were considered. A receiver antenna connected with Vector Network Analyser (VNA) was placed on the ceiling near the wall, as shown in Fig. 10 (b). During measurement, the transmitter antenna connecting with the other port of the VNA was attached on five different locations on the human body as right chest, left waist, left wrist, right ear, left ankle, as shown in Fig. 10 (a). During the measurement, the test subject was standing still at 1 to 6 metre locations with the interval of 1 metre facing towards the receiver antenna. The VNA transmission power was set to 0 dBm. For each location and measurement scenario 10 sweeps were considered.

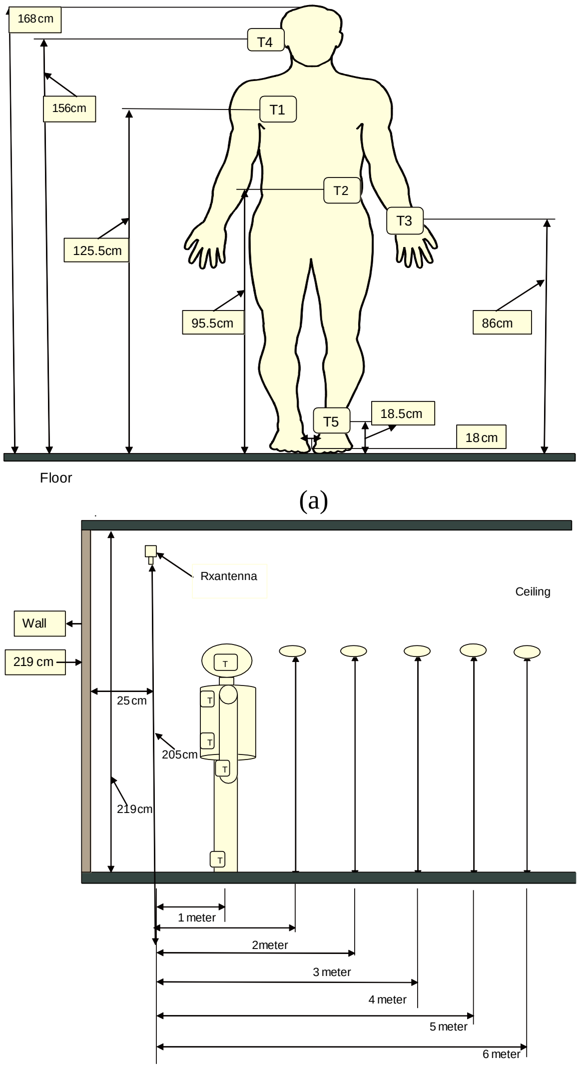

(a)

(b)

Fig. 10. Off-body measurement settings at 1.9 GHz, (a) locations of the antenna on the human body, and (b) measurement scenarios and side view showing transmitter antenna and the antenna on the human body.

The path loss for each different off-body channel is calculated directly from the measurement data S21 (10 sweep) averaging at 1.9 GHz. Figure 11 shows the comparison of path loss for five different off-body channels, when subject was standing still at 1~6 metre locations measured in indoor environment. At one metre distance location, the lowest path loss is noticed for the receiver to the chest link and the highest is noticed at the ear and ankle links. The chest link has the lowest communication distance and LOS communication with the receiver antenna as compared to the ankle link resulting the lowest path loss value for this link. Though, the communication distance between the receiver antenna and the right ear link is less but higher path loss value is noticed which is due to the different orientation of the transmitter antenna located on the right ear. At one metre distance, the average path loss of five off-body links is 45.84 dB, while at six metre distance it is noticed to be 54.27 dB. Results show that as the distance increases, the path loss for most of the off-body radio channels increases. This antenna shows good off-body radio channel performance at 1.9 GHz.

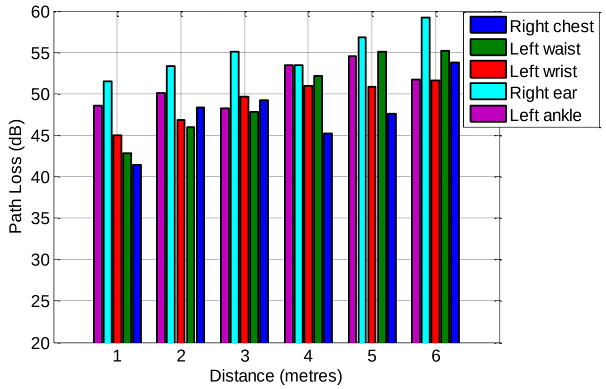

Fig. 11. Comparison of path loss for five different off-body channels, when subject was standing still at 1~6 metre locations measured in an indoor environment.

In this case, the path loss was modeled as a function of distance for 30 different receiver locations at 1.9 GHz. A least square fit technique is performed on measured path loss for all 5 off-body channels (1-6 metre) at 30 different transmitter locations to extract the path loss exponent (see Table 2). Figure 12 shows the measured value and modelled path loss for off-body channel versus logarithmic Tx-Rx separation distance showing path loss exponent for the dual band and dual mode antenna at 1.9 GHz. In this study, the path loss exponent is found to be 1.27. Results and analysis show that this proposed dual band and dual mode (DBDM) antenna shows very good path loss exponent value at 1.9 GHz for off-body radio propagation.

Figure 13 shows the deviation of measurements from the average path loss fitted to a normal distribution for dual band antenna dual mode antenna at 1.9 GHz. In the indoor, the standard deviation of the normal distribution for this antenna is σ =3.11.

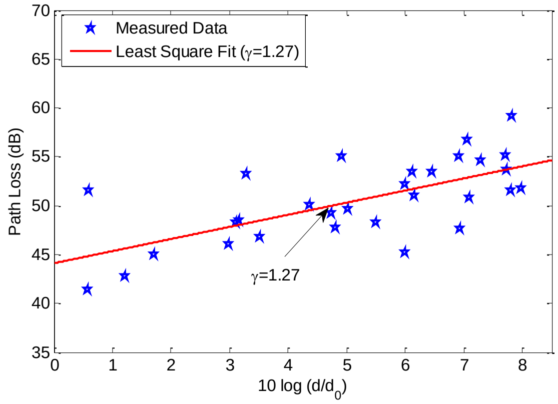

Fig. 12. Measured and modelled path loss for off-body channel versus logarithmic transmitter (Tx) and receiver (Rx) separation distance for the dual band and dual mode (DBDM) antenna at 1.9 GHz.

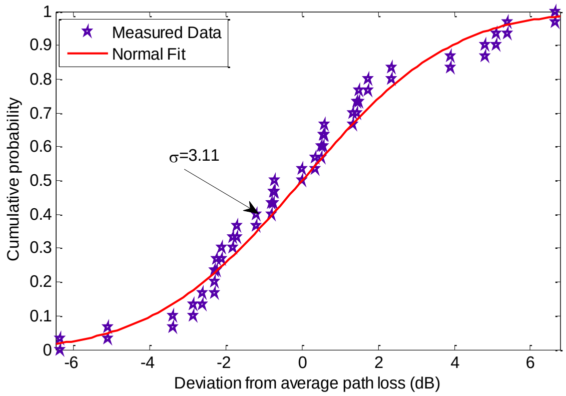

Fig. 13. Deviation of measurement from the average path loss (fitted to normal distribution) for the dual band and dual mode antenna at 1.9 GHz for off-body case.

Table 2: Off-body path loss parameters at 1.9 GHz

Path Loss Parameters	Results
γ	1.27
$PL_{dB}(d_0)$ (dB)	44.11
σ (dB)	3.11

IV. CONCLUSION

The on-body radio channel performance at 2.45 GHz and off-body radio channel performance at 1.9 GHz of a dual band and dual mode (DBDM) antenna is experimentally investigated in this paper. Measurements are performed both in the anechoic chamber and in an indoor environment. On and off-body radio channels have been characterized and analyzed. For on-body case, the path loss for ten different on-body radio channels measured in the anechoic chamber and sensor laboratory is shown and analysed. For off-body case, the path loss for five different off-body radio channels at 1 to 6 metre distance locations measured in indoor environment is investigated. A least square fit method was performed on the measured path loss results for on-body radio propagation at 2.45 GHz and off-body radio propagation at 1.9 GHz. The proposed dual band and dual mode (DBDM) antenna shows very good on-body and off-body radio channel performance; hence it will be suitable candidate for body-centric wireless communications in order to set up power-efficient communication between body mounted devices and also with the off-body units.

ACKNOWLEDGMENT

The authors of this paper would like to thank John Dupuy for his help with the antenna fabrication. The authors also would like to thank Peter for his help during the measurement.

REFERENCES

[1] P. S Hall and Y. Hao, *Antennas and Propagation for Body-Centric Wireless Communications*. Artech House, 2006.

[2] C. Kunze, U. Grossmann, W. Stork, and K. Muller-Glaser, "Application of ubiquitous computing in personal health monitoring systems," in *Biomedizinische Technik*: *36th Annual Meeting of the German Society for Biomedical Engineering*, pp. 360-362, 2002.

[3] N. F. Timmons and W. G. Scanlon, "Analysis of the performances of IEEE 802.15.4 for medical sensor body area networking," in *1st Annual IEEE Communications Society Conf. Sensor Ad. Hoc Communications and Networks (SECON)*, pp. 16-24, Oct. 4-7, 2004.

[4] WSN for Healthcare: A Market Dynamics Report, Published Aug. 2008.

[5] M. Presser, T. Brown, A. Goulianos, S. Stavrou, and R. Tafazolli, "Body-centric context aware application scenarios,'' antennas and propagation for body-centric wireless communications," 2007 *IET Seminar*, Apr. 24, 2007.

[6] A. Alomainy, Y. Hao, A. Owadally, C. G. Parini, Y. Nechayev, C. C. Constantinou, and P. S. Hall, "Statistical analysis and performance evaluation for on-body radio propagation with microstrip patch antenna," *IEEE Transactions on Antennas and Propagation*, vol. 55, no. 1, Jan. 2007.

[7] Y. Nechayev, P. Hall, C. C. Constantinou, Y. Hao, A. Owadally, and C. G. Parini, "Path loss measurements of on-body propagation channels," in Proc. *2004 International Symposium on Antennas an Propagation*, Sendai, Japan, pp. 745-748, Aug. 2004.

[8] Y. Hao, A. Alomainy, P. S. Hall, Y. I. Nechayev, C. G. Parini, and C. C. Constantinou, "Antennas and propagation for body-centric wireless communications," *IEEE/ACES International Conference on Wireless Communications and Applied Computational Electromagnetics*, Honolulu, Hawaii, USA, Apr. 3-7, 2005.

[9] Z. Hu, Y. Nechayev, P. S Hall, C. Constantinou, and Y. Hao, "Measurements and statistical analysis of on-body channel fading at 2.45 GHz," *IEEE Antennas and Wireless Propagation Letter*, vol. 6, pp. 612-615, 2007.

[10] S. L. Cotton, G. A. Conway, and W. G. Scanlon, "A time-domain approach to the analysis and modeling of on-body propagation characteristics using synchronized measurements at 2.45 GHz," *IEEE Trans. Antennas & Propagation, Special Issue on Antennas & Propagation on Body-Centric Wireless Communications*, vol. 57, no. 4, pp. 943-955, Apr. 2009.

[11] S. L. Cotton and W. G. Scanlon, "An experimental investigation into the influence of user state and environment on fading characteristics in wireless body area networks at 2.45 GHz," *IEEE Trans. Wireless Communications*, vol. 8, no. 1, pp. 6-12, Jan. 2009.

[12] M. M. Khan, M. A. Rahman, M. A. Talha, and T. Mithila, "Wearable antenna for power efficient on-body and off-body communications," *Journal of Electromagnetic Analysis and Application*, vol. 6, pp. 238-245. doi: 10.4236/jemaa.2014.69024

[13] Electronic Imaging: Board of Regents (1997), National Institute of Health National Library of Medicine USA, Board of Regents, Bethesda, MD, Tech, Rep. NH 90-2197. http://www.brooks.af.mil/AFRL/HED/hedr

[14] C. Gabriel and S. Gabriel, "Compilation of the Dielectric Properties of Body Tissues at RF and Microwave Frequencies," 1999. http://www.brooks.af.mil/AFRL/HED/hedr/reports/dielectric/Title/Title.html

[15] Institute for Applied Physics (2014), Italian National Research Council, "Calculation of the Dielectric Properties of Body Tissues." http://niremf.ifac.cnr.it/tissprop/

[16] M. M. Khan, Q. H. Abbasi, A. Alomainy, and Y. Hao, "Performance of ultra wideband wireless tags for on-body radio channel characterisation," *International Journal of Antennas and Propagation*, Article ARTN 232564, 10.1155/2012/232564

[17] A. Alomainy, A. Sani, A. Rahman, J. G. Santas, and Y. Hao, "Transient characteristics of wearable antennas and radio propagation channels for ultra-wideband body centric wireless communications," *IEEE Transactions on Antennas and Propagations*, vol. 57, no. 4, Apr. 2009.

[18] S. S. Gassemzadeh, R. Jana, C. W. Rice, W. Turin, and V. Tarohk, "A statistical path loss model

for in-home UWB channels," *IEEE Conference Ultrawide Band Systems and Technologies*, Baltimore, pp. 5964, 2002.

Mohammad Monirujjaman Khan received his Ph.D. degree from Antenna and Electromagnetic Group, Queen Mary University of London (QMUL). He is working as an Assistant Professor in the Department of Electrical and Computer Engineering, North South University, Dhaka, Bangladesh. His main research interests include compact and efficient antennas for medical and sports applications in wireless body area networks and wireless personal area networks, radio propagation channel modelling and characterization, small antennas design, cognitive radio and system and wearable systems. He has authored and co-authored more than 60 technical papers in leading journals and peer-reviewed conferences. Khan is acting as a reviewer for many leading IEEE and IET journals in the area of antennas, radio wave propagation and communication systems.

Fast Solutions of Wideband RCS of Objects by Combing Improved Ultra-wide Band Characteristic Basis Function Method and Best Uniform Approximation

Wenyan Nie [1] and Zhonggen Wang [2]

[1] School of Mechanical and Electrical Engineering
Huainan Normal University, Huainan, 232001, China
wynie5240@163.com

[2] School of Electrical and Information Engineering
Anhui University of Science and Technology, Huainan, 232001, China
zgwang@ahu.edu.cn

Abstract **─** The ultra-wide band characteristic basis function method (UCBFM) is an efficient approach to calculate wideband radar cross section (RCS) of objects, but its calculation errors at lower frequency points are great and the reduced matrix at each frequency point needs to be reconstructed, which are very time-consuming. To solve these problems, an effective numerical method for fast calculating wideband RCS of objects by combining improved UCBFM (IUCBFM) and best uniform approximation is proposed. This method improves the construction of the ultra-wide band characteristic basis functions (UCBFs) through solving the secondary level characteristic basis functions (SCBFs). In consideration of the mutual coupling effects among sub-blocks, the improved UCBFs contain more current information characteristics, which greatly improve the calculation precision at lower frequency points. Moreover, to avoid the reconstruction of reduced matrix at each frequency point, the best uniform approximation technology is used to fast predict the surface current at any frequency point in the given frequency band and further realize the fast calculation of wideband RCS of objects. Compared with traditional UCBFM, the method in this paper significantly improves the calculation accuracy and efficiency. Numerical results demonstrate that the proposed method is accurate and efficient.

Index Terms **─** Best uniform approximation, Method of Moments (MoM), Ultra-wide band Characteristic Basis Function Method (UCBFM), wideband radar cross section.

I. INTRODUCTION

Accurate prediction of wideband radar cross section (RCS) of objects is of great significance to the studies of high-resolution radar imaging technology, anti-stealth and target identification. One of the most popular methods for radar cross sections (RCS) prediction is the frequency domain integral equation solved using method of moments (MoM) [1], but it places a heavy burden on memory and solving time when dealing with electrically large problems. Moreover, each frequency point in the given frequency band needs to be calculated one by one, it will be time-consuming. With the successive proposal of efficient methods, for example, fast multipole method (FMM) [2], multilevel fast multipole method (MLFMM) [3,4], adaptive integration method (AIM) [5], adaptive cross approximation (ACA) algorithm [6], and characteristic basis function method (CBFM) [7-9], the calculation efficiency by these methods at single frequency point is greatly improved. However, if the RCS is highly frequency dependent, one needs to do the calculations at finer increment of frequency to obtain an accurate representation of the frequency response, which must be computationally intensive. Thus, how to utilize the information carried by few frequency points to obtain wideband RCS in the given frequency band is of great importance. Therefore, scholars put forward many efficient methods. In [10], MLFMM is combined with impedance interpolation technology to analyze the wideband electromagnetic scattering problems. In [11], MLFMM is combined with the best uniform approximation to calculate the wideband RCS of objects. However, all the above methods still rely on an iteration method to solve linear equations, which needs to face unpredictable problems of convergence rate. In [12-14], asymptotic waveform evaluation (AWE) technology is used to analyze the wideband electromagnetic scattering problems and achieves good results. But this technology needed to store dense impedance matrix and

Submitted On: September 21, 2015
Accepted On: July 27, 2016

frequency derivative of impedance matrixes, which enlarged the memory requirement. So in [15], AWE based on the CBFM (AWE-CBFM), is proposed to analyze the wideband electromagnetic scattering problems. In [16], adaptive modified CBFM combined with model-based parameter estimation technology (AMCBFM-MBPE) is proposed to analyze the wideband and wide-angle electromagnetic scattering problems. Though the above two methods utilized CBFM to accelerate the solving speed of interpolation point and reduce memory consumption, these two methods need to recalculate the characteristic basis functions (CBFs) at each interpolation point. Hence, in [17], an ultra-wide band characteristic basis function method (UCBFM) is proposed to analyze the wideband electromagnetic scattering problems, without having the construction of CBFs for each frequency repeatedly. The CBFs constructed at the highest frequency point, termed ultra-wide band characteristic basis functions (UCBFs), entail the electromagnetic behavior at lower frequency range; thus, it follows that they can also be employed at lower frequency points without going through the time consuming step of constructing them again. However, the calculation errors of the RCS by UCBFM are great at lower frequency points; its universality is not strong. The lower accuracy at lower frequency points can be explained that the procedure are employed at lower frequency points using the discretization carried out at the highest frequency, this could lead to an increase of the condition number when calculating the impedance matrix [17]. Moreover, the corresponding reduced matrix at each frequency point still needs to be reconstructed, which is time-consuming.

In consideration of the calculation errors by UCBFM are great at lower frequency points and the reduced matrix at each frequency point shall be reconstructed. An improved ultra-wide characteristic basis function method (IUCBFM) is presented in this paper. This approach fully considers the mutual coupling effects among sub-blocks, the secondary level characteristic basis functions (SCBFs) are calculated after the primary characteristic basis function (PCBFs) are obtained. Because IUCBFM considers the mutual coupling effects among sub-blocks, improved UCBFs (IUCBFs) contain more current information characteristics and have a stronger universality. Thus, it could greatly improve the calculation accuracy at lower frequency points. Furthermore, to avoid the reconstruction of reduced matrix at each frequency point, IUCBFM is combined with the best uniform approximation technology to quickly predict the surface current at any frequency point within the frequency band and further realize the calculation of wideband RCS of objects. The numerical results indicate that compared with traditional UCBFM, the method in this paper has significant improvements in calculation accuracy and efficiency.

II. THE UCBFM

The UCBFM firstly divides the object into M blocks. Refer to the literature [18], the optimized selection of the number of dividing blocks is $M \approx 0.9N^{1/3}$, where N is the total number of the RWG basis functions. Then, it establishes a model at the highest frequency point f_h. Multi-angle plane wave excitations are set to irradiate each block. Suppose N_θ and N_ϕ respectively represent the numbers of plane wave excitations in directions of θ and ϕ, in total $N_{\text{pws}} = 2N_\theta N_\phi$ (two polarization modes are considered), noted as $\mathbf{E}_{ih}^{N_{\text{pws}}}$. To obtain PCBFs of each block, one must solve the following system:

$$\mathbf{Z}_{ii}(f_h)\cdot\mathbf{J}_{ih}^{CBF} = \mathbf{E}_{ih}^{N_{\text{pws}}}, \tag{1}$$

where, $\mathbf{Z}_{ii}$ is an $N_i \times N_{\text{i}}$ self-impedance matrix of block i, for $i = 1, 2, \cdots, M$, N_{i} represents the number of the unknown numbers in block i; $\mathbf{E}_{ih}^{N_{\text{pws}}}$ is an $N_i \times N_{\text{pws}}$ excitation matrix; and $\mathbf{J}_{ih}^{CBF}$ is the PCBFs matrix of dimension $N_i \times N_{\text{pws}}$.

Typically, the number of plane waves we have used to generate the CBFs would exceed the number of degrees of freedom (DoFs) associated with the block, to eliminate the redundant information in $\mathbf{J}_{ih}^{CBF}$ caused by overestimation, an orthogonalization procedure based on singular value decomposition (SVD) method is used to reduce the final number of CBFs, only those whose relative singular values above a certain threshold, for example, 1.0E-3, are retained as UCBFs. Suppose there are K UCBFs for each block after SVD, where K is always smaller than N_{pws}. The surface current can be expressed as a liner combination of the UCBFs as follows:

$$\mathbf{J} = \sum_{m=1}^{M}\sum_{k=1}^{K}\alpha_m^k(f)J_m^{CBF_k}, \tag{2}$$

where, $J_m^{CBF_k}$ represents the k^{th} UCBFs of block m; and $\alpha_m^k(f)$ represents the unknown weight coefficients. Galerkin method is used to convert the traditional MoM equation into a linear equation about coefficient matrix $\boldsymbol{\alpha}(f)$. We can get a $KM \times KM$ reduced matrix:

$$\mathbf{Z}^{\boldsymbol{R}}(f)\cdot\boldsymbol{\alpha}(f) = \mathbf{V}^{\boldsymbol{R}}(f), \tag{3}$$

where, $V_i^R(f) = \mathbf{J}^{\text{T}}\cdot\mathbf{E}_i(f)$, for $i = 1, 2, 3, \cdots, M$; and T represents transposition. $\mathbf{Z}^{\boldsymbol{R}}(f)$ represents the reduced impedance matrix of dimension $KM \times KM$. Its detailed calculation expression can be expressed as below:

$$Z_{ij}^{R}(f)=\mathbf{J}^{\mathrm{T}}\cdot\mathbf{Z}_{ij}(f)\cdot\mathbf{J},\tag{4}$$

where, $\mathbf{Z}_{ij}(f)$ represents the impedance matrix between blocks i and j at frequency f. Because the dimensionality of $\mathbf{Z}^{\boldsymbol{R}}(f)$ is small, $\alpha(f)$ can be obtained by directly solving Eq. (3). Then, $\alpha(f)$ is substituted into Eq. (2). In this way, the surface current $\boldsymbol{J}$ at any frequency f can be obtained. Though UCBFs can be reused at each frequency point, when f changes, the impedance matrix $\mathbf{Z}_{ij}(f)$ needs to be recalculated and $\mathbf{Z}^{\boldsymbol{R}}(f)$ also needs to be reconstructed. It can be seen from Eq. (4) that numerous vector–matrix–vector products are present in the reduced matrix calculation process. Thus, it is not advisable to reconstruct the reduced matrix at each frequency point.

III. THE IUCBFM

To improve the calculation accuracy of UCBFM at lower frequency points, the construction of UCBFs is improved by considering the mutual coupling effects among sub-blocks. A model is established at the highest frequency point f_h in the given frequency band and the number of plane wave excitations is reduced. For each plane wave excitation, the SCBFs are calculated after the PCBFs are obtained. The PCBFs of block i can be solved by the following formula:

$$\mathbf{Z}_{ii}\mathbf{J}_{i}^{P}=\mathbf{E}_{i},\tag{5}$$

where, $\mathbf{E}_i$ represents the excitation vector of block i, for $i=1,2,3\cdots M$; $\mathbf{Z}_{\boldsymbol{ii}}$ represents the self-impedance of block i, with dimensionality of $N_i\times N_i$. The PCBFs of block i can be obtained by directly solving Eq. (5). After the PCBFs of each block are solved, according to Foldy-Lax equation theory [19,20], the SCBFs on a block are calculated by replacing the incident field with the scattered fields due to the PCBFs on all blocks except from itself. By solving Eq. (6), we can obtain the first-order SCBFs. Similarly, higher-order SCBFs can be calculated. If the second-order SCBFs are calculated, these SCBFs can be calculated as:

$$\mathbf{Z}_{\boldsymbol{ii}}\mathbf{J}_{i}^{S1}=-\sum_{j=1(j\neq i)}^{M}\mathbf{Z}_{ij}\mathbf{J}_{j}^{P},\tag{6}$$

$$\mathbf{Z}_{\boldsymbol{ii}}\mathbf{J}_{i}^{S2}=-\sum_{j=1(j\neq i)}^{M}\mathbf{Z}_{ij}\mathbf{J}_{j}^{S1}.\tag{7}$$

By solving Eq. (6) and Eq. (7), we can obtain all-order SCBFs. Let N_θ^{new} and N_ϕ^{new} respectively indicate the number of plane wave excitations in the θ and ϕ directions in the IUCBFM. After Eq. (5), Eq. (6) and Eq. (7) are solved, each block can obtain $6N_\theta^{new}N_\phi^{new}$ CBFs, including $2N_\theta^{new}N_\phi^{new}$ $\mathbf{J}_i^{P}$, $2N_\theta^{new}N_\phi^{new}$ $\mathbf{J}_i^{S1}$ and $2N_\theta^{new}N_\phi^{new}$ $\mathbf{J}_i^{S2}$. To reduce the linear dependency among these CBFs, we also need to use an SVD procedure. After the SVD procedure, the CBFs are retained as IUCBFs. The construction of IUCBFs fully considers the mutual coupling effects among sub-blocks, this not only enables IUCBFs to contain more current information characteristics but also greatly decreases the number of plane wave excitations, which improves the construction efficiency of IUCBFs.

IV. THE BEST UNIFORM APPROXIMATION

To avoid the reconstruction of reduced matrix at each frequency point, IUCBFM is combined with the best uniform approximation [21] to analyze the wideband electromagnetic scattering problems. After Chebyshev nodes in the given frequency band are solved, IUCBFM is applied to calculate the surface current at each Chebyshev node. There is no need to recalculate CBFs at each Chebyshev node, because the IUCBFs can be reused at each Chebyshev node. Finally, the best uniform approximation technology is used to fast predict the surface current at any frequency point in the frequency band and further realize the fast calculation of wideband RCS.

For a given frequency band $f\in[f_a,f_b]$, it corresponds to range of wave-number $k\in[k_a,k_b]$. The normalized transformation of k is given by:

$$\tilde{k}=\frac{2k-(k_a+k_b)}{k_b-k_a},\tag{8}$$

According to Eq. (8), the range of $\tilde{k}$ is easy to obtain as $[-1,1]$. Then, the surface current $I(k)$ can be calculated by:

$$I(k)=I\left(\frac{\tilde{k}(k_b-k_a)+(k_a+k_b)}{2}\right),\tag{9}$$

and the Chebyshev approximation for $I(k)$ is given by:

$$I(k)=I\left(\frac{\tilde{k}(k_b-k_a)+(k_a+k_b)}{2}\right)\approx\sum_{l=0}^{n-1}c_lT_l(\tilde{k})-\frac{c_0}{2},\tag{10}$$

where, $c_l=\dfrac{2}{n}\sum_{i=1}^{n}I(k_i)T_l(\tilde{k}_i)$, $T_l\left(\tilde{k}\right)$ is the Chebyshev polynomial.

The recursion formula about $T_l\left(\tilde{k}\right)$ is concluded as:

$$\begin{cases}T_0\left(\tilde{k}\right)=1\\T_1\left(\tilde{k}\right)=\tilde{k}\\\cdots\\T_{l+1}\left(\tilde{k}\right)=2\tilde{k}T_l\left(\tilde{k}\right)-T_{l-1}(\tilde{k})\end{cases},\tag{11}$$

$\tilde{k}_i(i=1,2\cdots n)$ denotes the Chebyshev node within the range of normalized wave-number and its expression is:

$$\tilde{k}_i = \cos\left(\frac{i-0.5}{n}\pi\right), \tag{12}$$

the corresponding wave-number $k_i \in [k_a, k_b]$ could be obtained by:

$$k_i = \frac{\tilde{k}_i(k_b - k_a) + (k_a + k_b)}{2}. \tag{13}$$

By solving Eq. (10), the surface current of the object at any frequency point in the whole wideband can be got and further fast calculation of wideband RCS can be realized.

V. NUMBERICAL RESULTS

To verify the validity and accuracy of the proposed method, three test samples are presented. All simulations are completed on a personal computer with an Intel(R) Core(TM) i3-2120 CPU with 3.3 GHz (only one core is used) and 4 GB RAM. The threshold of the SVD is set to 10^{-3}, and all the objects are illuminated by a normally incident $\hat{x}$ -polarized plane wave with the incident direction of $(\theta,\phi) = (0^\circ, 0^\circ)$.

First, we consider the scattering problem of a PEC sphere with radius of 0.3 m over a frequency range of 0.1 GHz to 1 GHz. The geometry is divided into 2346 triangular patches with an average length of $\lambda/10$ at 1 GHz. The object is divided into 8 blocks, and each block is extended by $\Delta = 0.15\lambda$ in all directions, thus resulting in 5250 unknowns. Referring to the literature [17], we construct the CBFs for the UCBFM, 20 plane wave excitations in directions of θ and ϕ are set, this approach results in a total of 800 CBFs. After SVD, 106 UCBFs (average value) are retained on each block; the construction time of UCBFs is 256s. In IUCBFM, 8 plane wave excitations in directions of θ and ϕ are set and the second-order SCBFs are calculated. This results in only 384 CBFs for each block, including 128 PCBFs, 128 first-order SCBFs and 128 second-order SCBFs. Although the SVD procedure is respectively used on PCBFs and all-order SCBFs. After SVD, the numbers of $\boldsymbol{J}^P$, $\boldsymbol{J}^{S1}$, and $\boldsymbol{J}^{S2}$ retained on each block are shown in Table 1. It can be seen that the second-order SCBFs $\boldsymbol{J}^{S2}$ have a strong linear correlation and have small influences on final current. Thus, the calculation of the first-order SCBFs is enough. With the decreasing number of incidence wave excitations and dimensionality of CBFs matrix, the construction time of IUCBFs is 171s, with a higher efficiency. The $\theta\theta$ polarization bistatic RCS calculated at 300 MHz by UCBFM and IUCBFM are shown in Fig. 1. It can be seen that the IUCBFs contain more current information characteristics and have higher accuracy at lower frequency points. The number of UCBFs and the accuracy of the two methods mainly depend on the threshold of the SVD. The computational time and accuracy of the two methods at different threshold of the SVD are shown in Table 2. The relative error *Err* is defined as $\left(\|\mathbf{I}-\mathbf{I}_{\text{MOM}}\|_2 / \|\mathbf{I}_{\text{MoM}}\|_2\right) \times 100\%$, where $\mathbf{I}_{\text{MOM}}$ is the current coefficient vector computed at the frequency of 300 MHz by the MoM, and $\mathbf{I}$ is the current coefficient vector computed by the UCBFM or the IUCBFM. $\|\bullet\|_2$ denotes vector-2 norm. Through a comparison of *Err* versus the threshold of the SVD given in Table 2, we find that the IUCBFM can yield a satisfactory result with a small threshold, and the IUCBFM has a higher efficiency. In consideration of the CPU time and the number of the UCBFs, the threshold of SVD is selected as 10^{-3}. With a frequency step of 9 MHz, the wideband RCS obtained by using UCBFM and IUCBFM are shown in Fig. 2. It can be seen that the results at the lower frequency points calculated by IUCBFM are more accurate than those calculated by UCBFM.

Table 1: Number of CBFs retained on each block after the SVD of IUCBFM

CBFs	1	2	3	4	5	6	7	8
$\boldsymbol{J}^P$	52	52	52	52	52	52	52	52
$\boldsymbol{J}^{S1}$	47	47	47	47	47	47	47	47
$\boldsymbol{J}^{S2}$	0	0	0	0	0	0	0	0

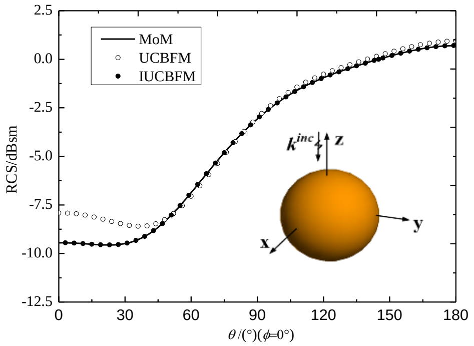

Fig. 1. Bistatic RCS in $\theta\theta$ polarization of the PEC sphere at 300 MHz.

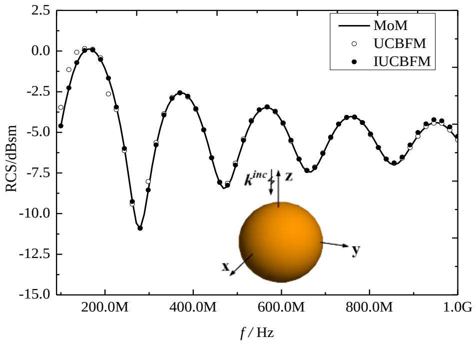

Fig. 2. Wideband RCS of the PEC sphere.

Table 2: CPU time and accuracy for varying the threshold

Threshold of SVD	UCBFM			
	SVD Time (s)	Number of UCBFs	CPU Time (s)	Relative Error (%)
0.05	129.6	337	208.1	15.23
0.01	129.7	510	236.9	11.23
0.005	129.9	638	248.5	9.13
0.001	130.1	852	289.3	7.78
0.0008	130.2	1053	302.3	7.70
0.0005	130.4	1261	335.1	7.68.
Threshold of SVD	IUCBFM			
	SVD Time (s)	Number of UCBFs	CPU Time (s)	Relative Error (%)
0.05	43.3	294	141.5	9.12
0.01	46.9	451	170.6	7.68
0.005	47.8	586	192.8	4.12
0.001	48.7	792	208.3	2.67
0.0008	48.8	905	225.4	2.63
0.0005	48.9	1026	254.6	2.60

We then consider the scattering problem of a complex conductor with top width of 0.15 m, bottom width of 0.075 m, height of 0.25 m. The frequency range starts from 0.1 GHz and terminates at 3 GHz. The discretization in triangular patches is conducted at 3 GHz with a mean edge length of $\lambda/10$, thus leading to 5084 unknowns. The target is divided into 4 blocks in the axis z direction. In UCBFM, 20 plane wave excitations in directions of θ and ϕ are set, 146 UCBFs are retained on each block. With a frequency step of 29 MHz, the wideband RCS of the target is calculated by UCBFM. When IUCBFM is used, 8 plane wave excitations in directions of θ and ϕ of are set and the first-order SCBFs are calculated. 124 IUCBFs are retained on each block after SVD. The wideband RCS of the target is calculated by combing IUCBFM and the best uniform approximation (IUCBFM-Chebyshev). As shown in Fig. 3, the results obtained by the IUCBFM-Chebyshev with order of 10 agree well with the results obtained by the commercial software FEKO, which used the conventional MoM solver.

Finally, a 252.3744 mm PEC NASA almond is considered. We present the results for the problem of scattering over a frequency range from 0.1 GHz to 3 GHz. The geometry is divided into 2684 triangular patches with an average length of $\lambda/10$ at 3 GHz, thus resulting in 5752 unknowns. The target is divided into 4 blocks in the axis x direction. In UCBFM, 20 plane wave excitations in directions of θ and ϕ are set, 121 UCBFs are retained on each block. In IUCBFM, 8 plane wave excitations in directions of θ and ϕ are set. 102 IUCBFs are retained on each block. The wideband RCS calculated by using UCBFM and IUCBFM-Chebyshev with order of 9 are shown in Fig. 4. It can be seen that the results calculated by IUCBFM-Chebyshev have a better coincidence with those of FEKO.

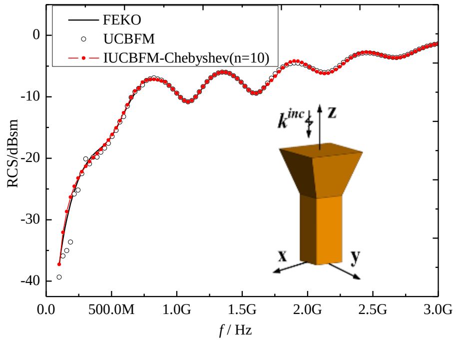

Fig. 3. Wideband RCS of the composite PEC conductor.

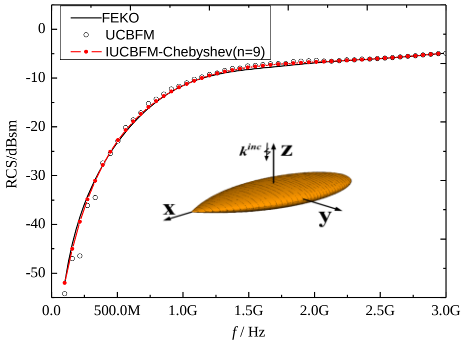

Fig. 4. Wideband RCS of the PEC NASA almond.

Table 3: CPU time and the relative error of the two methods

Problems	Method	UCBFs Construction (s)	Total Time (s)	Relative Error (%)
Problem 1: Sphere	MoM	---	52142	---
	UCBFM	256	39628	7.15
	IUCBFM	171	33469	2.95
Problem 2: Composite Conductor	FEKO	---	---	---
	UCBFM	268	31732	7.09
	IUCBFM-Chebyshev	206	4589	3.01
Problem 3: Nash Almond	FEKO	---	---	---
	UCBFM	297	26641	6.91
	IUCBFM-Chebyshev	198	3496	3.21

The CPU time and the relative error of the above three problems using UCBFM, IUCBFM and IUCBFM-Chebyshev are summarized in Table 3. We use the relative error (percent) of RCS to estimate the accuracy of the proposed method. The relative error is defined as:

$$\mathrm{Rel.Error}(\%) = \left(\frac{1}{N} \sum_{k=1}^{N} \frac{\left| \mathrm{RCS}_{f_k}^{\mathrm{pm}} - \mathrm{RCS}_{f_k}^{\mathrm{ref}} \right|}{\left| \mathrm{RCS}_{f_k}^{\mathrm{ref}} \right|} \right) \times 100, \quad (14)$$

where $\mathrm{RCS}_{f_k}^{\mathrm{pm}}$ is the RCS provided by the UCBFM, or the IUCBFM at the frequency of f_k, $\mathrm{RCS}_{f_k}^{\mathrm{ref}}$ is the RCS provided by the MoM (FEKO), N is the total number of frequency points. Compared with the traditional UCBFM, IUCBFM improves the construction efficiency of UCBFs, but the calculation time of the wideband RCS does not decrease significantly. The reason for this is that the impedance matrix $\boldsymbol{Z}_{ij}(f)$ should be recalculated when the f changes, and the reduced matrix at each frequency point needs to be reconstructed, there are many vector–matrix–vector products in the calculation of the reduced matrix, so the computation cost of IUCBFM is very expensive. In order to avoid the reconstruction of reduced matrix at each frequency, the IUCBFM combined with the best uniform approximation is used to calculate the wideband RCS of problem 2 and problem 3. It can be seen from the calculation time of problem 2 and problem 3 that, because the reduced matrix reconstruction at each frequency point is cut down, the calculation efficiency of IUCBFM-Chebyshev is greatly improved.

VI. CONCLUSION

This paper puts forward an effective numerical method for calculating wideband RCS of objects by combining IUCBFM and best uniform approximation. This method improves the construction of UCBFs, the IUCBFs contain more current information characteristics and have a stronger universality, it improves the calculation accuracy at lower frequency points. In addition, in order to avoid the reconstruction of reduced matrix at each frequency point, the best uniform approximation technology is used to fast predict the surface current at any frequency point in the given frequency band and further realize the fast calculation of wideband RCS of objects. Several numerical results have indicated that compared with traditional UCBFM, the method proposed in this paper owns higher accuracy and efficiency.

ACKNOWLEDGMENT

This work was supported by the National Natural Science Foundation of China under Grant No. 61401003, the Natural Science Foundation of Anhui Provincial Education Department under Grant No. KJ2016A669, and the Natural Science Foundation of Huainan Normal University under Grant No. 2015xj09zd.

REFERENCES

[1] R. F. Harrington, *Field Computation by Moment Method*. New York: Macmillan, pp. 22-57, 1968.

[2] R. Coifman, V. Rokhlin, and S. Wandzura, “The fast multipole method for the wave equation: A pedestrian prescription,” *IEEE Ant. Propag. Mag.*, vol. 53, no. 3, pp. 7-12, 1993.

[3] J. M. Song, C. C. Lu, and W. C. Chew, “Multilevel fast multipole algorithm for electromagnetic scattering by large complex objects,” *IEEE Trans. Antennas Propag.*, vol. 45, no. 10, pp. 1488-1493, 1997.

[4] M. Chen, R. S. Chen, and X. Q. Hu, “Augmented MLFMM for analysis of scattering from PEC object with fine structures,” *Applied Computational Electromagnetics Society (ACES) Journal*, vol. 26, no. 5, pp. 418-428, 2011.

[5] E. Bleszynski, M. Bleszynski, and T. Jaroszewicz, “Adaptive integral method for solving large-scale electromagnetic scattering and radiation problems,” *Radio Sci.*, vol. 31, no. 5, pp. 1225-1251, 1996.

[6] Z. Liu, R. Chen, J. Chen, and Z. Fan, “Using adaptive cross approximation for efficient calculation of monostatic scattering with multiple incident angles,” *Applied Computational Electromagnetics Society (ACES) Journal*, vol. 26, no. 4, pp. 325-333, 2011.

[7] V. V. S Prakash and R. Mittra, “Characteristic basis function method: A new technique for efficient solution of method of moments matrix equations,” *Microw. Opt. Technol. Lett.*, vol. 36, no. 2, pp. 95-100, 2003.

[8] E. Lucente, A. Monorchio, and R. Mittra, “An iteration free MoM approach based on excitation independent characteristic basis functions for solving large multiscale electromagnetic scattering problems,” *IEEE Trans. Antennas Propag.*, vol. 56, no. 4, pp. 999-1007, 2008.

[9] K. Konno and Q. Chen, “The numerical analysis of an antenna near a dielectric object using the higher-order characteristic basis function method combined with a volume integral equation,” *IEICE Trans. Commun.*, vol. E97-B, no. 10, pp. 2066-2073, 2014.

[10] Z. H. Fan, Z. W. Liu, and D. Z. Ding, “Preconditioning matrix interpolation technique for fast analysis of scattering over broad frequency band,” *IEEE Trans. Antennas Propag.*, vol. 58, no. 7, pp. 2484-2487, 2010.

[11] T. Chao, Y. J. Xie, and Y. Y Wang, “Fast solutions of wide-band RCS pattern of objects using MLFM with the best uniform approximation,” *Journal of Electronics & Information Technology*, vol. 31, no. 11, pp. 2772-2775, 2009.

[12] C. J. Reddy, M. D. Deshpande, and C. R. Cockrell, “Fast RCS computation over a frequency band using method of moments in conjunction with asymptotic evaluation technique,” *IEEE*

Trans. Antennas Propag., vol. 46, no. 8, pp. 1229-1233, 1998.

[13] X. Wang, S. X. Gong, and J. L. Guo, "Fast and accurate wide-band analysis of antennas mounted on conducting platform using AIM and asymptotic waveform evaluation technique," *IEEE Trans. Antennas Propag.*, vol. 59, no. 12, pp. 4624-4633, 2011.

[14] C. J. Reddy, M. D. Deshpande, and C. R. Cockrell, "Fast RCS computation over a frequency band using method of moments in conjunction with asymptotic waveform evaluation technique," *IEEE Trans. Antennas Propag.*, vol. 46, no. 8, pp. 1229-1233, 1998.

[15] Y. F. Sun, Y. Du, and Y. Sao, "Fast computation of wideband RCS using characteristic basis function method and asymptotic waveform evaluation technique," *Journal of Electronics (in Chinese)*, vol. 27, no. 4, pp. 463-467, 2010.

[16] G. D. Han, Y. H. Pan, and B. F. He, "Fast analysis for 3D wide-band & wide-angle electromagnetic scattering characteristic by AMCBFM-MBPE," *Journal of Microwaves*, vol. 25, no. 6, pp. 32-37, 2009.

[17] M. Degiorgi, G. Tiberi, and A. Monorchio, "Solution of wide band scattering problems using the characteristic basis function method," *IET Microwaves Antennas and Propagation*, vol. 6, no. 1, pp. 60-66, 2012.

[18] K. Konno, Q. Chen, K. Sawaya, and T. Sezai, "Optimization of block size for CBFM in MoM," *IEEE Trans. Antennas Propag.*, vol. 60, no. 10, pp. 4719-4724, 2012.

[19] L. Tsang, C. E. Mandt, and D. H. Ding, "Monte Carlo simulations of the extinction rate of dense media with randomly distributed dielectric spheres based on solution of Maxwell's equations," *Optics Letters*, vol. 17, no. 5, pp. 314-316, 1992.

[20] Z. G. Wang, Y. F. Sun, and G. H. Wang, "Analysis of electromagnetic scattering from perfect electric conducting targets using improved characteristic basis function method and fast dipole method," *J. Electromagn. Waves Appl.*, vol. 28, no. 7, pp. 893-902, 2014.

[21] H. D. Raedt, K. Michielsen, and J. S. Kole, "Solving the Maxwell equations by the Chebyshev method: A one step finite-difference time-domain algorithm," *IEEE Trans. Antennas Propag.*, vol. 51, no. 11, pp. 3155-3160, 2003.

Wenyan Nie was born in Anhui Province, China, in 1981. She is currently a Lecturer with Huainan Normal University. She received the B.S. and M.S. degrees from Anhui University of Science and Technology in 2004 and 2007, respectively. Her research interests include computational electromagnetic methods, antenna theory and design.

Zhonggen Wang was born in Jiangsu Province, China, in 1981. He received the Ph.D. degree in Electromagnetic Field and Micro-wave Technique from the Anhui University of China, Hefei, P. R. China, in 2014. His current research interests include computational electromagnetics, signal and information processing techniques in electromagnetics.

Geometrical Optics Based Path Loss Model for Furnished Indoor Environment

E. M. Cheng [1], Z. Abbas [2], MohamedFareq AbdulMalek [3], K. Y. Lee [4], K. Y. You [5], S. F. Khor [6], and M. Afendi [1]

[1] School of Mechatronic Engineering
Universiti Malaysia Perlis (UniMAP), Arau, 02600, Perlis, Malaysia
emcheng@unimap.edu.my, afendirojan@unimap.edu.my

[2] Faculty of Science
Universiti Putra Malaysia (UPM), Serdang, Selangor, 43400, Malaysia
za@upm.edu.my

[3] Faculty of Engineering and Information Sciences
University of Wollongong in Dubai, Dubai Knowledge Village, Dubai, United Arab Emirates
mohamedfareqmalek@uowdubai.ac.ae

[4] Faculty of Engineering and Science
Universiti Tunku Abdul Rahman (UTAR), Petaling Jaya, 46200, Selangor, Malaysia
kylee@utar.edu.my

[5] Faculty of Electrical Engineering
Universiti Teknologi Malaysia (UTM), Skudai, 81310, Johor, Malaysia
kyyou@fke.utm.my

[6] School of Electrical System Engineering
Universiti Malaysia Perlis (UniMAP), Arau, 02600, Perlis, Malaysia
sfkhor@unimap.edu.my

Abstract ─ This paper describes the Geometrical Optics (GO) based path loss model for indoor environment path loss prediction. Both Geometrical Optics based total rays model and direct ray path loss model were developed. Optimization was then conducted to improve both models in path loss prediction for case of Line-Of-Sight (LOS) indoor environment. Both Geometrical Optics based total rays model and direct ray model were optimized with log-distance-dependent expression using least-square approach. This log-distance-dependent expression includes all effects due to multiple reflection and all uncertainties which is distance-dependent. The path loss measurement was conducted in Division of Information Technology (DITSC), Universiti Putra Malaysia. Both models were optimized with measured path loss which was collected from DITSC. The value of correction factor and coefficient in additional expression for optimized GO were developed and presented in this paper. The optimized GO based modes ware validated at five buildings in Universiti Putra Malaysia by referring to the absolute mean error for its accuracy and effectiveness in path loss prediction. The optimized direct ray model shows the best accuracy compared with optimized total rays model, direct ray model and total rays model.

Index Terms ─ Geometrical Optics, indoor propagation, optimization, path loss.

I. INTRODUCTION

If an antenna is deployed in building, a picocell is formed. Picocells are increasingly used not only in private location (i.e., office building), but also in public place, e.g., coffee shop, library, airport, railway station and etc. The rapid growth of wireless local area network (WLAN) is due to the implementation of this technology in all fields. Therefore, indoor wireless system plays a very important role in education, medical, business, entertainment and etc. Picocell propagation is also relevant to determine the case of propagating from microcellular and macrocellular into building, which could either act as a source of

Submitted On: March 18, 2015
Accepted On: July 27, 2016

interference or due to the enhancement to the coverage [1]. There is similarity between the indoor propagation and outdoor propagation where they are dominated by the same propagation mechanism, i.e., reflection, transmission and diffraction, but conditions are much more variable. The mounted antenna is also crucial in large-scale propagation, e.g., mounted antenna at desk level received different signal vastly than those mounted on the ceiling.

In order to determine the propagation phenomenon, buildings are categorized into residential home in suburban areas, residential home in urban areas, traditional building with fixed walls (hard partitions), and the office area with movable wall panels (soft partitions), factory building, research laboratory in university, and sports arenas. Hard partition is the obstructions within the building which cannot be easily moved such as concrete wall, beam or pillars. While soft partition is the movable obstructions within the building, e.g., office furniture, electrical appliances, or the machinery, which have a height less than the ceiling height. Inside the building, propagation geometry can be classified as Line-Of-Sight (LOS) where the transmitter and receiver are visible to one another or Non-Line-Of-Sight (NLOS), where objects block a visible propagation path [2].

The indoor wireless measurement was conducted in this study. Indoor wireless measurement is different from the outdoor measurement in two aspects - the distances covered are much smaller and the variability of the indoor environment is much greater for a much smaller range of transmitter-receiver separation distances. Propagation path characteristics for indoor communication systems are very unique compared to outdoor systems because there are obstacles that reflect, diffract, or shadow the transmitted radio waves, e.g., wall, ceiling, floor, and various type of office furniture. Reflections from obstacles and their path differences are unpredictable since the pedestrian moves horizontally. In the indoor radio channel, the distances covered of wave propagation are much smaller, and the higher variability of the environment is presented in smaller range of distance between transmitter and receiver, even though in scenario of Line-Of-Sight (LOS). The performance of indoor propagation channel is highly affected by the building material, the building type, and layout of the building, especially obstacle appears along the LOS propagation channel. On top of that, signal levels is also greatly changed due to the movement of people, mounting of the antenna, opening and closing of doors etc., inside the office. Therefore, some indoor propagation models, e.g., empirical models are not suitable to be used to characterize the propagation channels in the environment due to the aforementioned unique characteristics of propagation. In addition, direct ray model [3] or free space propagation model [4] from transmitting antenna to receiving antenna might not be able to describe the LOS propagation accurately. The multiple reflections caused infinite ray received by receiving antenna. It occurred at indoor environment due to the presence of obstacles (scatterers), ceiling and ground. This aspect is very crucial to be studied.

II. PROPAGATION MODELS

Path loss is one of the most important characteristics for the propagation environment. The path loss needs to estimate accurately to select optimum location of base station (mobile communication system) [5] or access point [6] with transmitting antenna (WLAN system).

Therefore, it required an accurate propagation model as a tool for estimation.

A propagation models is a set of mathematical expressions and algorithms used to represent the radio characteristics in a given environment. Propagation model can be presented in empirical (a.k.a statistical) [7], theoretical [8] (a.k.a deterministic), or a combination of both (a.k.a semi-empirical or semi-deterministic [9]). The empirical model is based on the measurements taken in a specific location. Meanwhile, the theoretical models deal with the fundamental principles of radio wave propagation phenomenon.

In the empirical models, all environmental influences are implicitly taken into account regardless of whether they can be separately recognized. This is the main advantage of empirical model. On the other hand, the accuracy of this model is not only relying on the accuracy of model, the similarities between the environment to be analysed and the measurement where the measurement taken are also important [10].

The deterministic models are based on the principles of physics. Therefore, it is free from the influence of dissimilarity of environment (i.e., pressure, temperature, and climate) and can maintain its accuracy. In practice, their implementation needs a rigorous computation especially when looking for the parameters (i.e., incident angle) of the model, which is sometime either impractical or impossible to obtain. For that reason, the implementation of the deterministic models is commonly restricted to smaller areas such as indoor environment. Nevertheless, if the deterministic models are implemented correctly, greater accuracy of prediction can be expected compared to empirical models.

The problem of the indoor field level prediction can be considered statistically or theoretically. While almost all statistical (empirical) models are based on the same general model, there are several distinguished theoretical models of which ray-tracing models are the most common use as propagation model for indoor environment.

The general idea of each of the presented models can be easily applied to any specific frequency band.

However, the major indoor radio systems operate today, i.e., 1.8-2 GHz frequency band is commonly used [11].

The characteristic for indoor environment is within short distance and, strongly rely on the material of obstacle especially its permittivity [12], conductivity and permeability. However, great variability of condition may affect the indoor radio propagation. For example, signal levels vary greatly depending on whether the interior doors are open or closed inside the building. In addition, the location of antenna mounted also play a significant impacts in large-scale fading. Antenna mounted at desk level exhibit the different signals variation than those mounted on the ceiling.

In this work, path loss, L [dB] can be determined by subtracting the signal strength at a specific position (Eq. 1) from the reference signal strength. The reference distance (1m) is utilized to normalize the path loss that occurs at 1m from the antenna so that only propagation effects are included in the path loss [13]. It is presented in the value of 30 dBμV/m in this paper [3].

III. MEASUREMENT SITES

A. Division of Information Technology (DITSC)

Foyer in DITSC as shown in Fig. 1 is the first measurement site. A transmitting antenna is located at this site is mounted on the ceiling. The antenna is deployed in such a way, so that the antenna is in line-of-sight at all the measuring position in Site C. However, there are two obstacles that contribute to the multipath signal (apart from the wall and ceiling), i.e., the wooden round table with wooden pillar (reception) and the wooden shelf as shown in Fig. 1 and Fig. 2, respectively. The area of Site C is the widest among the rest. Therefore 11 measuring positions are chosen. The plan of Site C is shown in Fig. 3.

Fig. 1. Foyer of building.

Fig. 2. Foyer of building.

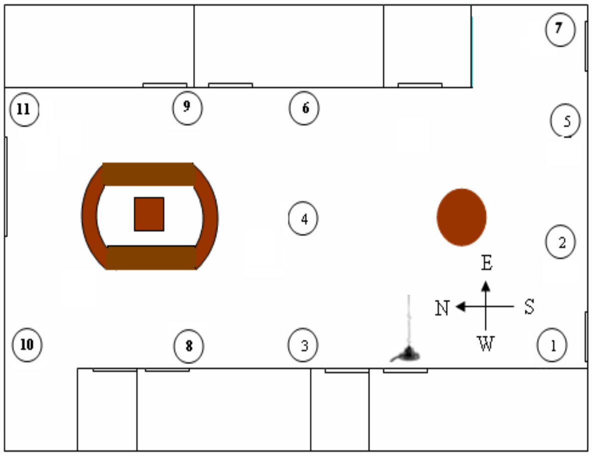

Fig. 3. Plan of Site C.

B. Validation of optimized model

After the optimization, the validity of optimized model must be proved. The effectiveness can be measured by comparing the optimized model [Eq. (3) and Eq. (4)] with its original model in terms of absolute mean error and mean relative error. Then, others location, e.g., first floor in Division Information Technology (DITFF) (Fig. 4), ground floor in Faculty Science (FSGF) (Fig. 5), second floor in Faculty Science (FSSF) (Fig. 6), third floor of Building of Mathematics (BMTF) (Fig. 7) and foyer of Building of Annex (BAF) (Fig. 8) were selected to validate the optimized model.

For validation purposes, four measurement sites, i.e., DITFF, FSGF, FSSF, BMTF and BAF were chosen to validate the optimized models. These measurement sites provide the LOS region for the measurement.

Fig. 4. First floor in Division Information Technology (DITFF).

Fig. 5. Ground floor in Faculty of Science (FSGF).

Fig. 6. Second floor in Faculty Science (FSSF).

Fig. 7. Third floor of Building of Mathematics (BMTF).

Fig. 8. Foyer in Building of Annex (BAF).

IV. GEOMETRICAL OPTICS (GO)

GO is a high-frequency method for approximating wave propagation for incident, reflected, and refracted fields. It uses the ray concept, so it is often referred to as ray optics. It was developed to analyze the propagation of light (waves) at high frequencies [14].

The final form of the GO equation is:

$$E(s) = E_0(0)e^{j\varphi_0(0)}\sqrt{\frac{\rho_1\rho_2}{(\rho_1+s)(\rho_2+s)}}\; e^{-j\beta s}, \qquad (1)$$

where $\varphi_0(0)$ = field phase at reference point (s = 0), and the parameters ρ_1, ρ_2, and s are as illustrated in Fig. 9. The spreading factor $\sqrt{\frac{\rho_1\rho_2}{(\rho_1+s)(\rho_2+s)}}$, can be reduced to $\sqrt{\frac{1}{s}}$, as expressed in [4].

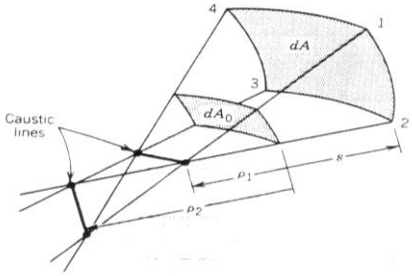

Fig. 9. Astigmatic tube of rays [14].

The GO field is a very useful description of the incident field, reflected field, and refracted field. However, such a description leads to incorrect predictions when considering fields in the shadow region behind an obstruction, since it predicts that no fields exist in the shadow region. This suggested that there is an infinitely sharp transition from the shadow region to the illuminated region. In practice, the transition from the illuminated region to the shadow region is never completely sharp, because some energy propagates into the shadow region.

V. MODEL OPTIMIZATION

The least-squares approach [15] is applied to Geometrical Optics model, in order to produce the best-fitting line through the measured data points for Site C in DITSC by associated it with the multiple reflections.

An improved (optimized) geometrical optic (IGO) model is proposed based on the geometrical optics model (GO) [Eq. (1)] by introducing an additional term, $A\log_{10}(d+x)+B$:

$$L_{IGO}(d,h_r,h_t,\varepsilon_r)[dB] = L(d,h_r,h_t,\varepsilon_r)[dB] + A\log_{10}(d+x)+B \quad , \quad (2)$$

where L [dB] is predicted path loss from Eq. (1) and $L_{IGO}[dB]$ is improved path loss due to optimization. In addition, h_r is the height of receiving antenna; h_t is the height of transmitting antenna; ε_r is relative permittivity of propagation medium and x is corrective constant for distance, d. A and B is coefficient and constant of correction factor, respectively. The additional expression that described in logarithm of distance is derived from the concept of log-distance model where both theoretical and measurement-based propagation models indicate that average received signal power decreases logarithmically with distance in indoor environment. In addition, this model also considers the fact that the surrounding environmental clutter may have vast difference at the same separation or distance between the transmitter antenna and receiving antenna due to the obstacles [4].

The additional term were also found by minimizing the differences between measurement data with improved model from Eq. (1) using the objective function:

$$F = \sum_{i=1}^{n} (L_{measured} - L_{IGO})^2 \, , \quad (3)$$

where $L_{measured}$ and L_{IGO} represent the measured and IGO path loss, respectively. n is the number of measured data points. The additional term was figured out by using the least-square technique through Eq. (3).

From least-square technique, the correction factor and coefficient of additional expression for direct ray is listed in Table 1. Single ray (direct ray model) and total rays model are considered in this work. The total rays model included the multiple reflected ray until the third order [16]. These optimized models and original models are compared for its accuracy in predicting path loss.

The optimizations of models are based on the measurement data that acquire from DITSC. The generated parameters after the optimization are listed in Table 1. Therefore, the additional expression is:

$$-7.4\ \log_{10}(d+3.3)+9.2 \, , \quad (4)$$

for fitting of direct ray model while,

$$-9.0\ \log_{10}(d-0.01)+10.5 \, , \quad (5)$$

for fitting of total ray model in DITSC with coefficients and constants are as given in Table 1. These additional expression are included in direct ray model and total rays model, respectively to compensate the non-inclusion of infinity ray, loss due to mismatch of impedance on the connector, dissipation of energy due to the heat, and the deviation due to random error where it's assumed distance-dependent.

In this background of development, it is definitely constrained and limited by all the climatic, and environmental factors during the measurement. Since all the measurements were conducted at non-busy hour, the effect due to moving object or population density were not taken into account. In addition, the optimized model is not applicable for outdoor propagation and operating frequency out from ISM band.

Table 1: Optimized parameter (based on measurement data in DITSC) with its correction factor as well as coefficient and constant in additional term for total rays model and direct ray model

Models	Parameter	Fitted Parameter
Direct ray	A	-7.4491
	B	9.1925
	x	3.2896
Total ray	A	-9.0175
	B	10.4744
	x	-0.0129

A. Effectiveness of optimized models

The effectiveness of optimized model with its correction factors and coefficients are illustrated in Fig. 10.

The information shown in Table 2 and Table 3 implied that optimized direct model has better agreement with measured path loss. Therefore, the objectives to introduce optimized direct ray model in comparison is achieved. The original model is proved to be improved via optimization. The improved model is more realistic to be used.

For the case in DITSC, the optimization was conducted on total rays model too, apart from direct ray model. The optimized total rays model in DITSC shows better improvement than the original total rays model if compared with the optimized direct ray model from original direct ray model through Table 2. The idea of optimization of total rays model is inclusion higher order of multiple reflected rays in total rays model. Therefore, it is more practical if compared with direct ray model.

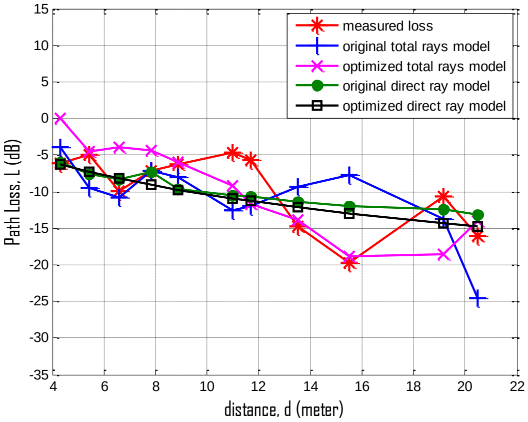

Fig. 10. Comparison of optimized models and original models with measurement data in DITSC.

The insignificant improvement that exhibited by optimized direct ray model in DITSC as listed in Table 2 if compared with optimized total rays model (direct ray + multiple reflected ray) explained that the inclusion of first, second and third order of multiple reflected rays and additional term [Eq. (5)] indeed give major contribution in predicting path loss at DITSC. Besides, the multiple reflected rays in total rays model are improved too via the corrected distance. Hence, it seems that the optimized total ray model became the main contributor in DITSC (Fig. 10).

The direct ray model and optimized direct ray model in DITFF (Fig. 11) give the least of mean relative error among the theoretical model and its optimized model, i.e., 8.23% and 7.43%, respectively. It can be noticed that there is an improvement of about 0.8% for mean relative error while 0.06 dB for absolute mean error. It can be explained easily by comparing the environment where the same height between the floor and ceiling and with the same antenna used can be noticed as in DITSC.

Total rays model in DITFF, however shows satisfactory results even though the mean relative error increases about 0.7% after it has been optimized. The conditions in DITFF are similar to the case in DITSC. The characteristic of vertical polarization possessed by the antenna is tally matches with the multiple reflected rays that occur in vertical plane (between the ceiling and floor).

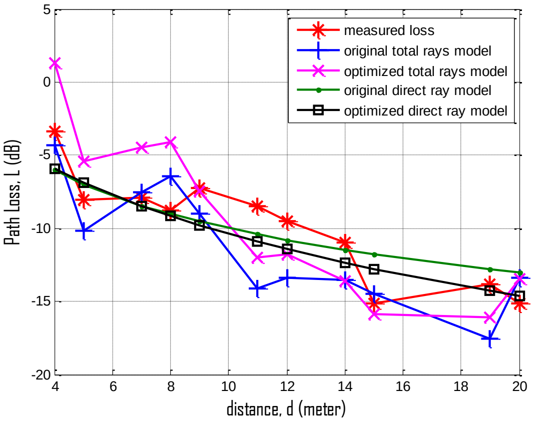

Fig. 11. Comparison of optimized models and original models with measurement data in DITFF.

Table 2: Comparison between the original and optimized total rays model

Measurement Site	Total Rays Model		Optimized Total Rays Model	
	Absolute Mean Error (dB)	Relative Mean Error (%)	Absolute Mean Error (dB)	Relative Mean Error (%)
DITSC	4.78	29.57	3.44	16.61
DITFF	2.35	12.00	2.61	12.70
FSGF	3.72	25.39	3.67	23.00
FSSF	12.85	754.49	14.15	730.50
BMTF	11.50	270.00	13.01	305.00
BAF	11.32	143.33	14.09	164.14

Table 3: Comparison between the original and optimized direct ray model

Measurement Site	Direct Ray Model		Optimized Direct Ray Model	
	Absolute Mean Error (dB)	Relative Mean Error (%)	Absolute Mean Error (dB)	Relative Mean Error (%)
DITSC	3.14	18.64	3.25	18.17
DITFF	1.56	8.23	1.50	7.43
FSGF	7.47	45.53	2.23	13.17
FSSF	1.91	55.04	0.69	14.38
BMTF	1.55	34.25	0.90	11.02
BAF	2.23	25.12	0.76	10.06

The effectiveness of optimized direct ray model in validation for FSGF (Fig. 12) is shown in Table 2. The optimized direct ray model improved the mean relative error from 45.53% to 13.17% as well as the absolute mean error from 7.47 dB to 2.23 dB. Unexpectedly, the relative mean error for total rays model of about 25.39%, while optimized total rays model of about 23.00% in FSGF is relatively high even though it shows improvement of about 2.39%. The case of total rays model and optimized total rays model in FSSF (Fig. 13) is worse than other measurement site because it indicates extremely high percentage in mean relative error (754.49% and 730.50%, respectively) and absolute mean error for both model (12.15 dB and 15.15 dB, respectively). On the contrary, the optimized direct ray model gives better agreement with measurement data if compared with direct ray model because it gives 14.38% of mean relative error. It also improves the mean relative error (40.66%) and the absolute mean error (1.22 dB) for direct ray model.

The cases in BMTF (Fig. 14) and BAF (Fig. 15) however show similar condition as in FSSF where both of the measurement sites gave abnormal figure of absolute mean error and mean relative error for total rays model and optimized total rays model as illustrated in Table 2. The mean relative error in BMTF (305%) implies the failure of optimization in this case because the mean relative error has not been improved. Similarly, for the case in BAF, optimized total rays give relatively higher mean relative error (164.14%) than total rays model (143.33%).

However, the optimized direct ray model shows better agreement with measurement data in BMTF and BAF. In BMTF, the mean relative error improved from 34.25% to 11.02% and 1.55 dB to 0.90 dB for absolute mean error. Meanwhile, the mean relative error and absolute mean error in BAF reduces from 25.12% to 10.06% and 2.23 dB to 0.76 dB, respectively

From Table 2, it can be noticed that most of the case in optimized total rays model shows no improvement. However, all the cases in optimized direct ray model show positive improvement. It can be observed in Table 3. The total rays model comprise of first, second, third order of reflected ray model and direct ray model. Therefore, the total rays model consists of many parameters and it's a very complex model. All the uncertainties in total rays model may be amplified after the optimization (optimized total rays model). No tendency of improvement but even worse is observed.

As a matter of fact, actual field strength is governed the inverse square law. Nevertheless, the field strength is distorted and hence deviates from inverse square law due to the presence of the obstruction and interference. It can be noticed at Fig. 10 to Fig. 15.

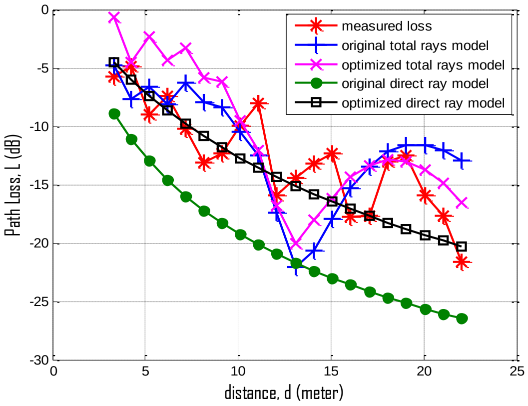

Fig. 12. Comparison of optimized models and original models with measurement data in FSGF.

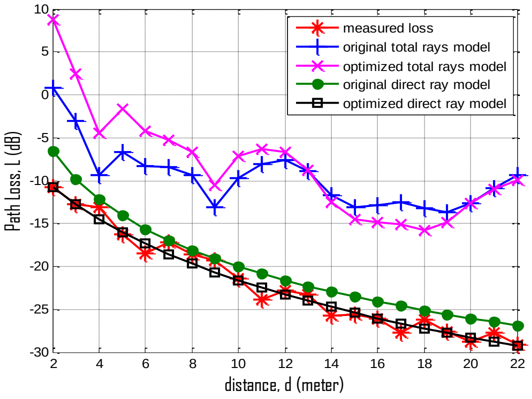

Fig. 13. Comparison of optimized models and original models with measurement data in FSSF.

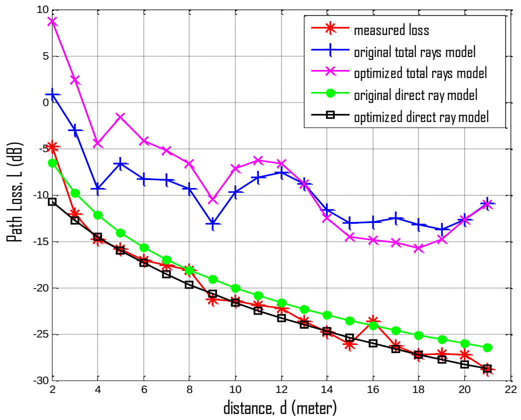

Fig. 14. Comparison of optimized models and original models with measurement data in BMTF.

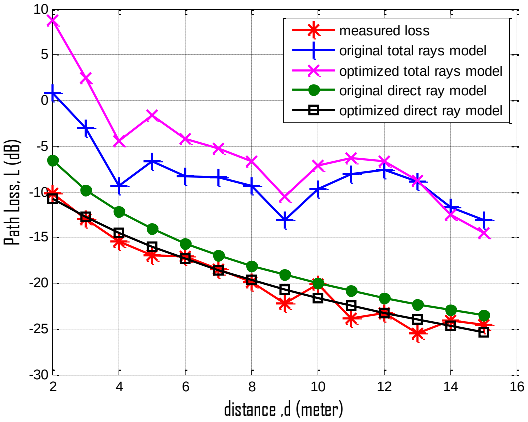

Fig. 15. Comparison of optimized models and original models with measurement data in BAF.

VI. CONCLUSION

In this project, we successfully optimized the direct ray model which is GO based through measurement at DITSC that can predict path losses in furnished indoor environments with obstacles. This study highlights the improvement of accuracy of optimized GO (direct ray model) in predicting path loss in furnished indoor environment. The direct and total ray models are optimized with addition of log-distance expression. These optimized models were validated by comparing the measured path loss at DITFF, FSGF, FSSF, BMTF and BAF. After the comparison, it can be noticed that the total rays model has the absolute and relative mean error of 2.35 dB and 12.00%, respectively at DITFF when compared with measured path loss. The optimized total ray model meets the failure in improving the accuracy as some of the measurement sites have even greater error after the optimization. Its absolute and relative mean error is increased to 2.61 dB and 12.70%. Absolute and relative mean errors for the other measurement sites were even worse than DITFF.

On the other hand, the direct ray model performs considerable good by exhibiting good agreement with measured path loss for all measurement sites especially DITFF if comparing with total ray model and optimized total ray model. The absolute and relative mean error shows considerably low, i.e., 1.56 dB and 8.23%, respectively for DITFF. After the direct ray model has been optimized, the absolute and relative mean error show decrement in term of absolute and relative mean error. The comparisons among the direct and total ray model as well as optimized direct and total ray model were came to learn that the optimized direct ray model exhibit the best accuracy in predicting path loss at all measurement sites. Meanwhile, the error in total rays model has been amplified aster optimization and it is inconvenient to be used as prediction tool in this work.

ACKNOWLEDGMENT

The author thanks the staff members in the Division Information Technology, Universiti Putra Malaysia, for their assistance in setting up and conducting the measurements described here.

REFERENCES

[1] S. R. Saunders, *Antennas and Propagation for Wireless Communication Systems*. New York: John Wiley & Sons Publisher, 1999.

[2] J. B. Anderson, T. S. Rappaport, and S. Yoshida, "Propagation measurements and models for wireless communications channels," *IEEE Communications Magazine*, pp. 42-49, 1995.

[3] E. M. Cheng, Z. Abbas, M. Fareq, K. Y. Lee, K. Y. You, and S. F. Khor, "Comparative study between measurement and predictions using geometrical optics and uniform theory of diffraction for case of non-line-of-sight (NLOS) in indoor environment," *Wireless Pers. Commun.*, vol. 71, pp. 2197-2213, 2012.

[4] T. S. Rappaport, *Wireless Communications: Principle and Practice*. Englewood Cliffs, NJ: Prentice-Hall, 1996.

[5] V. Erceg, L. J. Greenstein, S. Y. Tjandra, S. R. Parkoff, A. Gupta, B. Kulic, A. A. Julius, and R. Bianchi, "An empirically based path loss model for wireless channels in suburban environments," *IEEE Journal on Selected Areas in Communications*, vol. 17, no. 7, pp. 1205-1211, 1999.

[6] V. S. Abhayawardhana, I. J. Wassell, D. Crosby, M. P. Sellars, and M. G. Brown, "Comparison of empirical propagation path loss models for fixed wireless access systems," *IEEE 61st Vehicular Technology Conference, 2005, VTC 2005-Spring*, vol. 1, pp. 73-77, 2005.

[7] A. Bose and C. H. Foh, "A practical path loss model for indoor WiFi positioning enhancement," *2007 6th International Conference on Information, Communications & Signal Processing*, pp. 1-5, 2007.

[8] W. Joram and L. B. Henry, "A theoretical model of UHF propagation in urban environments," *IEEE Transactions on Antenna and Propagation*, vol. 36, no. 12, pp. 1788-1796, 1988.

[9] K. Guan, Z. Zhong, B. Ai, and T. Kurner, "Semi-deterministic path-loss modeling for viaduct and cutting scenarios of high-speed railway," *IEEE Antennas and Wireless Propagation Letters*, vol. 12, pp. 789-792, 2013.

[10] A. Nešković, N. Nešković, and D. Paunović, "Modern approaches in modeling of mobile radio systems propagation environment," *IEEE Communications Surveys*, Third Quarter, pp. 2-12, 2000.

[11] R. Allan, "Application of FSS Structures to Selectively Control the Propagation of Signals into and out of Buildings Annex 2: Radio System Issues," ERA Report 2004-0072 A2, ERA Project 51-CC-12033, Final Report, pp. 1-29, 2004.

[12] P. Bernardi, R. Cicchetti, and O. Testa, "An accurate UTD model for the analysis of complex indoor radio environments in microwave WLAN systems," *IEEE Transactions on Antenna and Propagation*, vol. 52, no. 6, pp. 1509-1520, 2004.

[13] K. W. Chung, J.-M. Sau, and R. D. Murch, "A new empirical model for indoor propagation prediction," *IEEE Transactions on Vehicular Technology*, vol. 47, no. 3, pp. 996-1001, 1998.

[14] C. A. Balanis, *Advanced Engineering Electromagnetics*. Canada: John Wiley & Sons Inc., 1989.

[15] R. Akl, D. Tummala, and X. Li, "Indoor propagation modeling at 2.4 GHz for IEEE 802.11 networks," *The Sixth IASTED International Multi-Conference on Wireless and Optical Communications, Wireless Networks and Emerging Technologies*, Banff, AB, Canada, July 3-5, 2006.

[16] E. M. Cheng, Z. Abbas, M. Fareq, S. F. Khor, K. Y. You, K. Y. Lee, M. S. Abdul Majid, and M. A. Rojan, "The effect of physical changes in a furnished indoor environment on wireless local area network (wlan) signals," *International Journal of Mechanical & Mechatronics Engineering IJMME-IJENS*, vol. 14, no. 05, pp. 1-15, 2014.

Ee Meng Cheng was born in 1980. He obtained his B.Sc (Honours) - Instrumentation Science in Universiti Putra Malaysia in 2004. He pursued his M.Sc. in Wave Propagation at the Institute for Mathematical Research on 2005 in Universiti Putra Malaysia and his Ph.D. in Microwave at the Faculty of Science in 2007 in Universiti Putra Malaysia. Recently, he is a Senior Lecturer in School of Mechatronic Engineering, Universiti Malaysia Perlis. His main personnel research interest is in the computational electromagnetic modeling, microwave dielectric spectroscopy, wave propagation in RF & microwave and microwave sensors development for food and agricultural applications.

Zulkifly Abbas was born in Alor Setar, Malaysia, in 1962. He received the B.Sc. degree with honors in Physics from the University of Malaysia, Kuala Lumpur, in 1986, the M.Sc. degree in Microwave Instrumentation from The Universiti Putra Malaysia (UPM), Serdang, in 1994, and the Ph.D. degree in Electronic and Electrical Engineering from the University of Leeds, Leeds, U.K., in 2000. He is currently an Associate Professor with the Department of Physics, UPM, where he has been a Faculty Member since 1987. His main personnel research interest is in the theory, simulation, and instrumentation of electromagnetic wave propagation at microwave frequencies focusing on the development of microwave sensors for agricultural applications.

Mohd Fareq bin Abdul Malek obtained his B.Eng. (Honours) - Electronic and Communication Engineering in The University of Birmingham, United Kingdom in 1994. He pursued his M.Sc. (Eng.) in Microelectronic Systems and Telecommunications at The University of Liverpool, United Kingdom in 2003 and Ph.D. in Electrical Engineering (Radio Frequency and Microwave) on 2005 in The University of Liverpool, United Kingdom. Recently, he is an Associate Professor in Faculty of Engineering and Information

Sciences, University of Wollongong in Dubai. His main personal research interest is in electron maser, antenna design, embedded computing and microwave absorber development.

Kim Yee Lee was born in Muar, Johor, Malaysia. He received his B.Sc. Physics, M.Sc. Microwaves, and Ph.D. Microwaves, all from the Universiti Putra Malaysia in year 2002, 2004, and 2008 respectively. In December 2007, he joined Universiti Tunku Abdul Rahman as a Lecturer in Department of Electronics and Electrical Engineering. His areas of research include microwave measurement technique, microwave circuit and instrumentation, control and automation, material properties measurement, and instrumentation calibration.

Kok Yeow You was born in 1977. He obtained his B.Sc. Physics (Honours) degree in Universiti Kebangsaan Malaysia in 2001. He pursued his M.Sc. in Microwave at the Faculty of Science in 2003 and his Ph.D. in Wave Propagation at the Institute for Mathematical Research in 2006 in Universiti Putra Malaysia. Recently, he is a Senior Lecturer at Radio Communication Engineering Department, Universiti Teknologi Malaysia. His main personnel research interest is in the theory, simulation, and instrumentation of electromagnetic wave propagation at microwave frequencies focusing on the development of microwave sensors for agricultural applications.

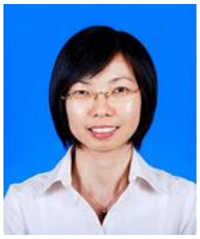

Shing Fhan Khor was born in 1982. She obtained her B.Sc. with Edu. (Honours)-Physics in Universiti Putra Malaysia in 2007. She pursued her Ph.D. in Materials Science at the Faculty of Science in 2011 in Universiti Putra Malaysia. Recently, she is a Senior Lecturer at School of Electrical Systems Engineering, Universiti Malaysia Perlis (UniMAP). Her main personnel research interest is in the glass science and focusing on dielectric, optical, mechanical and thermal properties.

Mohd Afendi bin Rojan was born in 1981. He is a Ph.D. holder from University of Tsukuba in Engineering Mechanics & Energy. He is currently a Senior Lecturer at School of Mechatronic Engineering, Universiti Malaysia Perlis (UniMAP). His main research interests include fracture mechanics, finite element analysis, and adhesive bonding.

On the Transmitted Beam Degradation through FSS in the Working Band by Plane-wave Spectrum Computation and Evaluation

Ming Jin [1,2] and Ming Bai [2†]

[1] State Key Laboratory of Remote Sensing Science
Institute of Remote Sensing and Digital Earth Chinese Academy of Sciences (CAS), Beijing, 100101, China P. R.
Jinmingaps@163.com

[2] School of Electronic Information Engineering
BEIHANG University, Beijing, 100191, China P. R.
[†]mbai@buaa.edu.cn

Abstract ─ In this paper, we implemented the combination of FDTD (Finite Difference Time Domain) and the plane-wave spectrum (PWS) algorithms, to evaluate beam transmission through frequency selective surface (FSS) in the near field region. The hybrid method takes advantage of the FDTD for the wideband analysis ability, and that of the PWS theory in the rapid re-composition for transmitted fields due to variable beam incidence. Consequently, it meets the need of beam transmission evaluation in the working band when the FSS is located among a serial of components, as in a millimeter Quasi-Optical (QO) instrument. After verifying the hybrid approach by results of other methods, we studied the degradations in the transmitted beams through an FSS design within the band of interest. The investigations are performed at the view of the transmission coefficient distributions in the PWS. It is found that the transmitted beam distortion is due to the non-flatness of the transmission coefficient distribution in the spectrum region covered by the beam incidence.

Index Terms ─ Beam transmission, frequency selective surfaces, plane-wave spectrum, quasi optical instruments.

I. INTRODUCTION

The frequency selective surface (FSS) has been widely employed as the beam filter in microwave and optical applications. Being artificial periodic structures, reflection and transmission properties of an FSS can be efficiently calculated by modeling only one single unit under the periodic boundary condition (PBC) [1-5], due to plane-wave incidence. In case a size-limited beam other than a plane wave needs to be evaluated, which is more realistic, the analysis on transformation of the beam by an FSS can be more challenging. Techniques and methods have been developed [6-7], strengthened by the plane-wave spectrum (PWS) concept, treating arbitrary beam as a combination of plane waves from different directions. In our previous works, the transmitted fields through an FSS [8] and scattering from a periodic cone structure [9] under variable beam incidence were computed by the FDTD-PWS hybrid approach. It was highlighted that the calculated field responses to each plane-wave (by PBC simulations) can be reused, for further evaluations on the fields due to any varied beam incidence, which can be instantly obtained by simply recomposing the pre-calculated responses [9]. However, the PBC condition used in those works is functional only at a single frequency, as a result the advantage in the wideband analysis ability of FDTD algorithm wasn't token.

In practical applications, such as in the millimeter quasi-optical (QO) feed instruments for reflector antennas as in Fig. 1, it is necessary to design a serial of components to construct the beam path, where the near fields of transmitted beam through an FSS should be evaluated accurately [10-15]. Also, it is significant to meet the need of analyzing the changing patterns of beam transmission through FSS via variable beam incidence (etc., with different beam waist radius), which is cared by QO designers in the design and optimization process [11-15]. And in practice, one would like to know the frequency response in a band other than at a point. Motivated by this need and the wideband FDTD-PBC technique reported in [3], we are to update and complete the FDTD-PWS hybrid method for modeling planar periodic structures under beam illuminations.

Similar works on the hybrid of FDTD and PWS should be mentioned [16-17]. In those reports, results by PBC simulations are used to compose the fields in periodic structures due to a current source illumination. Such a hybrid is convenient for wideband investigations, because both the PBC simulations and field composition are performed in the time domain. However, for evaluating beam transmission through FSS, pre-calculated field responses to each plane-wave cannot be re-used in

Submitted On: July 26, 2014
Accepted On: June 17, 2016

the time domain re-composition, for fields due to a varied beam incidence. This is because the waveform (in time) of each equivalent current source (for presenting the beam) changes as the beam incidence varies, while in that scheme the same waveform is shared by the illuminating current and excitation signals in PBC simulations. On the contrary, we chose to conduct the field composition in frequency domain, while the time-domain PBC simulations offer necessary results within the frequency band of interest, as in Fig. 2. In this way, the proposed FDTD-PWS combination can handle beam transmission evaluation through FSS in the pass band, while the PBC simulation results can be re-used for variable beam incidence. It should be stated that the two hybrid approaches of FDTD and PWS share the same spirit in principle, but are different in methodology as aimed at different applications.

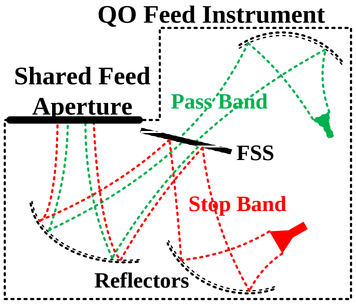

Fig. 1. Sketch of a FSS structure in a QO feed instrument.

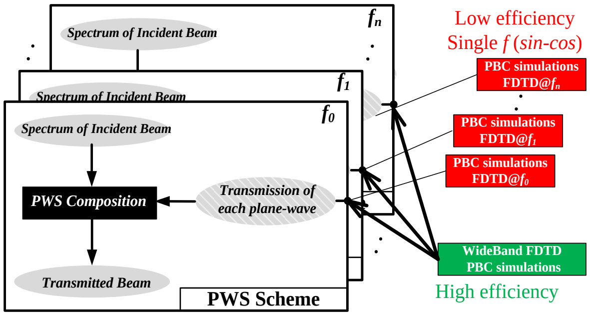

Fig. 2. Diagram of the band FDTD-PWS hybrid for analyzing beam transmission through FSS in the pass band.

For validating the updated FDTD-PWS hybrid method, we use the results obtained by directly modeling a finite-sized FSS screen with standard FDTD formulations. After that, we study the deforming effects on the transmitted beams by an FSS design within the pass band. The investigations are performed at the view of the transmission coefficient distributions in the PWS. As will be shown, such a spectrum analysis manner provides an intuitive perspective for beam propagation diagnostic through FSS.

The rest of this paper consists of five parts: in Section II, the configuration of beam transmission through FSS and the FDTD-PWS hybrid method is demonstrated; in Section III the FDTD-PWS calculations are verified; then the computation efficiency of the proposed hybrid is discussed in Section IV; in Section IV we study and discuss the deforming effects by the FSS; finally conclusions are drawn in Section V.

II. SECTION FORMATTING

A. Configuration

The configuration of beam transmission through FSS is presented in Fig. 3. Tangential components of the incident fields are sampled on the incident aperture (**IA**), for calculating the transmitted fields on the transmitted aperture (**TA**). And, the beam transmission coefficient T$_b$ is defined as:

$$\mathrm{T}_b = \frac{\iint (\vec{E}^t(x,y)|_{TA} \times \vec{H}^{t*}(x,y)|_{TA}) \cdot \hat{z}dxdy}{\iint (\vec{E}^i(x,y)|_{IA} \times \vec{H}^{i*}(x,y)|_{IA}) \cdot \hat{z}dxdy}. \tag{1}$$

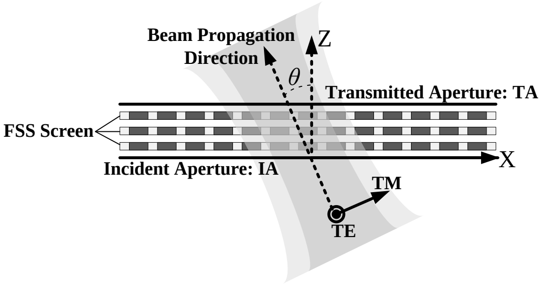

Fig. 3. Sketch of beam transmission through an FSS screen.

B. PWS solution for beam transmission through FSS

According to the PWS theory, tangential components of the transmitted fields at frequency f (wavelength λ) on **TA** can be obtained by using:

$$\begin{pmatrix} E_x^t(x,y)|_{TA} \\ E_y^t(x,y)|_{TA} \end{pmatrix} = \iint_{(k_x^2+k_y^2<k_0^2)} \tilde{M}(k_x,k_y,x,y) \begin{pmatrix} A_x^i(k_x,k_y) \\ A_y^i(k_x,k_y) \end{pmatrix} \frac{dk_x dk_y}{4\pi^2}, \tag{2}$$

where $k_0 = 2\pi/\lambda$, $k_x = k_0 sin\theta cos\varphi$, $k_y = k_0 sin\theta sin\varphi$; and $A^i_x(k_x,k_y)$ along with $A^i_y(k_x,k_y)$ stand for the PWS distributions of the incident fields $E^i_x(x,y)|_{IA}$ and $E^i_y(x,y)|_{IA}$ on **IA,** respectively. And,

$$\tilde{M}(k_x,k_y,x,y) = \begin{pmatrix} f_{xx}^t(k_x,k_y,x,y) & f_{xy}^t(k_x,k_y,x,y) \\ f_{yx}^t(k_x,k_y,x,y) & f_{yy}^t(k_x,k_y,x,y) \end{pmatrix}. \tag{3}$$

Here, $f_{\gamma\xi}^t(k_x,k_y,x,y)$ stands for the γ component distribution of the transmitted E-fields on **TA**, due to the plane-wave incidence of (k_x,k_y) with a unit ξ E-field component but without the other component. Here and in the rest of this paper, ξ and γ stand for x or y. The

$f^t_{\gamma\xi}(k_x,k_y,x,y)$ can be found from the results by PBC simulations of a single FSS unit, in which only the tangential ξ component of the incident *E*-field is included in the excitation via a soft source in FDTD.

Meanwhile, the incident spectrum $A^i{}_x(k_x,k_y)$ and $A^i{}_y(k_x,k_y)$ can be obtained by performing the inverse Fourier transform:

$$\begin{pmatrix} A^i_x(k_x,k_y) \\ A^i_y(k_x,k_y) \end{pmatrix} = \iint \begin{pmatrix} E^i_x(x,y)\,|_{IA} \\ E^i_y(x,y)\,|_{IA} \end{pmatrix} \cdot \mathrm{e}^{j(k_x\cdot x+k_y\cdot y)}\, dxdy\,. \qquad (4)$$

In this paper, the incident beam of Gaussian type is considered, which agrees with the general configuration in the QO feed instrument where the horns are designed to generate Gaussian-like beams that propagate in the routine guided by elliptical mirrors and FSSs (transparent or reflecting)[10-15]. In this case, the incident fields can be considered as band limited in the PWS (only propagating components are necessary to be considered in most cases). Therefore, the integration range of (2) and index range of (4) can be set to $k_x{}^2+k_y{}^2<k_0{}^2$.

On the other hand, if the reflected and transmitted fields are confined within the aperture of the FSS screen, then that can be considered as an infinite periodic structure for the incident beam. For that periodic structure with the period p_x and p_y, the $f^t_{\gamma\xi}(k_x,k_y,x,y)$ can be expressed as a summation of a set of Floquet harmonics:

$$f^t_{\gamma\xi}(k_x,k_y,x,y) = \sum_m \sum_n \alpha^{m,n}_{\gamma\xi}(k_x,k_y)\cdot \mathrm{e}^{-j\left[(k_x+\frac{2m\pi}{p_x})\cdot x+(k_y+\frac{2n\pi}{p_y})\cdot y\right]}\,. \qquad (5)$$

Generally, for the FSS structure designed without grid-lobes in the pass band, only the basic mode (*m*=0, *n*=0) of Floquet harmonics is propagable. By taking other harmonics (evanescent wave components) into consideration, one can evaluate all the local-field effects caused by the FSS structure, which however will not propagate far off the structure before vanishing.

Given that only the basic mode of Floquet harmonics is considered, Eq. (2) can be simplified into:

$$\begin{pmatrix} E^t_x(x,y)\,|_{TA} \\ E^t_y(x,y)\,|_{TA} \end{pmatrix} = \iint_{\left(k_x^2+k_y^2<k_0\right)} \tilde{M}_a \cdot \begin{pmatrix} A^i_x(k_x,k_y) \\ A^i_y(k_x,k_y) \end{pmatrix} \frac{dk_x dk_y}{4\pi^2}\,, \qquad (6a)$$

$$\tilde{M}_a(k_x,k_y,x,y) = \begin{pmatrix} \alpha_{xx}(k_x,k_y) & \alpha_{xy}(k_x,k_y) \\ \alpha_{yx}(k_x,k_y) & \alpha_{yy}(k_x,k_y) \end{pmatrix} \cdot e^{-j(k_x\cdot x+k_y\cdot y)}\,. \qquad (6b)$$

Here and in the rest of this paper, the upper-script$^{(0,0)}$ for $\alpha_{\gamma\xi}(k_x,k_y)$ is omitted.

The four transmission coefficients, $\alpha_{\gamma\xi}(k_x,k_y)$, consist of the FSS transmission function in the PWS. Without the consideration of evanescent waves, the Eq. (6) is in form of Fourier transformation, and allows a more efficient field re-composition than that using Eq. (2).

The formulations for obtaining the transmitted *H*-fields on **TA** are similar to that for the *E*-fields, and are not listed here for brevity. Meanwhile, the discretization's in the PWS for implementing Eqs. (2), (4), and (6) will not be discussed in detail here, as can be referred to [6,8-9]. Generally, the sampling interval of k_x and k_y is related to the size of FSS screen to be modeled: as the size of FSS aperture rises, the sampling interval in the PWS have to decrease accordingly for avoiding space aligns [9].

In implementation, the FDTD-PWS hybrid approach in modeling the planar periodic structure under the beam illumination can be divided into two procedures:

1) Sweeping of PBC simulations to obtain $f^t_{\gamma\xi}(k_x,k_y,x,y)$ or $\alpha_{\gamma\xi}(k_x,k_y)$ at each frequency;
2) Incident beam decomposition using Eq. (4) and field re-composition using Eq. (2) or Eq. (6).

C. Wideband PBC for the FDTD-hybrid

The FDTD-PWS approach used in this paper is updated from that in [8, 9], by using the complex-field PBC [3] for the wideband computations. In the complex-field PBC method, the complex-fields are iteratively updated in the time domain, and the tangential component of the wave number $\boldsymbol{k}_\rho$ is fixed. As a result, the plane-wave incident direction angle θ varies with frequency *f*. The advantages of the complex-field PBC method over others such as the split-field method [2, 5], include improved computational efficiency especially in the large incident angle situation, being robust for arbitrary material properties, as well as simplicity in implementation.

From the PBC calculations, both the transmission coefficients $\alpha_{\gamma\xi}(k_x,k_y)$ and the field distribution $f^t_{\gamma\xi}(k_x,k_y,x,y)$ can be recorded at cared frequencies for the field re-composition purpose. In practical, it would be storage expensive to restore the $f^t_{\gamma\xi}(k_x,k_y,x,y)$ results for Eq. (2), especially when evaluations at a large number of frequencies are to be carried out. Meanwhile, the $\alpha_{\gamma\xi}(k_x,k_y)$ recording and the field re-composition by Eq. (6) can be much more efficient in storage and computation. However, the evanescent waves are dropped out in this manner, and the local-fields by the FSS structure cannot be observed in the re-composed field results. In the following sections, both the results by Eq. (2) and Eq. (6) will be presented and compared, for the analysis on the transmitted beam degradations through FSS.

III. VALIDATION OF METHOD

A. Validation of FDTD-PBC results

The FSS structure considered in this work is designed for the beam transmission from 215 GHz to 225 GHz, at the direction of (θ=30°, φ=180°). For the FDTD formulations, each periodic unit of this FSS can be discretized into $30(x) \times 30(y) \times 50(z)$ Yee-cells. The calculated plane-wave coefficients by our in-house FDTD-PBC realization and one commercial software [18] are compared in Fig. 4.

As can be seen, the results match well with each other. This implies that the complex-field FDTD-PBC was implemented correctly for this study.

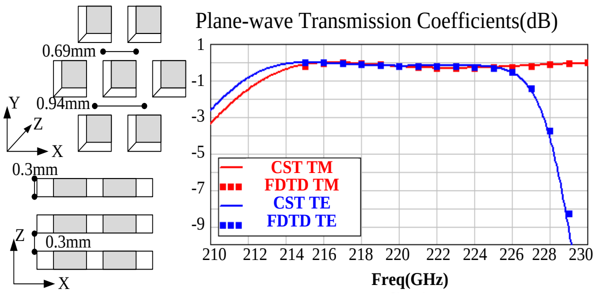

Fig. 4. Comparison of calculated plane-wave transmission coefficients (plane-wave incidence at θ=30°, φ=180°), dB.

In the PBC computation as well as in the field re-composition, the incident aperture **IA** and incident aperture **TA** are ten Yee-cells distant away from the FSS structure. That means the fields on an aperture that is very close to the FSS structure are investigated in this paper.

B. Validation of FDTD-PWS results

To validate the band FDTD-PWS hybrid method, we directly modeled the whole FSS screen by standard FDTD formulations to provide reference results, and the simulation in this way is denoted by "FDTD". Then on the transmitted aperture **TA**, field distributions calculated by the two methods due to normal beam incidence are compared in Fig. 7, and good agreements can be observed. We used Eq. (2) in the re-composition procedure of FDTD-PWS, so that the recomposed field distributions contain information of all the local-field effects by the FSS, and can be directly compared with that by FDTD. The incident beams considered in this set of simulations are of the Gaussian basic mode [10] with the waist radius ω_0 equaling 2λ, TM polarized. And in the Fig. 5, the beam transmission coefficient results are compared. For the FDTD-PWS method, results by Eq. (6) are presented, which agrees well with that by direct "FDTD" computations. That means, even on the aperture **TA** that is very close to the FSS structure, by using Eq. (6) for the field re-composition (considering only the propagable plane-wave components without evanescent ones) one can still investigate the beam transmission coefficient correctly and sufficiently.

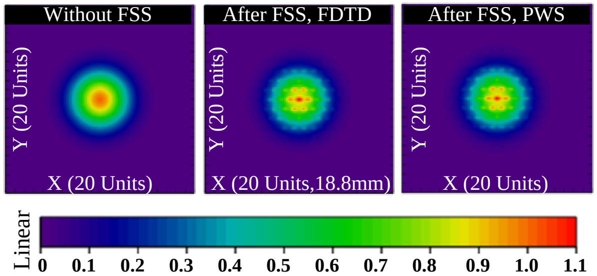

Fig. 5. Comparison of calculated transmission fields at 220 GHz on the transmitted aperture, by FDTD and FDTD-PWS (re-composition by Eq. (2)), normal beam incidence (ω_0 = 2λ, θ=0°, φ=180°), TM polarization, normalized by the maximum of reference free-space transmitted fields, linear.

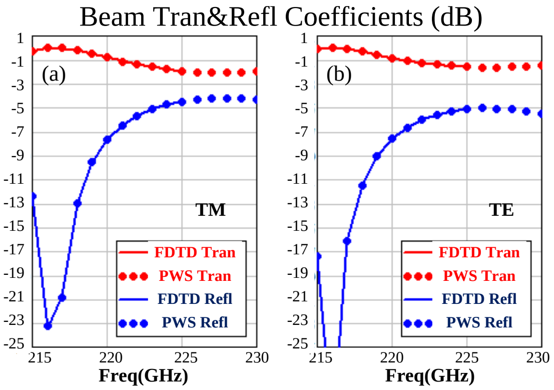

Fig. 6. Comparison of calculated beam transmission and reflection coefficients from 215 to 230 GHz, by the FDTD and band FDTD-PWS (Eq. 6), normal beam incidence (ω_0= 2λ, θ=0°, φ=180°), TE and TM polarization.

IV. SAMPLING IN K-DOMAIN AND COMPUTATION EFFICIENCY

In this section, the computation efficiency of the proposed FDTD-PWS method is discussed. First, an important issue is the sampling in the k_x-k_y domain. The discretized sampling in the k domain leads to periodic expansion in space domain. To model a planar FSS screen of aperture size L_ξ (ξ stands for x or y) without space alias, a sampling interval less than $k_0\lambda/L_\xi$ is necessary, leading to $2L_\xi/\lambda$ samplings in the k_ξ domain(-k_0~+k_0). After dropping evanescent compo-nents in the k_x-k_y domain ($k_x^2+k_y^2>k_0^2$), one requires PBC responses at $\pi L_x L_y/\lambda^2$ sampling positions for the PWS composition. By using an even smaller interval and a larger sampling number, field interference at aperture edges in the PWS composition (if exists) can be further reduced [9].

Actually, the main computation load of the FDTD-PWS is in the procedure of PBC simulations, which requires calculations at a number $\pi L_xL_y/\lambda^2$ of k_x-k_y spectrum positions. Consider the same time duration in the FDTD computation, the CPU load for simulating a finite-sized FSS screen (consists of $Nx*Ny$ units, leading to aperture size of $L_x=N_xp$, $L_y=N_yp$) is $Nx*Ny*\mathbf{O}(C)$, as a reference. In PBC simulations for the FDTD-PWS hybrid, at one k_x-k_y sampling point, the CPU load is $4\mathbf{O}(C)$, due to requirements of complex field computation and TE/TM excitation. That leads to totally $4\pi NxNyp^2/\lambda^2*\mathrm{O(C)}$ for the PBC simulation procedure. Further, if symmetry exist in the FSS unit, the computation burden can be cut to $\pi NxNy*p^2/\lambda^2*\mathrm{O(C)}$. In an ideal case, the CPU computation load of PBC simulations is $\pi p^2/\lambda^2$ times to a direct FDTD simulation for the FSS screen with symmetric unit structure, and for the parameters in this paper, this factor is 1.64 (λ@230GHz, p = 0.94mm). Further, in practical, the k_x-k_y region may not need to be fully sampled in ($k_x^2+k_y^2<k_0^2$), as one doesn't require those results in case of large incident angles. Therefore sampling in the spectrum region $k_x^2+k_y^2<t^2k_0^2$ (t<1) should be sufficient. Here t = sin($\theta_{\max}$), and $\theta_{\max}$ is the maximum incident direction angle necessary to be considered in the PBC simulations[9].

Table 1: Comparison of CPU run times by FDTD-PWS and FDTD for FSS structures of different aperture sizes (On an Intel Core i7 desktop)

Array Size (in Units)	FDTD-PWS		FDTD
	PBC Runs	Re-composition by Eq. (2)	
28×28	12(h) 536 runs	24(s) per frequency	9(h)
36×36	24(h) 884 runs	64(s) per frequency	16(h)
46×46	32(h) 1424 runs	170(s) per frequency	—

Table 2: Comparison of memory costs by FDTD-PWS and FDTD for FSS structures of different aperture sizes

Array Size (in Units)	FDTD-PWS		FDTD
	PBC Runs	Re-composition by Eq. (2)	
28×28	52(MB)	227(MB)	2294(MB)
36×36	54(MB)	370(MB)	5076(MB)
46×46	56(MB)	599(MB)	—

In the above tables, the CPU run times and memory cost of the two methods are listed to be compared. The advance in computation efficiency of the FDTD-PWS hybrid is in the re-composition procedure. When treating varied beam incidence, such as the many illumination cases considered in the next chapter, the FDTD-PWS requires only minutes to harvest results, meanwhile the FDTD need repeated direct computations costing hours. On the other hand, as the FDTD-PWS hybrid performs computation within a unit cell, the reduction of memory cost over FDTD for modeling the FSS screen should also be remarked.

V. DISCUSSIONS ON THE BEAM DEGRADATION

Here, the cases of oblique beam incidence are considered, where the incident beams are illuminating at the direction of (θ=30°, φ=180°), TE and TM polarized separately. The transmitted field distributions on **TA** calculated by both FDTD and FDTD-PWS (using Eq. (2)), are presented in Fig. 7, while the fields on **TA** but through free-space are also draw as references. Clearly those results of transmitted fields through FSS by the two methods agree well. It is worth noting that, to obtain results in Fig. 7 by the "FDTD" solution, repeating computations have to be performed. On the contrary, in the FDTD-PWS hybrid method, only the field re-composition procedure is required based on the restored PBC calculate results. As a result, the comparison between the computation times by two approaches for this problem, can be hours (FDTD) to minutes or even seconds (FDTD-PWS).

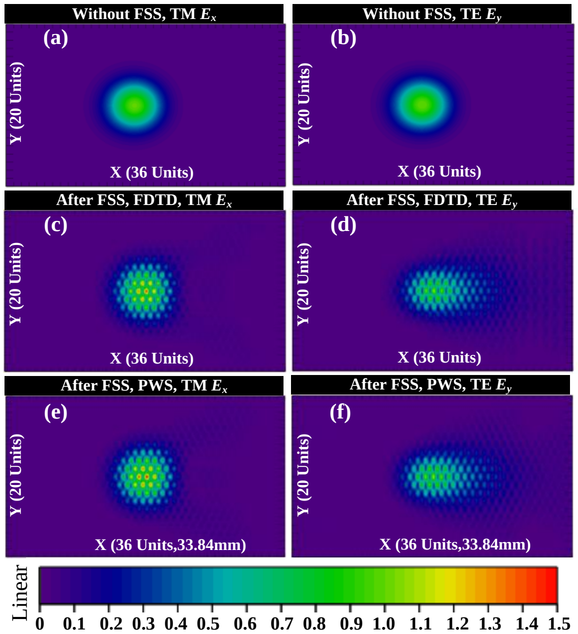

Fig. 7. Comparison of calculated transmission fields at 220 GHz on the transmitted aperture, by FDTD and FDTD-PWS (re-composition by Eq. (2)), oblique beam incidence (ω_0=2λ, θ=30°, φ=180°), TE and TM polarization, normalized by the maximum of reference free-space transmitted fields, linear.

On the other hand, it is evident that, in the transmitted field distributions, beam distortions can be observed in both the cases of TE and TM incidence. Also the transmitted beams show tangential shifts comparing to the referencing free-space transmitted beam. And the distortions in the TE transmitted beam are more severe than that in the TM transmitted beam. Meanwhile, the transmitted field distributions calculated by using Eq. (6) (without all the evanescent waves) are presented in Fig. 8. It is clear to readers that, the same distortion patterns in the transmitted field distributions in either the TE or TM incident case, are shared in the results by Eq. (2) and by Eq. (6). That implies, the reason for the transmitted beam distortions, should be blamed to the $\alpha_{\gamma\xi}(k_x,k_y)$ distributions, which define the FSS response to each incident plane-waves as in Eq. (6).

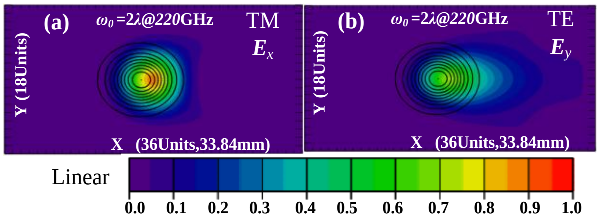

Fig. 8. Calculated transmission fields at 220 GHz on the transmitted aperture, by FDTD-PWS (using Eq. (6)), oblique beam incidence (ω_0 = 2λ, θ=30°, φ=180°), TE and TM polarization, normalized by the maximum of reference free-space transmitted fields (black lines contoured), Linear.

It would be interesting and intuitive to investigate the beam distortion effects by the FSS via $\alpha_{xx}(k_x,k_y)$ and $\alpha_{yy}(k_x,k_y)$ in the PWS, the magnitude distributions of which are contoured in Fig. 10 at different frequencies. When the beam incident direction is in the XOZ plane (φ=180°), the $\alpha_{xx}(k_x,k_y)$ plays a significant role for transmission of the TM polarized beam, while the $\alpha_{yy}(k_x,k_y)$ is vital for transmission of the TE one. In Fig. 10, spectrum regions covered by the incident spectrum $A^i_\xi(k_x,k_y)$ with the edge level of -20dB are closely curved, in cases of the waist radius ω_0 of incident Gaussian beam equaling 2λ and 4λ. Apparently when ω_0 increases, the corresponding spectrum coverage area decreases. However, in the practical design of QO instruments, more spaces are required by designers for placing corresponding elliptical reflectors [10], if a larger waist radius ω_0 of the propagating beam is to be realized.

It is evident that, when beams of ω_0 = 2λ are illuminating at 220 GHz, distributions of neither $\alpha_{xx}(k_x,k_y)$ nor $\alpha_{yy}(k_x,k_y)$ are flat in magnitude within the spectrum region covered by the incident beam (Fig. 10 (c) or (d)). Meanwhile, transmitted beam distortions occur. It is also interesting, to observe the relationship between the $\alpha_{xx}(k_x,k_y)$ distribution pattern and TM transmitted beam distortions, and that between $\alpha_{yy}(k_x,k_y)$ and the severely distorted TE transmitted beam (Fig. 8 and Fig. 10). The non-flatness patterns in $\alpha_{\xi\xi}(k_x,k_y)$ reveal themselves accordingly in the transmitted field distributions due to the corresponding polarized beam incidence. On the other hand, if the incident beams of ω_0 = 4λ are illuminating, the incident spectrum region are smaller in size. As a result, the area of non-flatness in $\alpha_{xx}(k_x,k_y)$ and $\alpha_{yy}(k_x,k_y)$ distributions are greatly reduced in percentage. The corresponding transmitted fields distributions by Eq. (6) are presented in Fig. 9. It can be seen that, the TM transmitted fields is nearly clean of distortions. Meanwhile, the TE transmitted fields still suffer notable distortions, as in the $\alpha_{yy}(k_x,k_y)$ distribution "cliff" exists in the edge area of spectrum region covered by the incident Gaussian beam (ω_0 = 4λ).

It is also intuitive to observe the transmitted beam propagation off the FSS structure in the vertical cut, the results of which at 220 GHz are presented in Fig. 11. Those results are by Eq. (6) and PWS propagation equations. At another view, the transmitted beam distortions can be observed, especially those in the TE transmitted beams due to the $\alpha_{yy}(k_x,k_y)$ magnitude "cliff" as in Fig. 10 (d).

Another interesting trend concluded from Fig. 10 is that, the area of flat $\alpha_{\xi\xi}(k_x,k_y)$ distributions are shrinking in size, as the frequency rise from 217 GHz to 225 GHz. That trend can also be observed in the beam transmission coefficient results presented in Fig. 12, that the curves of results is heading downside in the specific frequency region. And, as the incident beam waist width ω_0 in the spatial domain increases, the corresponding spectrum coverage area decreases. As a result, beam transmission coefficients are more close to the plane-wave ones, while beam distortions can be relieved.

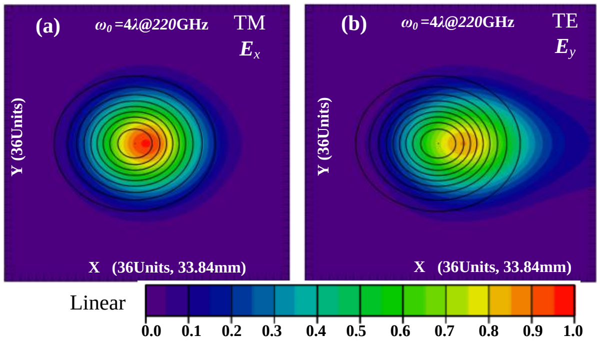

Fig. 9. Calculated transmitted E-fields at 220 GHz on the transmitted aperture, by FDTD-PWS (using Eq. (6)), oblique beam incidence (ω_0 = 4λ, θ=30°, φ=180°), TE and TM polarization, normalized by the maximum of free-space transmitted fields (black lines contoured), linear.

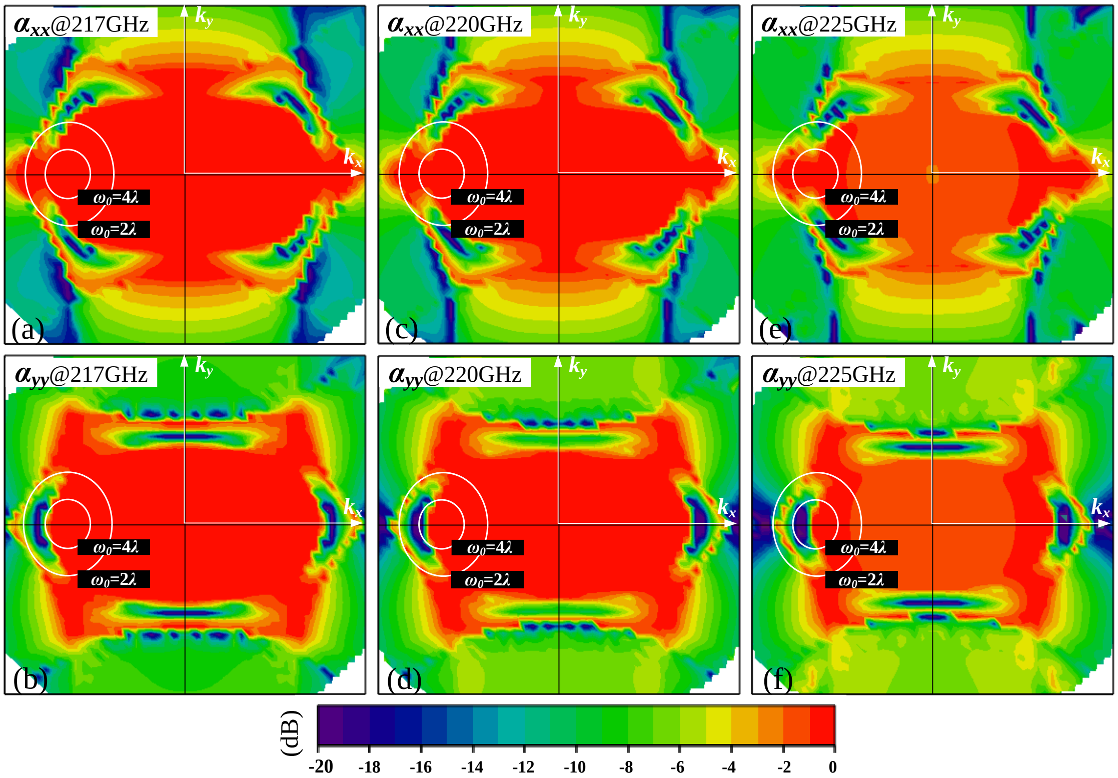

Fig. 10. Comparison of calculated plane-wave transmission coefficients of $\alpha_{xx}(k_x,k_y)$(first row) and $\alpha_{yy}(k_x,k_y)$ (second row), at 217 GHz (first column), 220 GHz (second column), and 225 GHz (third column), dB; spectrum regions (with -20 dB edge level) covered by the beam incidence of different $\omega_0(\theta=30^o,\ \varphi=180^o)$ are closely curved.

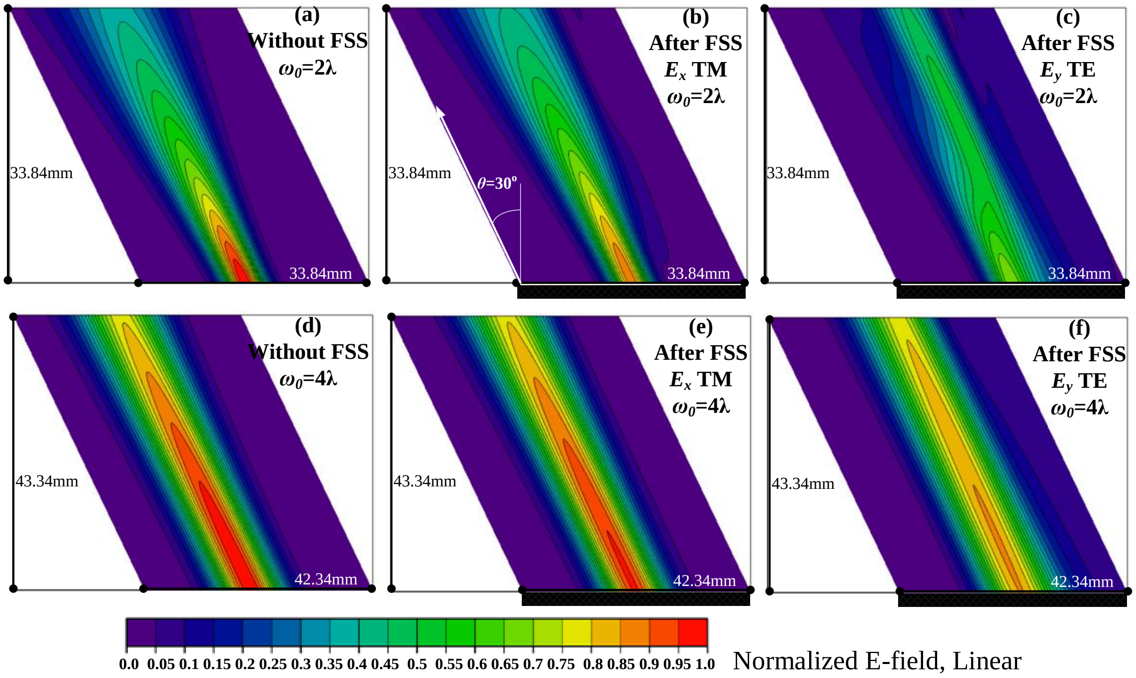

Fig. 11. Transmitted beam distributions in the vertical cut, oblique beam incidence of different $\omega_0(\theta=30^o,\ \varphi=180^o)$, TE or TM polarized, @ 220 GHz. The results are obtained by Eq. (6), in magnitude, linear, normalized by maximum of free-space transmitted beam.

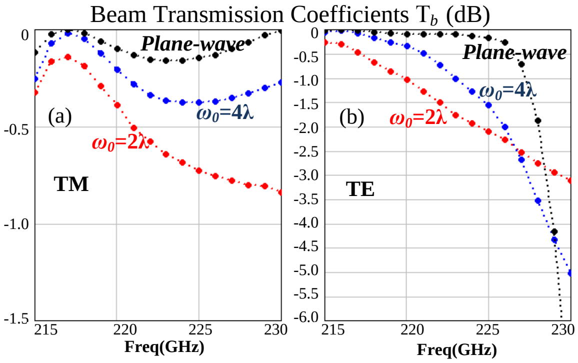

Fig. 12. Comparison of calculated beam and plane-wave transmission coefficients, oblique beam incidence (θ=30°, φ=180°), TM and TE polarization, dB.

It can be concluded that, the observed beam distortion is due to the non-flatness of the transmission coefficients distribution in spectrum region covered by the beam incidence. And, the investigation on $\alpha_{\xi\xi}$ (k_x,k_y) in the PWS provides an intuitive perspective for evaluating and diagnosing the beam propagation through an FSS.

At last, another set of the calculated T_b results are presented in Fig. 13, which are under beam incidence towards different directions. The varying trends of T_b versus beam incident direction can be clearly observed. These results contain information cared by QO designers in the practical design and optimization process, and can be efficiently obtained by the band FDTD-PWS hybrid method.

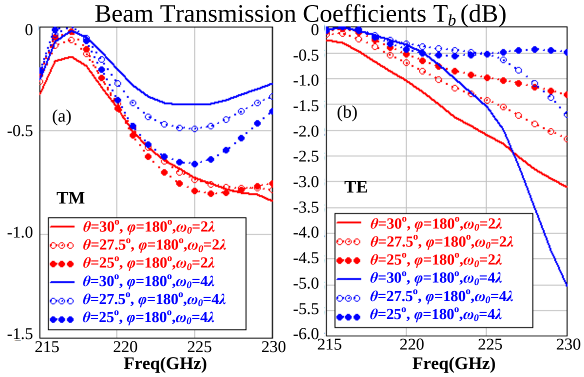

Fig. 13. Comparison of the calculated beam transmission coefficients at different beam incident angles, with the waist radius ω_0 = 2λ or 4λ; the beam transmission coefficients are obtained by the band FDTD-PWS; TM and TE polarization, dB.

VI. CONCLUSION

With implementation of the wideband complex-field PBC technique for modeling the FSS unit, we updated and completed the FDTD-PWS hybrid method. The proposed method takes advantage of the FDTD method in the wideband computation ability, while the PBC simulation results can be re-used in the rapid re-composition for fields due to variable beam incidence. Consequently, it meets the need of efficient beam transmission evaluation through FSS within the frequency band of interest. The solution has been validated by results of standard FDTD formulations in directly modeling the whole finite-sized FSS screen.

The degradations of the transmitted beams through a dual-polarized FSS design were studied, and that of TE polarized beams are more severe than that of TM polarized beams. Actually, it can be concluded that the observed beam distortion is highly related to the non-flatness in the magnitude distribution of plane-wave transmission coefficients, in the spectrum region covered by the beam incidence. It is demonstrated in this work that, the beam transmission performance of an FSS can be evaluated directly in the PWS, even on an aperture very close to the FSS structure. And such a spectrum analysis manner provides an intuitive perspective for the beam propagation diagnostic through periodical structures, especially for the practical design and optimization of full-polarized millimeter Quasi-Optical (QO) instruments.

ACKNOWLEDGMENT

This work is supported by the National Basic Research Program of China (973 Program) under Grant 2012CB315601.

REFERENCES

[1] R. Mittra, C. Chan, and T. Cwik, “Techniques for analyzing frequency selective surfaces: A review,” *IEEE Proceedings*, vol. 76, pp. 1593-1615, 1988.

[2] J. Roden, S. Gedney, M. Kesler, J. Maloney, and P. Harms, “Time domain analysis of periodic structures at oblique incident: Orthogonal and non-orthogonal FDTD implementations,” *IEEE Trans. Microwave theory Tech.*, vol. 46, no. 4, pp. 420-427, 1998.

[3] F. Yang, J. Chen, R. Qiang, and A. Elsherbeni, “A simple and efficient FDTD/PBC algorithm for scattering analysis of periodic structures,” *Radio Science*, vol. 42, RS4004, 2007.

[4] K. ElMahgoub, F. Yang, A. Z. Elsherbeni, V. Demir, and J. Chen, “FDTD analysis of periodic structures with arbitrary skewed grid,” *IEEE Trans. Antennas Propagat.*, vol. 58, no. 8, pp. 2649-2658, 2010.

[5] M. Bai, B. Liang, and H. Ma, “An efficient FDTD algorithm to analyze skewed periodic structures impinged by obliquely incident wave,” *Journal of the Applied Computational Electromagnetic Society*, vol. 30, no. 10, pp. 1068-1073, 2015.

[6] M. Pasian, M. Bozzi, and L. Perregrini, “Accurate modeling of dichroic mirrors in beam-waveguide

antennas," *IEEE Trans. Antennas Propagat.*, vol. 61, no. 4, pp. 1931-1938, 2013.

[7] V. Prakash, N. T. Huang, and R. Mittra, "Accurate analysis of interaction between microwave antennas and frequency selective surface (FSS) radomes," *ICAP 2003*, vol. 1, pp. 401-404, March 31-April 3, 2003.

[8] M. Jin, M. Bai, N. Ou, and J. Miao, "The plane-wave approach for beam transmission through planar FSS structures," *ICMMT 2012, IEEE International*, pp. 128-131, May 2012.

[9] M. Bai, M. Jin, N. Ou, and J. Miao, "On scattering from an array of absorptive material coated cones by the PWS approach," *IEEE Trans. Antennas Propagat.*, vol. 61, no. 6, pp. 3216-3224, 2013.

[10] P. Goldsmith, *Quasi-optical Systems: Gaussian Beam Quasi-optical Propagation and Applications*. Piscataway, NJ, IEEE Press, 1998.

[11] R. Martin and D. Martin, "Quasi-optical antennas for radiometric remote sensing," *Electronics and Commnications Engineering Journal*, vol. 8, no. 1, pp. 37-48, 1996.

[12] L. Costes, C. Bushell, M. Buckley, et al., "Microwave humidity sounder (MHS) antenna," *Proc. SPIE*, 3870, pp. 412-426, 1999.

[13] R. Jorgensen, G. Padovan, P. de Maagt, D. Lamarre, and L. Costes, "A 5-frequency mili-meter wave antenna for a spaceborne limb sounding instrument," *IEEE Trans. Antennas Propagat.*, vol. 49, no. 5, 2001.

[14] S.-W. Zhang, J. Li, Z.-Z. Wang, et al., "Design of the second generation microwave humidity sounder (MWHS-II) for Chinese meteorological satellite FY-3," *Proc. IGARSS'12*, Munich, pp. 4672-4675, 2012.

[15] M. Candotti, A. Baryshev, and N. Trappe, "Quasi-optical assessment of the ALMA band 9 front-end," *Infrared Physics & Technology*, vol. 52, no. 5, pp. 174-179, 2009.

[16] R. Qiang, J. Chen, and F. Yang, "Finite difference time domain modeling of finite-sized electro-magnetic source over periodic structure via a plane wave spectral expansion approach," *Radio Science*, vol. 45, RS5003, 2010.

[17] R. Qiang, J. Chen, F. Capolino, and D. R. Jackson, "ASM-FDTD: a technique for calculating the field of a finite source in the presence of an infinite periodic artificial material," *Microwave and Wireless Components Letters, IEEE*, vol. 17, no. 4, pp. 271-273, 2007.

[18] https://www.cst.com/Products/CSTMWS

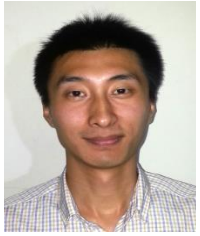

Ming Jin received his B.Sc. and Ph.D. degrees from Beihang University (BUAA), Beijing, China, in 2007 and 2013, respectively. From 2007 to 2013, he has been a Research Assistant in the Microwave Engineering Laboratory, Beihang University. From Dec. 2010 to Mar. 2011, he was a Visiting Scholar at Arizona State University. From 2013 to 2015, he was with the Science and Technology on Electromagnetic Scattering Laboratory. He is now with the State Key Laboratory of Remote Sensing Science, Institute of Remote Sensing and Digital Earth, Chinese Academy of Sciences. His research interests include, computational electromagnetic and microwave imaging.

Ming Bai received his B.Sc. and Ph.D. degrees from Physics Department of the University of Science and Technology of China (USTC) in 1996 and 2002, respectively. From 2002 to 2006, he worked as a Postdoctoral Researcher in the Laboratory of Nano-technology (LFSP), Spanish National Research Council (CSIC). He joined Beihang University (BUAA) China, in 2006. Currently he worked as a Professor in Microwave Engineering Lab., Beihang University. His research interests include computational electromagnetic and microwave imaging.